

**A comprehensive analysis of the nucleus of the
radio source 3C 84 with VLBI**

INAUGURAL-DISSERTATION

zur Erlangung des Doktorgrades der
Mathematisch-Naturwissenschaftlichen Fakultät der
Universität zu Köln



vorgelegt von

Georgios Filippas Paraschos
aus Amarousio Attikis, Griechenland

Köln, 2022

Berichtersteller:

Prof. Dr. Andreas Eckart

Prof. Dr. Peter Schilke

Prof. Dr. J. Anton Zensus

Tag der letzten mündlichen Prüfung: 27.09.2022

Erklärung

Ich versichere, dass ich die von mir vorgelegte Dissertation selbständig angefertigt, die benutzten Quellen und Hilfsmittel vollständig angegeben und die Stellen der Arbeit – einschließlich Tabellen, Karten und Abbildungen –, die anderen Werken im Wortlaut oder dem Sinn nach entnommen sind, in jedem Einzelfall als Entlehnung kenntlich gemacht habe; dass diese Dissertation noch keiner anderen Fakultät oder Universität zur Prüfung vorgelegen hat; dass sie – abgesehen von unten angegebenen Teilpublikationen – noch nicht veröffentlicht worden ist sowie, dass ich eine solche Veröffentlichung vor Abschluss des Promotionsverfahrens nicht vornehmen werde. Die Bestimmungen dieser Promotionsordnung sind mir bekannt. Die von mir vorgelegte Dissertation ist von Prof. Dr. A Eckart und Prof. Dr. J. A. Zensus betreut worden.

Köln, den 27.09.2022

A handwritten signature in black ink, appearing to be 'M. Hagen', written in a cursive style.

Relevante zur Doktorarbeit Teilpublikationen¹

Paraschos, G. F.; Kim, J. -Y.; Krichbaum, T. P. and Zensus, J. A., *Pinpointing the jet apex of 3C 84*, 2021, A&A, 650, L18

Oh, J.; Hodgson, J. A.; Trippe, S.; Krichbaum, P.; Kam, M.; **Paraschos, G. F.;** Kim, J.-Y.; Rani, B.; Sohn, B. W.; Lee, S.-S.; Lico, R.; Liuzzo, E.; Bremer, M. and Zensus, A., 2022, *A persistent double nuclear structure in 3C 84*, 2022, MNRAS, 509, 1, 1024-1035

Paraschos, G. F.; Kim, J. Y.; Krichbaum, T.; Oh, J.; Hodgson, J. A.; Gurwell, M. A. and Zensus, A., 2022, *Pinpoint the jet apex in 3C 84*, PoS, European VLBI Network Mini-Symposium and Users' Meeting 2021, 43

Paraschos, G. F.; Krichbaum, T. P.; Kim, J. -Y.; Hodgson, J. A.; Oh, J.; Ros, E. and Zensus, J. A.; Marscher, A. P.; Jorstad, S. G.; Gurwell, M. A.; Lähteenmäki, A.; Tornikoski, M.; Kiehlmann, S. and Readhead, A. C. S., 2022, *Jet kinematics in the transversely stratified jet of 3C 84 A two-decade overview*, A&A, 665, A1

¹Siehe Lebenslauf am Ende für eine umfassende Liste.

Abstract

Jets powered by active galactic nuclei (AGN) are some of most powerful phenomena of the cosmos. Understanding the underlying physical mechanisms is necessary to enhance our knowledge of the universe. The focus of this thesis lies on the innermost region of the radio source 3C 84, harboured in the radio galaxy NGC 1275, which exhibits such energetic jets. Perhaps connected to this jet activity is a perpendicularly to the bulk jet flow oriented structure, which was recently revealed in a RadioAstron space very-long-baseline interferometry (VLBI) image. Interpreting this structure and its implications to jet physics is one of the main motivations of this thesis. It is accomplished by utilising millimetre-VLBI observations of 3C 84 at the highest resolution, with the available data covering a period of more than twenty years and at different frequencies.

The thesis is organised as follows: in Sect. 1 an overview of the astrophysical background required to interpret the data is introduced. This includes brief descriptions of the radiation received by the telescopes, of black holes and AGN, as well as of astrophysical jets. AGN classification schemes and the relevant details of jet physics are also discussed.

Section 2 offers a review of the technical background, including the basics of the technique of interferometry and VLBI arrays, calibrating a VLBI data set and imaging it.

In Sect. 3 we utilise quasi-simultaneous observations at 15, 43, and 86 GHz and create the highest resolution spectral index images of 3C 84 to date. Our analysis reveals the existence of a spectral index gradient in the north-south direction, with values between $\alpha_{43-86} \sim 2$ upstream of the 86 GHz VLBI core and $\alpha_{43-86} \sim -2$ downstream. In this context, we discuss the spectral index distribution. We determine the location of the jet apex to be $400 - 1500 R_s$ (Schwarzschild radii) upstream of the 86 GHz VLBI core, by means of two-dimensional cross-correlation analysis. In that region, the magnetic field appears to be a mix between poloidal and toroidal, with a strength of $2 - 4$ G.

Section 4 presents an alternative approach for pinpointing the jet apex of 3C 84, by directly imaging the core region. The temporal stacking of a number of 86 GHz data sets at different epochs confirms the existence of a double component structure present in the core region, concurring the RadioAstron result. Both a conical and a parabolic jet expansion profile are then fit to the data to determine the shape of the expansion. This constrains the position of the jet apex to $200 - 3000 R_s$ upstream of the 86 GHz VLBI core. Our analysis also reveals a possible change of viewing angle along the jet flow (perhaps in-

dicative of jet bending) and sets an upper limit for the viewing angle of 35° for the inner jet.

Section 5 showcases a comprehensive study of the evolution and jet kinematics of 3C 84 over more than twenty years. Our analysis reveals the ejection of numerous components from the core region, which seem to move at subluminal speeds, with newer components being faster. We also checked for possible differences between the velocities of the 43 and 86 GHz components individually but only found marginal evidence of faster motion at 86 GHz. The jet width appears frequency dependent, with the jet width decreasing with increasing frequency, which might be explained by stratification in the context of the spine-sheath jet stratification scenario. We also produced spectral index maps at 43 – 86 GHz, which show that the orientation of the spectral index gradient position angle is time variable. This further indicates that the black hole is positioned off-centred from the total intensity maximum and that the jet axis is changing with time.

Finally, in Sect. 6 our analysis and results are summarised and in Sect. 7 an outlook for the future is provided.

Zusammenfassung

Astrophysikalische Jets, die von aktiven galaktischen Kernen (AGN) angetrieben werden, sind einige der energischsten Phänomene des Kosmos. Das Verständnis der zugrunde liegenden physikalischen Mechanismen ist notwendig, um unser Wissen über das Universum zu erweitern. Der Schwerpunkt dieser Arbeit liegt auf dem innersten Bereich der Radioquelle 3C 84, die sich im Kern der Radiogalaxie NGC 1275 befindet und solche energiereichen Jets aufweist. Diese Jet-Aktivität steht möglicherweise im Zusammenhang mit einer senkrecht zur Hauptströmung des Jets orientierten Struktur, die kürzlich in einer RadioAstron Weltraum very-long-baseline interferometry (VLBI) Beobachtung entdeckt wurde. Die Interpretation dieser Struktur und ihre Bedeutung für die Jet-Physik ist die Hauptmotivation dieser Arbeit. Dazu werden Millimeter-VLBI Beobachtungen von 3C 84 mit der höchsten Auflösung über mehr als zwanzig Jahre und bei verschiedenen Frequenzen verwendet.

Die Doktorarbeit ist wie folgt aufgebaut: Im Abschnitt 1 wird ein Überblick über den theoretischen Hintergrund gegeben, der zur Interpretation der Daten erforderlich ist. Kurz beschrieben werden die von den Teleskopen empfangene Strahlung und die daraus resultierenden Erkenntnisse zu Schwarzen Löchern und AGN, sowie astrophysikalischen Jets. Außerdem werden AGN-Klassifizierung und relevante Details der Jet-Physik diskutiert.

Im Abschnitt 3 nutzen wir quasi-simultane Beobachtungen bei 15, 43 und 86 GHz und erstellen die höchstauflösendsten Spektralindexbilder von 3C 84 bis dato. Unsere Analyse deutet auf die Existenz eines Spektralindexgradienten in Nord-Süd-Richtung, mit Werten zwischen $\alpha_{43-86} \sim 2$ stromaufwärts des 86 GHz VLBI-Kerns und $\alpha_{43-86} \sim -2$ stromabwärts. In diesem Zusammenhang diskutieren wir die Spektralindexverteilung. Mit Hilfe einer zweidimensionalen Kreuzkorrelationsanalyse bestimmen wir die Position des Jet-Apex; sie befindet sich $400 - 1500 R_s$ (Schwarzschild Radii) stromaufwärts vom 86 GHz VLBI-Kern. In dieser Region scheint das Magnetfeld eine Mischung aus poloidalem und toroidalem Feld zu sein, mit einem Wert von $2 - 4 G$.

Im Abschnitt 4 wird ein alternativer Ansatz vorgestellt, um die Position des Jet-Apex von 3C 84 durch die direkte Abbildung der Kernregion zu lokalisieren. Die zeitliche Stapelung einer Reihe von 86 GHz Datensätzen, beobachtet zu verschiedenen Epochen, bestätigt die Existenz einer Doppelkomponentenstruktur in der Kernregion, die mit dem RadioAstron-Ergebnis übereinstimmt. Um die Form der Expansion zu bestimmen, werden die Daten an ein konisches und ein parabolisches Jetexpansionsprofil angepasst. Dadurch wird die Position des Jet-Apex auf $200 - 3000 R_s$ stromaufwärts des 86 GHz VLBI-Kerns einge-

grenzt. Unsere Analyse zeigt auch eine mögliche Änderung des Sichtwinkels entlang des Jet-Flusses (vielleicht ein Hinweis auf eine Jet-Krümmung) und legt eine Obergrenze für den Sichtwinkel von 35° fest.

Abschnitt 5 beinhaltet eine umfassende Studie der Entwicklung und Jet-Kinematik von 3C 84 über mehr als zwanzig Jahre. Unsere Analyse zeigt den Ausstoß zahlreicher Komponenten aus der Kernregion, die sich anscheinend mit relativ langsamer Geschwindigkeit bewegen, wobei neuere Komponenten schneller sind. Wir haben auch nach möglichen Unterschieden zwischen den Geschwindigkeiten der 43 und 86 GHz-Komponenten gesucht, fanden aber nur marginale Hinweise für eine schnellere Bewegung bei 86 GHz. Die Jet-Breite scheint frequenzabhängig zu sein, wobei die Jet-Breite mit zunehmender Frequenz abnimmt, was durch eine Schichtung im Zusammenhang mit dem Spine-Sheath Jet-Stratifikationsszenario erklärt werden könnte. Wir haben auch Spektralindexkarten bei 43 – 86 GHz erstellt, die zeigen, dass die Ausrichtung des Positionswinkels des Spektralindexgradienten zeitlich variabel ist und dass sich die Orientierung des inneren Jets mit der Zeit verschiebt. Dies ist ein weiterer Hinweis darauf, dass das Schwarze Loch nicht in der Mitte des Gesamtintensitätsmaximums liegt.

Schließlich, werden im Abschnitt 6 unsere Analyse und Ergebnisse zusammengefasst und im Abschnitt 7 wird ein Ausblick auf noch offene und zukünftig zu behandelnde Fragen gegeben.

Contents

1	A brief description of the underlying astrophysical concepts	1
1.1	Fundamental physical concepts	1
1.1.1	Synchrotron radiation	1
1.1.2	Inverse Compton scattering	6
1.1.3	Black body radiation	7
1.2	Black holes: A historical overview	8
1.3	AGN & Astrophysical jets	10
1.3.1	AGN unification	12
1.3.2	Central engine	15
1.3.3	Accretion	16
1.3.4	Jet launching & Collimation	18
1.3.5	Relativistic beaming effects	21
1.4	3C 84 in the context of radio astronomy	23
1.4.1	Thesis motivation	28
2	Basics of radio astronomy & interferometry	30
2.1	First Principles	30
2.2	Interferometry & VLBI arrays	35
2.2.1	VLBA	39
2.2.2	GMVA	40
2.2.3	Other VLBI arrays	42
2.3	Calibration of a VLBI data set	44
2.3.1	Calibration practicalities	44
2.3.2	Exemplary calibration of a GMVA data set	47
2.4	Imaging of a VLBI data set	49
2.4.1	Imaging practicalities	50
2.4.2	Exemplary imaging of a GMVA data set	54
3	Paper 1: Pinpointing the jet apex of 3C 84	57
4	Paper 2: A persistent double nuclear structure in 3C 84	66
4.1	Main results	66
5	Paper 3: Jet kinematics in the transversely stratified jet of 3C 84: A two-decade overview	69
6	Conclusions	93
7	Outlook	96

CONTENTS

A Appendix	98
References	101

List of Figures

1.1	Electron motion causing synchrotron radiation.	3
1.2	Synchrotron spectrum.	5
1.3	Doppler beaming.	5
1.4	Inverse Compton scattering schematic.	6
1.5	First (simulated) BH image.	10
1.6	AGN conceptualisation.	12
1.7	AGN unification overview plot.	13
1.8	AGN classification table.	15
1.9	Sketch of Ergosphere.	17
1.10	Types of accretion flows.	18
1.11	Sketch of jet formation process.	19
1.12	Jet instabilities.	20
1.13	Sketch of superluminal motion.	21
1.14	Hubble & Chandra images of NGC 1275.	24
1.15	VLBI images of 3C 84 at different frequencies.	26
2.16	Black hole image taken with the EHT.	31
2.17	Radio telescope & receiver system.	33
2.18	Antenna pattern.	35
2.19	Two antenna interferometer.	36
2.20	GMVA.	42
2.21	Manual phase calibration.	48
2.22	Data flow chart in AIPS.	49
2.23	Example of CLEANing.	53
2.24	(u, v) plot and amplitude.	55
2.25	Calibration and imaging data flow chart.	56
4.26	Jet apex in 3C 84.	67
1.27	15 GHz total intensity images.	98
1.28	43 GHz total intensity images.	99
1.29	86 GHz total intensity images.	100

List of Tables

1	Re-imaged 15 GHz VLBA epochs of 3C 84	40
2	Re-imaged 43 GHz VLBA epochs of 3C 84	41
3	Analysed GMVA epochs (86 GHz) of 3C 84	43

1 A brief description of the underlying astrophysical concepts

Humans have evolved optical sensors on the retinas of their eyes, which are sensitive to the visible part of the electromagnetic spectrum. This fact is directly connected to the spectrum of the Sun, whose flux peaks at these wavelengths. When looking up at the sky, initially with their naked eyes and later with primitive optical telescopes, early astronomers could only distinguish stars and galaxies in this narrow optical band; a rather limited view of the cosmos.

Fortunately, technological advancements allowed astronomers, in the beginning of the twentieth century, to reveal a ‘hidden’ part of the universe, by observing radio waves. The newly evolved radio astronomy branch enabled astronomers to peer through thick, gaseous and dusty discs, dense clouds, and dusty torii and discover previously unthought marvels.

In this introductory section of the thesis, the ideas and theoretical concepts needed to approach the subjects of black holes (BH), Active Galactic Nuclei (AGN) and the jets emanating from them, will be reviewed through the lens of radio astronomy. A special emphasis will be put on the introduction of the radio source 3C 84 – on which this thesis mainly focuses. The motivation for this thesis follows then naturally.

1.1 Fundamental physical concepts

Before delving into the world of supermassive black holes (SMBH), highly energetic AGN, and powerful jets, some basic concepts need to be clearly defined. This section introduces a selection of the key notions.

1.1.1 Synchrotron radiation

²A fundamental concept, which governs the emission mechanisms of a source, is the collision between particles with each other or with photons. A thermodynamic equilibrium can be achieved, when the time frame of the collisional system is long enough, so that the more energetic particles can disperse their energy effectively among the lower energy particles. However, in many cases the astrophysical plasma is too thin and the number of occurring collisions is insufficient for this procedure to take place. In such cases the spectrum is

²This section makes use of material presented in Rybicki & Lightman (1979), Longair (2011), and Mastichiadis & Vlahakis (2015).

characterised as non-thermal, and is described by a power law of the form:

$$\mathcal{F}_\nu \propto \nu^{+\alpha}, \quad (1.1)$$

where \mathcal{F}_ν is the frequency (ν) dependent source flux and α the spectral index of the source.

Synchrotron radiation is a type of radiation produced by highly energetic electrons, gyrating in magnetic fields. It is one of the most prominent astrophysical radiation processes, present in numerous phenomena, such as jets emanating from SMBHs inside AGN.

In the following, the expressions describing synchrotron radiation will be derived from first principles. For a charged particle e with mass m , the relativistic equations describing its motion in a magnetic field (\mathbf{B})³ are:

$$\frac{d}{dt}(\gamma m \mathbf{v}) = \frac{e}{c} \mathbf{v} \times \mathbf{B} \quad (1.2)$$

$$\frac{d}{dt}(\gamma m c^2) = 0. \quad (1.3)$$

Here \mathbf{v} is the velocity of the charged particle, c the speed of light in a vacuum, and γ is the Lorentz factor. Equations 1.2 and 1.3 can be combined into:

$$m\gamma \frac{d\mathbf{v}}{dt} = \frac{e}{c} \mathbf{v} \times \mathbf{B}. \quad (1.4)$$

Separating the velocity into components parallel and perpendicular to the field lines, it follows that \mathbf{v}_\parallel is constant, whereas \mathbf{v}_\perp is given by the following equation:

$$m\gamma \frac{d\mathbf{v}_\perp}{dt} = \frac{e}{c} \mathbf{v}_\perp \times \mathbf{B}, \quad (1.5)$$

and since $|\mathbf{v}|$ is also constant, $|\mathbf{v}_\perp|$ has to be constant as well. It can then be shown, that the solution to Eq. 1.5 describes a helical motion, with a gyration frequency of

$$\omega_B = \frac{qB}{mc}. \quad (1.6)$$

The next step is to employ the Larmor formula, which connects the total power emitted P_{syn} to the acceleration \mathbf{a} of a charged particle as follows:

$$P_{\text{syn}} = \frac{2e^2}{3mc^3} |\mathbf{a}|^2. \quad (1.7)$$

³Vector quantities are denoted with bold font.

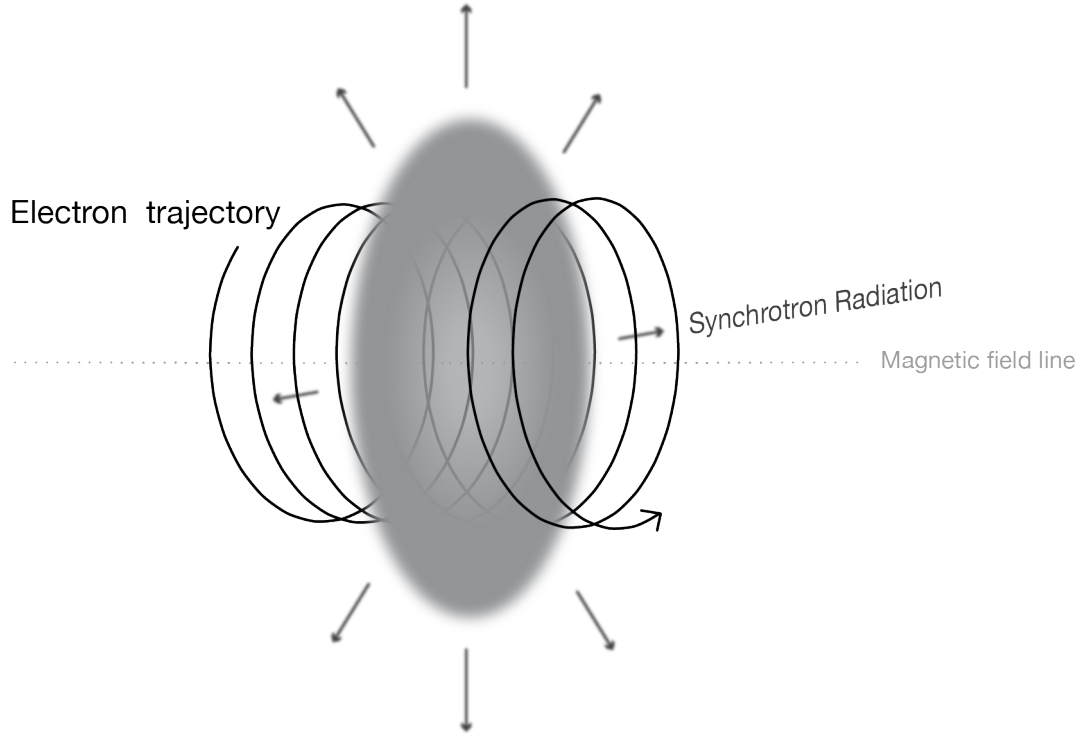


Figure 1.1: Sketch of electrons moving in a helical path, dictated by the magnetic field lines and emitting synchrotron radiation.

Plugging Eq. 1.5 into Eq. 1.7 results in:

$$P_{\text{syn}} = \frac{2e^4}{3m^2c^3} \gamma^2 \beta_{\perp}^2 B^2, \quad (1.8)$$

where the fact that $|\mathbf{a}_{\perp}| = \omega_B |\mathbf{v}_{\perp}|$ is taken advantage of, and $\beta_{\perp} = |\mathbf{v}_{\perp}| / c$.

Equation 1.8 can be further simplified by assuming that the charged particles are electrons and are isotropically distributed ($\langle \beta_{\perp}^2 \rangle = \frac{2}{3} \beta^2$). Specifically, using the Thomson cross section, which is defined as

$$\sigma_T \equiv \frac{8\pi}{3} r_0, \quad (1.9)$$

with $r_0 \equiv \frac{e^2}{mc^2}$, the radiated power may be rewritten as:

$$P_{\text{syn}} = \frac{4}{3} \sigma_T c \beta^2 \gamma^2 u_B. \quad (1.10)$$

Here $u_B = B^2 / 8\pi$ is the magnetic field energy density.

Equation 1.10 describes the power radiated away and therefore the energy losses of the electrons. By dividing the total energy of the electrons ($E_e = \gamma mc^2$) by the total emitting power, the synchrotron cooling time τ_{syn} can be de-

rived as follows:

$$\tau_{\text{syn}} = \frac{6\pi mc}{\sigma_T \gamma B^2} \approx 25 \gamma^{-1} B^{-2} [\text{yrs}]. \quad (1.11)$$

It is interesting to note that high energy electrons lose their energy faster than their low energy counterparts. Furthermore, from Eq. 1.10 it follows that in a proton-electron plasma, where the particles possess the same Lorentz factor, the power radiated from the electrons is much greater, because then Eq. 1.10 simplifies to $P \propto 1/m^2$.

The last step to describe synchrotron radiation, is to find a mathematical expression, which describes the observed spectrum. As Fig. 1.2 suggests, the synchrotron spectrum consists of an optically thin and an optically thick part, with the maximum denoted by the so-called turnover frequency $\nu_m \approx \frac{1}{2\pi} \frac{qB}{mc^2} \gamma^2$. A relation between the flux and frequency in the optically thick regime can be derived, by considering an electron, the motion of which is described by Eq. 1.5. The motion is relativistic, hence the radiation is beamed into a cone characterised by an opening angle of $1/\gamma$ (see Fig. 1.3). It can then be shown that the peak of the spectrum of the single electron will be located at the critical frequency ν_c , given by the following expression:

$$\nu_c = \frac{\gamma^2 eB}{2\pi mc}. \quad (1.12)$$

The flux on the other hand can simply be written as $\mathcal{F}_\nu \propto \nu^2 E_{\text{avg}}$, where E_{avg} is the mean particle energy. But E_{avg} is just the energy of the particles, whose frequency equals the critical frequency, or, in mathematical terms: $E_{\text{avg}}^2 \propto \nu_c = \nu$. Thus for the optically thick regime, $\mathcal{F}_\nu \propto \nu^{2.5}$ and $\alpha_{\text{thick}} = 2.5$ (see also Eq. 1.1). This is commonly referred to as synchrotron self-absorption (SSC).

For the optically thin regime, under the assumption that the electrons are distributed as a power law of the form $N(E) \propto E^{-p}$, it can be shown that the optically thin spectral index is $\alpha_{\text{thin}} = -(p-1)/2$. The overall spectrum is then given by the following equation (see Condon & Ransom 2016; Türler et al. 1999):

$$\mathcal{F}_\nu = \mathcal{F}_\nu^m \left(\frac{\nu}{\nu_m} \right)^{2.5} \left\{ \frac{1 - \exp\left(-\tau_m \left(\nu/\nu_m\right)^{-(p+4)/2}\right)}{1 - \exp(-\tau_m)} \right\}, \quad (1.13)$$

where \mathcal{F}_ν^m and τ_m are the turnover values of the flux and optical depth respectively.

A detailed derivation of the relations described above is beyond the scope of this work; the interested reader may consult the textbooks by Rybicki & Lightman (1979) and Longair (2011).

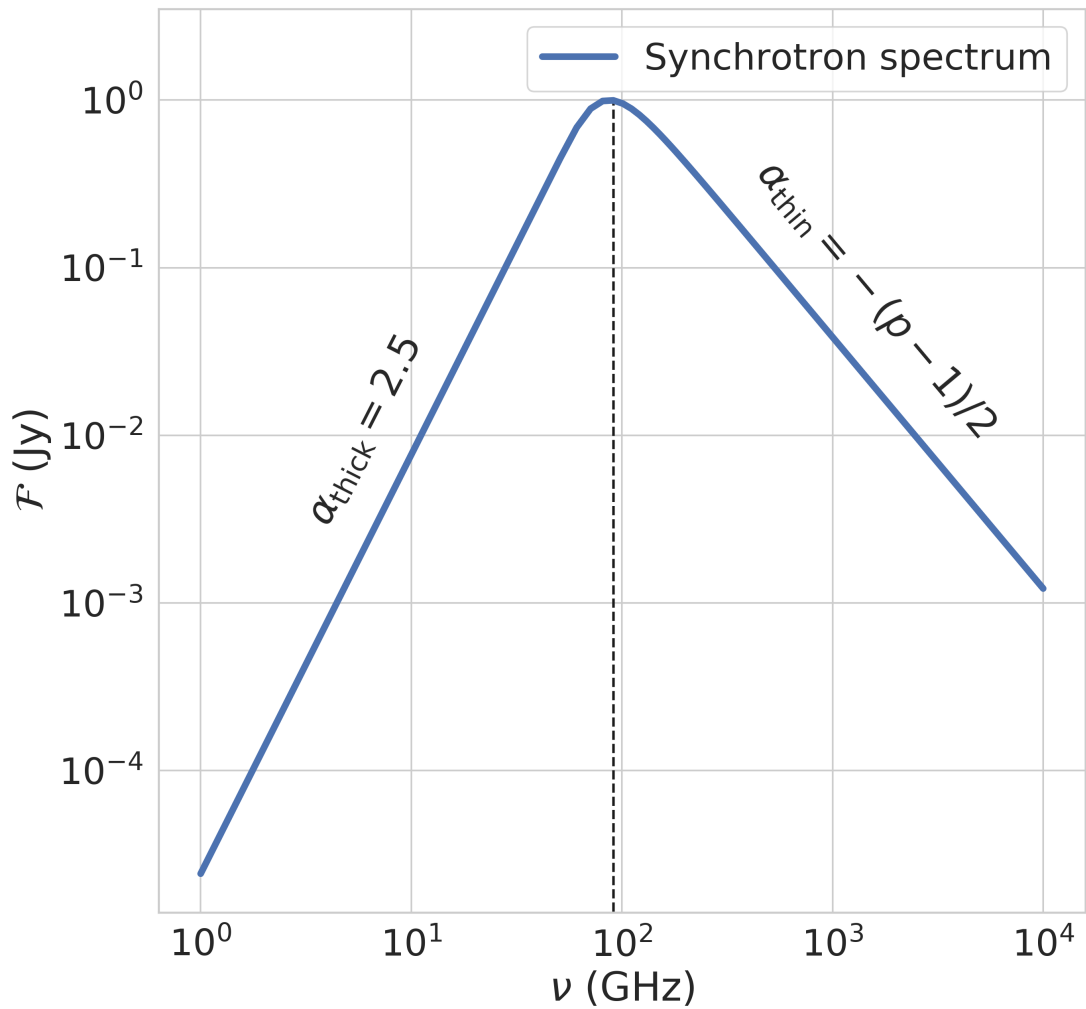


Figure 1.2: Exemplary synchrotron spectrum plot. The dashed black line corresponds to the peak of the spectrum, at 86 GHz.

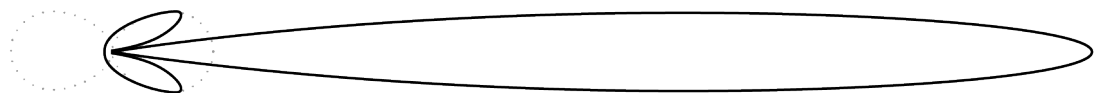


Figure 1.3: Sketch of the angular distribution of the emitted radiation of an electron when the velocity and acceleration are perpendicularly oriented to each other. The dashed line denotes the shape of a dipole in the rest frame of the electron and the solid line the beamed shape in the reference frame of the observer. Image adapted from Condon & Ransom (2016).

1.1.2 Inverse Compton scattering

In 1923, Arthur Compton discovered that the wavelength of hard X-ray photons increases when scattered by electrons at rest (Compton 1923). In this phenomenon, called Compton scattering, the incoming photon transfers some of its energy to the electron, and its wavelength decreases by an amount dependent of the transferred energy.

Here the opposite effect will be reviewed, in which a highly energetic, relativistic electron up-scatters low energy photons. This effect is known as Inverse Compton scattering and is of major interest and importance in astrophysical settings. Figure 1.4 illustrates this phenomenon.

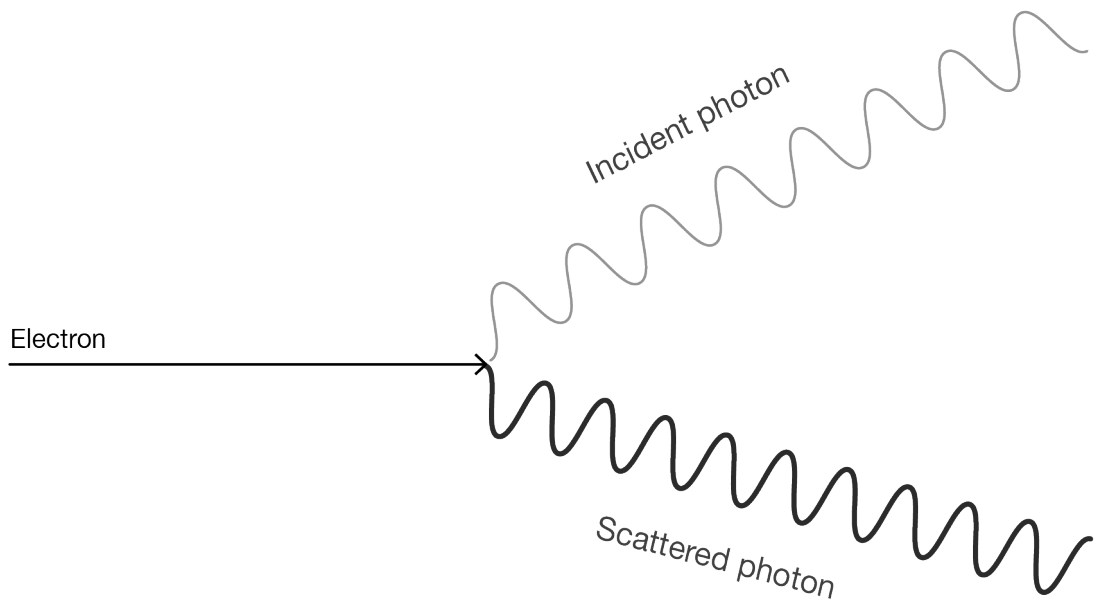


Figure 1.4: Sketch of the inverse Compton scattering phenomenon. The solid, straight line denotes the highly energetic electron. The upper, longer wavelength line represents the incident photon. The lower, shorter wavelength line corresponds to the up-scattered, high energy photon.

Similar to synchrotron radiation, one can calculate the rate of energy loss of a single electron, along the lines leading to Eq. 1.10. The final equation is the following:

$$P_{\text{ICS}} = \frac{4}{3} \sigma_{\text{T}} c \beta^2 \gamma^2 u_{\text{rad}}, \quad (1.14)$$

where u_{rad} is the energy density of the photon field. It is noteworthy that Eqs. 1.10 and 1.14 resemble each other, with the only difference being in the energy density factor. And the similarities continue, as in the inverse Compton scattering case the power law index α_{ICS} is given by the same relation as in the synchrotron radiation case:

$$\alpha_{\text{ICS}} = -\frac{p-1}{2}. \quad (1.15)$$

For a detailed derivation of the above relation, the interested reader is directed to the works by Blumenthal & Gould (1970) and Rybicki & Lightman (1979).

Finally, it is interesting to examine the photon field relating to the inverse Compton scattering process. In general, any photon field can supply the required photons. Commonly, a distinction is made between the seed photons originating from inside the bulk jet flow or outside. In the former case, the seed photons might be supplied by the synchrotron radiation itself, in which case the process is known as synchrotron self-Compton. In the latter case, the seed photons might originate from a plethora of sources, such as a dusty torus, broad line regions (BLR) or even the cosmic microwave background (CMB). Since electrons can transfer a larger amount of energy to photons through the inverse Compton process than by ‘cooling’ via synchrotron radiation, inverse Compton scattering is the primary energy sink for electrons if the seed photon number density is high enough. An upper limit for the temperature of synchrotron self-absorbed sources exists – the inverse Compton limit, which is $\leq 10^{12}$ K (Kellermann & Pauliny-Toth 1969). Electrons with temperatures exceeding the inverse Compton limit quickly cool down to this limit, as inverse Compton ‘cooling’ is much faster than synchrotron ‘cooling’.

1.1.3 Black body radiation

⁴It is worthwhile to briefly mention the concept of the thermal black body radiation, even though in the remainder of this thesis, the dominant form of radiation will be non-thermal. In order to inspect this type of thermal radiation, one has to consider Planck’s function:

$$B_\nu(T) = \frac{2h\nu^3/c^2}{\exp(h\nu/k_B T) - 1}, \quad (1.16)$$

where $h \approx 6.63 \times 10^{-27}$ erg s and is called Planck’s constant. Depending on the value of the exponent in the exponential function of the denominator, a distinction between two limits can be made. If $h\nu \gg k_B T$, Eq. 1.16 simplifies to Wien’s law:

$$I_\nu^W(T) = \frac{2h\nu^3}{c^2} \exp(-h\nu/k_B T). \quad (1.17)$$

On the other hand, if $h\nu \ll k_B T$, the more relevant to this work regime is known as the Rayleigh-Jeans law:

$$I_\nu^{RJ}(T) = \frac{2\nu^2}{c^2} k_B T. \quad (1.18)$$

⁴This section is based mostly on Rybicki & Lightman (1979).

Especially in radio astronomy, a way of characterising the brightness of a source at a specified frequency is done by utilising Eq. 1.18 and the concept of the brightness temperature T_B . Simply put, the brightness temperature is defined for any value of I_ν^{RJ} by solving for T_B :

$$T_B = \frac{c^2}{2\nu^2 k_B} I_\nu^{RJ}. \quad (1.19)$$

Following Lobanov (2015), Eq. 1.19 can be rewritten in a more practical way, based on interferometric visibilities (see also Sect. 2):

$$T_B = \frac{\pi \mathcal{B}^2 \nu_0}{2k_B \log_e(\nu_0/\nu_q)}, \quad (1.20)$$

where \mathcal{B} is the baseline distance, ν_0 is the zero-spacing visibility and

$$\nu_q = \nu_0 \exp\left(-\frac{\pi^2 \theta_r^2 q^2}{4 \log_e(2)}\right). \quad (1.21)$$

Here $q = \mathcal{B}/\lambda$ (λ is the observing wavelength), and θ_r is the emitting region size (see Sect. 2.2 for a detailed discussion of the terms introduced in this paragraph). It should be noted that, even though the radiation from BH-launched jets for example is not thermal, the concept of T_B is still oftentimes applied.

Two other temperatures are also defined via the Planck function – the colour temperature T_c , and the effective temperature T_{eff} . The former is used when obtaining a spectrum resembling that of a black body, for which the absolute value of the brightness might be unknown. T_c is then used to determine the temperature of this source, regardless of the absolute brightness scale. The latter is determined by equating the measured total, integrated flux of the source (\mathcal{F}) to a black body flux, such that $T_{\text{eff}} \equiv (\mathcal{F}/\sigma_{\text{SB}})^{\frac{1}{4}}$, with σ_{SB} being the Stefan-Boltzmann constant.

1.2 Black holes: A historical overview

⁵Black holes have always fascinated humanity, from the moment they were first postulated, to the present day. Here a timeline of the major breakthroughs will be reviewed, which is connected to the postulation of BHs and the subsequent, very recent, first observation. The starting point is in the 1970s. At that time, evidence for the existence of BHs was only very indirect. Towards this, the Uhuru satellite was launched in late 1970, to study binary X-ray sources. At that

⁵This section is partly based on Luminet (2019).

point it was known that X-ray binaries not associated with supernovae remnants, were linked to mass transfer systems containing a collapsed star (Giacconi 1974). Uhuru added to that knowledge by observing Hercules X-1, Centaurus X-3 and Cygnus X-1, with perhaps the most significant of its achievements being the conclusion that the latter contains a BH (see Giacconi 1974; Giacconi et al. 1974). This conclusion was based on the fact that the central X-ray emitting component was compact, and had an optical counterpart, with a mass of more than $20 M_{\odot}$. Close in time Lynden-Bell & Rees (1971) considered BH models of galactic nuclei to discuss quasars as possibly being powered by mass accreting BHs, concluding that BHs can indeed power them. Balick & Sanders (1974) and Balick & Brown (1974) mapped Sagittarius A* (SgrA*) at 86 GHz with the NRAO interferometer, achieving a resolution of two arcseconds (as) and revealing thermal emission from hot, optically thick regions. They concluded that gas might have formed into a disc around SgrA*. Later in the same year, strong emission in the inner, one parsec (pc) core region of SgrA* was reported, with $T_B \geq 10^7$ K (Balick & Brown 1974), suggesting that the emission is of non-thermal origin.

Along with the observational discoveries, theoretical advancements in BH physics were following suit. The first calculation in Kerr geometry took place in 1973 when Bardeen (1973) calculated the apparent shape of a Kerr BH (Kerr 1963; see also Bardeen et al. 1972). At the same time, the shape of the circular orbit of a star was published, complete with depictions of the primary and secondary images of the star by Cunningham & Bardeen (1973).

The first (simulated) bolometric image of a BH, which is surrounded by an accretion disc (Lynden-Bell 1969; Novikov & Thorne 1973; Shakura & Sunyaev 1973), was produced and published by Luminet (1979), using a computer (see Fig. 1.5). The picture shows a Schwarzschild BH (i.e. not rotating) with a geometrically thin disc, which is characterised by gas elements moving in a circle and for which the absorption by clouds is negligible. Theoretical calculations aiding in depicting the thin disc realistically had already been developed by that time, by Shakura & Sunyaev (1973) and Page & Thorne (1974). Of course, the Einstein effect and Doppler boosting had to be taken into account as well. The resulting disc in Fig. 1.5 is the sum of these effects.

Almost a decade later, the first simulated, non-bolometric image of a geometrically thin relativistic accretion disc around a Schwarzschild black hole were published by Fukue & Yokoyama (1988). The authors also compared their optical and X-ray images to a bolometric one, highlighting the apparent wavelength shifts in the accretion disc.

It was in the 1990s when the first (simulated) accretion disc images of rotat-

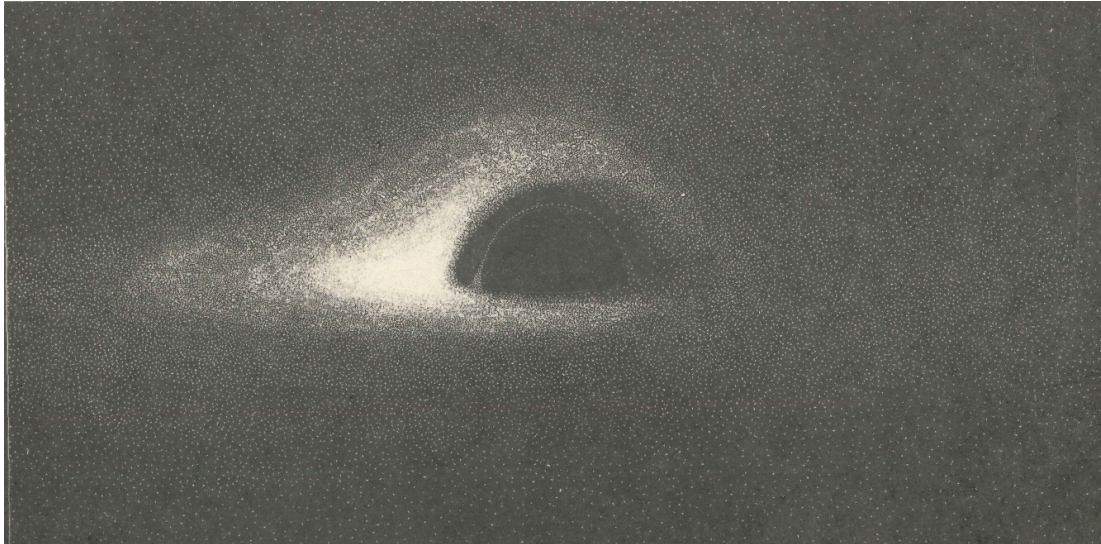


Figure 1.5: First bolometric, simulated image of a BH accretion disc, produced with a computer. The physical assumptions are that the BH is non-rotating, and has a geometrically thin disc. The gas elements are moving in a circular orbit and the cloud absorption is negligible. The view presented is that of a distant observer but close enough to resolve the image. Image credit: Luminet (1979) (image taken from https://upload.wikimedia.org/wikipedia/commons/3/38/Luminet%27s_Simulation_of_a_Black_Hole_Accretion_disc.jpg).

ing Kerr BHs were published. First Viergutz (1993) computed a coloured image (in contours) of a slightly thick disc, with the secondary image included. Some years later, Fanton et al. (1997) developed a ray-tracing programme to create an image of an optically thick and geometrically thin accretion disc, and Bromley et al. (1997) studied frame dragging effects around an extreme Kerr BH.

At the turn of the millennium technological advancements caught up with theoretical advancements in simulations, and the feasibility of imaging the vicinity and ultimately the shadow of a BH with Very Long Baseline Interferometry (VLBI, see Sect. 2) was already being considered (Falcke et al. 2000; Doeleman et al. 2001). This became ultimately a reality, when in 2019 the Event Horizon Telescope (EHT) collaboration published the first images of the shadow of the BH in M 87 (Event Horizon Telescope Collaboration et al. 2019a,b,c,d,e,f), along with the first EHT images of a BH powered jet (Kim et al. 2020). In 2022, the first image of the SMBH of our Galaxy followed (Event Horizon Telescope Collaboration et al. 2022a,b,c,d,e,f).

1.3 AGN & Astrophysical jets

AGN constitute an extreme category of astrophysical sources. They account for some of the brightest astrophysical sources and their emitted power can

outshine our Galaxy by orders of magnitude. This power, however, is not just the sum of all stars in these galaxies (as is in our Galaxy for example), but rather it originates from their active core. Their radiation is characterised as non-thermal (see Sect. 1.1.1) and it covers a broad part of the entire electromagnetic spectrum. Furthermore emission from AGN can be set apart from emission of 'regular' galaxies by studying the spectrum. While non-active galaxies present a spectrum characterised by absorption lines, AGN emission is usually rich in emission lines.

Although some emission lines were already reported at the turn of the previous century (Fath 1909), it was Carl Seyfert who realised that a fraction of the galaxies he studied exhibited powerful cores and broad emission lines (Seyfert 1943). In his honour, a subgroup of active galaxies is nowadays called 'Seyfert galaxies'. Nonetheless, in the current nomenclature, a number of other objects are also part of the active galaxy denomination, such as quasars and radio-galaxies. They are all part of what is referred to as the AGN 'zoo' and it consists of a number of subgroups, which will be described in Sect. 1.3.1. Figure 1.6 illustrates an artistic impression of the main components constituting a typical AGN.

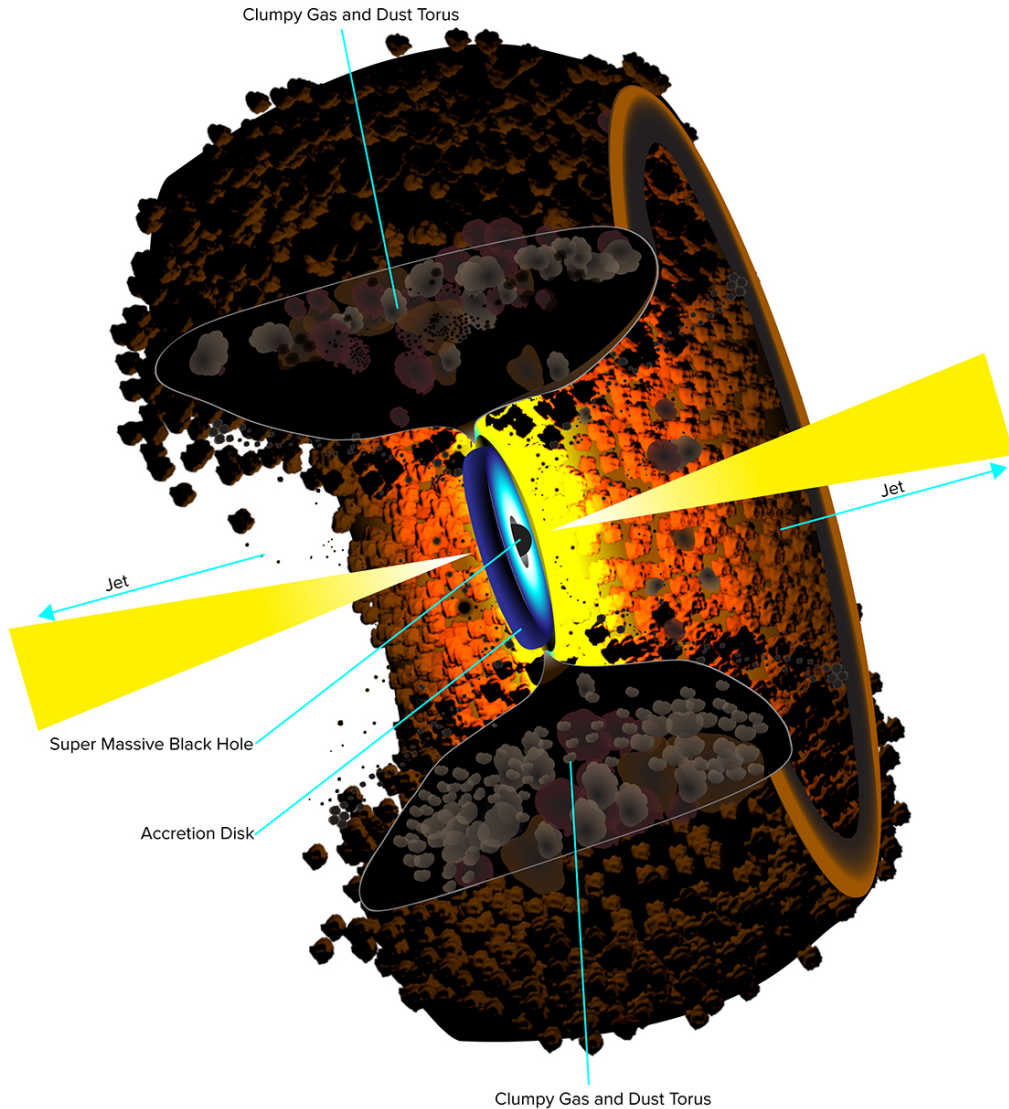


Figure 1.6: Artistic impression of the main constituents of an AGN. Image credit: B. Saxton NRAO/AUI/NSF (image taken from <https://public.nrao.edu/gallery/a-unified-agn-model/>).

1.3.1 AGN unification

⁶As will be described in Sect. 2.2, powerful radio telescopes opened a new window into observations of the night sky and astronomers quickly discovered a plethora of new types of galaxies. Almost contemporaneously (Barthel 1989; Blandford & Rees 1978; Kristian 1973; Orr & Browne 1982; Penston et al. 1974; Rowan & Stephenson 1977; Scheuer & Readhead 1979; Weedman 1973), efforts were made to answer the fundamental question of whether all these different classes of galaxies were intrinsically different or if they could be explained by a common, unifying model. Overviews of the current understanding of the AGN

⁶This section is partly based on Urry & Padovani (1995).

1 A BRIEF DESCRIPTION OF THE UNDERLYING ASTROPHYSICAL CONCEPTS

unification problem are presented in Antonucci (1993) and Urry & Padovani (1995), and will briefly be reviewed in the rest of this section. The reader is recommended to use Fig. 1.7 as reference for the following description of the AGN ‘zoo’.

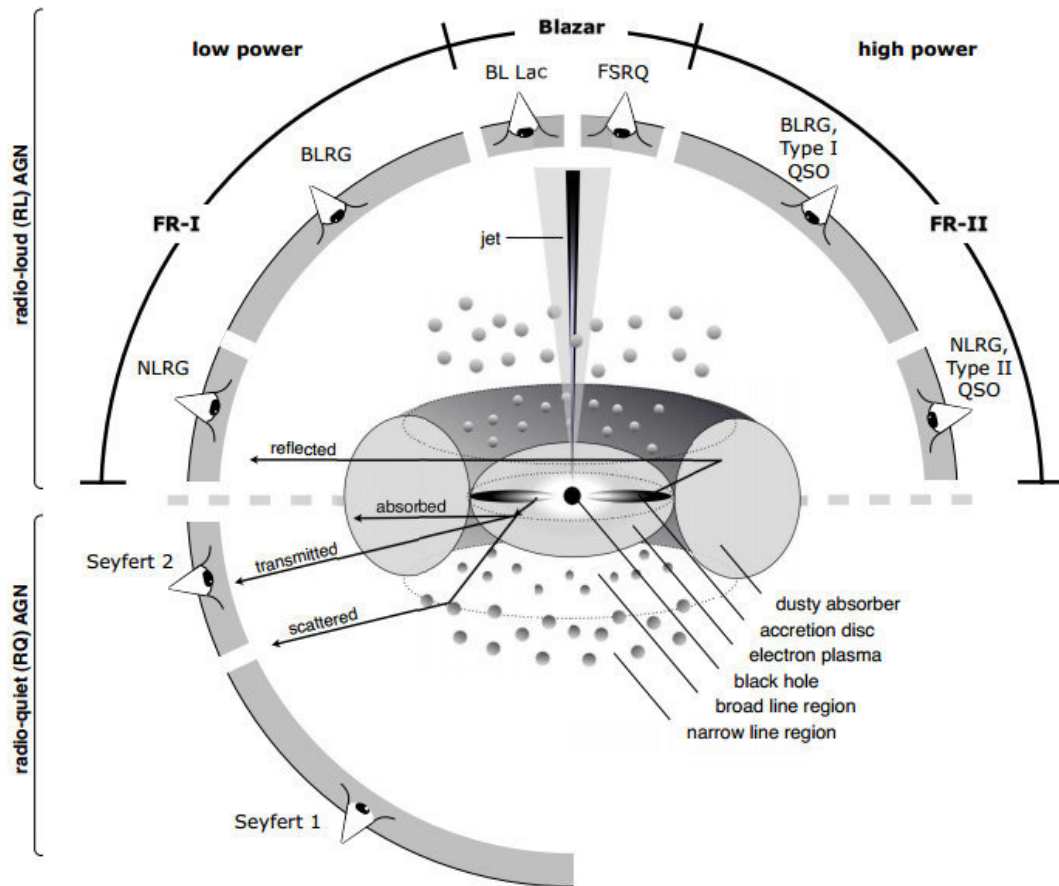


Figure 1.7: Sketch of the current understanding of AGN. The viewing angle dictates the type of object classified. Image taken from Beckmann & Shrader (2012).

Even though the number of AGN characteristics is vast, leading to numerous classifications, it is common practice to classify AGN based on only two parameters, namely radio-loudness and emission line width. Conventionally, the radio loudness parameter R is used to distinguish between radio-loud and radio-quiet sources. It is defined as the ratio of the AGN radio luminosity at 5 GHz to the optical luminosity at 4400 \AA (Kellermann et al. 1989, 1994). If $R \geq 10$ for a given source, then it is defined as radio-loud, if not, it is defined as radio-quiet (e.g. Stocke et al. 1992). It is noteworthy that radio-loud AGN, only account for 10 – 15% of all AGN. Furthermore, each of the two categories is additionally divided, based on the optical emission line properties, into types 0, 1, and 2. Type 0 AGN exhibit ‘unusual’ emission line properties, type 1 AGN are char-

acterised by broad optical lines and type 2 AGN by narrow lines.

Type 0 radio-loud AGN are referred to as blazars. They are the most extreme subclass of AGN, and are responsible for some of the most powerful events in the cosmos. As can be seen in Fig. 1.7, they correspond to a jet pointing directly at the observer's line of sight and are therefore subject to highly relativistic effects (see Sect. 1.3.5). Based on their optical properties, blazars are further split into BL Lacertae objects (BL Lacs) and Flat Spectrum Radio Quasars⁷ (FSRQs). BL Lacs lack strong emission or absorption features in their optical spectra and are comparatively weaker radio frequency flux emitters. FSRQs, on the contrary, are powerful radio frequency flux emitters and feature broad emission lines in their optical spectra. For this reason they are also placed in the type 1 radio-loud category. Along with them, this group also consists of Broad-Line Radio-Galaxies (BLRG) and Steep Spectrum Radio-Quasars (SSRQ). As a whole, they are characterised by broad emission lines stemming from the hot gas, along with bright continua. BLRGs are placed on the low power side of Fig. 1.7, whereas FSRQs and SSRQs on the high power side (see Fig. 1.7). The division between FSRQs and SSRQs is usually made at a spectral index value of 0.5, for the radio spectrum, at a few GHz. Type 2 radio-loud AGN are part of a class of radio-galaxies called Narrow-Line Radio-Galaxies (NLRG). They have weak continua and rather narrow emission lines, which might be explained by the obscuration of a dusty torus between the source and the observer. Two of the morphological types constituting this category are the Fanaroff-Riley type I and type II radio-galaxies (FRI, FR II; Fanaroff & Riley 1974). Referring again to Fig. 1.7, FRI type galaxies, which are characterised by often-symmetric radio jets, whose intensity decreases from the core towards the outer regions, are on the low power side. FR II type galaxies are on the high power side, and usually exhibit prominent radio-lobes connected to the core by well-collimated jets. It should be noted, however, that, depending on the viewing angle, BLRGs can potentially be FRI or FR II type galaxies as well.

Only about 10% of radio-quiet AGN exhibit unusual absorption features (Urry & Padovani 1995). If their optical and ultraviolet spectra resemble that of P-Cygni, they are classified as Broad Absorption Line (BAL) quasars (Turnshek 1984) and constitute the subclass type 0 of radio-quiet AGN. Broad line radio quiet AGN (type 1) are split into Quasars (Quasi-stellar objects; QSOs) and Seyfert 1 galaxies. As shown in Fig. 1.7, QSOs are on the high power side. Since they are usually observed at great distances (the peak of the QSO population is at $z = 2$ (Hewitt & Burbidge 1993)), no galactic surrounding around the emitter can be

⁷The word quasar is a contraction of the words quasi-stellar radio source, because when they were identified in visible wavelengths, they resembled star-like emitters.

distinguished. Seyfert 1 galaxies, contrastingly, are located on the low power side and are therefore usually large spiral galaxies, only found nearby. Along with Seyfert 2 galaxies, which are the narrow line (type 2 radio-quiet) counterpart of Seyfert 1 galaxies, they constitute a common type of AGN observed in the local universe. An overview of the analysis presented in this section is presented in Fig. 1.8.

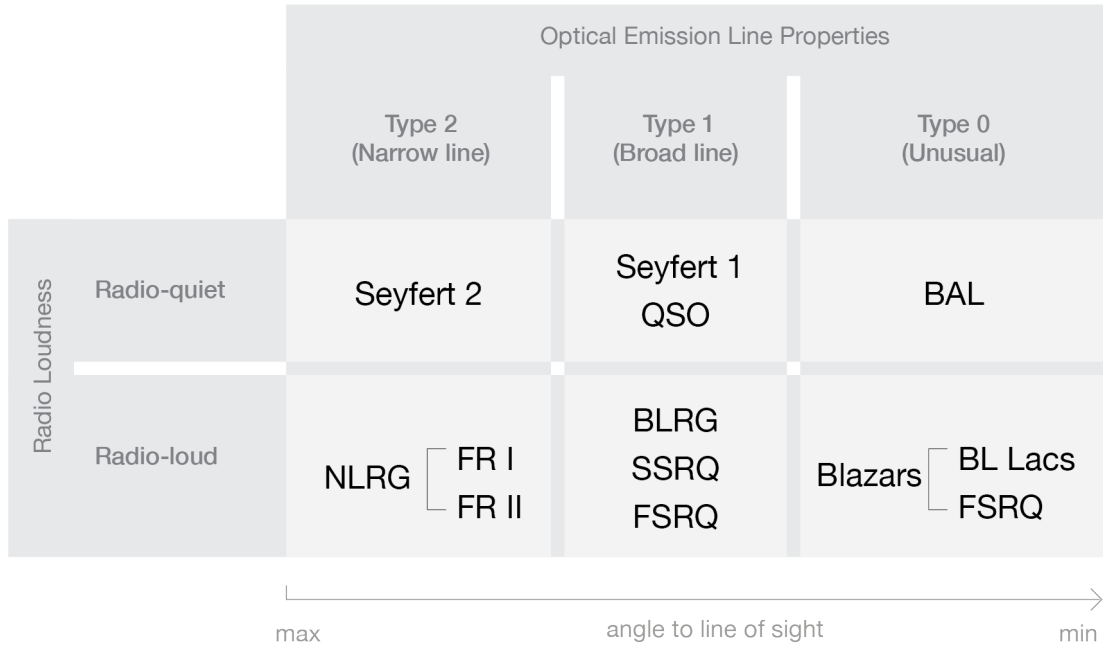


Figure 1.8: A simplified schematic view of the taxonomy of AGN. Image adapted from Padovani (1999).

1.3.2 Central engine

As detailed in Sect. 1.2, the existence of SMBHs is the only plausible explanation behind the radiative output of an AGN. A BH is generally characterised by two quantities: its mass (M_{BH}) and its spin (α_s). Combining them yields a fundamental characteristic of BHs, the so-called event horizon. The event horizon is a boundary beyond which not even light can escape, as everything is pulled towards the singularity. For a Schwarzschild BH – that is a non-rotating BH – the radius which defines this boundary is called the Schwarzschild radius (R_s). It is simply the distance at which the gravitational escape velocity is equal to the speed of light, and it is given by the following expression:

$$R_s = \frac{2GM_{\text{BH}}}{c^2}, \quad (1.22)$$

where G is the gravitational constant. A derivative quantity is the so-called gravitational radius, commonly defined as $R_g = R_s/2$ (e.g. Romero & Gutiérrez

2020).

A more realistic description of a BH should take into account that it is originating from a gravitational collapse of stars and gas and therefore has most probably retained their angular momentum. Kerr (1963) described a BH, which is spinning, with the spin defined as:

$$\alpha_s = \frac{jc}{GM_{\text{BH}}^2}, \quad (1.23)$$

where j is the angular momentum of the BH. In this so-called Kerr metric, the event horizon radius is given by the following formula:

$$R_k = 2R_g \left(1 - \sqrt{1 - \alpha_s^2} \right). \quad (1.24)$$

Figure 2.16 presents the first ever image of the event horizon of such a BH, congruous with a Kerr BH.

In a spinning BH, energy extraction is possible via the Penrose mechanism (Penrose 1969; Penrose & Floyd 1971). The concept is based on the ellipsoidal region just outside the event horizon, surrounding the BH and co-rotating, called the ergosphere. The ergosphere radius is given by the following formula:

$$R_e = R_g \left(1 + \sqrt{1 - \alpha_s^2 \cos^2(\theta_p)} \right), \quad (1.25)$$

where θ_p is the angle measured from the pole of the rotation. Since the ergosphere is located outside the event horizon, matter can escape and thus energy can be extracted. The phenomenon of co-rotation is called the Lense-Thirring effect or frame-dragging and it causes the inertial frame to be dragged in the direction of the BH spin (see e.g. Misner et al. 1973, and Fig. 1.9).

1.3.3 Accretion

A portion of the matter (e.g. stars, dust, and gas) rotating around a BH will inevitably cross the event horizon and fall onto the BH, thus turning some of its gravitational energy into heat and electromagnetic radiation. This mechanism of accretion is the fundamental driver behind AGN emission (Lynden-Bell 1969; Salpeter 1964) and is generally referred to as the accretion flow. Under the assumption of a spherical accretion flow onto the BH, the rate of accretion \dot{M} can be approximated by the following expression:

$$\dot{M} = \pi r^2 v \rho, \quad (1.26)$$

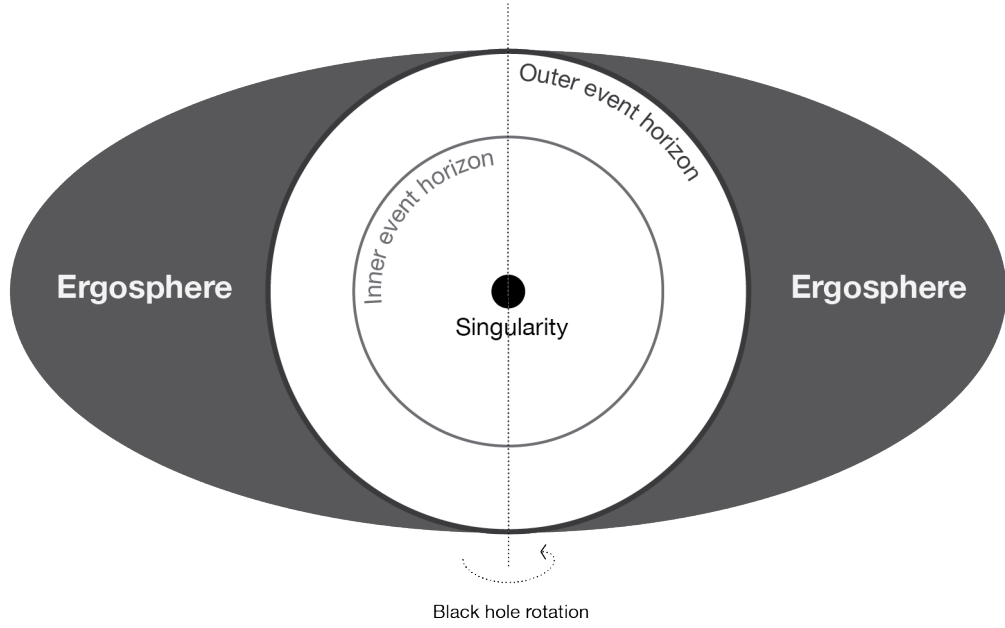


Figure 1.9: Sketch of the ergosphere, located outside the event horizon and the rotation axis of the BH.

where ρ is the density of the accreting matter, v its velocity, and r the radial distance from the BH. This type of spherically symmetric accretion was first proposed by Herman Bondi (Bondi 1952) and is referred to as Bondi accretion. By equating the velocity (v or the speed of sound c_s of the environmental gas if $c_s > v$) of the accreting matter to the escape velocity, a critical radius can be determined, within which the total matter is captured. Equation 1.26 can then be rewritten as:

$$\dot{M} = \frac{4\pi\rho G^2 M_{\text{BH}}^2}{c_s^3}. \quad (1.27)$$

In terms of the accretion rate, the corresponding bolometric luminosity can be written as $L_{\text{bol}} = \eta_e \dot{M} c^2$, with η_e being the accretion efficiency factor. The typical values for η_e are of the order of 0.1; matter accretion is thus a very efficient AGN powering mechanism.

However, there are limitations on the accretion onto a BH, dictated mainly by the radiation pressure acting on the in-falling material. This upper limit can be quantified by equating the pressure gradient of the in-falling matter to that of the radiation pressure. This limit, called the Eddington luminosity, was first identified by Eddington and hence bears his name. In mathematical terms, and assuming that the in-falling matter mostly consists of ionised hydrogen:

$$L_{\text{Edd}} = \frac{4\pi G c m_p M_{\text{BH}}}{\sigma_T}, \quad (1.28)$$

where m_p is the mass of a proton. Two derivative quantities can be defined – the Eddington ratio λ_{Edd} and the Eddington accretion rate \dot{M}_{Edd} . The Eddington ratio is defined as the ratio of the bolometric luminosity to the Eddington luminosity:

$$\lambda_{\text{Edd}} \equiv \frac{L_{\text{bol}}}{L_{\text{Edd}}}. \quad (1.29)$$

When $\lambda_{\text{Edd}} = 1$, the Eddington limit is reached. The Eddington accretion rate is defined as follows:

$$\dot{M}_{\text{Edd}} \equiv \frac{L_{\text{Edd}}}{\eta_e c^2}. \quad (1.30)$$

The different types of accretion along with the respective spectral state and AGN type are displayed in Fig. 1.10.

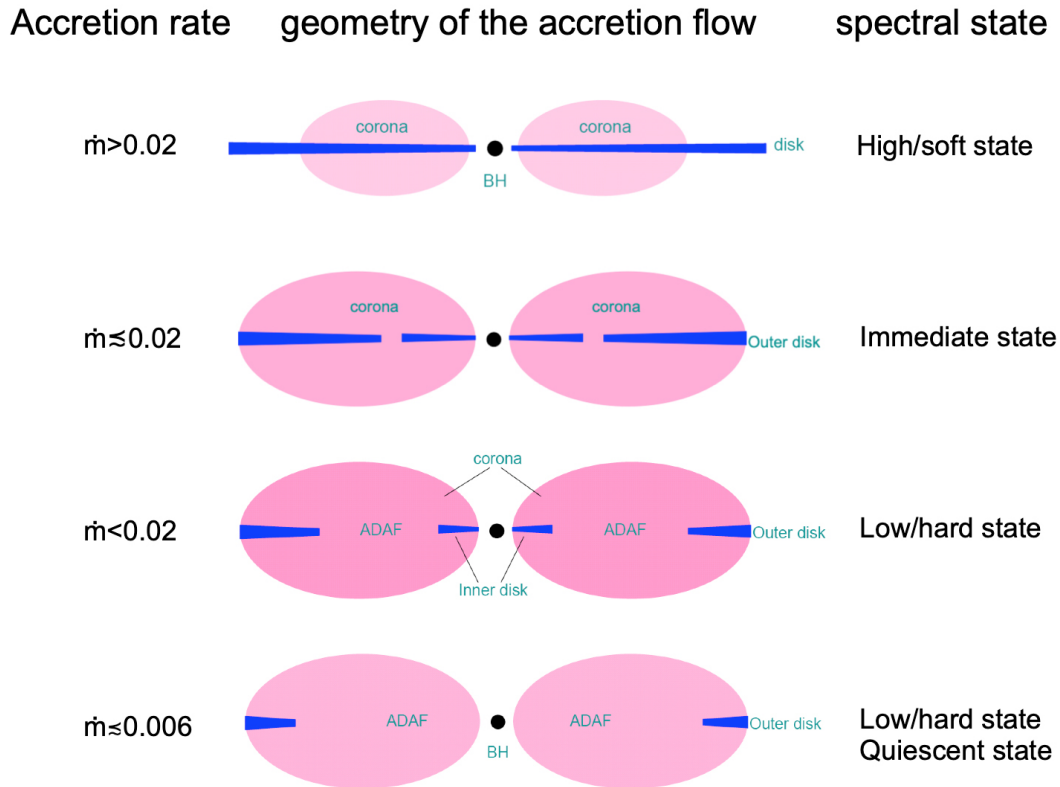


Figure 1.10: Accretion flow types depending on the accretion rate. Image taken from Liu (2013).

1.3.4 Jet launching & Collimation

The detailed process which leads to jet formation and collimation is still a subject of very active investigation and debate within the scientific community. The current consensus is that jets are predominantly formed by means of relativistic magneto-hydrodynamic (RMHD) processes. The two main theoretical interpretations are the Blandford and Payne model (BP; Blandford & Payne

1982) and the Blandford and Znajek model (BZ; Blandford & Znajek 1977). In the BP scenario, the magnetic field lines are anchored in the accretion disc, the rotation of which generates a centrifugally driven outflow. The energy is extracted via the Penrose mechanism (see also Sect. 1.3.3). A fraction of the accreting matter could then be launched in this way and be accelerated further downstream. In the BZ scenario, energy is directly extracted from the ergosphere of the spinning BH. The magnetic field lines are again dragged by the BH. Both jet launching scenarios result in a bipolar outflow, along the poles of rotation of the BH. An illustration of the jet formation by magnetic field lines is presented in Fig. 1.11.

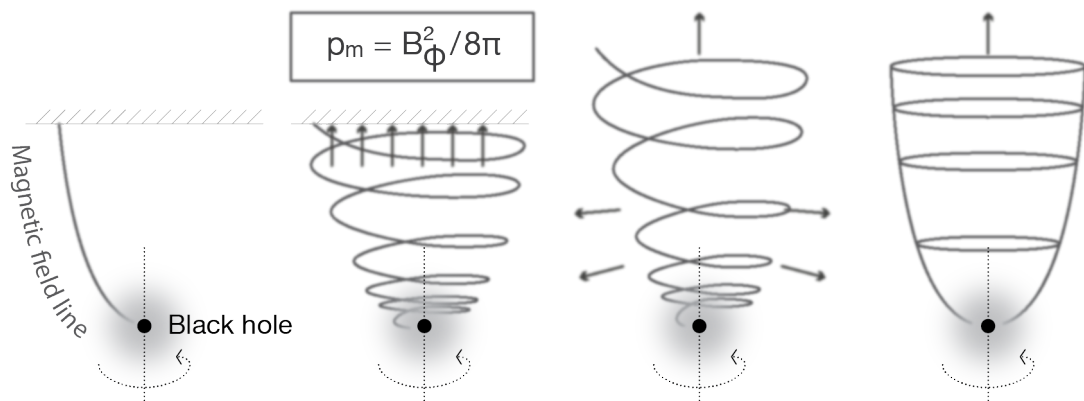


Figure 1.11: Jet formation schematic via matter acceleration along magnetic field lines. The magnetic field lines start out with a predominantly poloidal component. As time passes, the BH rotation winds the magnetic field lines tight, until at some point the pressure is large enough to push away (i.e. launch) the plasma that was holding the magnetic field lines in place (acting like a magnetic ‘spring’). The magnetic field lines then end up with both a poloidal and a toroidal component. Image adapted from Davis & Tchekhovskoy (2020).

So far, it has not been possible to observationally determine if either of the BP or BZ jet launching scenarios is definitely causing the jet in a given AGN. Another reasonable alternative is that both mechanisms are at play to some degree, manifested in a stratified ‘spine-sheath’ scenario (see e.g. Tchekhovskoy 2015). In this case, a faster inner spine is launched via the BZ mechanism, whereas the outer, slower sheath is launched via the BP mechanism.

Another open question relating to jet propagation is the jet’s ability to maintain collimation over large distances. Considering a cylindrical column of plasma, confined by a purely azimuthal (toroidal) magnetic field, any small disturbance will be amplified until the column is out of equilibrium and collapses. Such an instability is referred to as a current-driven (CD) kink instability and it occurs in magnetically dominated jets (e.g. Bateman 1978). Another example of a mode

1 A BRIEF DESCRIPTION OF THE UNDERLYING ASTROPHYSICAL CONCEPTS

of instability is the so-called Kelvin-Helmholtz (KH) instability (see e.g. Ferrari et al. 1978, and references therein). This type of instability occurs in kinetically dominated jets and is a manifestation of the velocity shear in single fluid or the velocity difference between two fluids (e.g. between the jet and the surrounding ambient medium). Figure 1.12 displays CD and KH instabilities.

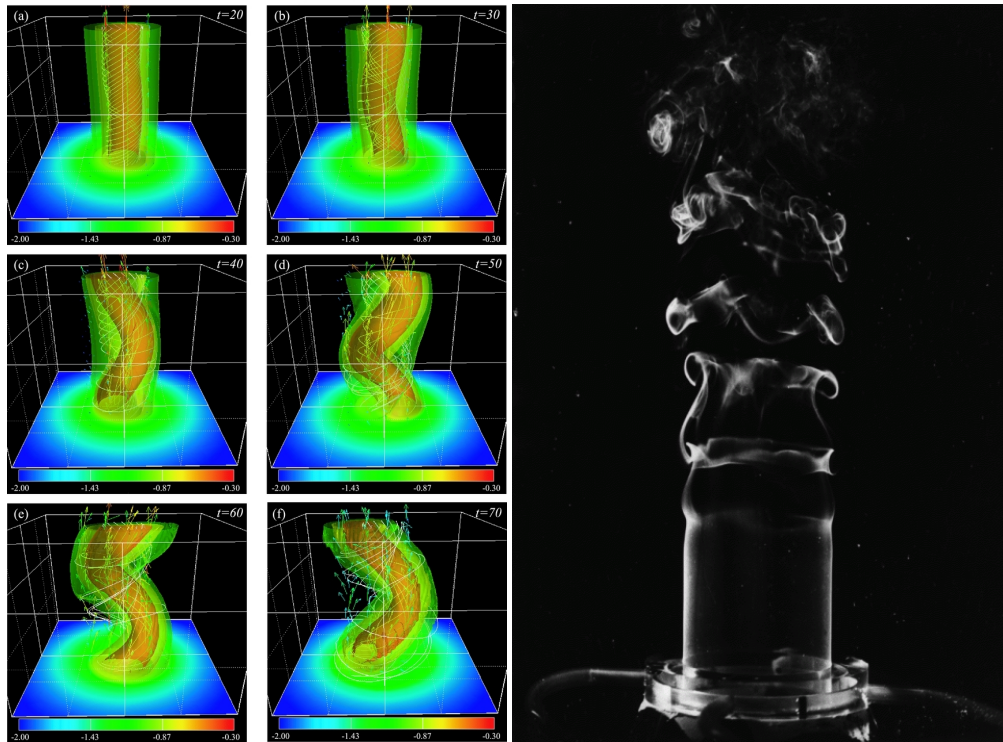


Figure 1.12: Different types of jet flow instabilities. *Left*: Formation of a current-driven kink instability in a numerical jet simulation. Image adapted from Mizuno et al. (2011). *Right*: Kelvin-Helmholtz instability gradually developing in an initially laminar flowing jet. Image credit: Nicole Sharp (image taken from <https://fyfluiddynamics.com/2011/02/this-photo-shows-the-development-of-a-flow/>).

However, observational evidence suggests that jets remain intact despite instabilities such as the ones described above; they may even be responsible for the curved paths that some jets seem to follow (e.g. Tchekhovskoy & Bromberg 2016). The existence of an axial (poloidal) component increases the jet stability as long as its magnitude is comparable to the azimuthal component's one. This might explain the resilience of jets to CD instabilities. KH instabilities on the other hand might be counteracted by stabilising sheaths around the jet (Mizuno et al. 2007). Future, higher resolution simulations might be able to shed more light on the intrinsic processes behind jet collimation.

1.3.5 Relativistic beaming effects

Outflows like the one studied in this thesis move at relativistic speeds and are therefore subject to relativistic effects. Two are the main effects of concern for this analysis: superluminal motion and Doppler boosting.

Superluminal motion is an apparent effect, in which astronomical sources eject components, which then seem to move faster than the speed of light. Figure 1.13 serves as a handy guide to illustrate this description.

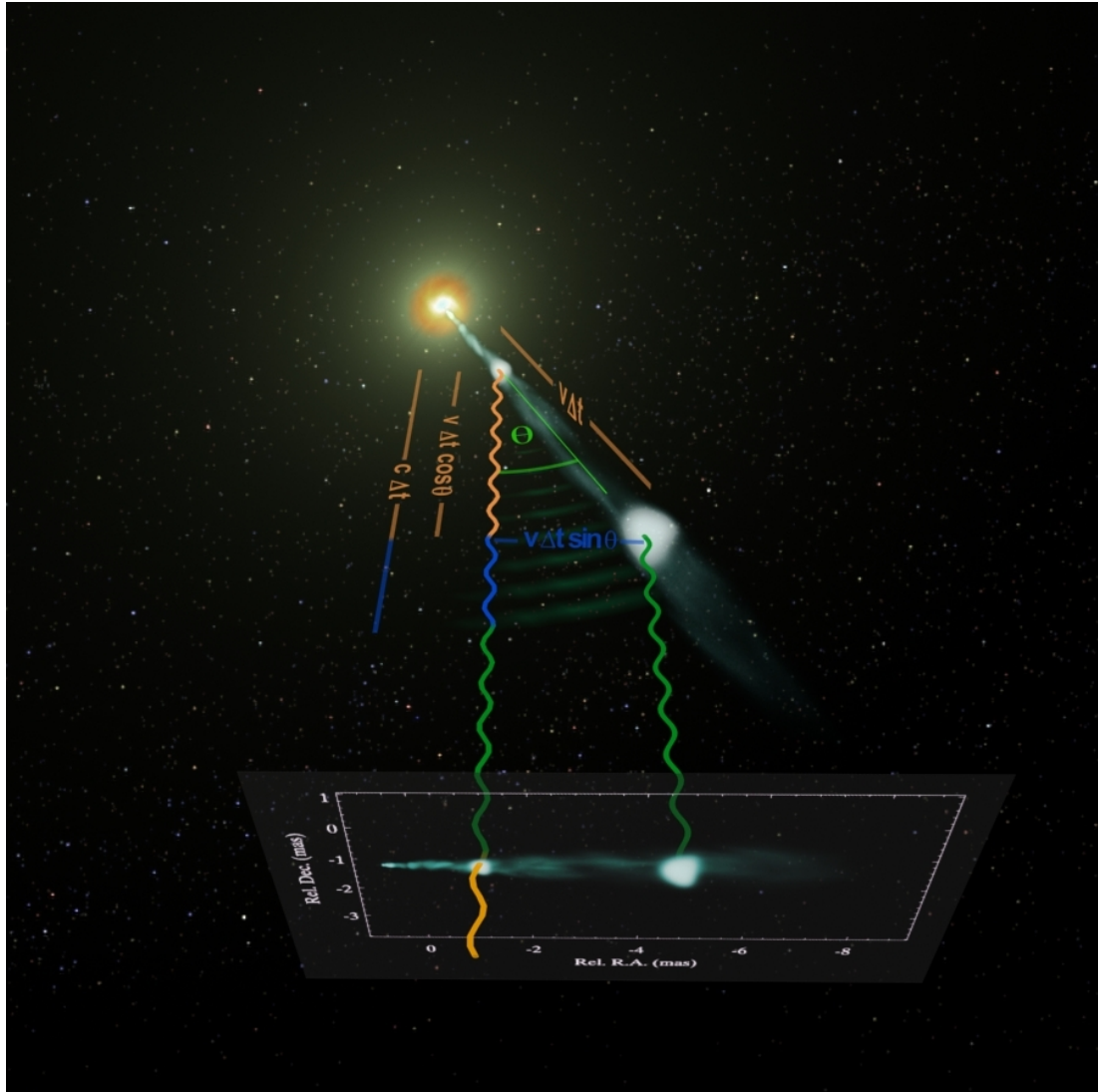


Figure 1.13: Schematic of the apparent superluminal motion effect when measuring the radiation of a jet at an inclination. The plot showcases the motion of an ejected blob as a two dimensional projection on the sky. Image credit: Prof. Dr. W. Steffen (image taken from https://www.iaa.csic.es/~jlgomez/Jose_L._Gomez/Animations_files/superlum_jetplanos_050408_1_composite.png).

In this example, a cosmological source ejects a component moving with a velocity v , at an angle θ to the observer (white blob in Fig. 1.13), some photons of

which leave the component at time t_1 (at the leftmost position) and some other photons leave the component at another time t_2 (at the rightmost position). The light rays reach the observer at time t'_1 and t'_2 respectively. In this setting, it is assumed that the source is far enough, such that the positions, at which the radiation was emitted, can be presumed to be approximately the same, equal to D_L . Using simple geometrical arguments, it can then be shown that the relation between $\Delta t = t_2 - t_1$ and $\Delta t' = t'_2 - t'_1$ is:

$$\Delta t' = (1 - \beta \cos(\theta)) \Delta t, \quad (1.31)$$

where $\beta \equiv v/c$. Even though the component has covered a distance $d_{\text{int}} = v\Delta t$, to the observer it appears that the component covered a fraction of the distance, namely $d_{\text{app}} = v\Delta t \sin(\theta)$, as can be seen in Fig. 1.13. The apparent speed is then just

$$v_{\text{app}} = \frac{v\Delta t \sin(\theta)}{\Delta t'}, \quad (1.32)$$

which can be rewritten and generalised by plugging Eq. 1.31 into Eq. 1.32 and dividing both sides by the speed of light as follows:

$$\beta_{\text{app}} = \frac{\beta \sin(\theta)}{1 \mp \beta \cos(\theta)}. \quad (1.33)$$

The sign in the denominator is negative if the component is approaching and positive if the component is receding. Indeed, if the viewing angle is small enough and β large enough, it can occur that $\beta_{\text{app}} \gg 1$.

Doppler boosting is a phenomenon, which was already briefly touched upon in Sect. 1.1.1. It refers to the relativistic aberration effect describing particles moving at velocities comparable to the speed of light, the emission of which gets boosted towards their movement direction. It is customary to begin the description by defining the Doppler factor (\mathcal{D}) as the ratio of the energy measured at infinity to the energy measured at the co-moving frame of the ejection feature (Bao & Wiita 1997). Ignoring the effects of gravity on the path of the radiation, the Doppler factor is given by the simplified form of Eq. 1.34:

$$\mathcal{D} = \left\{ (1 \pm \beta \cos(\theta)) \Gamma \right\}^{-1}, \quad (1.34)$$

where Γ is the bulk Lorentz factor and the sign again depends on if the source is approaching or receding. The wavefront received by the observer appears to have a shorter wavelength, dependent on \mathcal{D} . In terms of luminosity, which is

equal to the energy emitted per unit of time, this relation can be expressed as:

$$L_{\text{app}} = \mathcal{D}^{\xi} L_{\text{int}}. \quad (1.35)$$

Here L_{app} is the apparent (measured) luminosity, L_{int} is the intrinsic (emitted) luminosity and $\xi = 3 - \alpha$ if the source of radiation (for example a jet-flow) is continuous or $\xi = 2 - \alpha$ if it consists of individual components. It follows that for small viewing angles, the approaching section of the outflow can get extremely boosted, whereas the receding part de-boosted, resulting in only the approaching jet being detectable (blazars). To quantify this phenomenon, one can define the jet-to-counter-jet ratio⁸ R :

$$R \equiv \frac{\mathcal{F}_{\text{appr}}}{\mathcal{F}_{\text{rec}}} = \left(\frac{1 + \beta \cos(\theta)}{1 - \beta \cos(\theta)} \right)^{\xi}, \quad (1.36)$$

where $\mathcal{F}_{\text{appr}}$ is the total, integrated flux of the jet (approaching), \mathcal{F}_{rec} is the one of the counter-jet (receding). Neighbouring radio-galaxies, such as 3C 84, which is the primary focus of this thesis, however, sometimes do exhibit a pc-scale counter-jet (Vermeulen et al. 1994; Walker et al. 1994; see also Sect. 1.4). Utilising Eq. 1.36 holds valuable insights into this source, as will be discussed in Sect. 4.

1.4 3C 84 in the context of radio astronomy

As Scharwächter et al. (2013) put it, the numerous classifications of NGC 1275 (the host galaxy of 3C 84) in the literature – among others, NGC 1275 has been classified as a FRI galaxy, a peculiar Seyfert galaxy (Seyfert 1.5), a post-merger galaxy, a cooling flow galaxy, a low-ionisation nuclear emission-line region (LINER), and even a BL Lac object – demonstrate the fact that there is a plethora of physical phenomena to explore in just this one source.

3C 84 is the prominent radio source in the galaxy NGC 1275 (Perseus A), depicted in Fig. 1.14 both in optical and in X-rays. Using Equatorial (J2000) coordinates, 3C 84 is located at $03^{\text{h}}19^{\text{m}}48.1601^{\text{s}}$ in right ascension (RA), $+41^{\text{d}}30^{\text{m}}42.106^{\text{s}}$ in declination (DEC), measured for the VLBA Calibrator Survey (Beasley et al. 2002). The redshift is $z = 0.0176$ (Strauss et al. 1992) corresponding to $D_{\text{L}} = 78.9 \text{ Mpc}^9$. The mass estimates of the SMBH range between $3.2 \times 10^8 M_{\odot}$ (Park & Trippe 2017) and $2.0 \times 10^9 M_{\odot}$ (Giovannini et al. 2018).

Being one of the most prominently bright radio sources in the northern sky

⁸It is implicitly assumed that the jet and counter-jet are intrinsically symmetric.

⁹ D_{L} is the luminosity distance. Λ cold dark matter cosmology (Λ CDM) is assumed, with $H_0 = 67.8 \text{ km/s/Mpc}$, $\Omega_{\Lambda} = 0.692$, $\Omega_{\text{M}} = 0.308$ (Planck Collaboration et al. 2016).

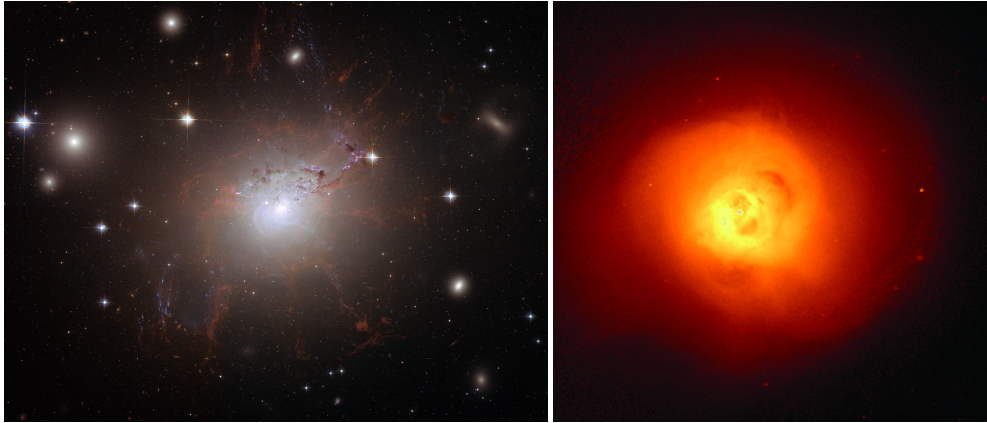


Figure 1.14: NGC 1275 at optical and X-ray wavelengths. *Left*: Composite optical B, V, and R filter image of NGC 1275 taken with the Hubble Space Telescope. The image reveals fine structures – filaments consisting of cold gas – supported by the magnetic field lines of the galaxy. They are created when radio bubbles rise from the central region, within the surrounding hot gas. Image credit: NASA, ESA, and the Hubble Heritage (STScI/AURA)-ESA/Hubble Collaboration (image taken from https://commons.wikimedia.org/wiki/File:NGC_1275_Hubble.jpg). *Right*: Composite image of NGC 1275 taken with Chandra, at 1.4 Ms exposure in the 0.5 – 7 keV band, revealing the structure of the X-ray emitting gas in detail. Image taken from Fabian et al. (2011).

(a jet power as high as $10^{44} - 10^{45}$ erg/s has been reported by Abdo et al. 2009; MAGIC Collaboration et al. 2018), 3C 84 has been a frequent target of observations since the very beginning of radio astronomy. The Perseus cluster, which harbours NGC 1275 and 3C 84 was discovered in 1905 (Wolf 1906). Very early works by Hubble & Humason (1931), Humason (1932), and Seyfert (1943) had already identified the peculiar morphology of NGC 1275 along with its almost stellar nucleus. Since the 1950s, there was already speculation about the origin of the radiation. While Ryle et al. (1950) proposed that the source of radiation was the entire galactic cluster, Baade & Minkowski (1954) theorised that the radio emission was due to galaxy collision and that the source should be identified solely with NGC 1275, which was then confirmed by Baldwin & Elsmore (1954). However, in the 1960s, Burbidge et al. (1963) and Burbidge & Burbidge (1965) showed that the emission originated from the nuclear region of the galaxy, based on newer observations. The first photographs of NGC 1275 ($H\alpha$ interference-filter) were published in 1970 by Lynds (1970), and were in support of violent phenomena occurring in the nucleus. Nevertheless, the question, whether a link between the galactic merger and the abundant nuclear activity exists, remains unanswered (Haschick et al. 1982; Hu et al. 1983; Rubin et al. 1977).

From some of the earliest interferometric (VLBI) observations of 3C 84, conducted in the late 1970s and early 1980s, the first centimetre spectral index map

of 3C 84 was published by Unwin et al. (1982). The hybrid maps presented a milliarcsecond resolution, and revealed a strong, inverted spectrum (due to SSC) and that the source consisted of three main components of compact emission on milliarcsecond scales.

The first 3 mm (86 GHz) images of 3C 84 were produced by Backer et al. (1987), Wright et al. (1988), and Baath et al. (1992), achieving even better, sub-milliarcsecond resolutions. They revealed the existence of a two-component jet in the nuclear region, which exhibited significant structural changes in the time frame of these publications. Changes to the direction of the jet flow and to the position angle (P. A.) of ejected components were also reported.

Bartel et al. (1988), Dhawan et al. (1990), and Krichbaum et al. (1992) published some of the first 7 mm (43 GHz) images of 3C 84. Specifically noteworthy was the discovery of the perpendicularity of some of these components to the bulk jet flow, in the work by Bartel et al. (1988). Krichbaum et al. (1992) and Dhawan et al. (1998) revealed in their work, which studied the kinematics of the jet, that the jet components followed an asymmetric path, with curved trajectories.

At 1.3 cm (22 GHz), works by Marr et al. (1989) and Venturi et al. (1993) revealed a fast moving knot, as well as multiple ejection events and features, one of which, as shown in Sect. 5 (Paraschos et al. 2022b), appears to be coincident with the diffuse emission region C2 (e.g. Nagai et al. 2014, 2010).

High dynamic range images at 8.4 GHz (Walker et al. 1994) and 22.2 GHz (Vermeulen et al. 1994) revealed for the first time the existence of a pc-scale counter-jet, north of the compact VLBI core. Follow up work by Walker et al. (2000) (see also Fig. 1.15) confirmed the existence of the emission in the northern region, with the observations validating the assertion, that the spectra are consistent with free-free absorption. The authors proposed the existence of a free-free absorbing disc around the central engine. Newer maps at 15 GHz and 43 GHz by Fujita & Nagai (2017) and at 43 GHz and 86 GHz by Wajima et al. (2020) also revealed the existence of components in the north of the core at these frequencies, with a strongly inverted spectrum. These observational properties can be summarised as the influence of dense ionised gas in a free-free absorbing circumnuclear disc, with the possible existence of clouds superimposed in the nuclear region of 3C 84.

Suzuki et al. (2012), Nagai et al. (2014), and Punsly et al. (2021) studied 3C 84 at 43 GHz, taking advantage of the recent technological advancements, enabling them to produce high resolution, high sensitivity images. Specifically, Suzuki et al. (2012) monitored the central region of 3C 84 between 2002 and 2008 studying the kinematics of the ejected components. Nagai et al. (2014)

1 A BRIEF DESCRIPTION OF THE UNDERLYING ASTROPHYSICAL CONCEPTS

studied the sub-pc scale of 3C 84 and discovered a limb brightening in the restarted jet, which the authors attributed to possibly transverse velocity stratification. Punsly et al. (2021) considered VLBI observations of 3C 84, conducted between 2018 and 2020, and found a double or triple nuclear structure in the core.

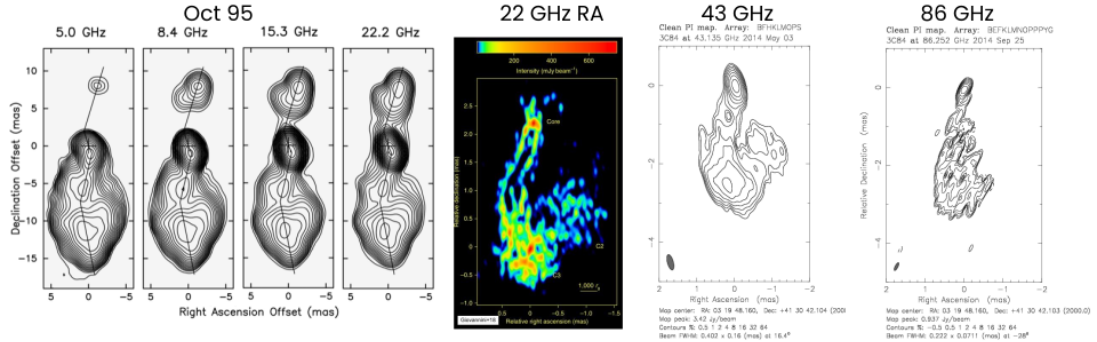


Figure 1.15: VLBI images of 3C 84 at different frequencies. From left to right: 5, 8.4, 15.3, 22.2 GHz taken from Walker et al. (2000), 22 GHz observed with RadioAstron (space VLBI) taken from Giovannini et al. (2018), 43, and 86 GHz. The main distinguishable regions (following the naming convention of Nagai et al. 2014) are the core (C1) detectable at all frequencies, the diffuse emission region (C2), mostly detectable in the 22 GHz RadioAstron image and the 43 GHz image, and the bright knot (C3), mostly detectable in the same two frequencies. Furthermore, in the higher resolution RadioAstron image, the limb-brightened, double rail structure is prominent, together with the east-west elongation in the core region, which is perpendicularly oriented to the bulk jet flow. A definitive interpretation of the latter is still pending.

The same double rail structure was also identified in a high resolution *RadioAstron* study of 3C 84 (Giovannini et al. 2018; see also Fig. 1.15). Another perplexing feature of this image is the evident elongation of the VLBI core in the east-west direction – perpendicular to the bulk jet flow, the existence of which has numerous implications and interpretations. Savolainen et al. (2021) revisited the data from that observation, which also revealed a faint cocoon-like structure enveloping much of the pc-scale southern jet.

At 86 GHz Oh et al. (2022) published images of 3C 84, which were observed between 2008 and 2015 (see also Sect. 4). This study revealed that the VLBI core of 3C 84 consists of at least two components, oriented in the east-west

direction, matching the RadioAstron map. A large, historical, highly sensitive overview of 3C 84 at 86 GHz is presented in Paraschos et al. (2022b), (see also Sect. 5). The double nuclear structure is observed there as well, which, combined with the observations mentioned above, seems to confirm the existence of this elongation in the core at multiple frequencies.

3C 84 exhibits a high level of circular polarisation, up to 3%, with the sign also changing along the jet (Homan & Wardle 2004). This high degree of polarisation can be explained by nearly saturated Faraday conversion. The first linear polarised emission observations of 3C 84, at longer wavelengths, were presented by Taylor et al. (2006), revealing a very high Faraday rotation measure (RM) of ~ 7000 rad/m², which might explain the very low values of linear polarisation detected. The regions with the most prominent detections are the southern knot of the jet and the core. In more recent 43 GHz observations, Nagai et al. (2017), on the other hand, find the polarised emission to be located almost entirely in the southern knot, which has also moved with time. At 86 GHz, Kim et al. (2019) found that the limb brightening appears to continue further into the core region, than previously known. The RM model the authors applied suggests that the RM is due to an external Faraday screen. At even higher frequencies, Trippe et al. (2012) only found 3σ upper limits for the linear polarisation, using observations conducted with the IRAM Plateau de Bure Interferometer.

A high resolution spectral index map of 3C 84 at a frequency pair of 43 and 86 GHz were presented by Paraschos et al. (2021) (see also Sect. 3), utilising the images first presented in Kim et al. (2019). They find a robust spectral index gradient in the north-south direction. In combination with the 15 and 43 GHz pair, the authors furthermore determined the core shift, finding that the jet apex is located $400 - 1500 R_s$ upstream of the 86 GHz VLBI core. The magnetic field near the 86 GHz core was then estimated at $B = 1.80 - 4.0$ G.

3C 84 is a γ -ray emitting source (Abdo et al. 2009) with the emitted photons reaching energies in the TeV range (Aleksić et al. 2012). The location from which the γ -rays are emitted remains elusive. Nagai et al. (2012) monitored 3C 84 between 2009 and 2011, both with single dish and VLBI at 43 GHz. The authors introduced the C1, C2, and C3 notation, referring to the core, diffuse emission to the southwest of the core and bright knot in the south respectively. In that time frame, they found no clear association between the γ -rays and the radio light curves. Increases in the radio flux density could be correlated to two GeV flares detected during the observation window. Nagai et al. (2016) also associated the long term increase in γ -ray flux with the increase in the radio flux of C3. Interestingly, the flaring activity of the γ -rays shows variations in time

spans, which are as short as a week. Linhoff et al. (2021) excluded the region close to the BH (outside the Ly α radius) to be the source of the γ -rays, based on calculations of the optical absorption depth of high-energy photons in the BLR of 3C 84. Most recently, Hodgson et al. (2021) presented a detailed kinematics study of the 1 – 3 mas region of 3C 84 at 43 GHz, using the WISE code (Mertens & Lobanov 2015), and its connection to γ -ray emission. The authors find a 2 – 3 σ significance association between the γ -ray flares, and the splitting of slowly moving emission regions.

1.4.1 Thesis motivation

The technique of VLBI at the shortest possible wavelengths has revolutionised astronomy, by providing a direct view into the cores of AGN, which, at lower frequencies, are synchrotron self-absorbed, with an angular resolution down to 50 μ as. It is now possible to explore and image spatial scales orders of magnitude smaller than one pc in size.

Millimetre-VLBI specifically facilitates the direct imaging of the vicinity of SMBHs, which, depending on the distance and BH mass, may translate to several tens to a few hundred R_s . At these scales, it is the assumption of current AGN-launched jet models, that ultra-relativistic radio jets are formed and that the acting electromagnetic forces cause the initial jet acceleration. Imaging jets with millimetre-VLBI can thus be utilised to further the understanding of underlying mechanisms of jet formation, initial acceleration, jet expansion further downstream and, general propagation. For example, such images can assist in determining where the bulk energy is converted from magnetic to kinetic. Furthermore, the combination of millimetre-VLBI flux and size measurements of the source, with the observed spectral turnover frequency can provide a measure of the balance between kinetic and magnetic energy. This yields constraints to the existing theoretical jet launching scenarios.

Current millimetre-VLBI monitoring of γ -ray loud AGN jets, part of which is 3C 84, is aimed at determining the morphology of the jet base at sub-pc scales and the jet kinematics, as well as ascertaining why the bulk jet flow appears more curved in the central jet region than farther out. Some of the contemporary interpretations favour projection effects (purely geometrical origin) as an explanation, while others support the propagation of hydrodynamical or magnetic instabilities, or even precession-driven jet bending caused by a central binary SMBH system.

The main focus of the present thesis is the study of the structure and the structural variability of the nearby radio-galaxy 3C 84, which harbours an

AGN-jet, using VLBI imaging at the highest possible resolution. The goal is to better understand the details of jet launching, acceleration and collimation relating to the observed AGN activity throughout the entire electromagnetic spectrum, and draw generalised conclusions for other similar sources. Of particular interest is the testing of jet launching models (BP versus BZ jet launching scenarios), and the search for correlations between flaring activity and jet propagation on sub-pc scales. Using 3C 84 as the main target for this analysis is a natural consequence due to the number of advantages it offers. It is nearby and harbours a SMBH (i.e. observations of unmatched resolution are achievable), and as a radio-galaxy (i.e. not a blazar) features rather slow moving jet components, which show only moderate relativistic boosting effects.

The remainder of this thesis is structured as follows: a brief overview of the basic principles of radio astronomy and interferometry is presented in Sect. 2. Section 3 is devoted to the core shift analysis utilised to pinpoint the jet apex of 3C 84. Section 4 is dedicated to the discovery of a double nuclear structure present in the nucleus of 3C 84. Additional epochs are added to create a large, historical data set of 86 GHz observations of 3C 84, spanning more than two decades; the results are presented in Sect. 5. The thesis culminates with Sects. 6 and 7 where the conclusions of this work and the outlook are presented respectively.

2 Basics of radio astronomy & interferometry

The field of radio astronomy, which constitutes a subfield of observational astronomy, has a rather brief history. It was born when a young engineer, by the name of Karl Guthe Jansky, was tasked with identifying the source of noise disturbing transatlantic communications (at 20.5 MHz). He successfully identified the source of the interference to be the centre of the Milky Way, in 1931, by using a rotating antenna he had built, which quickly was nicknamed 'Jansky's Merry-go-round'. His discovery was published in 1933 (Jansky 1933a,b). The next defining moment in the history of radio astronomy was in 1937. In that year Grote Reber created the first parabolic reflecting antenna used as a radio telescope, which he then utilised to chart the Milky Way at 160 MHz (Reber 1944).

The onset of the second world war meant that radio antennae were used as radars to detect activities of the enemy. In this context it was James Hey (Hey 1946) who noticed that the Sun was producing radio waves, which appeared as noise on the radar readings. The next major development was in 1951, when the HI (21 cm) line in the interstellar medium (ISM) was discovered by Ewen & Purcell (1951). Then in 1965, Penzias & Wilson (Penzias & Wilson 1965) described a isotropic, unpolarised, and free from seasonal variations excess antenna temperature, which is now known to be the CMB¹⁰. In that same year, Weaver et al. (1965) also discovered the first OH line maser at 1665 MHz. Two years later, in 1967, the first pulsars were discovered by J. Bell-Burnell and A. Hewish (Hewish et al. 1968).

Of course radio astronomy has not been stagnant since those days, with advancements and breakthroughs happening regularly. The advancements of interferometry, which will be discussed in the next sections, opened a new window into the observation of the universe. The culmination of the achievements is the first image of the event horizon of a BH (see Fig. 2.16; Event Horizon Telescope Collaboration et al. (2021)).

2.1 First Principles

The great radio astronomical discoveries and advancements listed in the introduction of this section rely on the operation and measurements of radio telescopes. Here the theory behind their operation and how they function will be explored in more detail.

¹⁰This discovery was of such importance, that they received the Nobel price in physics in 1978.

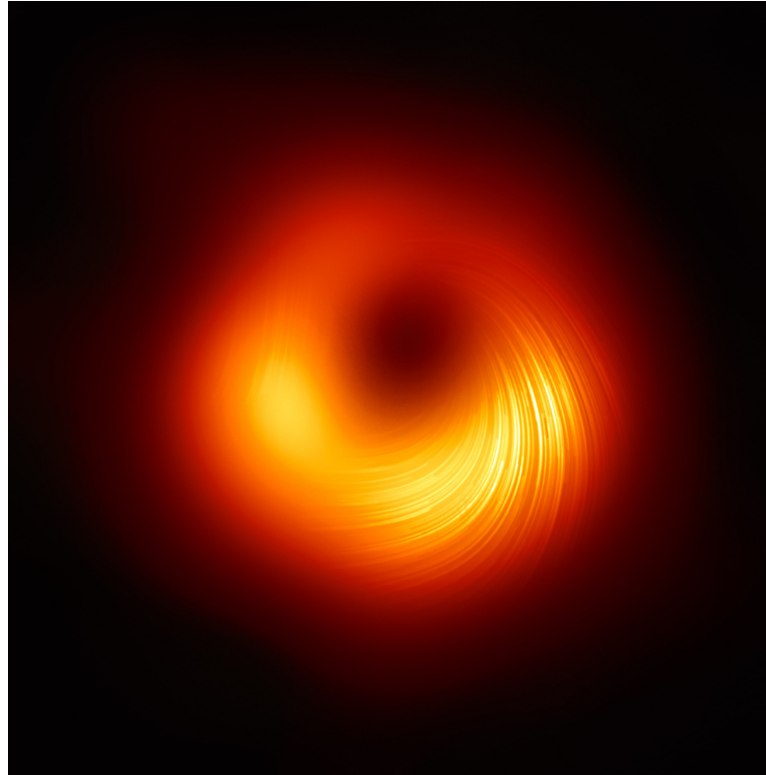


Figure 2.16: Polarisation field lines superimposed on a total intensity image of M 87 (Event Horizon Telescope Collaboration et al. 2021). Image credit: EHT Collaboration.

A radio telescope is essentially an antenna, used to detect the radio waves emitted from a radio source. There are three main types of antennae; their usage depends on the target wavelength. Wired antennae (half dipoles) are used for wavelength detection of more than 1 m. Hybrid antennae (wire reflectors) are utilised for detecting wavelengths ~ 1 m. Reflector antennae measure sub-meter wavelengths. The focus here will be on the latter.

The reflector, which coherently sums electric fields, and the feed, which is the waveguide, constitute the frontend, which together with the backend comprise the main parts of the telescope. There are a multitude of different frontends, differentiated by the focus geometry. The main ones are: the prime focus, the (offset) Cassegrain focus, the Nasmyth focus, the beam waveguide focus and the dual offset focus. Figure 2.17 (top, left) showcases the path that the photons follow.

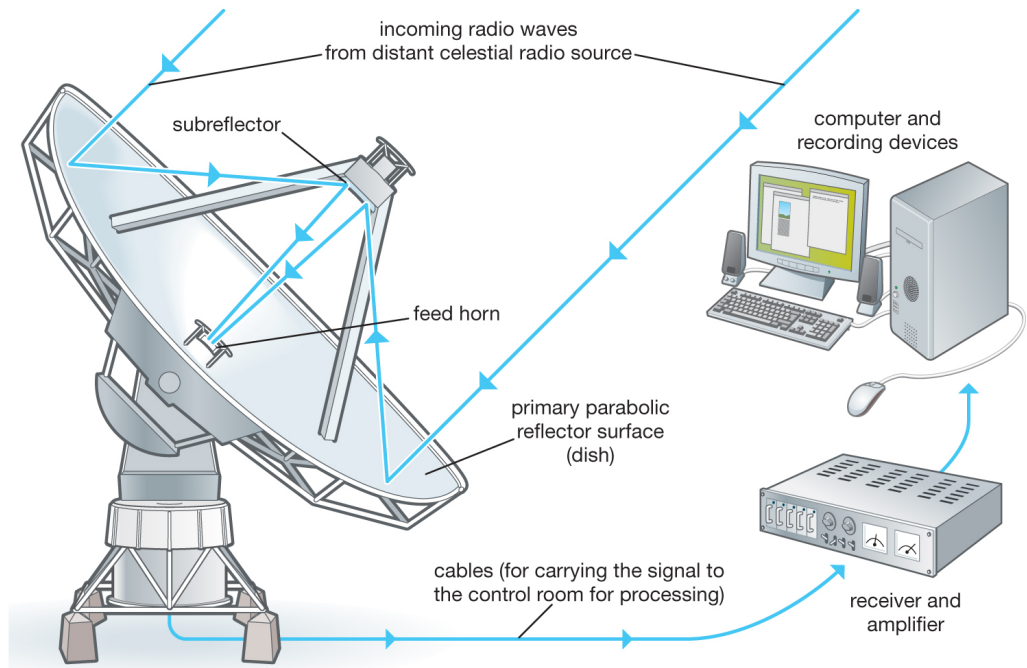
Regardless of the type of frontend, the signal is focused at some point and then guided into the backend, where the signal processing takes place. The backend is displayed in the top right part of Fig. 2.17. First, the signal arrives at the receiver, which is usually one of two types. If the receiver uses thermal-electric effects, it is referred to as a bolometric receiver. These types of receivers are usually used for sub-millimetre observations. In short, the incom-

ing photons generate heat and the total power (resistance) changes due to the material changing temperature. On the other hand, if the receiver uses the properties of the incoming light (recording the amplitude and phase), it is a heterodyne receiver (see Fig. 2.17 bottom). The incoming radio waves create an alternating current of the form $V_0 \sin(\omega t - \phi)$ inside the detector. The detector only works with one polarisation, but usually two are required. In reflectors, the polarisation is split into two, either in the feed itself, or inside a polariser, also called orthomode transducer (OMT). The main usage of the a heterodyne receiver is to 'down-convert' the signal. This is necessary, because the frequency of the incoming signal is too high to be easily sampled or processed. Signal losses also scale as the square of the frequency; lower frequencies therefore offer the additional advantage of less losses, during the filtering and digitisation process for example. The down-conversion fixes all these issue. The Low Noise Amplifier (LNA) is a cryogenically cooled device (for noise minimisation), which amplifies the incoming signal. Depending on the wavelength, the LNA is applied either before or after mixing. The last step, is the most important. It involves the usage of the mixer. As the name suggests, the mixer mixes the arriving signal with a single tone provided by the Local Oscillator (LO). The output is referred to as the intermediate frequency (IF) and is the main quantity used in the later calibration process. This IF signal is then forwarded further in the backend for signal processing and detection. Finally, it is fed into a computer for post-detection processing and digitisation. The digitisation is performed with a digital-to-analogue converter (ADC), through Nyquist sampling. Nyquist sampling is based on the Nyquist theorem, which states that any bandwidth-limited continuous function in a bandwidth $\Delta\nu$ can be reproduced with homogeneously distributed samples, split into $\leq \Delta\nu^{-1}$ wide time bins.

The signal put out by the computer is dimensionless and therefore needs to be matched to a physical quantity. This is where the Johnson-Nyquist theorem comes in handy. It states that the power (P_ν) of the signal can be thought of as the temperature (T_A) of a resistor in the following way:

$$P_\nu = k_B T_A, \tag{2.1}$$

where k_B is the Boltzmann constant. In other words, the antenna can be imagined as a resistor, where the thermal motion of the electrons create a current I , with $\langle I \rangle = 0$ but $\langle I^2 \rangle \neq 0$. It should be noted that T_A is not a real temperature; the real temperature of the antenna is close to the ambient temperature. Besides the antenna temperature, numerous other sources contribute to the noise level of the output registered, for example receiver components. Follow-



© 2012 Encyclopædia Britannica, Inc.

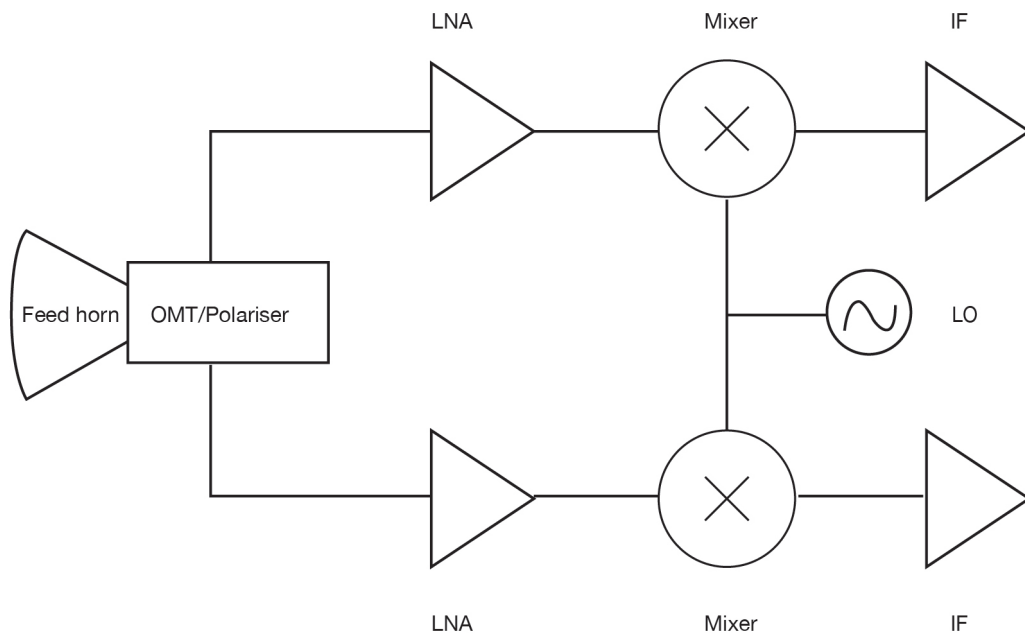


Figure 2.17: Radio telescope system and receiver circuit. *Top*: Schematic of the data flow in a radio telescope. Image credit: Encyclopedia Britannica, Inc. (<https://cdn.britannica.com/34/4634-050-DA53D88D/Radio-telescope-system.jpg>). *Bottom*: Heterodyne receiver system circuit sketch. Image recreated from Radio Astronomy lectures by Dr. A. G. J. van Leeuwen .

ing the same rationale, the output signal can be tied to a temperature, which is called the system temperature, and is thus described by the following equation:

$$T_{\text{sys}} = T_A + T_{\text{rec}} = T_{\text{atm}} + T_{\text{CMB}} + T_{\text{ground}} + T_{\text{loss}} + T_{\text{rec}} \dots, \quad (2.2)$$

where T_{atm} is the equivalent temperature from the atmosphere, T_{CMB} the temperature from the cosmic microwave background, T_{ground} the temperature from the ground, T_{loss} the temperature corresponding to the various losses in the signal propagation, and T_{rec} is equivalent temperature from the receiver. Generally, $T_{\text{sys}} \gg T_A$. The advantage of this approach is that it is possible to perform a ‘hot load’ (material at ~ 300 K) and ‘cold load’ (liquid nitrogen bath at ~ 77 K) calibration of the instrument instead of using an astronomical source at every observation. The K/Jy multiplication factor should be approximately stable and is periodically compared to the flux of known calibrator sources.

On the other hand, having measured the T_A , for example, from observing a distant radio-galaxy, one can estimate the estimate the flux by employing the Rayleigh-Jeans theorem, and solving for the brightness temperature T_B . It can then be shown, that for an extended source $T_A = T_B$. However, in reality this is calculation is not as straightforward and Eq. 2.1 is valid for an idealised system. An antenna does not respond to the input signal homogeneously for all solid angles; instead, it is characterised by an antenna reception pattern (see Fig. 2.18). The main distinguishing features are the main lobe (beam) and the sidelobes. This pattern stems from the so-called Fraunhofer diffraction, which is described by the following equation:

$$\theta \approx 1.22 \cdot \frac{\lambda}{D}, \quad (2.3)$$

where θ is the full width at half maximum (FWHM) of this main lobe, λ is the wavelength, and D is the diameter of the aperture. Besides the effects caused by the directionality of the antenna response pattern, the actual temperature measured also depends on the antenna efficiency η , which is defined as the ratio of the collected power to the incident power, and on the geometrical area of the dish A_{geom} . Combining these terms, the measured antenna temperature T_A^* is given by equation 2.4:

$$T_A^* = \frac{P_v^*}{k_B} = \frac{\eta A_{\text{geom}} \mathcal{F}_v}{2k_B}, \quad (2.4)$$

with \mathcal{F}_v being the net flux of the source. The thermal noise, which corresponds

to the uncertainty of this calculation σ_T is given by the radiometer equation:

$$\sigma_T = \frac{T_{\text{sys}}}{\sqrt{\Delta\nu \tau_{\text{int}}}}, \quad (2.5)$$

where τ_{int} is the integration time.¹¹

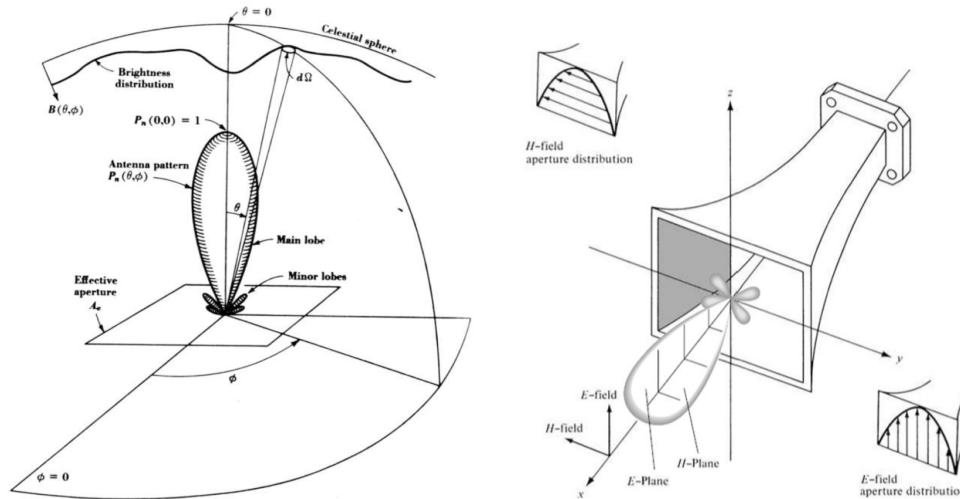


Figure 2.18: Beam pattern and horn of antenna. *Left*: Antenna beam pattern in three dimensions. Showcased are the main lobe and the sidelobes, in relation to the brightness distribution of the source projected on the celestial sphere. Image credit: Astronomy Instrumentation lecture by Prof. G. Woan (<https://radio.astro.gla.ac.uk/ralectures/beam%20patterns.pdf>). *Right*: Principal electric field (E) plane and magnetic field (H) plane patterns for a pyramidal horn antenna. The sketch shows the appearance of the antenna pattern in relation to a feed horn. Image credit: Antenna Theory and Design slides by Prof. J. Wang (http://is.buaa.edu.cn/_local/3/33/4C/1F4302A046B7FD33140ACF16957_D01288D7_3A1F7C.pdf).

2.2 Interferometry & VLBI arrays

While the single dish radio telescopes, which was the focus of the previous section, contributed to most of the major discoveries listed in the introduction, they suffer from two major limitations: their size and angular resolution. To conceptualise this, one can consider the 21 cm Hydrogen line and the telescope diameter needed, to achieve an angular resolution of just one arcsecond. Solving Eq. 2.3 for D shows that one would need a telescope with a diameter of 52.8 km. Currently, the two largest fully steerable telescopes are the Radio Telescope Effelsberg (EF) and the Robert C. Byrd Green Bank Telescope (GBT), both at a 100 m diameter. Even transit instruments like the Five-

¹¹This section is based on the Radio Astronomy lectures by Prof. A. G. J. van Leeuwen from Astron and Prof. K. M. Dasyra from the University of Athens.

hundred-meter Aperture Spherical radio Telescope (FAST) and the RATAN-600 (600 m diameter) do not come close to the size needed.

Fortunately, a procedure by the name of interferometry exists, with which a telescope, even larger than the Earth itself – if orbiting satellite antennae are involved – can be simulated. In the following, a brief overview of the basics of a connected two-antenna interferometer are presented, which are also illustrated in Fig. 2.19.

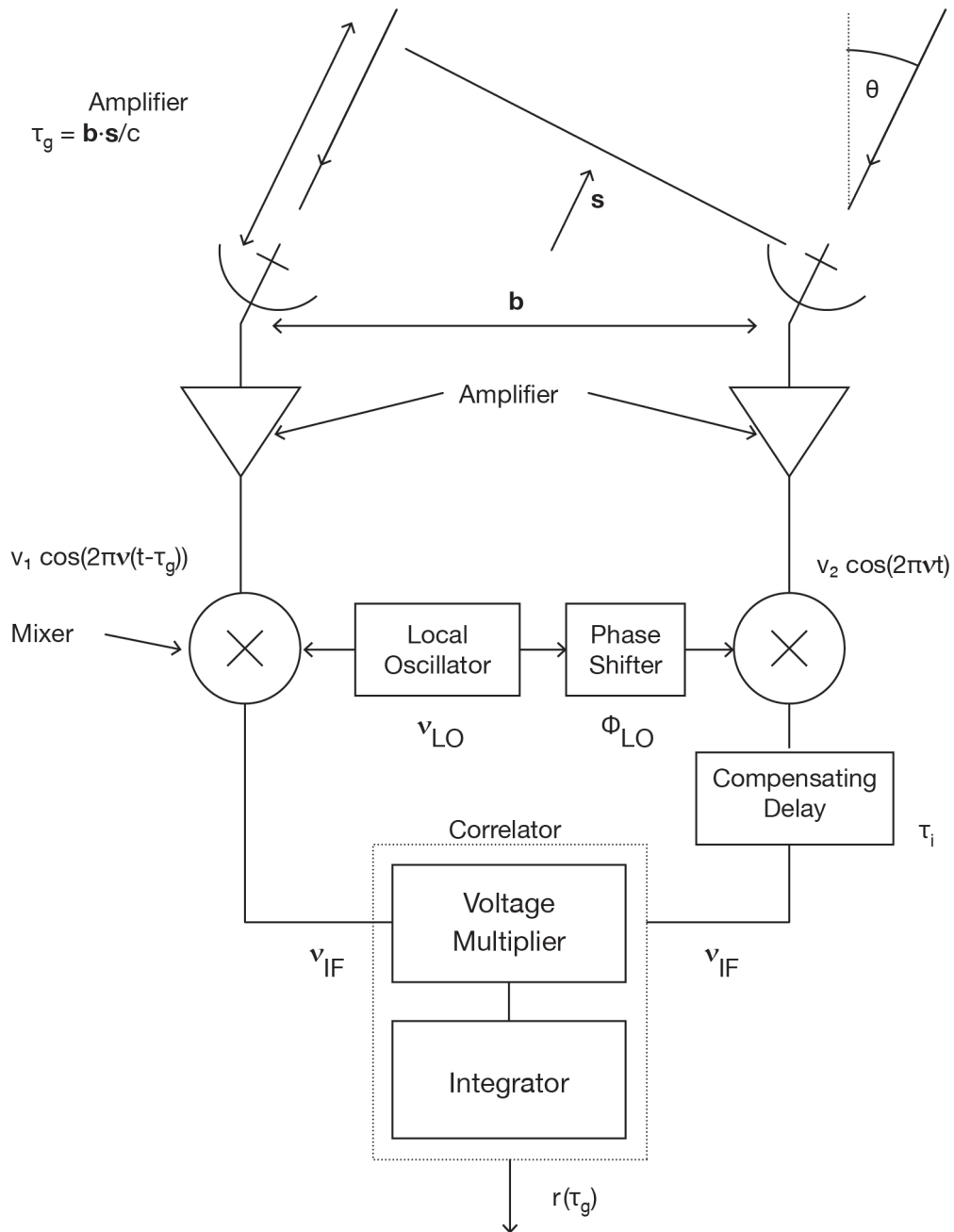


Figure 2.19: Schematic of a two antenna interferometer, with the backend circuit also displayed. Image taken from the Radio Astronomy lecture slides by Prof. K. M. Dasyra.

Similar as in a single dish system, the incident radiation from the extra-galactic source reaches the ‘closest’ of the two antennae, and after a delay, denoted as τ_g , the other one. This difference in time τ_g is referred to as the geometric delay between the two antennae, because it is a purely geometrical effect, caused by the different positions of the two antennae with regard to the source in the sky. Applying simple vector calculus, it can be shown that τ_g can be described by the following equation:

$$\tau_g = \frac{\mathbf{b} \cdot \mathbf{s}}{c}, \quad (2.6)$$

where \mathbf{b} is called the baseline, \mathbf{s} is the direction towards which the antennae are pointing at and c is the speed of light. The baseline is the vector distance separating the two antennae as seen from the source, and it is usually measured in units of wavelength. This plane is described by the unit vectors (\mathbf{u}, \mathbf{v}) , giving it the name (u, v) -plane. Following the schematic of Fig. 2.19, the signal voltages (V_1 and V_2) at the two telescopes are amplified and arrive at the mixer in the form:

$$V_1 = v_1 \cos \left(2\pi\nu (t - \tau_g) \right), \quad (2.7)$$

and

$$V_2 = v_2 \cos (2\pi\nu t), \quad (2.8)$$

where v_1 and v_2 are voltage amplitudes and ν is the frequency. After undergoing down-conversion, as described in Sect. 2.1, phase shifting and delay compensation (see Fig. 2.19), the signal arrives at the correlator.

The correlator performs a coherent combination of the two signals by averaging and multiplying them, as follows:

$$r^e (\tau_g) = \langle V_1 V_2 \rangle = \frac{v_1 v_2}{2} \cos (2\pi\tau_g). \quad (2.9)$$

However, as the cosine in Eq. 2.9 suggests, $r^e (\tau_g)$ is an even function. In order to correctly reconstruct the signal, the even part needs to be added. The correlator achieves this by adding a 90° phase rotation in one of the two signals (e.g. $V_2 \rightarrow V'_2$) and then repeating the procedure. Then:

$$r^o (\tau_g) = \langle V_1 V'_2 \rangle = \frac{v_1 v_2}{2} \sin (2\pi\tau_g). \quad (2.10)$$

and overall the response $r (\tau_g)$ is:

$$r (\tau_g) = r^o (\tau_g) - i r^e (\tau_g). \quad (2.11)$$

Equation 2.25 can be rewritten by introducing the complex visibility \mathcal{V} , which is

the eminent quantity used for calibration. It is defined as:

$$\mathcal{V} = \mathcal{V}_q \exp(i\Phi), \quad (2.12)$$

with \mathcal{V}_q being the visibility amplitude, which is the even and odd part of the response added in quadrature ($\mathcal{V}_q = \sqrt{r^o(\tau_g)^2 + r^e(\tau_g)^2}$) and Φ being the visibility phase ($\Phi = \arctan[r^o(\tau_g)/r^e(\tau_g)]$).

With the above formalism in mind, the fundamental theorem governing radio interferometry can now be introduced: the van Cittert-Zernike theorem (van Cittert 1934; Zernike 1938). It states that *for a spatially incoherent source a constant phase relation exists between the wavefronts emitted from that source*. In other words, it links the complex visibility to the true brightness distribution of the source $I_\nu(\mathbf{s})$, integrated over the solid angle of the source $d\Omega$, per frequency, through the Fourier transformation as follows:

$$V_\nu(\mathbf{b}) = \iint I_\nu(\mathbf{s}) \exp(-2\pi i \nu \mathbf{b} \cdot \mathbf{s}/c) d\Omega. \quad (2.13)$$

The above equation can be rewritten with the help of the directional cosines of the sky $\mathbf{s} = (l, m, n)$, which is defined with respect to the phase tracking centre \mathbf{s}_0 , in the following form:

$$V_\nu(u, v, w) = \iint I_\nu(l, m) \exp(-2\pi i (ul + vm + wn)) \frac{dldm}{\sqrt{1-l^2-m^2}}. \quad (2.14)$$

It is usually assumed that the observation only takes into account a minute area of the sky (tangential plane). In that regime $\sqrt{1-l^2-m^2} \approx 1$. A further assumption usually applied is that $w = 0$. Equation 2.14 simplifies to the following form:

$$V_\nu(u, v) = \iint I_\nu(l, m) \exp(-2\pi i (ul + vm)) dldm. \quad (2.15)$$

It is then straightforward to calculate $I_\nu(l, m)$ by applying the inverse Fourier transform to Eq. 2.15:

$$I_\nu^D(l, m) = \iint S(u, v) V_\nu(u, v) \exp(+2\pi i (ul + vm)) dudv. \quad (2.16)$$

Notice here that a sampling function $S(u, v)$ ¹² was inserted into the calculation, to account for the incomplete response of the interferometer. The D in the exponents denotes that this quantity is not the actual distribution of the source brightness, but a so-called dirty image of it. Thus, the dirty image is just the

¹²The sampling function is a sum of delta functions, which are the measured visibilities at each point in space, and zero everywhere else.

convolution of $I_\nu(l, m)$, with the dirty (synthesised) beam $B_\nu(l, m)$:

$$B_\nu(l, m) = \iint S(u, v) \exp(+2\pi i(ul + vm)) \, du dv. \quad (2.17)$$

A number of connected interferometer arrays exist, which work based on the principles described above, including the Atacama Large Millimeter/sub-millimeter Array (ALMA), and the Very Large Array (VLA). They can resolve radio sources in unprecedented detail. But they are still limited by their diameter D . Recalling the example with the HI line, an observation with an angular resolution of just one arcsecond requires an array with a diameter of many kilometres. Fortunately, the need to resolve ever so fine structures in quasars pushed ahead technological advancements, enabling radio astronomers to carry out the first VLBI observations, which combine many radio telescopes at different locations on Earth, in 1967 (Kellermann & Moran 2001; Moran 1998). Two were the major technological advancements, which made this possible: the first one is the development of time-tagging, which allows for the data from the telescopes to be synchronised, creating one data-stream at playback time. The second one is the transition to tape recorders at each observatory, which means that the antennae need not be physically connected to each other. The data are stored on magnetic tapes, and after the observations, all of them are shipped to the correlator, which then applies to them the procedure described above. However, the produced data set is not yet final; the geometrical delay needs to be compensated. This is achieved by applying an extremely detailed model to the data. The applied corrections need to be accurate to a fraction of the observed wavelength (converted into a time domain delay). Nevertheless, the geometric delay compensation model will always be imperfect. For this reason, further calibration needs to be applied, accounting for unpredictable delays and time offsets (see Sect. 2.3.1 for more details). To this day, the same steps are followed for correlating a VLBI observing session, except that nowadays the data are stored on magnetic discs and drives.

In the following sections the currently functioning VLBI arrays, which operate at centimetre and millimetre wavelengths will be examined more closely.

2.2.1 VLBA

¹³The Very Long Baseline Array (VLBA), as the name suggests, is a VLBI array covering mostly the continental part of the USA, with one antenna also located on Hawaii and another one on the Virgin Islands. It consists of the following

¹³The material of this section is adapted from <https://science.nrao.edu/facilities/vlba/introduction-to-vlba>.

Table 1: Re-imaged 15 GHz VLBA epochs of 3C 84

Date	Pol.	VLBA Stations
August 2010	Dual	BR, FD, HN, KP, LA, MK, NL, OV, PT, SC
June 2011	Dual	BR, FD, HN, KP, LA, MK, NL, OV, PT, SC
March 2012	Dual	BR, FD, HN, KP, LA, MK, NL, OV, PT, SC
July 2013	Dual	BR, FD, HN, KP, LA, MK, NL, OV, PT, SC
July 2014	Dual	BR, FD, HN, KP, LA, MK, NL, OV, PT, SC
June 2015	Dual	BR, FD, HN, KP, LA, MK, NL, OV, PT, SC
June 2016	Dual	BR, FD, HN, KP, LA, MK, NL, OV, PT, SC
April 2017	Dual	BR, FD, HN, KP, LA, MK, NL, OV, PT, SC
July 2018	Dual	BR, FD, HN, KP, LA, MK, NL, OV, PT, SC
June 2019	Dual	BR, FD, HN, KP, LA, MK, NL, OV, PT, SC
July 2020	Dual	BR, FD, HN, KP, LA, MK, NL, OV, PT, SC

ten, identical, 25 m antennae, from East to West: St. Croix (SC), Hancock (HN), North Liberty (NL), Fort Davis (FD), Los Alamos, (LA), Pie Town (PT), Kitt Peak (KP), Owens Valley (OV), Brewster (BR), and Mauna Kea (MK). First light with all ten antennae participating was achieved in May 1993. The baselines between them range between 200 km and 8600 km, allowing for compact radio sources to be detected ($T_B > 10^5$ K). The signals can be recorded in nine discrete bands in addition to two narrow bands (although not simultaneously). All antennae are equipped with receivers capable of observing at frequencies between 312 MHz and 96 GHz. In this work, presented in the following chapters, observations at 15, 43, and 86 GHz were utilised. For the first two frequencies, the VLBA was used exclusively. Tables 1, and 2 summarise the epochs used in this analysis, the polarisation, and the antennae, which were operational. Oftentimes, the VLBA is combined with other telescopes and arrays around the globe, to improve the sensitivity and the resolution (e.g. with the GBT, the Very Large Array or EF, creating the High Sensitivity Array). At higher frequencies, the VLBA is twice per year combined with European and Asian telescopes forming the Global millimetre-VLBI array.

2.2.2 GMVA

¹⁴As already introduced in 2.2.1, the Global millimetre-VLBI array (GMVA) is a VLBI array, spanning the whole Earth. It consists of antennae in America, Asia, and Europe. The American antennae are mostly comprised of the VLBA, with the ALMA, the Large Millimeter Telescope (LMT), and the GBT joining some observations. The European stations are the Yebes Observatory RT40m (YS), the

¹⁴The material of this section is based on <https://www3.mpifr-bonn.mpg.de/div/vlbi/globalmm/>.

Table 2: Re-imaged 43 GHz VLBA epochs of 3C 84

Date	Pol.	VLBA Stations
November 2010	Dual	BR, FD, HN, KP, LA, MK, NL, OV, PT, SC
May 2011	Dual	HN, KP, LA, MK, NL, OV, PT, SC
May 2012	Dual	BR, HN, KP, LA, MK, NL, PT, SC
August 2013	Dual	BR, FD, HN, KP, LA, MK, NL, OV, PT, SC
May 2014	Dual	BR, FD, HN, KP, LA, MK, NL, OV, PT, SC
September 2014	Dual	BR, FD, HN, KP, LA, MK, NL, OV, PT, SC
May 2015	Dual	BR, FD, HN, KP, LA, MK, NL, OV, PT, SC
October 2016	Dual	BR, FD, KP, LA, NL, OV, PT, SC
April 2017	Dual	BR, FD, HN, KP, LA, MK, NL, OV, PT, SC
September 2017	Dual	BR, FD, HN, KP, LA, MK, NL, OV, PT, SC
April 2018	Dual	BR, FD, HN, KP, LA, MK, NL, OV, PT, SC
October 2018	Dual	BR, FD, HN, KP, LA, MK, NL, OV, PT, SC
March 2019	Dual	BR, FD, HN, KP, LA, MK, NL, OV, PT, SC
May 2019	Dual	BR, FD, HN, KP, LA, MK, NL, OV, PT, SC
January 2020	Dual	BR, FD, HN, KP, LA, MK, NL, OV, PT, SC
April 2020	Dual	BR, FD, HN, KP, LA, MK, NL, OV, PT, SC
June 2020	Dual	BR, FD, HN, KP, LA, MK, NL, OV, PT, SC
October 2020	Dual	BR, FD, HN, KP, LA, MK, NL, OV, PT, SC
December 2020	Dual	BR, FD, HN, KP, LA, MK, NL, OV, PT, SC
March 2021	Dual	BR, FD, HN, KP, LA, MK, NL, OV, PT, SC
May 2021	Dual	BR, FD, HN, KP, LA, MK, NL, OV, PT, SC

IRAM 30 m telescope on Pico Veleta (PV), the Northern Extended Millimeter Array (NOEMA), the Effelsberg 100 m telescope (EF), the Onsala Space Observatory (ON), the Metsähovi Radio Observatory (MH), with the Greenland Telescope (GLT) joining particular observations. Finally, the Korean VLBI Network (KVN), consisting of the KVN Yonsei Observatory (KY), the KVN Ulsan Observatory (KY), and the KVN Tamna Observatory (KT), comprises the Asian antennae participating. Figure 2.20 showcases the locations of most of the aforementioned observatories. The observations are carried out in the 3 mm band, reaching angular resolutions down to $50 \mu\text{s}$. The great advantage of global millimetre-VLBI with the GMVA is that compact galactic and extra-galactic radio sources can be directly imaged at 86 GHz.

Most of this thesis resolves around the fringe-fitting, calibration, and imaging of GMVA data of 3C 84, starting in 1999 and reaching up to the end of 2020. Table 3 summarises the epochs that were fringe-fitted, calibrated and imaged.

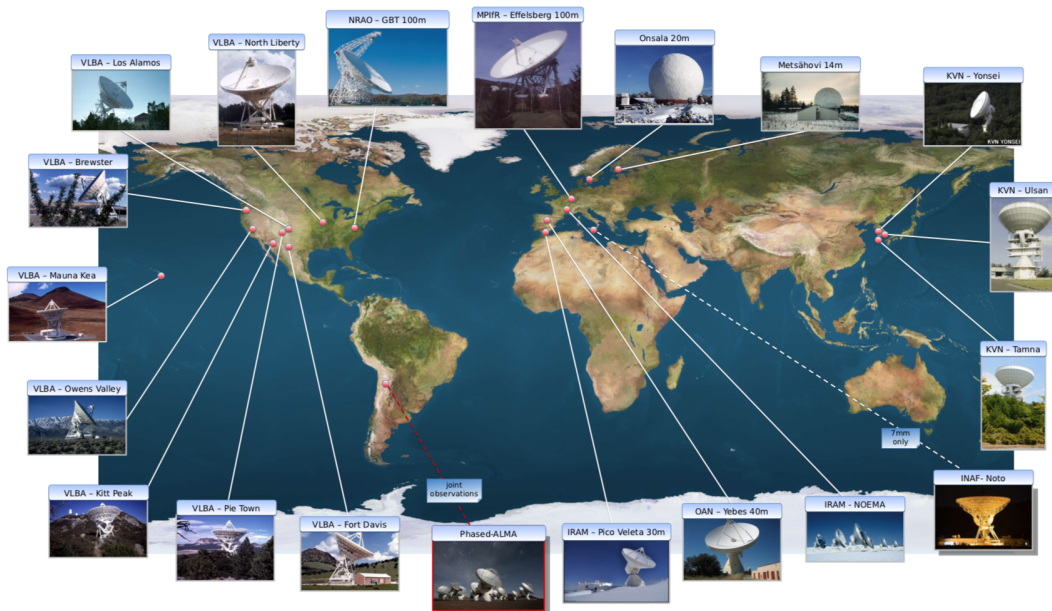


Figure 2.20: The telescopes comprising the GMVA (taken from Boccardi et al. 2017). Image credit: Helge Rottmann.

2.2.3 Other VLBI arrays

Besides the GMVA and VLBA, the data from which were used in this thesis, there are a number of other VLBI arrays in existence. The European VLBI Network (EVN) consists of multiple European antennae and is capable of measuring at frequencies up to 43 GHz. It is one of the most sensitive VLBI arrays in the world at centimetre-wavelengths, and the only one capable of observations taking place in real-time. Global-EVN measurements can also be performed,

Table 3: Analysed GMVA epochs (86 GHz) of 3C 84

Date	Pol.	GMVA Stations
May 1999*	Single	EF, KP, HAY, ON, PT, LA, MK, FD, PV, HAT, OV
October 1999*	Single	EF, KP, HAY, ON, PT, QUB, MK, FD, HAT
October 2004	Single	EF, ON, PV, PDB, MH, HN, FD, NL, OV, PT, KP, MK, LA
April 2005*	Single	EF, ON, PV, PDB, NL, BR, FD, PT, LA, KP, OV, MK
May 2008*	Single	EF, ON, PDB, FD, NL, OV, PT, BR, KP, MK, LA
May 2011*	Dual	BR, EF, FD, KP, LA, MH, NL, ON, OV, PDB, PT, PV
May 2012*	Dual	BR, EF, FD, KP, LA, MK, NL, PDB, PT, PV
September 2013*	Dual	BR, EF, FD, KP, MK, NL, ON, OV, PT, PV, YS
May 2014*	Dual	BR, EF, FD, KP, LA, OV, PT, PV
September 2014*	Dual	BR, EF, FD, KP, LA, MK, NL, OV, PDB, PT, PV, YS
May 2015*	Dual	BR, EF, FD, GBT, KP, LA, MK, NL, ON, OV, PT
September 2016	Dual	BR, EF, FD, KU, KY, LA, MH, NL, ON, OV, PT, YS
April 2017	Dual	BR, EF, FD, GBT, KP, KT, KU, LA, MH, MK, NL, ON, OV, PT, PV, YS
September 2017	Dual	BR, EF, FD, KP, LA, MH, MK, NL, ON, OV, PT, YS
April 2019	Dual	BR, EF, FD, KP, LA, MH, MK, NL, ON, OV, PT
April 2020	Dual	BR, EF, KP, LA, MH, MK, NL, ON, OV, PT, YS
October 2020	Dual	BR, EF, FD, KP, KT, KY, KU, LA, MH, MK, NL, ON, OV, PT, PV, YS

* For these epochs only re-imaging was performed.

by combining European antennae with American and Asian ones, again at up to 43 GHz.

The Event Horizon Telescope, as the name suggests, set its goal to image the immediate surroundings of a SMBH, at angular resolution scales comparable to its event horizon. To achieve this goal, the EHT observed in 2017 the centre of the radio-galaxy M 87, as well as Sagittarius A*, in the centre of our Galaxy, at 230 GHz. Observations at such a high frequency are capable of penetrating even the most optically thick materials. The first images of the event horizon of the SMBH in M 87 were published in 2019 as a result (e.g. Event Horizon Telescope Collaboration et al. 2019a). Subsequently, in 2022, the first image of the SMBH of our Galaxy was revealed (e.g. Event Horizon Telescope Collaboration et al. 2022a). At the time of observation the EHT was comprised of the following stations (Event Horizon Telescope Collaboration et al. 2019b): ALMA, Atacama Pathfinder Experiment (APEX), James Clerk Maxwell telescope (JCMT), LMT, PV, Submillimeter Array (SMA), Submillimeter Telescope (SMT), and the South Pole Telescope (SPT).

2.3 Calibration of a VLBI data set

In this section the concepts of phase and amplitude calibration will be introduced. Then, their application in the calibration data-flow of a GMVA epoch will be reviewed.

2.3.1 Calibration practicalities

The output of the correlator is not a final data product yet, to do science with. Even though the correlation procedure corrects many inherent issues of the visibilities, further steps need to be performed to account for effects such as atmospheric corruption and positional inaccuracies. This is done via a set of standard calibration routines. To conceptualise them, the observed visibility V_{ij} will be introduced, which differs from the true visibility \mathcal{V}_{ij} in the following way:

$$V_{ij}(t) = g_i(t) g_j^*(t) \mathcal{V}_{ij}(t) + \epsilon_{ij}(t) + \eta_{ij}(t), \quad (2.18)$$

where $g_i(t)$ is the complex element gain of station i , and $g_j^*(t)$ the complex conjugate of the element gain of station j , $\epsilon_{ij}(t)$ is the complex offset per baseline, and $\eta_{ij}(t)$ the stochastic complex noise. Conversely, the observed correlated phase $\phi_{ij}^c(t, \nu)$ differs from the true correlated phase $\phi_{ij}^v(t, \nu)$ as follows:

$$\phi_{ij}^c(t, \nu) = \phi_{ij}^v(t, \nu) + \phi_{ij}^e(t, \nu), \quad (2.19)$$

where ϕ_{ij}^e represents the numerous residual phase errors, introduced by atmospheric and positional effects.

Fringe-fitting is a calibration procedure used to estimate the various phase errors, such as offsets and drifts. Following Cotton (1995), a relation between the phase of the interferometer $\phi_{ij}^{\text{int}}(t, \nu)$ and the time dependent delay $\tau^{\text{del}}(t)$ exists, which states that:

$$\phi_{ij}^{\text{int}}(t, \nu) = 2\pi\nu\tau_{ij}^{\text{del}}(t). \quad (2.20)$$

Applying then the fringe-fitting technique, one can calculate the delay and delay rate of the phase by differentiating and expanding $\phi_{ij}^{\text{int}}(t, \nu)$ to the first term. In mathematical terms:

$$\Delta\phi_{ij}^{\text{int}}(t, \nu) = \phi_{0,ij} + \left(\frac{\partial\phi_{ij}}{\partial\nu}\Delta\nu + \frac{\partial\phi_{ij}}{\partial t}\Delta t \right), \quad (2.21)$$

where $\phi_{0,ij}$ is the zeroth order approximation, $\frac{\partial\phi_{ij}}{\partial\nu}$ is the delay and $\frac{\partial\phi_{ij}}{\partial t}$ the delay rate. Having determined the delays and the delay rates, the appropriate corrections can be applied to the visibilities, which are coherently integrated in frequency and time space. Several algorithms have been developed over the years to perform these operations. The most up-to-date ones utilise the fast Fourier transform (FFT) fringe search.

As mentioned in Sect. 2.1, the output of the computer is not yet in physical units¹⁵ of flux density. Since in radio astronomy the sources are usually faint, measuring their flux in $\frac{\text{erg}}{\text{cm}^2\text{sHz}}$ would be impractical to use, as it is an unwieldy amount. Instead a unit of Jansky¹⁶ is used; with $1 \text{ Jy} = 10^{23} \frac{\text{erg}}{\text{cm}^2\text{sHz}}$. It is customary to introduce at this point the concept of system equivalent flux density (SEFD), which is defined as follows:

$$\text{SEFD} = \frac{2k_B T_{\text{sys}}}{A_{\text{eff}}}, \quad (2.22)$$

where $A_{\text{eff}} = \eta A_{\text{geom}}$. They are the effective and geometrical area of the antenna respectively. Combining Eqs. 2.4 and 2.22, a Kelvin-to-Jansky conversion factor for the cross-correlation amplitude can be obtained:

$$\mathcal{F}_{ij} = C_{ij} d \frac{\sqrt{\text{SEFD}_i \text{SEFD}_j}}{2\Delta\nu\tau_{\text{int}}}, \quad (2.23)$$

where C_{ij} is a multiplication factor, dependent on the correlation coefficient per

¹⁵The units used by the correlator are called Whitneys.

¹⁶In honour of K. G. Jansky.

baseline (in arbitrary units) and d is a correction factor accounting for digital sampling losses.

Caution needs to be exercised when calibrating millimetre-VLBI data sets, as the atmospheric fluctuations affecting the opacity are more prominent. In this case, the T_{sys} needs to be modified, with a correction of the form:

$$T_{\text{sys}}^* = T_{\text{sys}} \exp(\tau_v \cdot \text{AM}), \quad (2.24)$$

where T_{sys}^* is the corrected system temperature value outside of the atmosphere, $\text{AM} = \sin(\text{Elv})$ is the elevation (Elv) dependent 'air mass' and τ_v is the atmospheric optical depth given by the formula:

$$\tau = \log\left(1 - \frac{T_{\text{sys}} - T_{\text{rec}}}{T_{\text{atm}}}\right), \quad (2.25)$$

where T_{rec} is the receiver temperature. T_{atm} , as mentioned in Eq. 2.2, is the average, ambient temperature of the atmosphere (Martí-Vidal et al. 2012). It is usually approximated by the following expression:

$$T_{\text{amb}} = 1.12 \cdot T_{\text{ground}} - 50\text{K}. \quad (2.26)$$

Typical opacity ranges, for example at the Effelsberg 100 m Telescope, are of the order of 0.1 – 0.2 at 3 mm.

Finally, large scale deviations from a perfectly reflecting surface can lead to loss of sensitivity. The gravitational force, which is acting on the dish, deforms the surface. The deformation is a function of the tilt in elevation and is commonly described with a polynomial in Elv denoted as $G(\text{Elv})$. Thus a further correction to the T_{sys}^* is applied:

$$T_{\text{sys}}^{**} \equiv \frac{T_{\text{sys}}^*}{G(\text{Elv})} = \frac{T_{\text{sys}}^*}{\alpha_0 + \alpha_1 \cdot \text{Elv} + \alpha_2 \cdot \text{Elv}^2 + \dots}. \quad (2.27)$$

Equation 2.22 can then finally be rewritten as:

$$\text{SEFD} = \frac{T_{\text{sys}}^{**}}{\Gamma_s}, \quad (2.28)$$

where Γ_s is the so-called antenna gain, given by the formula:

$$\Gamma_s = \frac{A_{\text{eff}}}{2k_B}. \quad (2.29)$$

2.3.2 Exemplary calibration of a GMVA data set

Table 3 displays the 86 GHz GMVA epochs used in this thesis. Epochs without an asterisk were fringe-fitted and calibrated by me. For epochs marked with a star, a previous fringe-fitting was adopted. In this section, the performance of the calibration and fringe-fitting is described, for the exemplary April 2020 epoch.

The observations of 3C 84 took place on April 25th and 26th 2020 in dual, circular polarisation, with a duration of 11.5 hours. They were part of the complementary monitoring of FERMI sources (sources emitting γ -rays) conducted by the VLBA-BU-BLAZAR group (Jorstad et al. 2017). The array was comprised of the following antennae: BR, EF, FD, KP, LA, MH, MK, NL, ON, OV, PT, and YS. The aggregate bitrate for recording was two Gigabits per second (Gbps), and two-bit digitisation was used. The scan length was of the order of seven minutes. The data were recorded with a polyphase filterbank, splitting the observing band into eight IF channels. The bandwidth for each IF is 32 MHz, for a total recording bandwidth of 2×256 MHz. Finally, for the correlation procedure, which was carried out at the Max-Planck-Institut für Radioastronomie (MPIfR) in Bonn, Germany, the DiFX correlator (Deller et al. 2011) was used.

The output of the correlator is a *uvfits* file, which is read into the standard Astronomical Image Processing System (AIPS, see Greisen 1990). After indexing the data and correcting for changes in the parallactic angle and the effects of the Nasmyth mount for the YS station, the first major step is to do what is called *manual phase calibration*. This step is crucial, as the standard *phase-cal injection tones* method is impossible for 86 GHz observations, since the VLBA stations lack them, and the purpose is to correct the instrumental delays. In a nutshell, first a global fringe-fit is performed, to identify high S/N FRING¹⁷ solutions per antenna. Based on these, the delay and phase offsets between the IFs are then eliminated (see Fig. 2.21).

A proper global fringe fit is the second step, over the full bandwidth, solving for the rates and delays, by combining all IFs. Here the purpose is to rid the data of time-dependent rates and delays. The S/N limit was set to 4.1. A number of different fringe solution intervals and delay/rate windows were then set, with the ultimate goal of maximising the detection total. The most detections were registered for fringe solution interval of 3.5 minutes, with the delay window being 200 nanoseconds and the rate window 400 MHz. Next, the system temperature (T_{sys}) and gain curve data, provided by each station, were read into AIPS, using the task ANTAB. They are needed for the flux amplitude calibration. Outliers

¹⁷All the AIPS tasks like FRING etc. can be found in the cookbook: <ftp://ftp.aoc.nrao.edu/pub/software/aips/TEXT/PUBL/COOKBOOK.PDF>.

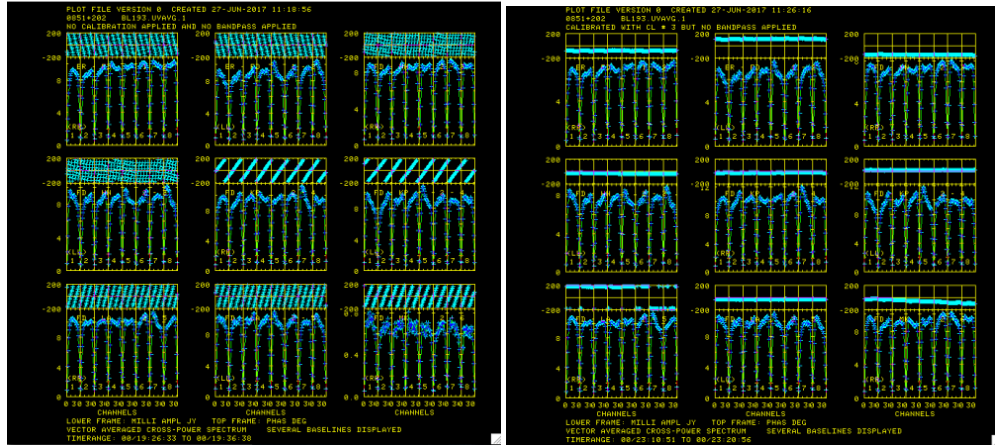


Figure 2.21: Plots generated with the task `POSSM`. *Left*: Appearance of phase (and amplitude) before fringe-fitting. *Right*: Same data after fringe-fitting. Note the smoothing out of the slopes in the phase. Image taken from the AIPS simple self calibration guide (<https://casaguides.nrao.edu/index.php/AIPS-Simple-Self-Cal>).

were flagged with the task `SNEDT`. The actual amplitude calibration and opacity correction (wherever necessary) was then performed with the task called `APCAL`. The penultimate step was to remove the cross-hand phase and delay offsets between the two polarisations, with the task `RLDLY`. Finally, after averaging over the frequencies, the *uvfits* file was exported with the tasks `SPLIT` and `FITTP`. A data flow chart of the procedure described above is displayed in Fig. 2.22.

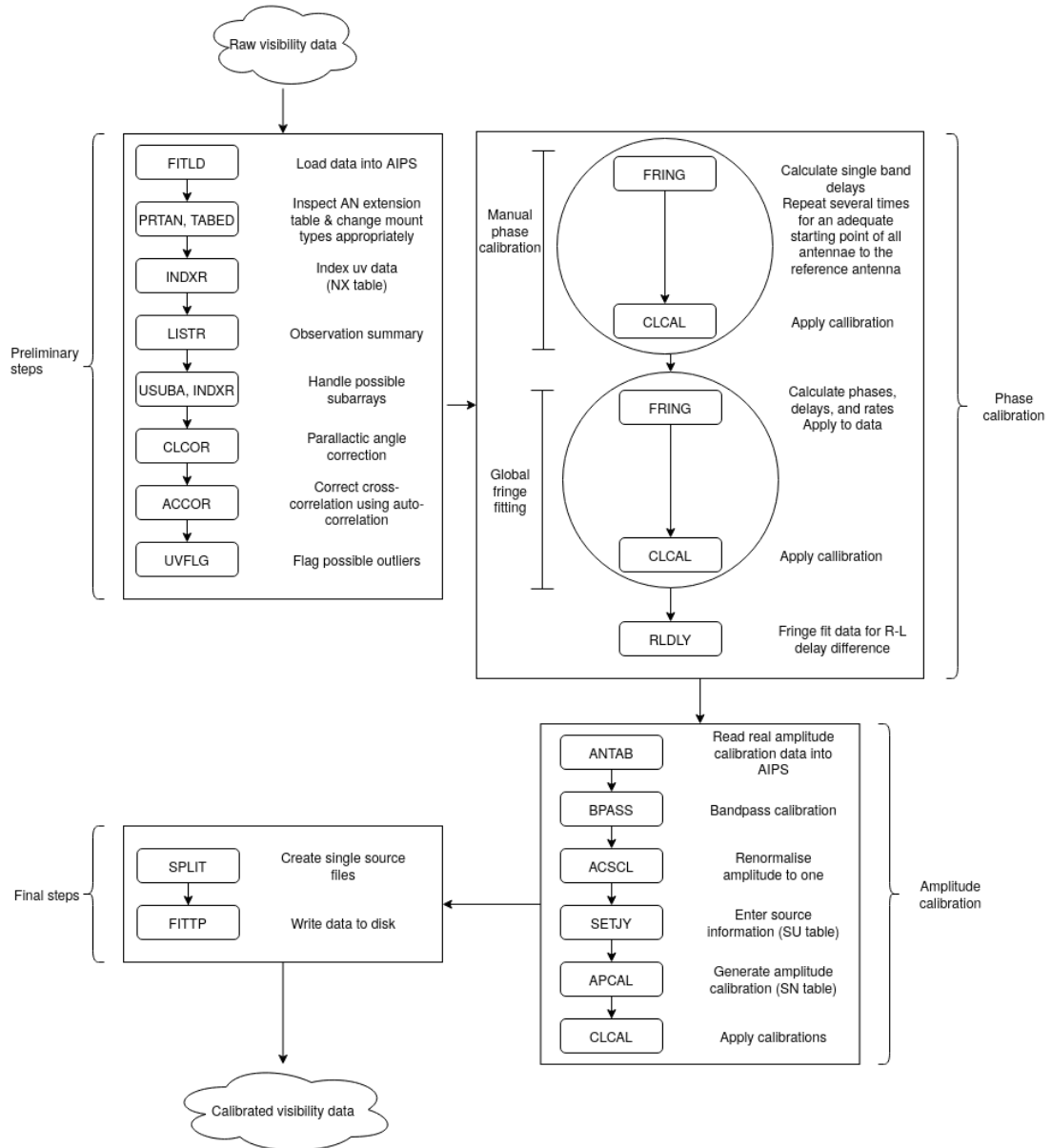


Figure 2.22: Data flow chart of the various tasks used in AIPS to obtain the final calibrated *uvfits* file. Tasks *POSSM* and *SNPLT* are regularly used between the various steps to inspect the data. Figure inspired by Fig. 3.2 in Karamanavis (2015).

The above steps are performed in a scripted, semi-automated manner, utilising *ParselTongue* (a Python interface to AIPS; see also Kettenis et al. 2006). A detailed description of the whole, aforementioned procedure is presented in Martí-Vidal et al. (2012). The rest of the epochs listed in Table 3 were fringe-fitted and calibrated in similar fashion.

2.4 Imaging of a VLBI data set

In this section the concept of the *CLEAN* and the *MEM* algorithms will be introduced and then the application of the former to a GMVA observation will be

briefly discussed.

2.4.1 Imaging practicalities

¹⁸While an inverse Fourier transform can theoretically be applied to the visibilities put out by the correlator to produce an image, this is in practice not as straightforward. The reason is that errors in amplitude and phase, due to limited (u, v) -coverage, scatter the power across the image, giving the appearance of excessive noise, and thus a simple deconvolution with the dirty beam produces artefacts (e.g. sidelobes).

Fortunately, a procedure exists to reduce the noise impact, which is based on the use of closure phases and closure amplitudes (Wilkinson 1989): self-calibration. The only prerequisite to applying this procedure is that the target source is of sufficient intensity, within the interferometer primary beam. It can be thought of as using the focus of a basic camera to sharpen a targeted object. The rationale behind self-calibration is rather simple: by defining the closure phase as an appropriate combination of the visibility phases between three baseline pairs, forming a triangle, the errors cancel each other out. Following Eq. 2.19, let $\phi_c^{(1)}, \phi_c^{(2)}, \phi_c^{(3)}$ be the measured phases for the three baselines, between the stations (1), (2), (3). Accordingly, $\phi_v^{(1)}, \phi_v^{(2)}, \phi_v^{(3)}$ are the true visibilities and e_2, e_3 are the errors contained such that:

$$\phi_c^{(1)} = \phi_v^{(1)} + e_2 - e_3 \quad (2.30)$$

$$\phi_c^{(2)} = \phi_v^{(2)} - e_2 \quad (2.31)$$

$$\phi_c^{(3)} = \phi_v^{(3)} - e_3. \quad (2.32)$$

Defining the observable closure phase as:

$$O_{123} = \phi_c^{(1)} + \phi_c^{(2)} - \phi_c^{(3)} = \phi_v^{(1)} + \phi_v^{(2)} - \phi_v^{(3)} \quad (2.33)$$

the errors indeed cancel out and thus the closure phase remains unaffected by phase errors. Similarly, the observable closure amplitude can be defined, although here four antennae are required. Here the station-based errors are multiplicative so the definition is as follows:

$$A_{1234} = \frac{|V_{12}| |V_{34}|}{|V_{13}| |V_{24}|} = \frac{|\mathcal{V}_{12}| |\mathcal{V}_{34}|}{|\mathcal{V}_{13}| |\mathcal{V}_{24}|}, \quad (2.34)$$

where the notation from Eq. 2.18 was followed. In this way, antenna based errors cancel out as well. Both closure quantities can be utilised to significantly

¹⁸This section is based on Sect. 9 of Wilson et al. (2013).

improve the quality of the visibility function.

The two main algorithms used are the Maximum Entropy Deconvolution Method (MEM, see Cornwell & Evans 1985; Gull & Daniell 1978; Jaynes 1957; Wernecke & D'Addario 1977 among others) and the CLEAN algorithm (Högbom 1974). The main usage of MEM is to distinguish between a number of contiguous images to determine the 'optimal' one. The difficulty lays in the fact that all possible images agree with the measured visibilities and that is the task for MEM to solve. The selected image needs to be consistent with all the previous data as well, and have maximum smoothness. This is achieved by maximising the entropy of the image; hence the name of the procedure. The caveat is that a reference image needs to be provided beforehand, supplying the a-priori knowledge necessary for the procedure to function. MEM is usually employed for handling extended sources, larger than a telescope primary beam. Point sources on the other hand, are best handled by CLEAN, which will be discussed in the next paragraph.

The CLEAN algorithm is the most widely used technique for improving radio interferometry images. As was already discussed, the dirty image, produced from the dirty beam (see Fig. 2.23) suffers from inherent issues related to large sidelobes, calibration errors, and noise, as well as generally low S/N ratios. In short, the CLEAN technique super-imposes a number of delta functions (simulating point sources) to approximate the unknown intensity distribution (previously, in Sect. 2.2, the notation I_{ν} was used) of the source. This method cannot be done analytically, only iteratively and the iteration halts when the residual brightness distribution is of the order of the theoretical noise limit in the intensities measured. The iterative algorithm, which, in essence, applies an FFT transform in the image plane works in the following steps:

1. The intensity peak of the dirty image is located. This is usually facilitated by so-called CLEAN window placement. These are support regions, designed to help the algorithm recognise the regions, in which the user assesses that source flux is present. It should be noted that this renders the method subjective to some degree.
2. A fraction f of the intensity peak located inside the CLEAN windows is then subtracted from the image, using an idealised Gaussian beam (CLEAN beam), whose size matches the main lobe of the dirty beam. The loop gain f , between zero and one, helps the iteration to converge.
3. The location and value of the subtracted peak are what constitute a CLEAN component (CC).

4. To arrive at the (first) CLEAN map, a CLEAN beam (commonly a Gaussian function with a FWHM comparable to the one of the dirty beam) is fitted to the centre of the beam of the interferometer, and then convolved with the CC. This is to fill out the pixels with missing information, due to the very nature of the interferometric observations.
5. Steps 1-3 are repeated n times, until the residual map peaks inside the CLEAN windows are beneath a limit, usually set by the noise in the visibilities.
6. Additional CLEAN windows are set around secondary intensity peaks and the previous steps are again repeated.

As presented, the CLEAN method harbours some subjectivity and depends on the personal biases (by manually setting clean windows) and experience of the user. However, it is a very powerful and computationally efficient method, which is one of the reasons, why it is the most widely adopted technique. As Thompson et al. (2017) showed, it also works successfully on different source morphologies, provided that the source is sufficiently compact and bright.

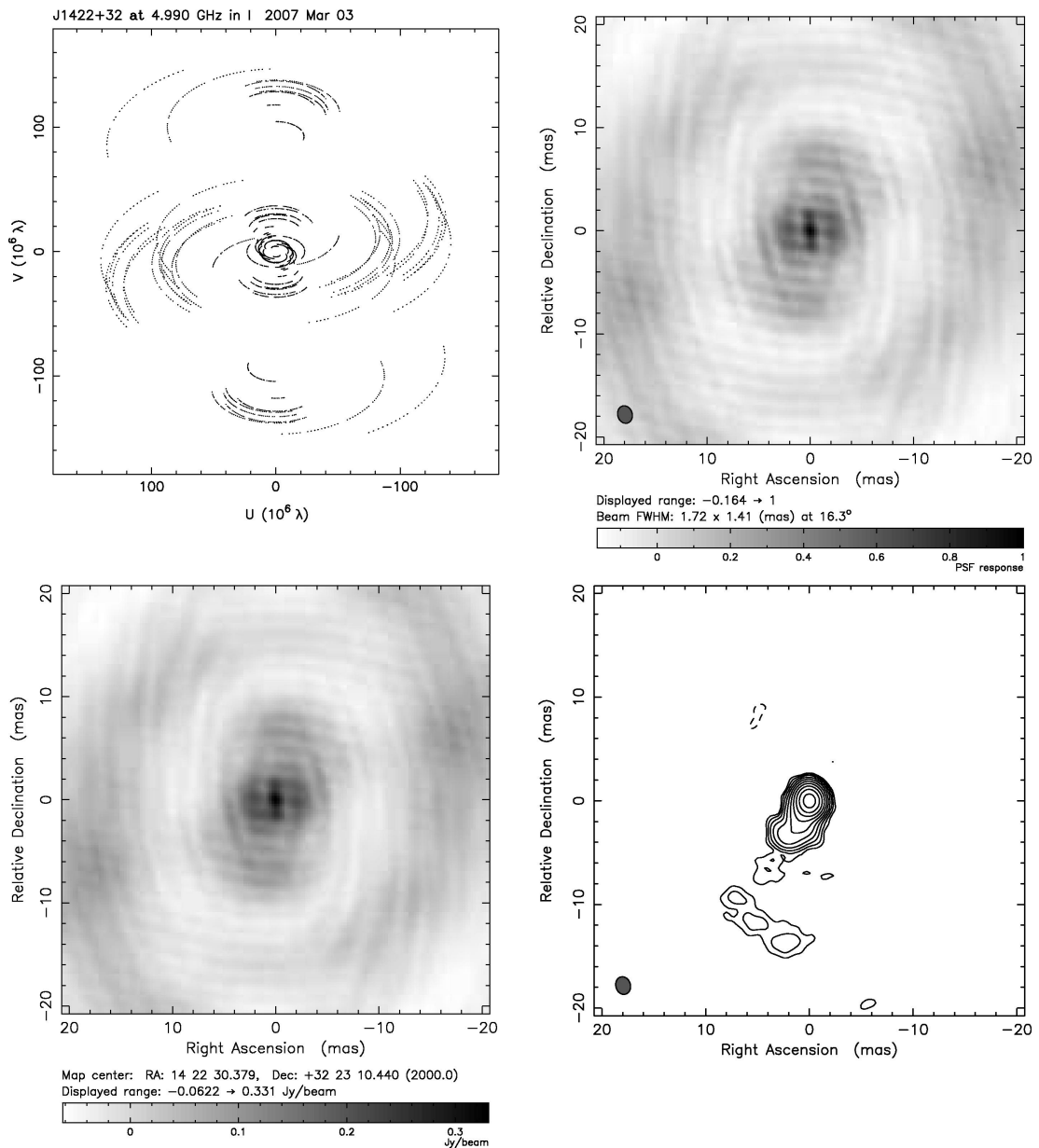


Figure 2.23: Illustration of the main concepts of image reconstruction with the CLEAN algorithm. *Top left*: Exemplary (u, v) plot of J1422+32. *Top right*: Dirty beam (see Eq. 2.17). *Bottom left*: Dirty image (see Eq. 2.17). *Bottom right*: CLEAN image of J1422+32. Figure taken from Frey & Mosoni (2009).

The last imaging step commonly applied to obtain the final CLEAN image is the self-calibration of the data set (Cornwell & Fomalont 1999). An exemplary, final CLEAN image is displayed in Fig. 2.23. Sect. 2.4.2 offers a review of how the CLEANING procedure described in this section can be applied to a GMVA data set.

2.4.2 Exemplary imaging of a GMVA data set

The *uvfits* file produced from the procedure detailed in Sect. 2.3.2 is then read into *DIFMAP* (Shepherd et al. 1994), which is a software package used for imaging. The data is inspected by eye to remove any previously unrecognised outliers in the visibilities (they can be caused by sub-optimal weather conditions or antenna related malfunctions among others). A point source model is then applied for a first step of phase self-calibration and then the data is coherently averaged over ten seconds. Then the standard *CLEANING* procedure is applied, together with iterative phase and amplitude self-calibration, until the χ^2 of the closure phases is minimised and the maximum flux density on the shortest baselines is achieved. The flux density depends mainly on the calibration described in Sect. 2.3.2 and suffers from uncertainty. A method of scaling the amplitude to reasonable values is described in the Appendix of Kim et al. (2019), and it is the one that was followed here as well. The (u, v) plot and the flux versus (u, v) distance plot of the April 2020 epoch are displayed in Fig. 2.24. The last step is to perform a two dimensional, multiple circular Gaussian function fit to the visibilities. The CC model is cleared for this purpose and the calibrated visibilities are iteratively fitted with an increasing number of such circular Gaussian functions, until again the χ^2 of the closure phases is minimised, the maximum flux density of the CC image is approximately reproduced and the image appears visually similar to the CC one. The task used for this analysis is called *MODELFIT*. The CC image contours and the superimposed circular, Gaussian *MODELFIT* components of the April 2020 epoch are displayed in one of the panels of Fig. 2 in Paraschos et al. (2022b) (see also Sect. 5). An overall flow chart of both the calibration and imaging methods is summarised in Fig. 2.25.

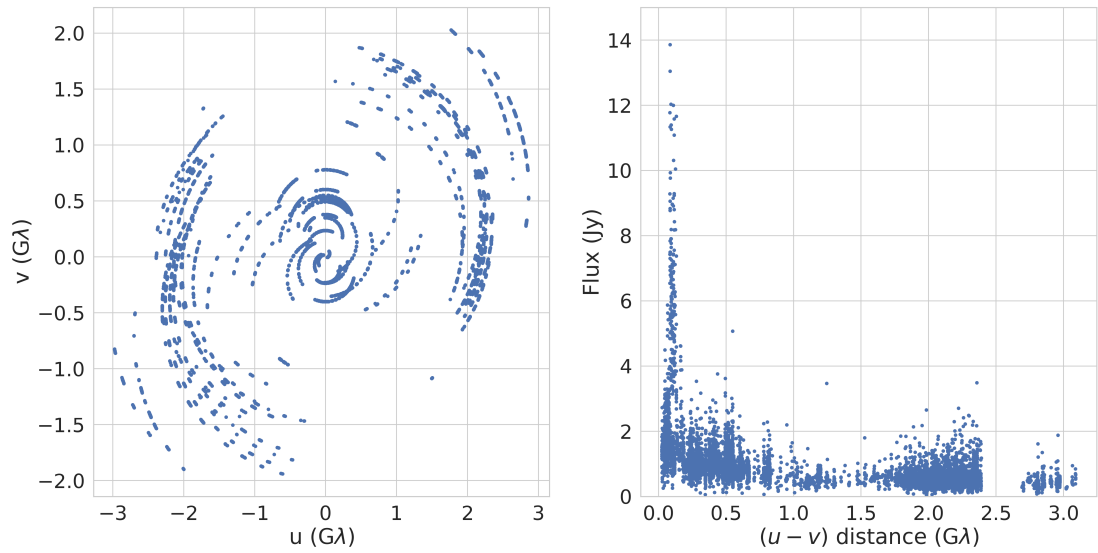


Figure 2.24: Characteristic diagnostic plots of a VLBI data set. *Left*: (u, v) plot of 3C 84 from the April 2020 session. *Right*: Amplitude as a function of the (u, v) distance for the same epoch.

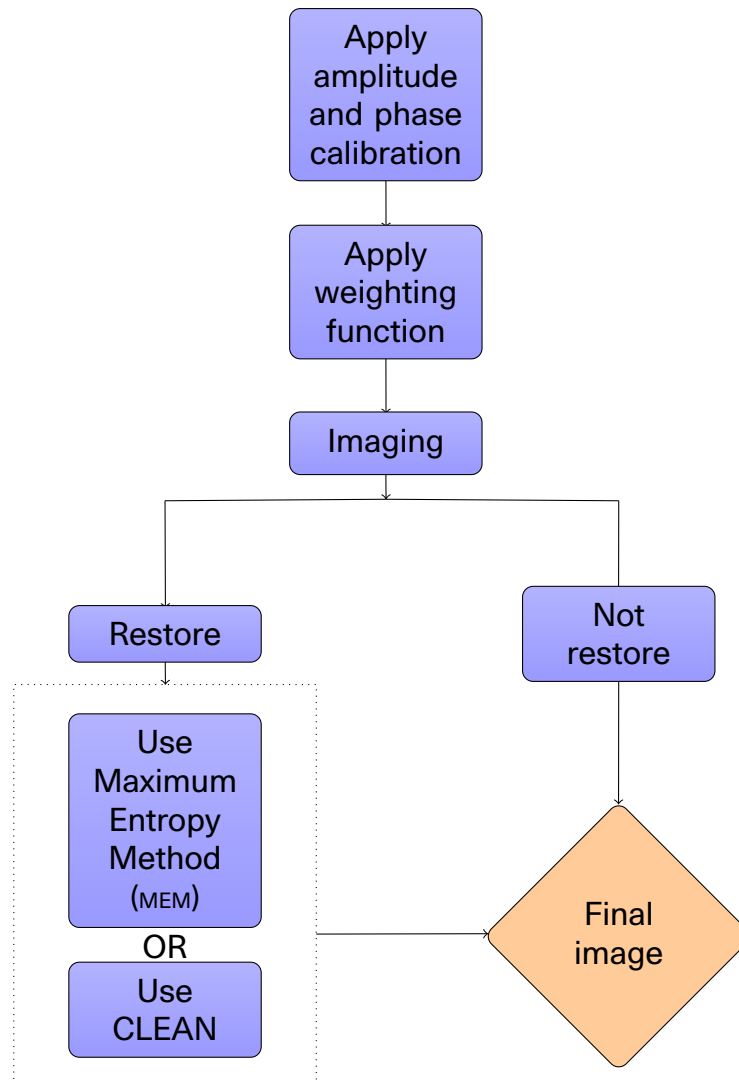


Figure 2.25: Simplified data flow chart of the calibration and imaging procedure. Figure adapted from Wilson et al. (2013).

3 Paper 1: Pinpointing the jet apex of 3C 84

The discovery of an east-west elongated structure, perpendicularly oriented to the bulk jet flow, in the core of 3C 84, in a recent *RadioAstron* map (Giovannini et al. 2018), generated a number of questions regarding the true nature of it and its implications. Possible explanations include the structure being an elongated uniform disc, a stationary shock or even spatial bending of the jet path, which would then follow a strongly curved trajectory. In these scenarios, the true location of the jet apex and by extension of the jet launching BH, plays the primary role. One way of shedding light on the true nature of this structure is by means of determining the spectral index and its gradient. As summarised in Fig. 4 of Paraschos et al. (2022a), the spectral index will differ depending on the nature of the structure.

Quasi-simultaneous VLBI observations of 3C 84 were taken in May of 2015 at 15, 43, and 86 GHz, providing the opportunity for a high-resolution spectral index study of 3C 84 at the three frequencies. The following peer-reviewed paper summarises this study and our attempt to determine the true location of the BH of 3C 84 via computation of the core shift, through a two-dimensional cross-correlation analysis. A byproduct of our analysis, besides the creation of spectral index maps of the source, is the calculation of the magnetic field strength and its topology in the vicinity of the BH.

For this work, some previously published images by Kim et al. (2019) were reused. I performed the cross-correlation analysis and re-imaged the data sets, to gain a second, independent measurement of the core shifts. Furthermore, I created all the figures and composed the majority of the text, the final form of which resulted from extensive discussions with the co-authors.

Credit: **G. F. Paraschos** et al., *A&A*, 650, L18, 2021, reproduced with permission © ESO.

LETTER TO THE EDITOR

Pinpointing the jet apex of 3C 84

G. F. Paraschos¹, J.-Y. Kim^{2,1}, T. P. Krichbaum¹, and J. A. Zensus¹

¹ Max-Planck-Institut für Radioastronomie, Auf dem Hügel 69, Bonn, Germany
 e-mail: gfparaschos@mpi-fr-bonn.mpg.de

² Korea Astronomy and Space Science Institute, 776 Daedeokdae-ro, Yuseong-gu, Daejeon 30455, Korea

Received 10 March 2021 / Accepted 8 June 2021

ABSTRACT

Nearby radio galaxies that contain jets are extensively studied with very long baseline interferometry (VLBI), addressing jet launching and the physical mechanisms at play around massive black holes. 3C 84 is unique in this regard because the combination of its proximity and large super massive black hole mass provides a high spatial resolution to resolve the complex structure at the jet base. For 3C 84, an angular scale of 50 μ as corresponds to 200–250 Schwarzschild radii (R_s). Recent RadioAstron VLBI imaging at 22 GHz has revealed an east-west elongated feature at the northern end of the VLBI jet, which challenges past interpretations. Here we propose instead that the jet apex is not located within the 22 GHz VLBI core region but more upstream in the jet. We base our arguments on a 2D cross-correlation analysis of quasi-simultaneously obtained VLBI images at 15, 43, and 86 GHz, which measures the opacity shift of the VLBI core in 3C 84. With the assumption of the power-law index (k_r) of the core shift being set to 1, we find the jet apex to be located $83 \pm 7 \mu$ as north (upstream) of the 86 GHz VLBI core. Depending on the assumptions for k_r and the particle number density power-law index, n , we find a mixed toroidal-poloidal magnetic field configuration, consistent with a region that is offset from the central engine by about 400–1500 R_s . The measured core shift is then used to estimate the magnetic field strength, which amounts to $B = 1.80$ – 4.0 G near the 86 GHz VLBI core. We discuss some physical implications of these findings.

Key words. galaxies: individual: 3C 84 (NGC 1275) – galaxies: jets – galaxies: active – techniques: interferometric – techniques: high angular resolution

1. Introduction

3C 84 is a peculiar Seyfert 1.5-type radio galaxy (Véron-Cetty & Véron 2006). It is located relatively nearby, at a distance of 76.9 Mpc ($z = 0.0176$) (Strauss et al. 1992)¹, and harbours a central super massive black hole (SMBH) of $M_{\text{BH}} \sim 9 \times 10^8 M_\odot$ (Scharwächter et al. 2013). This makes 3C 84 a prime target to pinpoint the location of the SMBH and to study the magnetic field in the very inner jet region for this enigmatic radio galaxy. 3C 84 has been studied with centimetre- and millimetre-very long baseline interferometry (VLBI) for decades (e.g. by Walker et al. 1994, 2000; Dhawan et al. 1998; Suzuki et al. 2012; Nagai et al. 2014; Giovannini et al. 2018, and Kim et al. 2019, among others). It features a complex two-sided jet (Vermeulen et al. 1994; Walker et al. 1994; Fujita & Nagai 2017; Wajima et al. 2020), which commonly exhibits moving radio emitting features (blobs) that accelerate with apparent speeds from $\leq 0.1c$ on sub-milliarcsecond (sub-mas) scales to $0.5c$ on milliarcsecond (mas) scales (Krichbaum et al. 1992; Dhawan et al. 1998; Punsly et al. 2021). Bright and fast moving knots have been tracked over the years (Dhawan et al. 1990, 1998), and two components have also been ejected in the southern jet, called C2 and C3 (following the naming convention of Nagai et al. 2014). Recent high-resolution VLBI imaging of 3C 84 with the RadioAstron space telescope has revealed a limb-brightened double-railed jet, possibly anchored in a very wide jet base of $\sim 250 R_s$ diameter (Giovannini et al. 2018). This raises the question of whether

the jet in 3C 84 is launched via magneto-centrifugal acceleration from the accretion disk – the Blandford & Payne (1982) (BP) model – or via energy extraction directly from the ergosphere of the spinning central black hole – the Blandford & Znajek (1977) (BZ) model.

The unknown location of the SMBH in 3C 84 can be estimated by assuming its proximity to the jet apex. The latter can be determined from high-resolution VLBI imaging in the millimetre bands. VLBI imaging at these short wavelengths not only provides a higher angular resolution than in the centimetre bands, but also helps to overcome opacity effects; these effects are caused by the synchrotron self-absorption in the jet and by free-free absorption from the circum-nuclear gas of the accretion flow, which partially obscures the counter-jet and jet base (Walker et al. 1994; Fujita & Nagai 2017; Kim et al. 2019).

Here we present a new study of 3C 84, which measures the VLBI core shift. Such core shifts are also observed in the jets of several other galaxies and blazars (e.g. Lobanov 1998a; Fromm et al. 2013; Hada et al. 2011; Pushkarev et al. 2012; Haga et al. 2013; Park et al. 2021). Active galactic nucleus (AGN) jets emit synchrotron radiation, which is susceptible to synchrotron self-absorption. Synchrotron self-absorption is frequency dependent (Rybicki & Lightman 1979). When the VLBI core is associated with the $\tau = 1$ absorption surface (e.g. Konigl 1981; Lobanov 1998a), its position becomes frequency dependent. The optically thick VLBI core region becomes more transparent at higher frequencies and shifts in the direction of the opacity gradient. For a conical, homogeneous, and straight jet, this opacity gradient points towards the jet apex. With this assumption, the observed

¹ We assume Λ cold dark matter cosmology with $H_0 = 71 \text{ km s}^{-1} \text{ Mpc}^{-1}$, $\Omega_\Lambda = 0.73$, and $\Omega_M = 0.27$.

position shift of the VLBI core can be used to estimate the magnitude and topology of the magnetic field at the jet base (i.e. toroidal vs. poloidal field; see Lobanov 1998b; Hirovani 2005; Vlemmings et al. 2006; O’Sullivan & Gabuzda 2009; Pushkarev et al. 2012; Fromm et al. 2013).

This Letter is organised as follows: in Sect. 2 we briefly summarise the observations and data reduction and then present our spectral and core shift analysis results. We discuss our results in Sect. 3 and present our conclusions in Sect. 4.

2. Data, analysis, and results

In this section we present the 2D cross-correlation analysis used to produce the spectral index maps and core shift. We define the spectral index α as $S \propto \nu^{\alpha}$. The observations were made with the Very Long Baseline Array (VLBA) at 15 and 43 GHz and the Global Millimeter VLBI Array (GMVA) at 86 GHz during the period of 11–18 May, 2015. Total intensity and polarisation imaging results have already been published; for the details we refer to Kim et al. (2019). In this follow-up paper we used the same data but now focus on the spectral properties and opacity shift in the VLBI core region.

Following the analysis presented in Kutkin et al. (2014, and references therein), we computed the core shift and magnetic field strength and estimated the topology of the magnetic field. For the analysis described below, we convolved the maps with a circular beam with a size corresponding to the geometric mean of the major and minor axis of the lower-frequency beam (see Table A.1). After the convolution of each image pair, we selected a region within the optically thin part of the jet for the alignment, for which positions are frequency independent. For the 15–43 GHz pair, we selected region A3, which is around the bright and well-defined component C3 (Nagai et al. 2014), located ~ 2 mas south of the VLBI core (see Fig. 1). For the 43–86 GHz pair, we aligned the maps using region A2, which is located closer to the core (see Fig. 1). A2 is bright enough and well defined, and it also shows a steep spectrum (see e.g. Fig. 1), which justifies our choice.

The next step was to iteratively shift one image against the other in right ascension (RA) and in declination (Dec). For each position shift (i, j) the cross-correlation coefficient was calculated as follows (Lewis 1995):

$$\rho(i, j) = \frac{\sum_{x,y} [f^{v_1}(x, y) - \bar{f}_{i,j}^{v_1}] [f^{v_2}(x - i, y - j) - \bar{f}_{i,j}^{v_2}]}{\left\{ \sum_{x,y} [f^{v_1}(x, y) - \bar{f}_{i,j}^{v_1}]^2 \sum_{x,y} [f^{v_2}(x - i, y - j) - \bar{f}_{i,j}^{v_2}]^2 \right\}^{0.5}}, \quad (1)$$

where x and y are the pixel indices in the different images, $f^{v_1}(x, y)$ is the flux density of the selected feature in the static image at (x, y) , $f^{v_2}(x - i, y - j)$ is the flux density of the selected feature in the shifted map (shifted by $x - i$ and $y - j$), and $\bar{f}_{i,j}^{v_1,2}$ are the mean fluxes in the selected feature. The maximum $\rho(i, j)$ yields the best shift position. For further details on the method, we refer to Lewis (1995).

We aligned adjacent frequency maps pairwise to avoid artefacts due to the very different beam sizes at 15 and 86 GHz. In order to be as conservative as possible, we used the larger beam size at the longer wavelength (see Table A.1) for the alignment of each frequency pair. At 15–43 GHz, we obtain position shifts of $\Delta RA = 60 \pm 58 \mu\text{as}$ and $\Delta Dec = 240 \pm 53 \mu\text{as}$. At 43–86 GHz, we obtain position shifts of $\Delta RA = 20 \pm 52 \mu\text{as}$ and $\Delta Dec = 120 \pm 46 \mu\text{as}$. A description of our conservative error

estimation is presented in Appendix A. Table A.2 summarises the results.

We define the core of our images as the brightest and most compact component at the northernmost region of the jet. As a preparatory step for the 2D cross-correlation at 15 and 43 GHz, we fitted circular Gaussian components at 15 GHz to the C3 and core region and determined their relative distance to be 2.24 ± 0.02 mas. We then aligned the 15 GHz and 43 GHz maps by this shift and performed the cross-correlation. At 43 GHz and 86 GHz, the intensity peak is at the northernmost region of the jet and no additional shift is necessary. In this procedure and at all frequencies, we fitted a circular Gaussian to the VLBI core to identify their position shifts from the phase centres, finding $< 16 \mu\text{as}$ offsets at all frequencies (i.e. significantly smaller than the pixel scale and the image shifts). We thus ignore these offsets in the following analysis. The uncertainties of the image alignment for both frequency pairs is further discussed in Appendix A.

Figure 1 (left panel) displays the core shift values as a function of frequency. We used the VLBI core at 86 GHz as a reference, setting its position to zero. The two insets present the distribution of the cross-correlation coefficient for the 15–43 GHz pair (left) and the 43–86 GHz pair (right).

We then used this map alignment to calculate the spectral index distributions. In Fig. 1 (right panel) we show the spectral index maps at 15–43 GHz and at 43–86 GHz. The northern side of the core region exhibits an inverted spectral index of $\alpha_{15-43} = 1.0 \pm 0.3$. The α_{15-43} gradually decreases southwards, with a typical value of $\alpha_{15-43} = -0.5 \pm 0.4$ in the C3 region, consistent with past spectral index measurements at lower frequencies (e.g. Unwin et al. 1982; Bartel et al. 1988; Marr et al. 1989; Vermeulen et al. 1994; Walker et al. 1994; Taylor et al. 2006; Wajima et al. 2020).

For the 43–86 GHz pair, we detect a prominent spectral index gradient between regions A1 and A2 (see Fig. 1), from $\alpha_{43-86} = 2.0 \pm 0.5$ in the north-west to $\alpha_{43-86} = -1.0 \pm 0.6$ in the south-east. Details on the spectral index error estimation are given in Appendix A. Based on this, we conclude that the overall trend of the spectral index gradients from inverted in the northern region (A1) to steeper in the two southern regions (A2 and A3) are significant and real. We also note that the apparent difference between the spectral index in the two southern regions (A2: $\alpha \sim -1.0$; A3: $\alpha \sim -0.5$) may not be significant, due to residual calibration uncertainties. However, due to the nature of C3 (moving shock) and its interactions with the ambient jet, the flatter spectrum in region A3 is not unexpected (e.g. Nagai et al. 2014).

If the size of the emission region increases linearly with the distance, r , from the core, $w \propto r$, the magnetic field strength and particle density decrease with distance as $B \propto r^{-b}$ and $N \propto r^{-n}$, respectively. The distance between the jet apex and the apparent VLBI core, Δr_{core} , relates to the frequency with a power law of the form:

$$\Delta r_{\text{core}} = r_0 \left(\left(\frac{\nu}{86 \text{ GHz}} \right)^{-1/k_r} - 1 \right) [\mu\text{as}], \quad (2)$$

where $k_r = [2n + b(3 - 2\alpha_{\text{thin}}) - 2]/(5 - 2\alpha_{\text{thin}})$ (Lobanov 1998a), n and b are the particle number density and magnetic field strength power-law indices, respectively, and α_{thin} is the optically thin spectral index. According to the definition of Eq. (2), and using the 86 GHz core as the reference point, we can determine $|r_0|$, which is the distance to the jet apex. To obtain the absolute distances of the 15 GHz and the 43 GHz cores from the 86 GHz core, we added the ΔRA and ΔDec shifts listed

G. F. Paraschos et al.: Pinpointing the jet apex of 3C 84

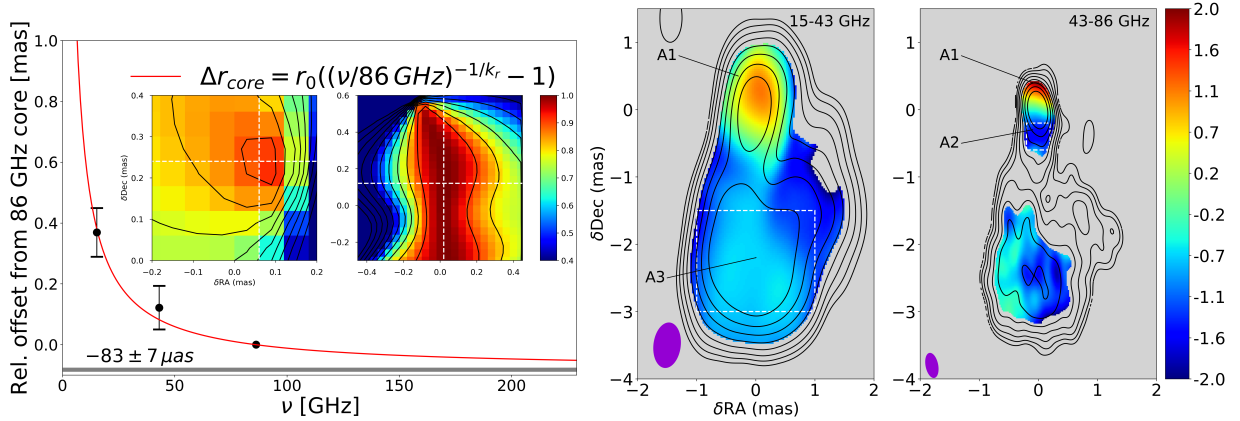


Fig. 1. Core offset position fit and spectral index maps at 15–43 GHz and 43–86 GHz of 3C 84. *Left:* core shift of 3C 84 at frequencies of 15, 43, and 86 GHz. The red line shows a fit to Eq. (2) to the core offset positions (for the numbers, see Table A.3). The shaded grey line denotes the distance from the 86 GHz total intensity peak to the true location of the jet apex. The insets show 2D cross-correlation coefficients of the images at two different frequency pairs. Each axis is in units of mas. The contours start at 1% and increase in steps of 10% relative to the maximum cross-correlation coefficient (0.9975 and 0.9995, respectively). The perpendicular dashed white lines intersect at the maximum of the colour map, which corresponds to the maximum value of $\rho(i, j)$. *Right:* spectral index maps after image alignment. *Left panel:* 15 GHz image in contours and the 15–43 GHz spectral index in colours. The contours start at $4.36 \text{ mJy beam}^{-1}$ and increase by a factor of two. The maps are convolved with a beam of $0.45 \times 0.67 \text{ mas}$, oriented at a PA = -9.44° . *Right panel:* 43–86 GHz spectral index in colours and the contours of the 43 GHz map, which start at $4.26 \text{ mJy beam}^{-1}$ and increase in steps of two. The maps are convolved with a beam of $0.20 \times 0.37 \text{ mas}$, oriented at a PA = 14.1° . We only display regions that have (i) a S/N of at least five for the total intensity contours and (ii) a spectral index in the range -2 to 2 , within 1 rms error (± 0.14 for the 15–43 GHz pair and ± 0.21 for the 43–86 GHz pair), gained from the uncertainty from a region the size of each beam, centred around the core shift location of each frequency (see Appendix A for further details). Boxes marked by dashed white lines correspond to the regions used for the 2D cross-correlation. A1, A2, and A3 are the three characteristic regions where the spectral indices were measured (see Table A.4).

in Table A.2 in quadrature. Table A.3 summarises the resulting positions. The limited frequency range and scarcity of the data points only allow a fit for one free parameter, namely r_0 . We therefore assumed a physically motivated value of $k_r = 1$, as also observed in other VLBI jets (e.g. Lobanov 1998a; Hada et al. 2011; Pushkarev et al. 2012; Fromm et al. 2013). We solved Eq. (2) via the least squares fit method for r_0 . We used the inverse variance of the data for their weighting. From the fit we obtain $r_0 = 83 \pm 7 \mu\text{as}$, which is marked as a grey line in Fig. 1 (left)². This corresponds to a projected distance of $0.030 \pm 0.002 \text{ pc}$, or $413 \pm 34 R_s$ (with the Schwarzschild radius, R_s). Adopting a viewing angle in the range of 20° – 65° (Fujita & Nagai 2017; Abdo et al. 2009), we determine the de-projected distance to be 0.028 – 0.11 pc , or 400 – $1500 R_s$. For the position angle (PA) of the jet apex, we obtain $-20^\circ \pm 14^\circ$ relative to the 86 GHz core position in the image plane. In Fig. 2 we over-plot the core positions at 15, 43, and 86 GHz, as well as the estimated position of the jet apex, on the intensity contours of the 86 GHz map. The estimated position of the jet apex, marked as a filled circle, is located north-west of the VLBI core at 86 GHz.

3. Discussion

3.1. Implications of the jet apex location

Over the years, a variety of interpretations have been proposed to explain the highly complex structure in 3C 84. Based on 22 GHz space-VLBI imaging with $20 \mu\text{as}$ resolution, Giovannini et al. (2018) found an east-west, broadly elongated structure at the

² We note the good agreement with the work of Oh et al. (2021), who find an offset of 54 – $215 \mu\text{as}$ from long-term, time-averaged 86 GHz GMVA imaging.

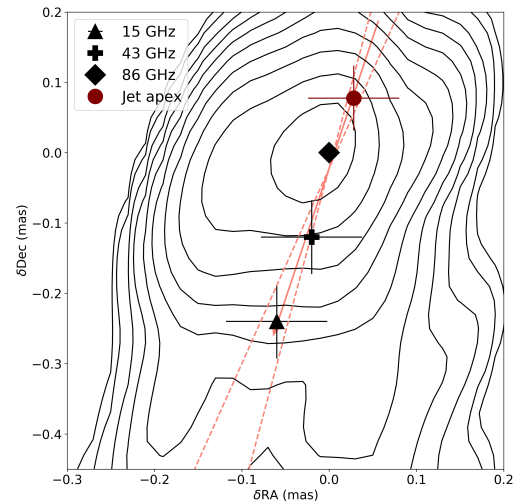


Fig. 2. Core locations at 15, 43, and 86 GHz (black) and extrapolated jet apex location (dark red), plotted over the 86 GHz total intensity map. The contours start at 0.1% of the image peak ($1.82 \text{ Jy beam}^{-1}$) and then increase in steps of two. The solid light red line is obtained from a 2D line fit to the core positions at different frequencies and the jet apex location with respect to the reference point (i.e. 86 GHz core). The broken light red lines show the 99% confidence interval of the fit.

northern end of the jet. The authors suggest that this may correspond to a broad jet apex of $\sim 120 R_s$ width, with some diffuse emission farther to the north, marking the onset of the counter-jet. Our analysis indicates a different scenario, in which the jet apex is located more upstream, at ~ 400 – $1500 R_s$ north-west of

the VLBI core at 86 GHz, as illustrated in Fig. 2. The measured orientation along $PA = -20^\circ \pm 14^\circ$ favours this scenario because it is in line with the direction of the northern counter-jet $PA = -25^\circ$, as seen on the larger mas scales (Vermeulen et al. 1994).

We point out that on sub-mas scales the northern emission from the counter-jet is not yet unambiguously detected. It is unclear if the emission seen north of the brightest jet components at 43 GHz and 86 GHz belongs to the jet or to the counter-jet. Fujita & Nagai (2017) report the detection of a counter-jet at 15 and 43 GHz in the northern 1–2 mas region. The apparent emission gap between this mas-scale region and the sub-mas-scale region close to the VLBI core (as seen at higher frequencies) may be explained by free-free absorption from optically thick and clumpy gas, for example a torus or accretion flow (e.g. Salomé et al. 2008; Fujita & Nagai 2017; Kim et al. 2019). The highly inverted spectrum ($\alpha_{43-86} \sim 2$ for the core region; see Fig. 1, right panel) could support such a scenario. However, highly inverted spectra (with spectral indices reaching up to $\alpha = +2.5$) are also possible for homogeneous self-absorbed synchrotron emitting components. Depending on homogeneity, the VLBI cores in many AGN jets more typically show inverted spectra with lower indices in the range of 0 to 1.5, though occasional higher values cannot be excluded. Dedicated spectral and Faraday rotation measure-sensitive polarimetric millimetre-VLBI observations in the future could help to clarify the situation.

3.2. Magnetic field strength and topology

Following Lobanov (1998a) and Eqs. (38) and (39) in Fromm et al. (2013), we determined the magnetic field strength in the jet. We assumed a power-law index $k_r = 1$. Details of the procedure and parameter ranges are given in Appendix B. Table B.1 summarises the relevant parameters. For the location of the jet apex with respect to the 86 GHz core ($r_0 = 76\text{--}90 \mu\text{as}$), we computed the magnetic field to be in the range of $B = 1.80\text{--}4.0 \text{ G}$ at the 86 GHz core; this is lower than the magnetic field strength estimate of $21 \pm 14 \text{ G}$ obtained by Kim et al. (2019), where the synchrotron self-absorption formula from Marscher (1983) was used with several assumptions. We followed the literature (Fromm et al. 2013; Kutkin et al. 2014; Lisakov et al. 2017 and references therein) to determine the magnetic field topology and thus assumed a power-law index of $n = 2$ for the radial dependence of the particle number density. From this, we derive $b = 1$ for the power-law index of the magnetic field, which is commonly interpreted as evidence for a toroidal magnetic field configuration.

We note that the above analysis of the magnetic field strength (see also Appendix B) largely relies on the Blandford & Königl (1979) jet model, where the particle number density and the magnetic field strength gradients depend on the shape of the jet (see also Lobanov 1998a). Thus, we can further examine our assumption by adopting a more realistic boundary shape of the jet and checking the dependence of b on n . That is, the radius (or transverse width) of a compact jet, w , depends on the core distance, r . Previous such studies of 3C 84 (Nagai et al. 2014; Giovannini et al. 2018) revealed that, on average, $w \propto r^{0.21}$. Thus, the jet cross-sectional area $A(r) \propto w^2 \propto r^{0.42}$. The total number of particles, N_{tot} , passing through each cross-section is assumed to be conserved. Therefore, assuming a slab of width dr , the total number of particle $N_{\text{tot}} \propto N(r)A(r)dr^3$ needs to be

constant, where $N(r) \propto r^{-n}$. This leads to the number density $N(r) \propto A(r)^{-1}$ or $N(r) \propto r^{-0.42}$, and thus we now have $n = 0.42$. We then obtain $b \approx 1.7$, which comes closer to a poloidal magnetic field configuration ($b = 2$). However, the underlying uncertainty in $b \approx 1.7$ could be large due to the $k_1 = 1$ assumption. Future millimetre-VLBI imaging of the electric vector polarisation angle (EVPA) distributions in the core region would independently and directly measure the b parameter.

We also note that the jet apex and the location of the central engine (the SMBH) may not coincide spatially. That is, the jet apex, which is the upstream end of a luminous flow of relativistic plasma, can only be physically associated with the central engine when the jet base emits synchrotron radiation. Therefore, the conversion of the magnetic or Poynting-flux energy into particle energy at the jet base (e.g. ‘magnetoluminescence’; Blandford et al. 2017) must be efficient enough. If this is not the case, the ‘physical’ origin of the jet (the location of the SMBH) may even be located beyond the position of the jet apex derived above.

Blandford & Payne (1982) and Blandford & Znajek (1977) presented two different jet launching scenarios. In the former the jet is powered by magnetic field lines anchored in the accretion disk, while in the latter the magnetic field lines are directly connected to the ergosphere of the spinning black hole. Depending on the chosen value of n , we conclude that the magnetic field configuration is either a toroidal or is of a mixed toroidal-poloidal nature. Such a scenario is also consistent with observational findings, which indicate the presence of toroidal fields in AGN jets from scales of parsecs to kiloparsecs (Molina et al. 2014; Knuettel et al. 2017). Under the assumption of the validity of the Blandford & Königl (1979) jet model, our data suggest that, at a distance of $\sim 400\text{--}1500 R_s$ from the jet apex, the magnetic field configuration is most likely mixed. We note that the initial magnetic field configuration of the BP model is expected to be toroidal, whereas the BZ model predicts a poloidal geometry (Davis & Tchekhovskoy 2020). Therefore, the observed mixed configuration either points to a stratified combination of both the BP and BZ models or to a jet launching process in which the initial field configuration is altered by some internal physical jet processes acting farther downstream, such as developing shocks and/or instabilities.

To date, the magnetic field strength of only a few other nearby AGN has been studied on scales of a few hundred R_s . Baczko et al. (2016) determined the magnetic field strength of NGC 1052 to be $\geq 100 \text{ G}$ at $\sim 4 R_s$. Kim et al. (2018) computed the magnetic field of M 87 to be in the range of $\sim 60\text{--}210 \text{ G}$ on $\sim 10 R_s$ scales.

Adopting $b = 1$ and extrapolating to $10 R_s$, the magnetic field of 3C 84 is of the order of $70\text{--}600 \text{ G}$ and thus compares well to those in NGC 1052 and M 87. Furthermore, we can extrapolate the B_0 of 3C 84 to a distance of 1 pc from the jet apex, $B_{1 \text{ pc}}$, in order to compare this value to literature results of additional AGN jets from a time when such high spatial resolution imaging was not yet possible. Using $b = 1$, we obtain $B_{1 \text{ pc}}$ to be $60\text{--}180 \text{ mG}$. Pushkarev et al. (2012) obtain $B_{1 \text{ pc}} \sim 400\text{--}900 \text{ mG}$ for a total of ~ 100 jets in quasars and BL Lac objects based on their core shifts. The B field found in 3C 84 is a factor of four to six lower, which may indicate intrinsic differences between radio galaxies and the more luminous quasars and BL Lac objects.

It is interesting to compare our result to the magnetic field strength expected from the total jet power. Using the following equation (see Eq. (8.35) in Ghisellini 2013 and the listed assumptions),

³ We further assume a constant jet speed over the short distance scales discussed in this Letter.

G. F. Paraschos et al.: Pinpointing the jet apex of 3C 84

$$B \leq \sqrt{\frac{8\pi P}{A\Gamma^2\beta c}}, \quad (3)$$

where P is the total jet power, β is the intrinsic speed of the jet, Γ is the associated bulk Lorentz factor, and A is the total cross-section of the jet, we can compute an estimate for the magnetic field strength from the total jet power for 3C 84. We note that the equality holds only if the total energy budget of the jet is solely dominated by the magnetic field. [Abdo et al. \(2009\)](#) and [MAGIC Collaboration \(2018\)](#) report a jet power as high as $\sim 10^{44}$ – 10^{45} erg s $^{-1}$, stemming from the observed extreme tera-electronvolt γ -ray variability. Thus, for an emitting region the size of the jet cross-sectional area ($\sim 50 \mu\text{as}$), a magnetic field strength of $\lesssim 30$ – 60 G would be possible without exceeding the jet power. Our finding for the magnetic field strength does not exceed this upper limit. The moderately large magnetic field strength from the core shift, in comparison to the upper limit estimated from the jet power analysis, therefore also supports a scenario in which the magnetic field at the jet base is prominent, which, in turn, is in support of magnetic jet launching (e.g. [Narayan et al. 2003](#); [Tchekhovskoy et al. 2011](#)).

4. Conclusions

In this Letter we have studied the spectral index and core shift of 3C 84. Our major findings and conclusions can be summarised as follows.

1. We performed a 2D cross-correlation of the 15–43 GHz and 43–86 GHz image pairs, using quasi-simultaneous VLBI observations from May 2015. The analysis of the core shift reveals that the jet apex is located north-west of the VLBI core at 86 GHz, displaced by 76–90 μas , with the distance from the core as a function of the frequency, following Eq. (2).
2. With the detected core shift and the possible location of the jet apex north of the 86 GHz VLBI core, the east-west oriented VLBI core structure (which is also seen in the 22 GHz RadioAstron map) appears less likely to be the physical origin of the jet. We further note that a location of the true jet apex north of this east-west oriented feature and north of the 86 GHz $\tau \sim 1$ surface would also lead to a smaller initial jet-opening angle (as opposed to the 130° angle that has been suggested by [Giovannini et al. 2018](#)).
3. The new spectral index images at 15–43 GHz and, especially, 43–86 GHz reveal the presence of a strong spectral index gradient in the northwest-southeast direction, with an inverted spectrum of the millimetre-VLBI core ($\alpha_{43-86} \sim +2$). With a synchrotron turnover frequency of $\nu_m \geq 86$ GHz, 3C 84 will be a suitable target for VLBI studies at higher frequencies (e.g. with the Event Horizon Telescope, EHT; [Event Horizon Telescope Collaboration 2019](#)).
4. At a de-projected distance of 400–1500 R_s (76–90 μas) from the jet apex, the magnetic field topology is not purely poloidal; a mixed poloidal-toroidal configuration is suggested. This points towards a stratified combination of the BP and BZ models (acting in parallel) or towards an alteration to the initial magnetic field configuration due to some internal physical jet processes acting farther downstream (e.g. developing shocks and/or instabilities).
5. We measure the magnetic field to be in the range $B_0 = 1.80$ – 4.0 G at the jet apex. This value is lower compared to the maximum possible magnetic field strength derived from the total jet power, which is $\lesssim 30$ – 60 G. The magnetic

field also compares well with the magnetic field measured in some other nearby AGN, such as M 87 and NGC 1052, and suggests magnetic jet launching.

Overall, our study suggests that the complex nature of 3C 84 can be partially explained by the location of the jet apex being upstream from the VLBI core at 86 GHz. Questions about the nature of the east-west oriented elongated VLBI core, including whether it is a stationary or oblique shock or part of a curved filament in a wider jet channel, still remain open. A broader frequency coverage from quasi-simultaneous observations may be necessary to achieve an improved estimate of the power-law index (k_r) of the core shift. We plan to further investigate, and constrain our results, by employing millimetre-VLBI monitoring observations with the highest possible resolution (EHT, GMVA, Global-EVN) in the near future.

Acknowledgements. We thank T. Savolainen for providing software to calculate two dimensional cross-correlations. We also thank N. R. MacDonald for the proofreading and fruitful discussions which helped improve this manuscript. We thank the anonymous referee for the valuable comments, which improved this manuscript. G. F. Paraschos is supported for this research by the International Max-Planck Research School (IMPRS) for Astronomy and Astrophysics at the University of Bonn and Cologne. This research has made use of data obtained with the Global Millimeter VLBI Array (GMVA), which consists of telescopes operated by the MPIFR, IRAM, Onsala, Metsähovi, Yebes, the Korean VLBI Network, the Green Bank Observatory and the Long Baseline Observatory. The VLBA is an instrument of the Long Baseline Observatory, which is a facility of the National Science Foundation operated by Associated Universities, Inc. The data were correlated at the correlator of the MPIFR in Bonn, Germany. This work makes use of the Swinburne University of Technology software correlator, developed as part of the Australian Major National Research Facilities Programme and operated under licence. This study makes use of 43 GHz VLBA data from the VLBA-BU Blazar Monitoring Program (VLBA-BU-BLAZAR: <http://www.bu.edu/blazars/VLBAproject.html>), funded by NASA through the *Fermi* Guest Investigator Program. This research has made use of data from the MOJAVE database that is maintained by the MOJAVE team ([Lister et al. 2009](#)). This research has made use of the NASA/IPAC Extragalactic Database (NED), which is operated by the Jet Propulsion Laboratory, California Institute of Technology, under contract with the National Aeronautics and Space Administration. This research has also made use of NASA's Astrophysics Data System Bibliographic Services. Finally, this research made use of the following python packages: *numpy* ([Harris et al. 2020](#)), *scipy* ([Virtanen et al. 2020](#)), *matplotlib* ([Hunter 2007](#)), *astropy* ([Astropy Collaboration 2013, 2018](#)) and *Uncertainties*: a Python package for calculations with uncertainties.

References

- Abdo, A. A., Ackermann, M., Ajello, M., et al. 2009, *ApJ*, 699, 31
 Astropy Collaboration (Robitaille, T. P., et al.) 2013, *A&A*, 558, A33
 Astropy Collaboration (Price-Whelan, A. M., et al.) 2018, *AJ*, 156, 123
 Baczko, A. K., Schulz, R., Kadler, M., et al. 2016, *A&A*, 593, A47
 Bai, Y., Zou, H., Liu, J., & Wang, S. 2015, *ApJS*, 220, 6
 Bartel, N., Dhawan, V., Krichbaum, T., Graham, D. A., & Pauliny-Toth, I. I. K. 1988, *Nature*, 334, 131
 Blandford, R. D., & Königl, A. 1979, *ApJ*, 232, 34
 Blandford, R. D., & Payne, D. G. 1982, *MNRAS*, 199, 883
 Blandford, R. D., & Znajek, R. L. 1977, *MNRAS*, 179, 433
 Blandford, R., Yuan, Y., Hoshino, M., & Sironi, L. 2017, *Space Sci. Rev.*, 207, 291
 Davis, S. W., & Tchekhovskoy, A. 2020, *ARA&A*, 58, 407
 Dhawan, V., Bartel, N., Rogers, A. E. E., et al. 1990, *ApJ*, 360, L43
 Dhawan, V., Kellermann, K. I., & Romney, J. D. 1998, *ApJ*, 498, L111
 Event Horizon Telescope Collaboration (Akiyama, K., et al.) 2019, *ApJ*, 875, L2
 Fromm, C. M., Ros, E., Perucho, M., et al. 2013, *A&A*, 557, A105
 Fujita, Y., & Nagai, H. 2017, *MNRAS*, 465, L94
 Ghisellini, G. 2013, *Radiative Processes in High Energy Astrophysics* (Berlin: Springer-Verlag)
 Giovannini, G., Savolainen, T., Orienti, M., et al. 2018, *Nat. Astron.*, 2, 472
 Hada, K., Doi, A., Kino, M., et al. 2011, *Nature*, 477, 185
 Haga, T., Doi, A., Murata, Y., et al. 2013, *Eur. Phys. J. Web Conf.*, 61, 08004
 Harris, C. R., Millman, K. J., van der Walt, S. J., et al. 2020, *Nature*, 585, 357
 Hirofani, K. 2005, *ApJ*, 619, 73
 Hunter, J. D. 2007, *Comput. Sci. Eng.*, 9, 90

A&A 650, L18 (2021)

- Kim, J.-Y., & Trippe, S. 2014, *J. Korean Astron. Soc.*, **47**, 195
- Kim, J. Y., Krichbaum, T. P., Lu, R. S., et al. 2018, *A&A*, **616**, A188
- Kim, J. Y., Krichbaum, T. P., Marscher, A. P., et al. 2019, *A&A*, **622**, A196
- Knuettel, S., Gabuzda, D., & O'Sullivan, S. 2017, *Galaxies*, **5**, 61
- Konigl, A. 1981, *ApJ*, **243**, 700
- Krichbaum, T. P., Witzel, A., Graham, D. A., et al. 1992, *A&A*, **260**, 33
- Kutkin, A. M., Sokolovsky, K. V., Lisakov, M. M., et al. 2014, *MNRAS*, **437**, 3396
- Laing, R. A., & Peacock, J. A. 1980, *MNRAS*, **190**, 903
- Lewis, J. 1995, *Proceedings of Vision Interface*, 120
- Lisakov, M. M., Kovalev, Y. Y., Savolainen, T., Hovatta, T., & Kutkin, A. M. 2017, *MNRAS*, **468**, 4478
- Lister, M. L., Aller, H. D., Aller, M. F., et al. 2009, *AJ*, **137**, 3718
- Lobanov, A. P. 1998a, *A&A*, **330**, 79
- Lobanov, A. P. 1998b, *A&AS*, **132**, 261
- Lobanov, A. P. 2005, ArXiv e-prints [arXiv:astro-ph/0503225]
- MAGIC Collaboration (Ansoldi, S., et al.) 2018, *A&A*, **617**, A91
- Marr, J. M., Backer, D. C., Wright, M. C. H., Readhead, A. C. S., & Moore, R. 1989, *ApJ*, **337**, 671
- Marscher, A. P. 1983, *ApJ*, **264**, 296
- Molina, S. N., Agudo, I., Gómez, J. L., et al. 2014, *A&A*, **566**, A26
- Nagai, H., Haga, T., Giovannini, G., et al. 2014, *ApJ*, **785**, 53
- Narayan, R., Igumenshchev, I. V., & Abramowicz, M. A. 2003, *PASJ*, **55**, L69
- Oh, J., Hodgson, J. A., Trippe, S., et al. 2021, *MNRAS*, submitted
- O'Sullivan, S. P., & Gabuzda, D. C. 2009, *MNRAS*, **400**, 26
- Park, J., Hada, K., Nakamura, M., et al. 2021, *ApJ*, **909**, 76
- Punsly, B., Nagai, H., Savolainen, T., & Orienti, M. 2021, *ApJ*, **911**, 19
- Pushkarev, A. B., Hovatta, T., Kovalev, Y. Y., et al. 2012, *A&A*, **545**, A113
- Pushkarev, A. B., Kovalev, Y. Y., Lister, M. L., & Savolainen, T. 2017, *MNRAS*, **468**, 4992
- Rybicki, G. B., & Lightman, A. P. 1979, *Radiative Processes in Astrophysics* (New York: Wiley)
- Salomé, P., Revaz, Y., Combes, F., et al. 2008, *A&A*, **483**, 793
- Scharwächter, J., McGregor, P. J., Dopita, M. A., & Beck, T. L. 2013, *MNRAS*, **429**, 2315
- Schinzell, F. K., Lobanov, A. P., Taylor, G. B., et al. 2012, *A&A*, **537**, A70
- Strauss, M. A., Huchra, J. P., Davis, M., et al. 1992, *ApJS*, **83**, 29
- Suzuki, K., Nagai, H., Kino, M., et al. 2012, *ApJ*, **746**, 140
- Taylor, G. B., Gugliucci, N. E., Fabian, A. C., et al. 2006, *MNRAS*, **368**, 1500
- Tchekhovskoy, A., Narayan, R., & McKinney, J. C. 2011, *MNRAS*, **418**, L79
- Unwin, S. C., Mutel, R. L., Phillips, R. B., & Linfield, R. P. 1982, *ApJ*, **256**, 83
- Vermeulen, R. C., Readhead, A. C. S., & Backer, D. C. 1994, *ApJ*, **430**, L41
- Véron-Cetty, M. P., & Véron, P. 2006, *A&A*, **455**, 773
- Virtanen, P., Gommers, R., Oliphant, T. E., et al. 2020, *Nat. Meth.*, **17**, 261
- Vlemmings, W. H. T., Diamond, P. J., & Imai, H. 2006, *Nature*, **440**, 58
- Wajima, K., Kino, M., & Kawakatu, N. 2020, *ApJ*, **895**, 35
- Walker, R. C., Romney, J. D., & Benson, J. M. 1994, *ApJ*, **430**, L45
- Walker, R. C., Dhawan, V., Romney, J. D., Kellermann, K. I., & Vermeulen, R. C. 2000, *ApJ*, **530**, 233

Appendix A: Error estimation

The total error budget of our cross-correlation analysis depends on the cross-correlation image alignment error (σ_{ccf}), the image parameters, the correlation region, and the rms error (σ_{core}) of the core shift (Lisakov et al. 2017). The image size, convolving beam size, and pixel scale should be varied with frequency. Before we performed a cross-correlation of two images, these three parameters needed to be set to a common value. To consolidate the image parameter differences, we chose the beam size and map size of the lower-frequency map and the pixel scale of the higher-frequency map. We found minor offsets, which were taken as the uncertainties for the image alignment, as described in the next paragraph. The error of the core position (σ_{core}) depends primarily on the maximum resolution, d_{lim} , that can be achieved for a given map, which is given by Eq. (A.1) and taken from Lobanov (2005):

$$d_{\text{lim}} = \left[\frac{16}{\pi} \Theta^2 \ln 2 \ln \left(\frac{S/N}{S/N - 1} \right) \right]^{1/2} \text{ [mas]}. \quad (\text{A.1})$$

Here, Θ is the radius of the circular beam and S/N is the signal-to-noise ratio. For the 15–43 GHz pair, we calculated the S/N from the ratio of the image peak and rms error to be ~ 500 by averaging the S/Ns from the 15 and 43 GHz images. We followed the same procedure for the 43–86 GHz pair and determined the S/N to be ~ 375 . We followed Schinzel et al. (2012) and used Eq. (7) therein:

$$\sigma_{\text{core}} = \frac{\mathcal{D}}{S/N}, \quad (\text{A.2})$$

where \mathcal{D} is either equal to d_{lim} or to the central component size, d , if $d_{\text{lim}} < d$. In our case $d_{\text{lim}} > d$, so the first case applied. The final values for the error budget due to the uncertainty of the core position, σ_{core} , are $\sigma_{\text{core}}^{15-43} = 19 \mu\text{as}$ and $\sigma_{\text{core}}^{43-86} = 15 \mu\text{as}$.

Subsequently, we adhered to the following procedure to calculate the cross-correlation image alignment error, σ_{ccf} . First, two of the authors did independent imaging of the three available frequency maps to produce different sets of images. We then aligned them using the similar, though not identical, optically thin regions and observed the difference in the alignment. Then, we used half of the shift differences as the image alignment uncertainty. The resulting uncertainties are $\sigma_{\text{ccf}}^{\text{RA}} = 30 \mu\text{as}$ and $\sigma_{\text{ccf}}^{\text{Dec}} = 30 \mu\text{as}$ in the RA and Dec directions for the 15–43 GHz pair and $\sigma_{\text{ccf}}^{\text{RA}} = 40 \mu\text{as}$ and $\sigma_{\text{ccf}}^{\text{Dec}} = 20 \mu\text{as}$ for the 43–86 GHz pair, respectively. For the final values for each image, we added σ_{core} to σ_{ccf} in quadrature, thus $\sigma_{\text{tot}} = \sqrt{\sigma_{\text{core}}^2 + \sigma_{\text{ccf}}^2}$, and used σ_{tot} to calculate the errors shown in Table A.3.

We also estimated an error budget for our spectral index map by creating spectral index error maps. We used a combination of the image noise uncertainty and systematic amplitude calibration error to derive the error budget, as presented in Eq. (3) of Kim & Trippe (2014). The image alignment uncertainty, as described in the previous paragraph, yields uncertainties of ~ 0.3 for the 15–43 GHz pair and ~ 0.5 for the 43–86 GHz pair. For the 15–43 GHz pair, we find a systematic amplitude calibration error of 0.30 and for the 43–86 GHz pair 0.35; both these values refer to the entire region of emission. Adding these in quadrature produces total error estimates of $\Delta\alpha_{15-43}^{\text{entire}} = 0.4$ and $\Delta\alpha_{43-86}^{\text{entire}} = 0.6$. We also focused on the region around the core, this time examining only an area of the beam size for each pair, centred on the location of the core shift, where we found the spectral index gradient. The 15–43 GHz pair yields a systematic amplitude calibration error of 0.14, and the 43–86 GHz pair 0.21. Adding again

Table A.1. Summary of the image parameters.

Image	Beam [mas, deg]	Pixel scale [$\mu\text{as}/\text{pixel}$]
Figure 1, left	0.45×0.67 (–9.44)	30
Figure 1, right	0.20×0.37 (14.1)	20
Figure A.1, left	0.55×0.55 (0)	30
Figure A.1, right	0.27×0.27 (0)	20

Table A.2. Relative core shifts for the low- and high-frequency alignment pairs.

ν_{pair} [GHz]	ΔRA [μas]	ΔDec [μas]
15–43	60 ± 58	240 ± 53
43–86	20 ± 52	120 ± 46

Table A.3. Absolute distances from the extrapolated jet apex.

ν [GHz]	Δr [μas]
15	369 ± 80
43	122 ± 72
86	83 ± 7

Table A.4. Spectral index measurements per region.

Region	α_{15-43}	α_{43-86}
A1	1.0 ± 0.3	2.0 ± 0.5
A2	–	-1.0 ± 0.6
A3	-0.5 ± 0.4	–

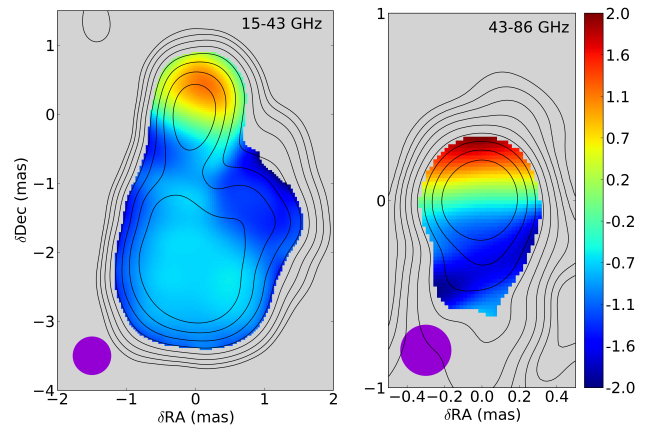


Fig. A.1. Spectral index maps after image alignment, convolved with a beam of a radius equal to the geometric mean of the lower-frequency map beam (see Table A.1). *Left panel:* 15 GHz image in contours and the 15–43 GHz spectral index in colours. The contours start at $4.41 \text{ mJy beam}^{-1}$ and increase with a factor of two. The spectral index map is convolved with a circular beam of 0.55 mas . *Right panel:* we zoomed in on the nuclear region of the 43–86 GHz spectral index image, shown in colour to better illustrate the spectral index gradient. The contours start at $4.38 \text{ mJy beam}^{-1}$, corresponding to the 43 GHz image, and increase in steps of two. The spectral index map is convolved with a circular beam of 0.27 mas . We apply the same cutoffs as in Fig. 1.

the error from the alignment in quadrature to these values yields total error estimates of $\Delta\alpha_{15-43}^{\text{core}} = 0.3$ and $\Delta\alpha_{43-86}^{\text{core}} = 0.5$. For the three regions, the spectral indices and their errors are summarised in Table A.4.

Appendix B: Magnetic field strength estimation

Table B.1. Fit parameters that appear in the text.

Parameter	Value
k_r	1
r_0	83 ± 7 [$\mu\text{as GHz}$]
b	1
Δr_{core}	$76-90$ [μas]
α_{thin}	-0.77
γ_{max}	10^3-10^5
PA	$-20^\circ \pm 14^\circ$
β_{app}	$0.1-0.2c$
θ	$20^\circ-65^\circ$
ϕ	$2.8^\circ-20^\circ$
Ω_r^y	$1.93-3.95$ [pc GHz]
B_0	$1.80-4.0$ [G]

Following Lobanov (1998a), the core shift (in mas) between two frequencies, ν_1 and ν_2 (in GHz), with $\nu_1 < \nu_2$, can be expressed in terms of the parameter Ω_r^y :

$$\Omega_r^y = 4.85 \times 10^{-9} \frac{\Delta r_{\text{core}} D_L}{(1+z)^2} \left(\frac{\nu_1^{1/k_r} \nu_2^{1/k_r}}{\nu_2^{1/k_r} - \nu_1^{1/k_r}} \right) [\text{pc GHz}^{1/k_r}], \quad (\text{B.1})$$

where Δr_{core} is the core shift in mas, D_L is the luminosity distance in pc, and z is the redshift. We find that $\Omega_r^{15-43} = 2.08 \pm 0.15$ [pc GHz] and $\Omega_r^{43-86} = 3.69 \pm 0.26$ [pc GHz]. For our subsequent analysis, we used a weighted mean of the two, yielding $\Omega_r = 3.10 \pm 0.13$ [pc GHz]. Equation (39) in Fromm et al. (2013), in turn, relates the magnetic field strength at a specified distance (in pc) from the jet base:

$$B_0 \approx \frac{2\pi m_e^2 c^4}{e^3} \left[\frac{e^2}{m_e c^3} \left(\frac{\Omega_r^y}{r_0 \sin \theta} \right)^{k_r} \right]^{\frac{5-2\alpha_0}{7-2\alpha_0}} \left[\pi C(\alpha_0) \frac{r_0 m_e c^2}{e^2} \frac{-2\alpha_0}{\gamma_{\text{min}}^{2\alpha_0+1}} \right. \\ \left. \times \frac{\phi}{\sin \theta} K(\gamma, \alpha_0) \left(\frac{\delta}{1+z} \right)^{\frac{3}{2}-\alpha_0} \right]^{\frac{-2}{7-2\alpha_0}} [\text{G}], \quad (\text{B.2})$$

with

$$K(\gamma, \alpha_0) = \frac{2\alpha_0 + 1}{2\alpha_0} \frac{[(\gamma_{\text{max}}/\gamma_{\text{min}})^{2\alpha_0} - 1]}{[(\gamma_{\text{max}}/\gamma_{\text{min}})^{2\alpha_0+1} - 1]} \quad (\text{B.3})$$

and $C(\alpha_0)$ being tabulated in Hirovani (2005) and r_0 a fixed distance so that $B = B_0(r_0/r)^b$. We set r_0 to be $76-90 \mu\text{as}$, which is the distance from the 86 GHz VLBI core to the jet apex. Furthermore, γ_{min} and γ_{max} are the minimum and maximum Lorentz factors for emitting electrons, θ is again the jet viewing angle, $\delta \equiv [\Gamma(1 - \beta \cos(\theta))]^{-1}$ is the Doppler factor, $\Gamma = (1 - \beta^2)^{-\frac{1}{2}}$ is the bulk Lorentz factor, and ϕ is the jet half opening angle. For γ_{max} we used the range $\gamma_{\text{max}} = 10^3-10^5$, reported by Abdo et al. (2009), and for γ_{min} we used a low value of 1. The jet speed and apparent jet speed are connected through Eq. (3.37) in Ghisellini (2013). For the jet half opening angle we used the formula $\phi = \arctan(\sin(\theta) \tan(\phi_{\text{app}}/2))$ from Pushkarev et al. (2017), having adopted the apparent opening angle range of $\phi_{\text{app}} = 3^\circ-20^\circ$. For the jet speed near the VLBI core, a typical value range of $\beta_{\text{app}} = 0.1-0.2c$ for 3C 84 (Krichbaum et al. 1992; Dhawan et al. 1998; Punsly et al. 2021) was adopted, with viewing angles in the range $\theta = 20^\circ-65^\circ$, as discussed in Sect. 2. For these parameters we computed the Doppler factor and obtain $\delta \sim 1.18-1.25$. For the optical thin spectral index we estimated α_{thin} based on the flux densities in the radio (Laing & Peacock 1980) and ultraviolet (Bai et al. 2015) bands in the time-averaged spectral energy distribution (SED), obtaining $\alpha_{\text{thin}} \sim -0.77$. This value agrees well with other spectral index measurements of the more extended jet emission in 3C 84 seen at longer wavelengths (e.g. Walker et al. 2000), as well as with our own results for the optically thin jet region on ~ 0.5 mas scales (Fig. 1).

⁴ We set as an upper limit the angle created by the upper and lower limit of the PA of the core shift, as displayed in Fig. 2. For the lower limit we used the full width at half maximum (FWHM) value of the bright component at a distance of ~ 2 mas from the VLBI core, as seen, for example, in Fig. 1.

4 Paper 2: A persistent double nuclear structure in 3C 84

Another way of studying the physical processes taking place in the core of 3C 84 is by direct imaging and at short millimetre-wavelengths. High-resolution images of the core of 3C 84 are a significant tool helping to shed light on the details of the jet launching and collimation occurring.

In this peer-reviewed paper we used 86 GHz GMVA observations of 3C 84 between 2008 and 2015 to study the core structure of the source. The elongated structure visible at 22 GHz in the *RadioAstron* map (Giovannini et al. 2018) appears as a double structure at 86 GHz, which persists over all epochs. To determine the transverse jet profile, we fitted a cone and a parabola to the temporally averaged image of the nuclear region. In this manner we placed another, independent constraint on the location of the jet apex. We further detected a possible variation of the viewing angle along the jet (jet bending).

For this work, I contributed to the image production and analysis by independently fringe-fitting, calibrating and imaging selected epochs. I also provided the analysis leading to the determination of the jet speed and jet viewing angle. Finally, I contributed to the overall authorship of the text of the paper, mainly in the Results and Discussion sections.

Credit: Oh et al. (including **G. F. Paraschos**), MNRAS, 509, 1024-1035 (2022). Due to the regulations of the copyright holder, the published version of this PhD thesis only contains a doi link, pointing to the publication: <https://doi.org/10.1093/mnras/stab3056>. In its place, an extended summary of the main results is presented in Sect. 4.1.

4.1 Main results

This work explores the nuclear structure of 3C 84 and its connection to the bright radio jet it harbours. The most striking feature observed in all six epochs used for this analysis, is the persistent elongation in the east-west direction of the core component, denoted as C1. We thus decomposed this region into two sub-components, denoted as C1a and C1b; they correspond to the blue dots in Fig. 4.26. By time-averaging these six CC images of 3C 84, observed at 86 GHz, we produced a stacked image, the contours of which are presented in Fig. 4.26. The lowest level of the contours corresponds to one percent of the flux peak (0.53 Jy/beam) and the levels increase by $\sqrt{2}$. The convolving beam size is the same for all ($0.138 \times 0.0435 \text{ mas}$, depicted in the bottom left corner of Fig. 4.26), The alignment of the images presented in Fig. 4.26 is along the

midpoint between C1a and C1b, which also serves as the reference point for the further analysis.

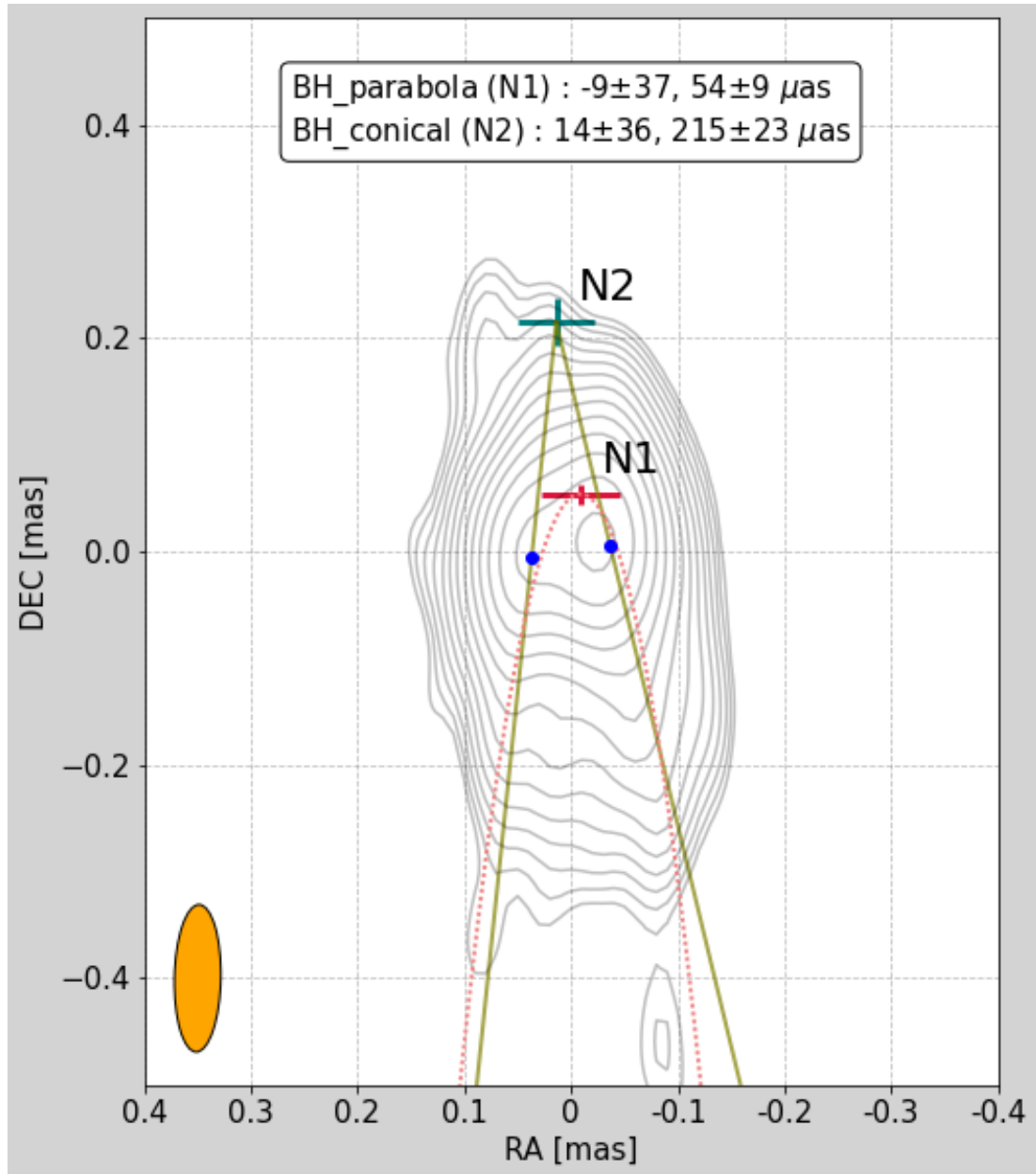


Figure 4.26: Limits to the position of the jet apex in 3C 84, based on conical and parabolic fits to the transverse jet profile. The point of alignment for the image stacking is the mid-point between the two components, called C1a and C1b. The image displayed here is rotated by 16° counterclockwise. The dark-green cross (N2) represents the jet apex location using a conical fit (continuous, olive-green line), whereas the red cross (N1) marks the jet apex position resulting from a parabolic fit (dotted, pink line). The dark blue dots display the average position of C1a and C1b throughout the epochs. The orange ellipse at the bottom left corner visualises the restoring beam size.

Since the main objective of this work is to identify and estimate the location of the jet apex, we further explored the nature of this elongation. A possi-

ble scenario explaining the observed two components might be a BP launched jet, with a broad jet footpoint originating from a wide accretion disc. Calculating however the size of the broad line region, revealed that it extends up to 10.8 light – days. This is a factor of three lower than the separation between C1a and C1b (~ 30 light – days). Since it is very unlikely that the accretion disc is larger than the broad line region, C1 cannot be the jet base, which should be located upstream of the reference point. To pinpoint the location more precisely, we fitted both a conical and a parabolic profile to the transverse flux density profile of the jet. They are denoted with the continuous, olive-green line and the dotted, pink line respectively, in Fig. 4.26. The apexes of the two profiles are labelled as N1 for the parabolic profile and N2 for the conical profile and are located $\sim 54 \mu\text{as}$ and $\sim 215 \mu\text{as}$ respectively upstream of the reference point. The exact coordinates of each apex position are shown in the legend of Fig. 4.26. N1 is marked as a red cross and N2 as a dark-green cross, with error bars indicating the positional uncertainties of the positions. Under the assumption of a BH mass of $3.2 \times 10^8 M_{\odot}$ we determine the upstream location of the jet apex to be $\sim 590 R_g$ and $\sim 2360 R_g$, respectively. Neither of the two extrapolated profiles is strongly preferred by the data, so the two apex positions are treated as upper and lower limits.

Combining these limits with an analysis of the jet-to-counter-jet ratio yields restraints to the viewing angle. The CC components in the jet and counter-jet side were summed, resulting in a ratio of 13.7 for N1 and a lower limit of 42.7 for N2, which translates into a viewing angle range of $20^{\circ} - 35^{\circ}$. Greater and smaller values for the viewing angle have been reported (e.g. Abdo et al. 2009; Fujita & Nagai 2017), indicating perhaps that the jet exhibits spatial bends along its path and rotation of the expelled jet components or a combination of them.

5 Paper 3: Jet kinematics in the transversely stratified jet of 3C 84: A two-decade overview

Expanding the work presented in the previous section and in Oh et al. (2022), we analysed and imaged all available epochs of 3C 84 at 86 GHz, compiling and presenting one of the longest data sets of any source to date, at 86 GHz¹⁹. This plurality of images allows to comprehensively study the kinematics of the components ejected from the core at 86 GHz and compare trajectories and speeds with the respective ones at 43 GHz²⁰. Velocities and ejection times were computed, tying the historical total flux variability light curves of 3C 84 from the past with the current observations. Additionally, temporal stacking of the images revealed the prominent, time-independent characteristics of 3C 84 at all three frequencies. Whenever sufficient sensitivity was present, and observations were close enough in time, spectral index maps at 43 and 86 GHz were produced, giving further insight into the spectral variability of the core region of 3C 84.

For this work, I performed the fringe-fitting and calibration of selected epochs, and the (re-)imaging of all epochs at 15, 43, and 86 GHz²¹, as explained in Tables 1, 2, and 3. Furthermore, I created all figures and composed the majority of the text, the final form of which again resulted from extensive discussions with the co-authors.

Credit: **Paraschos et al.**, A&A, in press (2022). Reproduced with permission © ESO.

¹⁹The Principal Investigator of each individual epoch can be looked up on the GMVA website: <https://www3.mpifr-bonn.mpg.de/div/vlbi/globalmm/>.

²⁰The images used here can be found on BU-Blazar group website: https://www.bu.edu/blazars/VLBA_GLAST/0316.html.

²¹The 15 GHz images used here can be found on the *astrogeo* website: http://astrogeo.org/vlbi_images/.

Jet kinematics in the transversely stratified jet of 3C 84

A two-decade overview

G. F. Paraschos¹✉, T. P. Krichbaum¹, J.-Y. Kim^{12,2,1}, J. A. Hodgson^{3,2}, J. Oh³, E. Ros¹, J. A. Zensus¹,
A. P. Marscher⁴, S. G. Jorstad^{4,5}, M. A. Gurwell⁶, A. Lähteenmäki^{7,8}, M. Tornikoski⁷,
S. Kiehlmann^{9,10}, and A. C. S. Readhead¹¹

¹ Max-Planck-Institut für Radioastronomie, Auf dem Hügel 69, Bonn 53121, Bonn, Germany
e-mail: gfparaschos@mpi-fr-bonn.mpg.de

² Korea Astronomy and Space science Institute, 776 Daedeokdae-ro, Yuseong-gu, Daejeon 30455, Republic of Korea

³ Department of Physics and Astronomy, Sejong University, 209 Neungdong-ro, Gwangjin-gu, Seoul 05006, Republic of Korea

⁴ Institute for Astrophysical Research, Boston University, Boston, MA 02215, USA

⁵ Astronomical Institute, Saint Petersburg State University, Universitetsky Prospekt, 28, Petrodvorets, 198504 St. Petersburg, Russia

⁶ Center for Astrophysics – Harvard & Smithsonian, 60 Garden Street, Cambridge, MA 02138, USA

⁷ Aalto University Metsähovi Radio Observatory, Metsähovintie 114, 02540 Kylmälä, Finland

⁸ Aalto University Department of Electronics and Nanoengineering, PO BOX 15500, 00076 AALTO, Finland

⁹ Institute of Astrophysics, Foundation for Research and Technology-Hellas, 71110 Heraklion, Greece

¹⁰ Department of Physics, Univ. of Crete, 70013 Heraklion, Greece

¹¹ Owens Valley Radio Observatory, California Institute of Technology, Pasadena, CA 91125, USA

¹² Department of Astronomy and Atmospheric Sciences, Kyungpook National University, Daegu 702-701, Republic of Korea

Received 16 February 2022 / Accepted 18 May 2022

ABSTRACT

3C 84 (NGC 1275) is one of the brightest radio sources in the millimetre radio bands, which led to a plethora of very-long-baseline interferometry (VLBI) observations at numerous frequencies over the years. They reveal a two-sided jet structure, with an expanding but not well-collimated parsec-scale jet, pointing southward. High-resolution millimetre-VLBI observations allow the study and imaging of the jet base on a sub-parsec scale. This could facilitate the investigation of the nature of the jet origin, also in view of the previously detected two-railed jet structure and east-west oriented core region seen with *RadioAstron* at 22 GHz. We produced VLBI images of this core and inner jet region, observed over the past twenty years at 15, 43, and 86 GHz. We determined the kinematics of the inner jet and ejected features at 43 and 86 GHz and compared their ejection times with radio and γ -ray variability. For the moving jet features, we find an average velocity of $\beta_{\text{app}}^{\text{avg}} = 0.055 - 0.22c$ ($\mu^{\text{avg}} = 0.04 - 0.18 \text{ mas yr}^{-1}$). From the time-averaged VLBI images at the three frequencies, we measured the transverse jet width along the bulk flow. On the ≤ 1.5 parsec scale, we find a clear trend of the jet width being frequency dependent, with the jet being narrower at higher frequencies. This stratification is discussed in the context of a spine-sheath scenario, and we compare it to other possible interpretations. From quasi-simultaneous observations at 43 and 86 GHz, we obtain spectral index maps, revealing a time-variable orientation of the spectral index gradient due to structural variability of the inner jet.

Key words. galaxies: jets – galaxies: active – galaxies: individual: 3C 84 – techniques: interferometric – techniques: high angular resolution

1. Introduction

Studying the kinematics of active galactic nucleus (AGN) jets on the sub-parsec (pc) scale has only recently been made possible by the advancement of technology utilised in centimetre and millimetre very-long-baseline interferometry (VLBI). Still, only a few sources provide the necessary criteria required to resolve the complex physical phenomena at play. The best-suited candidate AGN should be nearby and harbour a supermassive black hole, which powers a jet, preferably transversely resolved, and which is oriented with respect to the observer at a moderately large viewing angle to avoid strong Doppler beaming effects. The existence of measurements over a long timeline at high cadence, and at different frequencies, is also advantageous.

3C 84, the radio source associated with the central galaxy NGC 1275 in the Perseus cluster (Ho et al. 1997), fulfils all these criteria. The prominent type 2 radio galaxy is indeed

very nearby ($D_L = 78.9 \text{ Mpc}$, $z = 0.0176$, Strauss et al. 1992)¹ and harbours a supermassive black hole ($M_{\text{BH}} \sim 9 \times 10^8 M_{\odot}$, Scharwächter et al. 2013). A multitude of epochs at numerous frequencies are available in the literature, as the source has been studied in detail for over more than half a century (Baade & Minkowski 1954; Walker et al. 1994, 2000; Dhawan et al. 1998; Suzuki et al. 2012; Nagai et al. 2014; Dutson et al. 2014; Giovannini et al. 2018; Kim et al. 2019; Paraschos et al. 2021). Two jets emanate from the central engine (Vermeulen et al. 1994; Walker et al. 1994; Fujita & Nagai 2017); one moves southward and is very prominent, while the northern one is much fainter and is obscured by free-free absorption on milli-arcsecond (mas) scales (Wajima et al. 2020). The

¹ We assume Λ cold dark matter cosmology with $H_0 = 67.8 \text{ km s}^{-1} \text{ Mpc}^{-1}$, $\Omega_{\Lambda} = 0.692$, and $\Omega_M = 0.308$ (Planck Collaboration XIII 2016).

subject of the exact value of the viewing angle is still in contention. VLBI studies at 43 GHz indicate a viewing angle of $\theta_{\text{LOS}} \approx 65^\circ$ (Fujita & Nagai 2017) based on the jet-to-counter-jet ratio; on the other hand, spectral energy distribution (SED) fittings of γ -rays place the viewing angle on the lower side, at $\theta_{\text{LOS}} \approx 25^\circ$ (Abdo et al. 2009) or even $\theta_{\text{LOS}} \approx 11^\circ$ (Lister et al. 2009a). We note that the different viewing angles are measured in different regions and therefore suggest a spatial bending of the jet. Nevertheless, the viewing angle is large enough to allow for excellent tracking of the different radio emitting features (Oh et al. 2022). The jet kinematics derived from observing these features over multiple VLBI maps yield rather slow speeds, accelerating from $\beta_{\text{app}} \leq 0.1c$ on sub-mas scales up to $\sim 1.4c$ on mas scales (Krichbaum et al. 1992; Dhawan et al. 1998; Suzuki et al. 2012; Punsly et al. 2021; Hodgson et al. 2021; Weaver et al. 2022).

In this work, we present a comprehensive tracking and cross-identification of travelling features visible in the central 0.5 mas jet region of 3C 84, both at 43 and 86 GHz, and spanning a time range of more than two decades. Tracing the individual travelling features over such a time range provides valuable insight into the physical mechanisms in action at a relatively small distance to the supermassive black hole. The component position registration at different frequencies bears the potential to study the stratification of the inner jet.

Furthermore, we look at the expanding and collimating behaviour of the jet by adding images (stacking process) that are observed close in time (quasi-simultaneous) at 15, 43, and 86 GHz. From this we obtain an estimate of the initial expansion profile within the first milli-arcsecond radius from the VLBI core. In this context, we also discuss the pressure power-law index derived from the expansion profile and the implications for the medium surrounding the inner jet.

This paper is organised as follows. In Sect. 2, we summarise the observations and data reduction. In Sect. 3, we present our analysis and results. In Sect. 4, we discuss our results, and in Sect. 5, we put forward our conclusions.

2. Observations and data reduction

2.1. Data description and total intensity calibration

We analysed all available 86 GHz VLBI observations of 3C 84, which make a total of twenty-four full-track VLBI experiments, ranging from April 1999 to October 2020, which to our knowledge are all available epochs of 3C 84 at the particular frequency observed with the Coordinated Global Millimeter VLBI Array (CMVA) and its successor, the Global Millimeter VLBI Array (GMVA). The observations were made at a cadence of roughly one per year. The superior resolution that the 3 mm VLBI offers provides a unique opportunity to study the pc-scale jet of 3C 84 in great detail. The post-correlation analysis was done in a similar manner as described in Kim et al. (2019) and using the standard procedures in AIPS (Greisen 1990; see also Martí-Vidal et al. 2012).

Furthermore, we obtained 18 VLBI images of 3C 84 from the VLBA-BU-BLAZAR monitoring programme at 43 GHz. Further details of the structure of the programme, as well as a description of the data reduction and results can be found in Jorstad et al. (2005, 2017). The earliest epochs available are from 2010; we chose one or two epochs per year, up to the most recent one (May 2021), to match the cadence of the 86 GHz epochs.

The same selection procedure was followed for the 15 GHz images. In this case, we used the Astrogate VLBI FITS image database². We point out here that the images comprising this database are of heterogeneous quality, given the nature of observations. Since the earliest available epoch is dictated by the lack of 43 GHz images before 2010, the first 15 GHz epoch analysed is from 2010, again reaching up to 2020. An overview of the behaviour of 3C 84 at 15 GHz is also presented in Britzen et al. (2019), where the authors analysed epochs between 1999 and 2017.

Complementary elements to our analysis are the radio variability and total flux light curves of 3C 84 at different frequencies. For this investigation, we obtained radio light curves at 4.8, 8.0, and 14.8 GHz, ranging from 1980 to 2020, from the University of Michigan Radio Observatory (UMRAO), at 15 GHz from the Owen's Valley Radio Observatory (OVRO; see also Richards et al. 2011, for a description of the observations and the data reduction), at 37 GHz from the Metsähovi Radio Observatory (MRO), and at 230 and 345 GHz from the Submillimeter Array (SMA). Additionally, we used the publicly available³ γ -ray light curve of NGC 1275 (3C 84) at MeV-GeV energies, for which observations were carried out in survey mode (Atwood et al. 2009; see also Fermi Large Area Telescope Collaboration 2021). Detailed studies of the γ -ray emission in 3C 84 are available in the literature; for example, in Abdo et al. (2009), Aleksić et al. (2012), Nagai et al. (2012, 2016), Hodgson et al. (2018, 2021), Linhoff et al. (2021). In this work, we focused on possible correlations of the γ -ray variability with the VLBI component ejection. Finally, we used three historical measurements of the total intensity flux of 3C 84 from the Mauna Kea Observatory (MKO) at 1.1 mm (Hildebrand et al. 1977), the National Radio Astronomy Observatory (NRAO) at 1.3 mm (Landau et al. 1983), and at the NASA Infrared Telescope Facility (IRTF) at 1.0 mm (Roellig et al. 1986).

2.2. Imaging

After having obtained the frequency-averaged 86 GHz data through fringe fitting and calibration, we analysed them with the DIFMAP package (Shepherd et al. 1994). We again followed the procedure described in Kim et al. (2019) to obtain CLEAN component (CC) images. The second step of our imaging procedure was to fit circular Gaussian components to the visibilities, which provides a fit to the data with best possible χ^2 , and until the CC image was satisfactorily reproduced. In our analysis, we omitted Gaussian components, which represent the more extended emission beyond $r \geq 0.5$ mas. Their physical interpretation would be more ambiguous, owing to S/N limitations and their low brightness temperature. Figure 1 displays the contour maps of the CLEAN images with circular Gaussian model fit components super-imposed as orange circles. Details of the contour levels and rms noise magnitude are given in the caption. The individual beam sizes and pixel scales are summarised in Table F.1.

Imaging with VLBI and Gaussian component model fitting can be subjective. Some alternative methods have been utilised recently, such as wavelet-based analysis (e.g. Mertens & Lobanov 2015) and CC cluster analysis techniques (e.g. Punsly et al. 2021). Inspired by the latter and in order to increase the robustness of our

² http://astrogeo.org/vlbi_images/

³ https://fermi.gsfc.nasa.gov/ssc/data/access/lat/msl_1c/source/NGC_1275

results, as a third step we implemented an additional CC cluster analysis, which yields very similar results, within the error budgets, for the feature identification and their velocities as computed from the Gaussian component model fitting (see Sect. 3.1). In view of uv-coverage limitations and residual calibration effects, we regard the latter method as most reliable, based on the smaller number of free fit parameters.

For the 15 and 43 GHz maps, we downloaded the respective data files (already fringe fitted and calibrated) from the websites mentioned in Sect. 2.1. We then followed the same steps as with the 86 GHz data sets. Figure 2 showcases the circular Gaussian components, super-imposed on the CC images, and the individual beam sizes and pixel scales are summarised in Table F.2 for the 43 GHz epochs. The circular Gaussian component model fitting for the 15 GHz data was exclusively done to align the images to each other, as in some epochs the C3 region (Nagai et al. 2014) was brighter than the nucleus. Cross-identifying features at this frequency with the higher frequency maps is virtually impossible, due to the large beam size at 15 GHz. The beam sizes and pixel sizes are summarised in Table F.3.

3. Analysis and results

3.1. Component cross-identification

Figures 1 and 2 showcase the travelling features over time labelled with identifiers (IDs). Our procedure for identifying a travelling feature through the epochs was as follows: starting from the 43 GHz maps, we established the trajectories of the main travelling features by requiring that the fit to their velocity produced the minimal dispersion. Continuity arguments also dictate that features cannot move upstream, barring some level of uncertainty regarding their position. A formal description of our positional error estimation is presented in Appendix F. Nevertheless, we note that some features have been reported to move back and forth (e.g. Hodgson et al. 2021), although further downstream, in the C3 region. Such a flip is interpreted as new features emerging. The model parameters are presented in Table F.4.

We established the trajectories of the core features at 86 GHz. Of course, one should expect to identify more features at 86 GHz than at lower frequencies, since the generally smaller beam size resolves a finer structure near the core. A comprehensive table of the model parameters is shown in Table F.5. Five of the six 43 GHz features could be robustly cross-identified with 86 GHz features based on the matching position, time of appearance, and velocity. We labelled these features as in Table F.6. We note here, however, that our analysis implicitly assumes that the features are first visible at 86 GHz near the core and only later become visible at 43 GHz, once they have travelled further downstream. It can be argued that a scenario, in which the ejection near the core is not picked up at 86 GHz due to the sparse cadence, and is instead only later detected downstream at 43 GHz, is also possible. Finally, we point out that for the cross-identification we only focused on the positional information provided by the visibility phases and not the absolute flux information, since the flux density at 86 GHz can be subject to large uncertainties. The relative fluxes, however, are less uncertain.

In order to render the results more robust, we used the CC cluster method for estimating feature velocities as follows: first we super-resolved each image, with a beam size at least half of the nominal value presented in Tables F.1–F.3, to visually recognise each bright feature location, corresponding to a CC cluster. Then, we computed the coordinates of the CC cluster

centroid by calculating the average of the CC coordinates in the image plane, inside a radius the size of the corresponding modelled Gaussian component. We used the jackknife technique (Efron & Stein 1981) to estimate the mean position. For the procedure described above, we only considered CC components with a flux above 5% of the maximum flux CC inside the radius, defined as described earlier in the section. This approach produced a second set of feature coordinates, allowing us to estimate their velocities more confidently (see Sect. 3.2) by averaging these values and the ones obtained by fitting the standard Gaussian component coordinates.

3.2. Kinematics

In Fig. 3, we show the cross-identified features. Each travelling feature is colour-coded and the open and filled symbols correspond to the 43 and 86 GHz travelling features, respectively. The dashed lines describe the velocity and (back-extrapolated) temporal point of ejection. The velocities and their uncertainties of the cross-identified features ‘F1’, ‘F2’, ‘F3’, ‘F4’, and ‘F5’ are listed next to the first time each feature is identified. They were calculated from a weighted averaging of the velocities obtained from the Gaussian component positions and from the CC cluster centroids.

Having established the feature correspondence through the years, we performed a weighted linear regression analysis to each trajectory. A formal description of the fitting procedure is presented in Appendix B. Figure 3 displays the apparent motions of the travelling features. We find that the average velocity of the 86 GHz features amounts to $\mu^{W_{\text{avg}}} = 0.13 \pm 0.05 \text{ mas yr}^{-1}$ ($\beta_{\text{app}}^{W_{\text{avg}}} = 0.16 \pm 0.06c$), whereas for 43 GHz the features move, on average, at $\mu^{Q_{\text{avg}}} = 0.071 \pm 0.026 \text{ mas yr}^{-1}$ ($\beta_{\text{app}}^{Q_{\text{avg}}} = 0.087 \pm 0.032c$). In order to compare the two, we also computed the 86 GHz velocity of features ejected after 2010. This calculation yields an average velocity of $\mu^{W_{\text{avg}}^{2010}} = 0.15 \pm 0.03 \text{ mas yr}^{-1}$ ($\beta_{\text{app}}^{W_{\text{avg}}^{2010}} = 0.18 \pm 0.04c$) at 86 GHz⁴. These latter two values show a difference within their respective error budgets. Performing a z test reveals that the difference between the two values is statistically significant, to at least 2σ . Slightly larger velocities at 86 GHz may indicate that higher frequency observations trace the inner part of the jet sheath, which moves faster, whereas lower frequency 43 GHz observations detect the slower moving outer part of the sheath (see transverse velocity stratification as discussed in, e.g. Ghisellini et al. 2005). This spine-sheath scenario is more extensively discussed in Sect. 4.3.

For earlier epochs (between 1999 and 2002), we tracked the travelling features further downstream, increasing the number of data points for the fit. The feature velocities, for which an adequate number of data points for a fit were identified, are displayed in Table F.7. Among these earlier epoch features, ‘W1’ seems to be the most intriguing. Back-extrapolating to determine the ejection year, we find that the feature emerged in 1981.63 ± 2.5 , which corresponds to the onset the total intensity maximum (flare) at centimetre radio wavelengths (see Fig. 4). W1 can be tentatively identified in past maps from the literature. At 22 GHz, Venturi et al. (1993) reported a travelling feature ejection they called ‘C’⁵ in 1986, which can also be identified

⁴ These values are obtained by computing the weighted mean of the data points, with the weights being the inverted squares of their uncertainties.

⁵ This component is different from the centre of alignment we used in our maps, also labelled C.

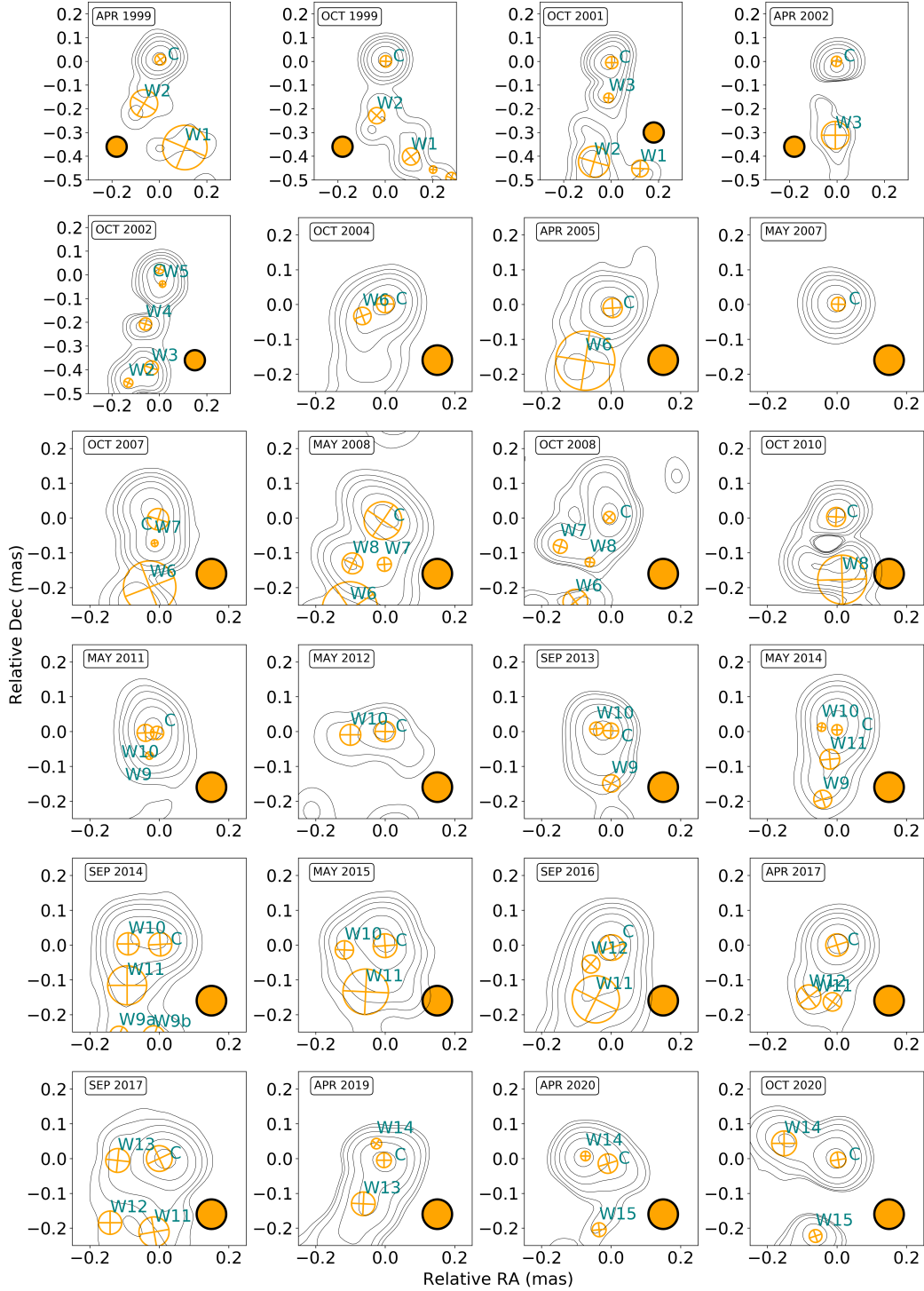


Fig. 1. Circular Gaussian components super-imposed on 86 GHz CLEAN images. The legend of each panel indicates the epoch at which the observations were obtained. The beam of each epoch is displayed in the panels as a filled orange circle. The contour levels correspond to 3%, 5%, 10%, 20%, 40%, and 80% of the intensity peak for all epochs, except May 2012, where 10%, 20%, 40%, and 80% of the intensity peak were used because the data quality was limited. The epochs are convolved with the same circular beam with a radius of 0.088 mas. This radius size was obtained by geometrically averaging the beam sizes of all displayed epochs. A summary of the beam parameters of each individual epoch and peak fluxes is provided in Table F.1. Each feature is labelled based on its date of emergence, with the lower number indicating an earlier ejection time. As a centre of alignment, we always used the north-westernmost feature inside the core region, which we labelled ‘C’. We note that feature ‘W2’ was detectable in the April 2002 epoch and feature ‘W6’ was not detectable in the May 2007 epoch due to S/N limitations. A summary of the characteristics of each feature is provided in Table F.5.

G. F. Paraschos et al.: Jet kinematics in the transversely stratified jet

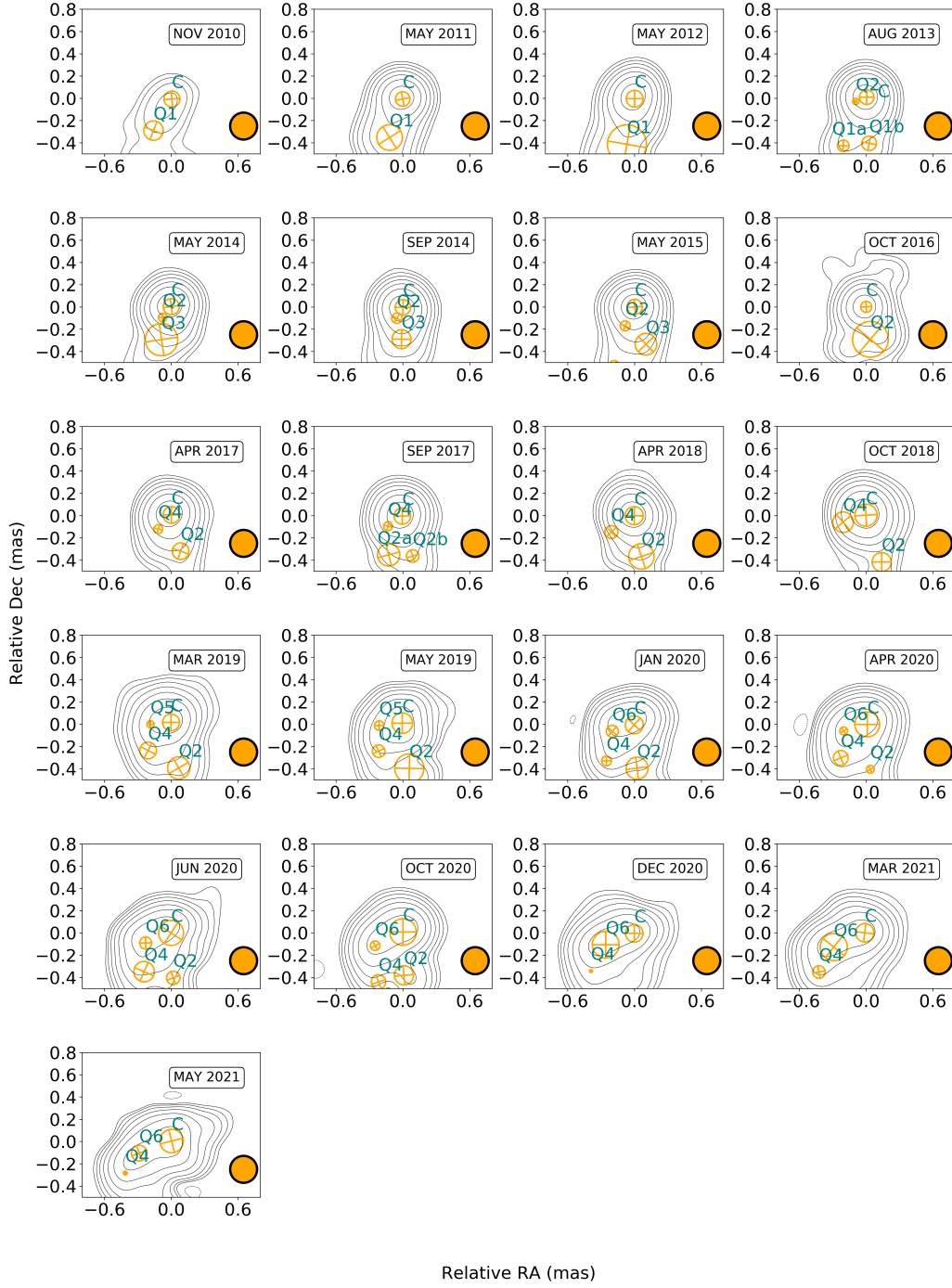


Fig. 2. Circular Gaussian components super-imposed on 43 GHz CLEAN images. The legend of each panel indicates the epoch at which the observations were obtained. The beam of each epoch is displayed in the *bottom right* side as a filled orange circle. The contour levels correspond to -1% , 1% , 2% , 4% , 8% , 16% , 32% , and 64% of the intensity peak, except in November 2010, where, due to lower data quality, the contour levels were adjusted to -10% , 10% , 20% , 40% , and 80% of the intensity peak. The epochs are convolved with the same circular beam, with a radius of 0.24 mas. This size was obtained by geometrically averaging the beam sizes of all displayed epochs. A summary of the beam parameters and peak fluxes is provided in Table F.2. Each feature is labelled based on its date of emergence, with the lower number indicating an earlier ejection time. As a centre of alignment, we always used the north-westernmost feature inside the core region, which we labelled as ‘C’. We note that feature ‘Q1’ seems to split into two (labelled ‘Q1a’ and ‘Q1b’) in August 2013; similarly, ‘Q2’ seems to split into two (labelled ‘Q2a’ and ‘Q2b’) in September 2017. These splits might be due to improved sensitivity in these epochs or variations of the intrinsic brightness and size of the jet feature or a combination of the two. A summary of the characteristics of each feature is provided in Table F.4.

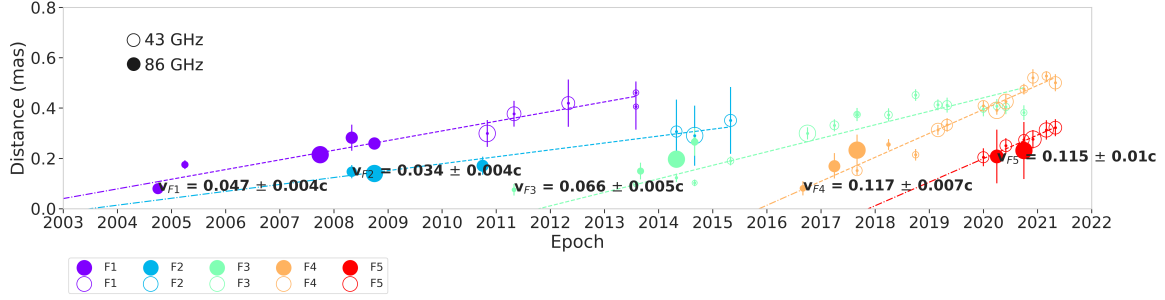


Fig. 3. Plot of motion of the cross-identified, colour-coded features. The empty and filled symbols correspond to the 43 and 86 GHz features, respectively. The velocity fit with the uncertainty is displayed above the first occurrence of each feature. The size of each symbol is normalised to the flux of the central feature (C) of that epoch. The velocities are also listed in Table F.6.

as a bright feature in the 1 mas region south-west of the nucleus, in the 43 GHz map presented in Romney et al. (1995). The position matches that of feature W1 in our 1999 86 GHz image. The trajectory of motion furthermore places W1 in the region where the diffuse blob C2 emerged (Nagai et al. 2010, 2014). We included three flux density measurements at 1 mm from the literature, denoted with green boxes in Fig. 4, to facilitate a comparison between the ejection time of W1 and the flux density peak. Although there are only three measurements available, the maximum flux at 1 mm appears roughly in 1982, consistent with the expectation that the flare first became visible at shorter wavelengths. In both cases, our analysis tentatively connects the appearance of C2 to the major outburst of early 1980s.

For newer epochs, the ejected features seem to move with the expected average velocity ($\mu^{W_{\text{avg}}} = 0.13 \pm 0.05 \text{ mas yr}^{-1}$ or $\beta_{\text{app}}^{W_{\text{avg}}} = 0.16 \pm 0.06c$). On the other hand, features moving perpendicularly to the bulk jet flow exhibit slower speeds. A characteristic example is that of ‘W10’, which was also identified by Oh et al. (2022). The authors find a velocity of $\leq 0.03c$, in agreement with our result of $\mu^{W_{10}} = 0.011 \pm 0.011 \text{ mas yr}^{-1}$ ($\beta_{\text{app}}^{W_{10}} = 0.013 \pm 0.013c$). Surprisingly, the emergence of a new feature, ‘W14’, in 2019 seems to not follow this rule. For it, we find a velocity of $\mu^{W_{14}} = 0.063 \pm 0.034 \text{ mas yr}^{-1}$ ($\beta_{\text{app}}^{W_{14}} = 0.078 \pm 0.042c$), close to the upper limit of $\sim 0.1c$, which has been observed for the core region of 3C 84 in the past.

The picture becomes clearer at 43 GHz, with just six travelling features needed to describe the central region of 3C 84. Here, we make a comparison with the reported velocity range of $\beta_{\text{app}} \approx (0.086 - 0.1)c$ by Punsly et al. (2021). The authors of this work only used observations between August 2018 and April 2020 to study the core of 3C 84 and arrived at this result both by grouping the pair of nuclear CC and by using circular Gaussian component models. In this work, on the other hand, we did not use all available epochs in that time frame, as the goal was the direct comparison with 86 GHz images at a comparable cadence. We did, however, double the cadence for 2020 and add the more recent epochs (up to May 2021) to facilitate our analysis. In our interpretation, three features emerged in that time frame: one feature (‘Q4’), which emerged in 2018, one in early 2019 (‘Q5’), and one which emerged in early 2020 (‘Q6’). This leads to different feature velocities, with Q4 moving at $\mu^{Q_4} = 0.094 \pm 0.007 \text{ mas yr}^{-1}$ ($\beta_{\text{app}}^{Q_4} = 0.116 \pm 0.008c$) and Q6 at $\mu^{Q_6} = 0.093 \pm 0.010 \text{ mas yr}^{-1}$ ($\beta_{\text{app}}^{Q_6} = 0.115 \pm 0.012c$). Averaging them leads to a virtually identical value of $\mu^{Q_{\text{comb}}} = 0.094 \pm 0.001 \text{ mas yr}^{-1}$ ($\beta_{\text{app}}^{Q_{\text{comb}}} = 0.116 \pm 0.001c$). The feature Q5 only appears in two epochs, therefore not fulfilling our cri-

terion set for feature velocity determination. We note here that for this comparison we used the velocity that we computed by fitting only the 43 GHz epochs.

Jorstad et al. (2017) did a similar kinematics analysis for epochs between 2007 and 2013 at 43 GHz and found moving feature velocities of $\beta_{\text{app}} \sim 0.2c$ further downstream ($\beta_{\text{app}} = 0.5 - 3.0 \text{ mas}$ from the VLBI core) than the region we are studying. This is in line with the known acceleration of features downstream along the jet in 3C 84 (Krichbaum et al. 1992; Dhawan et al. 1998; Suzuki et al. 2012; Punsly et al. 2021; Hodgson et al. 2021).

3.3. Outburst ejection relations

For 3C 84, a conclusive relation between radio features and γ -ray flares, as well as their ejection sites, is still elusive (see e.g. Nagai et al. 2012; Linhoff et al. 2021; Hodgson et al. 2018, 2021). The emergence of new VLBI features in AGN radiojets (often but not always) can be associated with the onset of radio flares (e.g. Savolainen et al. 2002; Karamanavis et al. 2016). Here, we investigate the possible association between the detected new VLBI features in 3C 84 and the total intensity light curves, by back-extrapolating their trajectory to estimate the ejection time, which is the time of zero separation from the VLBI core. We also explored the connection between the flare intensity and ejected feature velocity.

Figure 4 overlays the ejection time of each feature on the radio and γ -ray light curves of 3C 84 in the top panel, with the bottom panel displaying a zoomed-in version to aid the reader in comparing the ejection times with the finer details of the variability curves. The grey shaded area in the top panel of Fig. 4 denotes the ejection time of the oldest VLBI feature we can identify in our data set, which is W1. Also, for the features F1 and F2, only variability data at centimetre wavelength are available. The flux densities of the centimetre light curves are decaying, and no correspondence to flare activity is apparent. However, feature F3 seems to be associated with the onset of a centimetre flare peaking in 2013.19. At this time, no prominent flare in the γ -ray light curve is obvious. Feature F4 appears at the onset of a more prominent millimetre flare, which is visible in the centimetre and millimetre bands, with a peak in 2016.66. Interestingly, F4 could be associated with a γ -ray flare, which occurred at the onset of this radio flare and peaked in 2015.82. Feature F5 occurred during the decay phase of the centimetre and millimetre flare of 2016.66 and seems to correspond to a rising phase in the γ -rays, which reached the brightest γ -ray flux peak so far of 3C 84 in 2018.35. We further note that the peak of this γ -ray

G. F. Paraschos et al.: Jet kinematics in the transversely stratified jet

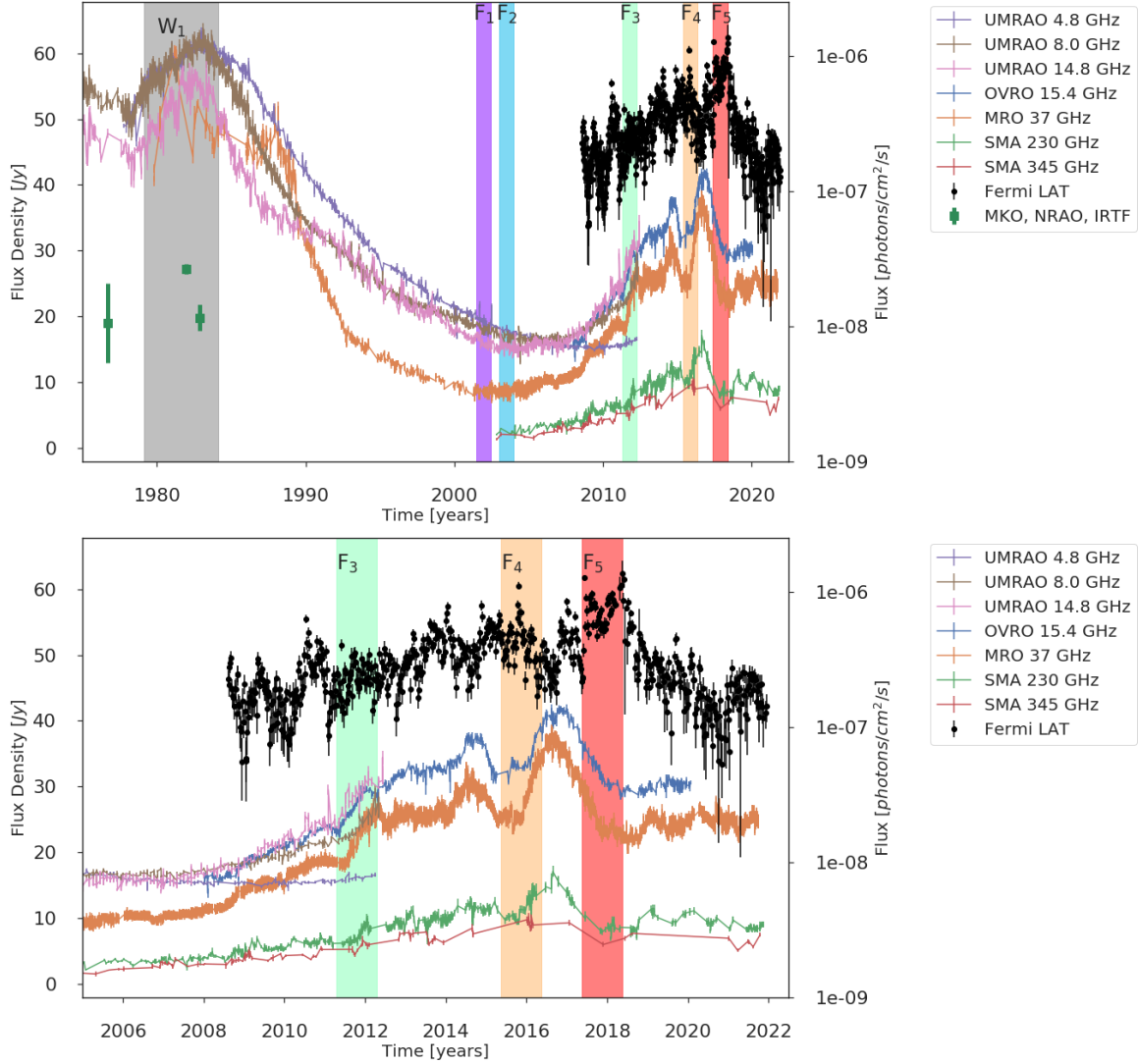


Fig. 4. Total variability radio light curves and γ -ray flux. *Top*: presented here are radio light curves of 3C 84 from 1980 to 2020 at 4.8, 8.0, 14.8, 15, 37, 230, and 345 GHz (in order of appearance in the legend). The black data points correspond to γ -ray flux. The dark-green data points are individual, historical, total flux measurements. The grey shaded area at the onset of the total intensity peak around 1983 could tentatively be connected to the ejection of feature W1, which may correspond to the prominent C2 region identified in later maps. The five other shaded areas are colour-coded in response to the cross-identified features F1 through F5, as described in Fig. 3, and denote the approximate ejection time. *Bottom*: zoomed-in version of the top panel showing the years 2005–2022.

flare occurred after the decay of the preceding radio flare, which is quite unusual. The good correspondence of the ejection times of the features F4 and F5 with two maxima in the γ -ray light curve, which bracket this prominent centimetre and millimetre-peak, is also remarkable.

The appearance of feature F4 at the onset of the big radio flare peaking in 2016.66 and the local γ -ray emission region of this event is located within the VLBI core region. The relatively long time lag between the peak of the radio flux in 2016.66 and the peak of the subsequent γ -ray flare of 2018.35, however, suggests that the γ -rays of this event are produced further downstream in the jet. This hypothesis is further supported by the lack of an enhanced radio flux following this γ -ray flare. It remains unclear how the

ejection of F5 relates to the observed variability in the radio bands.

Besides the individual associations between the features and the flares, there may also be one between the component velocities and the radio flux densities. The slowest feature F2 ($\mu^{F_2} \sim 0.024 \text{ mas yr}^{-1}$ or $\beta_{\text{app}}^{F_2} \sim 0.03c$) seems to correspond to the lowest flux level out of the five features, whereas the fastest feature F4 ($\mu^{F_4} \sim 0.09 \text{ mas yr}^{-1}$ or $\beta_{\text{app}}^{F_4} \sim 0.11c$) corresponds to the highest flux level. The remaining features also follow this pattern (see Fig. 5). This pattern might also be transferred to the γ -ray flux, with F3, the slower out of the three overlapping features, corresponding to a lower flux level than the two remaining ones. Such behaviour could be explained if jet features move along a curved trajectory, leading to a time-variable Doppler beaming.

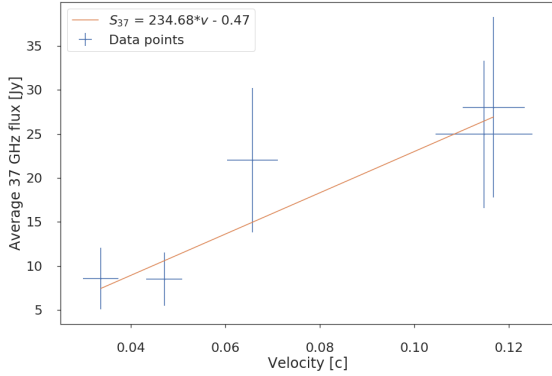


Fig. 5. Back-extrapolated apparent velocity of features F1 through F5 and the 37 GHz flux (S_{37}) associated with them. A clear, increasing trend is observed.

3.4. Image stacking

Even though image stacking smears out details from individual maps, it offers a better insight into the wider jet funnel and into its transverse profile and possible stratification. For that reason, we averaged all epochs in time at 15, 43, and 86 GHz and display them in Fig. 6. The centre of alignment was always chosen to be the core feature (labelled as C), which we defined as the north-westernmost feature in each epoch. With this choice, we eliminate effects due to time variability of the jet origin, as we can consistently align all images at the same position. We also refer to a previous core shift analysis (Paraschos et al. 2021) that shows a moderate frequency dependence of the VLBI core, typically much smaller than the beam size. The 86 GHz image showcases only the nucleus because in the southern region the diffuse flux is mostly resolved out, and thus a ridge line cannot be robustly traced. For completeness, we display the same stacked map of 3C 84 at 86 GHz in its entirety in the bottom right panel of Fig. F.1. An overview of the stacking, slicing, and Gaussian fitting procedure is detailed in Appendix C.

3.5. Spectral index

Following the procedure described in Paraschos et al. (2021), we created spectral index maps for selected epochs (see Fig. 7), by performing a two-dimensional cross-correlation analysis. We used the optically thin and still compact emission region C3 for the alignment, except for the data from October 2020, where C3 was not well determined. Instead, we used another optically thin feature in this observation, which is located south-west of the VLBI core and is centred at (0.2, -0.4) mas. In the two earliest epochs, we identify a spectral index gradient along the north-south direction, with spectral indices from $\alpha^{43-86} \sim 3-4$ in the north and $\alpha^{43-86} \sim -2$ in the south. In September 2014, September 2017, and October 2020, the orientation of the spectral index gradient changed towards a northwest-southeast direction. The spectral indices range again from $\alpha^{43-86} \sim +(2-4)$ in the northwest and $\alpha^{43-86} \sim -2$ in the southeast. Spectral indices much lower than -2 are likely due to beam resolution effects and/or uncertainties in the flux density scaling at 86 GHz and therefore may not be real. The uncertainty calculation for the individual epochs, as well as the spectral index uncertainty maps (Fig. D.1), are summarised in Appendix D.

4. Discussion

4.1. Projection effects

Our analysis presented in the previous section rests on the assumption that the jet does not significantly precess the VLBI core region and that bright VLBI features are expelled from the VLBI core region, which was identified as the most luminous feature in the radio maps. This hypothesis is physically motivated and ties well into the existing literature both for 3C 84 (see identification scheme in Nagai et al. 2014 and Oh et al. 2022), as well as for other prominent AGN jets like M 87 (Kim et al. 2018) and NGC 1052 (Baczko et al. 2016), to name only a few.

The fact that we are able to cross-identify jet components in 3C 84 at two frequencies and describe the motion of the VLBI components by a steady and linear function of time supports the assertion that we are in fact observing features ejected from the central engine. This holds for the feature trajectories from the core up to the ~ 1 mas region. The limited time base of this data set does not allow us to see strong deviations from linear motion, but the misalignment between inner (sub-mas) and outer (mas-scale) VLBI jets suggests spatially bent and non-ballistical component trajectories, similar to those seen in many other AGN jets.

4.2. Jet cross-section

We used the stacked images to measure the transverse jet profile. Since the jet of 3C 84 exhibits an increasingly complex structure with increasing distance from the core (likely due to the contribution of C2 Nagai et al. 2010, 2014), we split the region of interest into two: the core region ($z_0 < 0.75$ mas for 43 and 86 GHz observations and $z_0 < 1$ mas for 15 GHz ones; here, z_0 is the distance from the core ($z_0 = r|_{x=0}$)) and the region downstream ($z_0 > 0.75 - 1$ mas). Based on the shape of the intensity slices (see Fig. C.1), we fitted a single Gaussian function to the core region of the 86 GHz image and a double Gaussian function to the downstream region. For the 15 and 43 GHz images, we fitted a double Gaussian function in both regions. From the single Gaussian fit, we determined the full width at half maximum (FWHM) of each slice. To arrive at the deconvolved jet width, we subtracted the beam from the FWHM in quadrature. From the double Gaussian function fit, we considered the dominant (brighter) one to measure the transverse width of the main jet.

The results of our analysis are presented in Fig. 8. We find that the measured, deconvolved jet widths of the lower frequencies are overlapping close to the jet origin and the jet width becomes frequency dependent further downstream (see Fig. 8); that is, the jet width changes with frequency within core separations of $1.5 \leq z_0 \leq 4$ mas. To quantify the degree of change in jet width, we calculated the median of the differences ($w_{15} - w_{43}$) and ($w_{43} - w_{86}$): $\Delta r_{15-43} = 0.091 \pm 0.027$ and $\Delta r_{43-86} = 0.082 \pm 0.024$. The fact that the pairwise differences are both positive indicates the presence of a systematic trend. This is a characteristic property of a stratified jet, where different frequencies could map different parts of the jet (Pelletier & Roland 1989; Sol et al. 1989; Komissarov 1990). Similar limb brightening in 3C 84 was reported by Nagai et al. (2014), Giovannini et al. (2018), and Kim et al. (2019), although these studies were based only on single epochs. However, we note that the 86 GHz measurements may represent a lower limit to the true jet width; this is due to beam resolution effects and dynamic range limitations (see also Table F.9). In order to test the significance of the smaller 86 GHz jet width, we added a normally distributed random noise signal to the 15 and 43 GHz stacked images, such

5 PAPER 3: JET KINEMATICS IN THE TRANSVERSELY STRATIFIED JET OF 3C 84: A TWO-DECADE OVERVIEW

G. F. Paraschos et al.: Jet kinematics in the transversely stratified jet

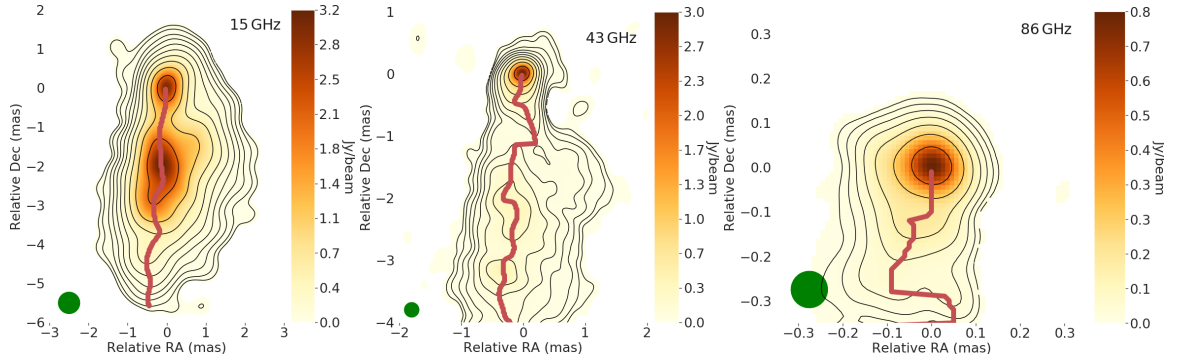


Fig. 6. Stacked images of 3C 84 at 15, 43, and 86 GHz. *Left:* 15 GHz stacked images of epochs from 2010 to 2020, as listed in Table F.3. The green disc represents the common circular beam used to convolve all images before averaging. The continuous red line depicts the ridge line, which is the point with the highest intensity at each slice. Each axis is in units of mas. The coloured region and contours correspond to regions with a S/N of at least five. Details of the beam size, flux, and rms are listed in Table F.9. The contour levels are -2% , -1% , -0.5% , 0.5% , 1% , 2% , 4% , 8% , 16% , 32% , and 64% of the intensity peak. *Middle:* same as left panel, but for 43 GHz. An epoch summary is listed in Table F.2. Details of the beam size, flux, and rms are listed in Table F.9. *Right:* same as left and middle panels, but for 86 GHz. An epoch summary is listed in Table F.1. The common convolving beam is listed in Table F.9. Details of the beam size, flux, and rms are listed in Table F.9 as well. For a zoomed-out view of the 86 GHz total intensity map at different time bins, including the 2010–2020 bin presented here, see Fig. F.1.

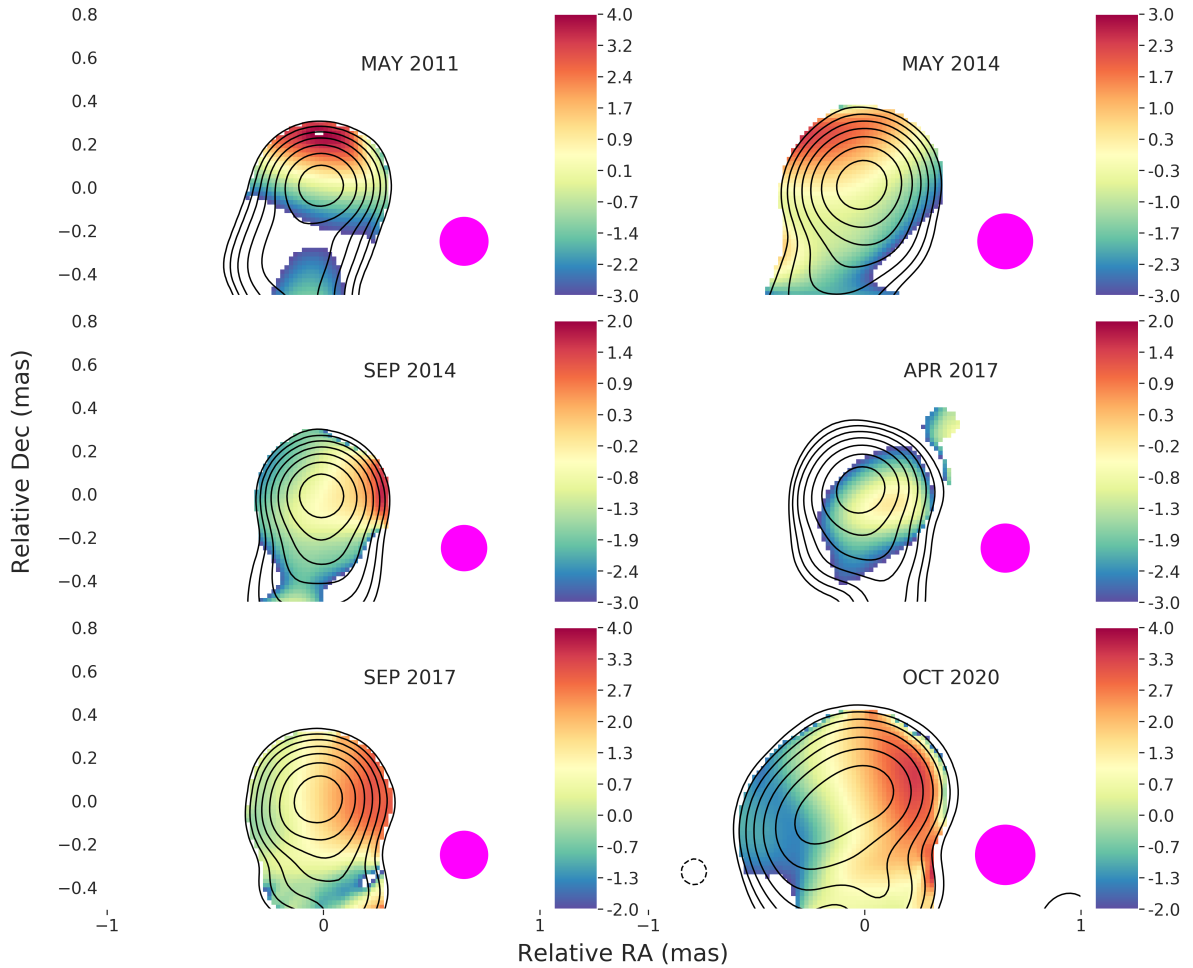


Fig. 7. Spectral index map of selected epochs. The contour levels were set at -1% , 1% , 2% , 4% , 8% , 16% , 32% , and 64% of the intensity peak at each epoch. The total intensity cut-off was set at 50σ . The limiting values for the spectral indices are indicated in the colour bars beside each panel. A summary of the image parameters is presented in Table F.10. The corresponding spectral index uncertainty maps are presented in Fig. D.1.

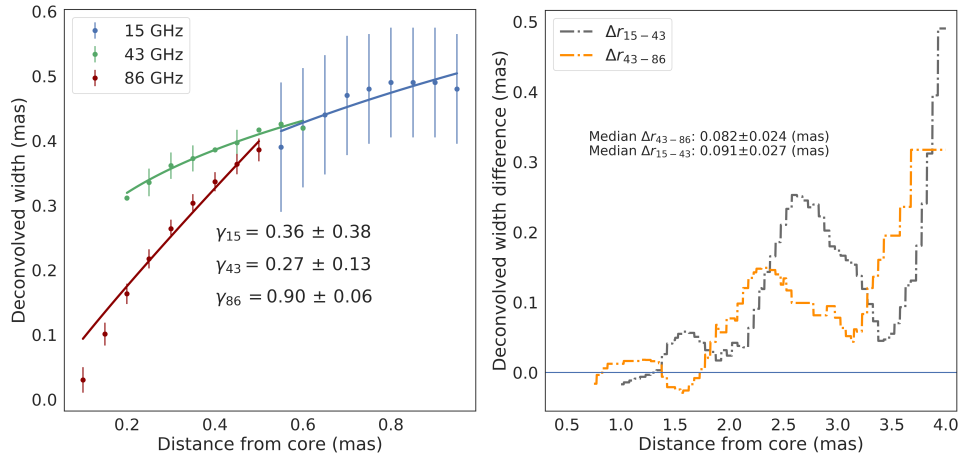


Fig. 8. Deconvolved jet width and jet width difference as a function of the distance from the core. *Left:* deconvolved jet width as a function of the distance (projected) from the VLBI core at 15, 43, and 86 GHz. The blue, green, and red markers correspond to slices taken from the 15, 43, and 86 GHz images shown in Figs. 6 and F.1, respectively. The corresponding solid lines mark the power-law fits with their indices: $\gamma_{15} = 0.36 \pm 0.38$, $\gamma_{43} = 0.27 \pm 0.13$, and $\gamma_{86} = 0.90 \pm 0.06$ (see Table F.12). All slices are drawn parallel to the abscissa and are evenly spaced at $50 \mu\text{as}$ apart. We note that the 86 GHz data points might be indicating a lower limit for the jet width due to dynamic range limitations. *Right:* difference between the jet width at 15 GHz and 43 GHz (Δr_{15-43} ; dashed grey line) and 43 GHz and 86 GHz (Δr_{43-86} ; dashed orange line). In both cases, the median values Δr_{15-43} and Δr_{43-86} are positive.

that their dynamic range matched that of the 86 GHz observations. Interestingly, we find that the systematic trend persists. The median values with added noise are $\Delta r_{15-43}^n = 0.099 \pm 0.030$ and $\Delta r_{43-86}^n = 0.085 \pm 0.021$ (i.e. still positive). This indicates that the frequency-dependent jet width may be real, even when accounting for dynamic range limitations at 86 GHz.

4.3. Jet collimation

A parameter frequently used in discriminating between jet formation models is the collimation profile; that is the width of the jet w , as a function of the distance from the core z_0 (see e.g. Daly & Marscher 1988). This parameter is fundamentally tied to the characteristics of the jet and the external medium, specifically the ratio of the external pressure P_{ext} to the internal pressure P_{jet} , as has been shown in theoretical models and simulations (Komissarov et al. 2007; Tchekhovskoy et al. 2008; Lyubarsky 2009). When the external pressure of the gas is described by a power law of the form $P \propto r^{-p}$, with $p < 2$, then the bulk jet flow follows a parabolic profile. On the other hand, if the opposite is true and $p > 2$, then the bulk jet flow follows a conical profile (Komissarov et al. 2009). In both cases, this pressure is counteracting the force-free expansion of the magnetised jet. In this regime, the power law from Eq. (C.4) is connected to P_{ext} by $\gamma = p/4$.

By using a stacked image of 3C 84 (constructed from numerous epochs) to highlight the underlying structure of the jet, we attempt here, for the first time for this source, a comparison of the collimation of the jet profile of 3C 84 in the nuclear region at three different frequencies. As shown in Fig. 8, we chose to fit a power-law function to the initial expansion region where the jet width is increasing but not yet affected by the presence of C2. The resulting power-law indices are $\gamma_{15} = 0.36 \pm 0.38$ at 15 GHz, $\gamma_{43} = 0.27 \pm 0.13$ at 43 GHz, and $\gamma_{86} = 0.90 \pm 0.06$ at 86 GHz, respectively. These power-law index values are summarised in Table F.12. Our result also appears to align well with the findings of Oh et al. (2022). In that work, the authors fitted both a conical and a parabolic jet profile, but they could not conclusively select

one over the other. Our measurement of $\gamma_{86} = 0.90 \pm 0.06$ at 86 GHz indicates an initially conical jet profile.

Figures 6 and F.1 showcase the complex structure of the jet of 3C 84 in the $z_0 > 0.75 - 1$ mas region. Plotting the jet width at all three frequencies produces a jagged outline as a result of both the jet collimation and expansion (Daly & Marscher 1988), as well as image artefacts due to a low S/N at the edge of the jet. On the contrary, the difference between the jet widths at 15, 43, and 86 GHz provides a better method of investigating and illustrating whether a systematic trend is present (see Fig. 8, right). We find a decrease in jet width with increasing frequency, suggesting a transverse jet stratification scenario (i.e. spine-sheath structure; see e.g. Pelletier & Roland 1989; Sol et al. 1989; Komissarov 1990). Similar stratified jet geometries – also seen via polarisation and rotation measure analyses (e.g. O’Sullivan & Gabuzda 2009; Hovatta et al. 2012; Gabuzda et al. 2017) in other AGNs – could result from twisted magnetic flux tubes (e.g. Tchekhovskoy 2015) or hybrid models, where the central black hole and the inner accretion disc both contribute to the jet formation (Paraschos et al. 2021; Mizuno 2022).

Another possible interpretation, however, is that the observed synchrotron radiation reflects magnetised jet plasma that is undergoing rapid synchrotron cooling transverse to the jet flow. Synchrotron losses within the jet might manifest as a frequency-dependent jet width, reflecting the radial dependence of the magnetic field strength and the underlying electron power-law distribution across the jet.

A halo or cocoon enveloping the extended emission in the pc-scale region (detected at lower frequencies, e.g. Taylor & Vermeulen 1996; Silver et al. 1998; Savolainen et al. 2021) has been put forth in the past as a possible explanation of the jet collimation in 3C 84 (e.g. Nagai et al. 2017; Giovannini et al. 2018). However, this halo or cocoon is extended and exhibits a steep spectrum. Such low surface brightness temperature features are too faint to be detectable at higher frequencies with the present millimetre-VLBI array.

We note that an increased, external pressure around the nucleus of 3C 84 – for example as provided by such a cocoon or

halo – would help to explain the observed downstream acceleration of moving features. In this picture, the higher external pressure on the nucleus confines the ejected features into a spatially restricted region, which the features can only traverse slowly. Further downstream, where the external pressure decreases, the features are able to accelerate more freely.

We compare the power-law indices of the jet expansion found in this work to other studies of 3C 84 from the literature. [Giovannini et al. \(2018\)](#) found a power-law index of $\gamma_{86} \sim 0.17$, utilising *RadioAstron* observations of 3C 84 at 22 GHz, and [Nagai et al. \(2014\)](#) computed a power-law index of $\gamma_{86} \sim 0.25$ using Very Long Baseline Array (VLBA) observations. Both these publications used a single epoch and took into account the entirety of the jet in their fittings. To contrast our results with these publications, we followed a similar procedure, performing a fit over the full length of the jet, which produces $\gamma_{15}^{\text{all}} = \sim 0.1$ at 15 GHz, $\gamma_{43}^{\text{all}} = \sim 0.3$ at 43 GHz, and $\gamma_{86}^{\text{all}} = \sim 0.4$ at 86 GHz, respectively. Our 43 GHz estimate of the power-law index is very similar to the one from [Nagai et al. \(2014\)](#) and the 22 GHz power law index by [Giovannini et al. \(2018\)](#) fits well into the picture of increasing power-law indices with frequency for the entirety of the southern bulk jet flow.

Collimation profile studies have also been published for several other AGNs. [Boccardi et al. \(2016\)](#) found that the power-law index of the collimation profile of Cygnus A is $\gamma_{43} \sim 0.55$, and [Hada et al. \(2013\)](#) showed that for M 87 the power-law index of the collimation profile is $\gamma_{\text{combined}} \sim 0.56 - 0.76$. While the 86 GHz data seem to agree with these values, the lower frequency measurements are divergent. This might indicate source-dependent intrinsic differences; for example, of the jet power or in the medium that surrounds these jets ([Boccardi et al. 2021](#)).

4.4. Implications of the spectral-index values and orientation

The spectral index of a synchrotron self-absorbed emission region usually ranges between $\alpha \leq +2.5$ in the optically thick regime and $-0.5 \leq \alpha \leq -1$ in the optically thin regime (see e.g. [Rybicki & Lightman 1979](#)). An optically thick external absorber located between the source and observer, however, could alter the spectrum, causing a stronger spectral inversion.

The highly inverted spectrum at the northern end of the 3C 84 jet (see Fig. 7) therefore suggests free-free absorption from a foreground absorber. In 3C 84, it could result, for example, from a circum-nuclear disc or torus ([Walker et al. 2000](#)). This view is further supported from recent VLBI observations at 43 GHz (KaVA) and 86 GHz (KVN), though at a lower angular resolution ([Wajima et al. 2020](#)). A foreground absorber would also act as an external Faraday screen, explaining the observed frequency-dependent polarisation in the central region ([Kim et al. 2019](#)), and it would also explain the apparent absence of the counter-jet on sub-mas scales at 86 GHz.

The observed variation in the orientation of the spectral index gradient on timescales of a few years (see Fig. 7) could challenge the interpretation via foreground absorption, unless the absorber were time variable or inhomogeneous. In any case, we have to consider the inclination of the jet relative to the observer. If we are observing the source as displayed in Fig. 14 in [Kim et al. \(2019\)](#), we would be peering into the bulk jet flow at an angle. The trajectories of the ejected features could be aligned or misaligned with the line of sight from time to time, thus temporarily affecting the orientation of the spectral index gradient. In this case, the variation of the orientation of the spectral index gradient in the core region could then be explained by the bent jet kinematics (helical motion, rotating jet base) rather than by some small-scale variations (sub-pc) in the foreground screen. Future

monitoring observations and more detailed simulations taking into account time-dependent jet bending (helical motion) and absorber variations may shed more light on the observed variation in the spectral index gradient orientation.

5. Conclusions

In this work, we presented a detailed kinematics analysis of 3C 84 at 43 and 86 GHz. Furthermore, we established an estimate for the environment around the jet flow in the core region. Our major findings and conclusions can be summarised as follows:

1. We cross-identify moving components ejected from the VLBI core at 43 and 86 GHz. The components move with velocities of $\mu^{\text{avg}} = 0.04 - 0.18 \text{ mas yr}^{-1}$ ($\beta_{\text{app}}^{\text{avg}} = 0.055 - 0.22c$) on average. We find marginal evidence ($\sim 2\sigma$) for a faster motion at 86 GHz.
2. The ejection of feature W1, identified at 86 GHz and possibly corresponding to C2, appears to be temporally coincident with the onset of the total intensity maximum (flare) at centimetre wavelengths in the early 1980s. For the cross-identified radio features (F1 through F5), however, a simple one-to-one correspondence between the onset of centimetre, millimetre, and γ -ray flares seems to be lacking. For components F4 and F5, the data suggest an association between component ejection and a subsequent brightening in the γ -ray band. The delayed γ -ray flare peak suggests that the region of γ -ray production is located not in the VLBI core, but further downstream.
3. The complexity of the source structure of 3C 84 complicates the measurement of the transverse jet width. However, in the innermost jet region ($z_0 \leq 1 \text{ mas}$), we can characterise the transverse jet profile at 86 GHz by one Gaussian function. Further downstream and at 15 and 43 GHz, a double Gaussian profile is more appropriate. In this downstream region ($z_0 > 1.5 \text{ mas}$), we find evidence for a systematic variation of the jet width with frequency. From a comparison of the brighter Gaussian profile at each frequency, we formally obtain the following power-law indices for the transverse jet profiles: $\gamma_{15} = 0.36 \pm 0.38$ at 15 GHz, $\gamma_{43} = 0.27 \pm 0.13$ at 43 GHz, and $\gamma_{86} = 0.90 \pm 0.06$ at 86 GHz.
4. The 86 GHz observations seem to trace the inner sheath part and suggest a parabolic jet flow profile. The 15 and 43 GHz observations, on the other hand, seem to outline the outer sheath, characterised by a more conical jet flow profile. The different profiles suggest different jet opening angles at each observed frequency or effects of synchrotron cooling transverse to the jet axis or a combination of the two.
5. The spectral index images of the individual epochs, reveal a strong spectral index gradient with a time variable orientation. Its position angle (PA) may be affected by moving jet features being ejected in different directions. Density or opacity variations in a foreground absorber, however, cannot be ruled out.

Overall, our study suggests that the jet stratification could partially explain the motion of the different features seen at 43 and 86 GHz. Currently, only a handful of VLBI observations of 3C 84 are available at intermediate frequencies (e.g. 22 GHz) and none at all at higher frequencies (e.g. 230 GHz). It is therefore important to bridge this gap by employing more and denser in-time-sampled VLBI monitoring observations in the near future. VLBI imaging at even shorter wavelengths (e.g. with the Event Horizon Telescope) will provide an even higher angular resolution, facilitating more detailed studies of the central super-massive black hole and the matter surrounding it.

Acknowledgements. We thank T. Savolainen for providing software to calculate two dimensional cross-correlations. We also thank N. R. MacDonald for the proofreading and fruitful discussions which helped improve this manuscript. We thank the anonymous referee for the useful comments. G.F. P. is supported for this research by the International Max-Planck Research School (IMPRS) for Astronomy and Astrophysics at the University of Bonn and Cologne. J.-Y. K. acknowledges support from the National Research Foundation (NRF) of Korea (grant no. 2022R1C1C1005255). This research has made use of data obtained with the Global Millimeter VLBI Array (GMVA), which consists of telescopes operated by the MPIfR, IRAM, Onsala, Metsähovi, Yebes, the Korean VLBI Network, the Green Bank Observatory and the Very Long Baseline Array (VLBA). The VLBA and the GBT are a facility of the National Science Foundation operated under cooperative agreement by Associated Universities, Inc. The data were correlated at the correlator of the MPIfR in Bonn, Germany. This work makes use of 37 GHz, and 230 and 345 GHz light curves kindly provided by the Metsähovi Radio Observatory and the Submillimeter Array (SMA), respectively. The SMA is a joint project between the Smithsonian Astrophysical Observatory and the Academia Sinica Institute of Astronomy and Astrophysics and is funded by the Smithsonian Institution and the Academia Sinica. This research has made use of data from the University of Michigan Radio Astronomy Observatory which has been supported by the University of Michigan and by a series of grants from the National Science Foundation, most recently AST-0607523. This work makes use of the Swinburne University of Technology software correlator, developed as part of the Australian Major National Research Facilities Programme and operated under licence. This study makes use of 43 GHz VLBA data from the VLBA-BU Blazar Monitoring Program (VLBA-BU-BLAZAR; <http://www.bu.edu/blazars/VLBAproject.html>), funded by NASA through the Fermi Guest Investigator Program. This research has made use of data from the MOJAVE database that is maintained by the MOJAVE team (Lister et al. 2009b). This research has made use of the NASA/IPAC Extragalactic Database (NED), which is operated by the Jet Propulsion Laboratory, California Institute of Technology, under contract with the National Aeronautics and Space Administration. This research has also made use of NASA's Astrophysics Data System Bibliographic Services. This research has also made use of data from the OVRO 40-m monitoring program (Richards et al. 2011), supported by private funding from the California Institute of Technology and the Max Planck Institute for Radio Astronomy, and by NASA grants NNX08AW31G, NNX11A043G, and NNX14AQ89G and NSF grants AST-0808050 and AST-1109911. S.K. acknowledges support from the European Research Council (ERC) under the European Unions Horizon 2020 research and innovation programme under grant agreement No. 771282. Finally, this research made use of the following python packages: *numpy* (Harris et al. 2020), *scipy* (Virtanen et al. 2020), *matplotlib* (Hunter 2007), *astropy* (Astropy Collaboration 2013, 2018), *pandas* (Pandas Development Team 2020; McKinney et al. 2010), *seaborn* (Waskom 2021), and *Uncertainties: a Python package for calculations with uncertainties*.

References

- Abdo, A. A., Ackermann, M., Ajello, M., et al. 2009, *ApJ*, 699, 31
- Aleksić, J., Alvarez, E. A., Antonelli, L. A., et al. 2012, *A&A*, 539, L2
- Astropy Collaboration (Robitaille, T. P., et al.) 2013, *A&A*, 558, A33
- Astropy Collaboration (Price-Whelan, A. M., et al.) 2018, *AJ*, 156, 123
- Atwood, W. B., Abdo, A. A., Ackermann, M., et al. 2009, *ApJ*, 697, 1071
- Baade, W., & Minkowski, R. 1954, *ApJ*, 119, 215
- Baczko, A. K., Schulz, R., Kadler, M., et al. 2016, *A&A*, 593, A47
- Boccardi, B., Krichbaum, T. P., Bach, U., et al. 2016, *A&A*, 585, A33
- Boccardi, B., Perucho, M., Casadio, C., et al. 2021, *A&A*, 647, A67
- Britzen, S., Fendt, C., Zajaček, M., et al. 2019, *Galaxies*, 7, 72
- Daly, R. A., & Marscher, A. P. 1988, *ApJ*, 334, 539
- Dhawan, V., Kellermann, K. I., & Romney, J. D. 1998, *ApJ*, 498, L111
- Dutson, K. L., Edge, A. C., Hinton, J. A., et al. 2014, *MNRAS*, 442, 2048
- Efron, B., & Stein, C. 1981, *Ann. Stat.*, 9, 586
- Fermi Large Area Telescope Collaboration 2021, *ATel.*, 15110, 1
- Fomalont, E. B. 1999, in *Synthesis Imaging in Radio Astronomy II*, eds. G. B. Taylor, C. L. Carilli, & R. A. Perley, *ASP Conf. Ser.*, 180, 301
- Fujita, Y., & Nagai, H. 2017, *MNRAS*, 465, L94
- Gabuzda, D. C., Roche, N., Kirwan, A., et al. 2017, *MNRAS*, 472, 1792
- Ghisellini, G., Tavecchio, F., & Chiaberge, M. 2005, *A&A*, 432, 401
- Giovannini, G., Savolainen, T., Orienti, M., et al. 2018, *Nat. Astron.*, 2, 472
- Greisen, E. W. 1990, in *Acquisition, Processing and Archiving of Astronomical Images*, 125
- Hada, K., Kino, M., Doi, A., et al. 2013, *ApJ*, 775, 70
- Harris, C. R., Millman, K. J., van der Walt, S. J., et al. 2020, *Nature*, 585, 357
- Hildebrand, R. H., Whitcomb, S. E., Winston, R., et al. 1977, *ApJ*, 216, 698
- Ho, L. C., Filippenko, A. V., & Sargent, W. L. W. 1997, *ApJS*, 112, 315
- Hodgson, J. A., Rani, B., Lee, S.-S., et al. 2018, *MNRAS*, 475, 368
- Hodgson, J. A., Rani, B., Oh, J., et al. 2021, *ApJ*, 914, 43
- Homan, D. C., Ojha, R., Wardle, J. F. C., et al. 2002, *ApJ*, 568, 99
- Hovatta, T., Lister, M. L., Aller, M. F., et al. 2012, *AJ*, 144, 105
- Hunter, J. D. 2007, *Comput. Sci. Eng.*, 9, 90
- Jorstad, S. G., Marscher, A. P., Lister, M. L., et al. 2005, *AJ*, 130, 1418
- Jorstad, S. G., Marscher, A. P., Morozova, D. A., et al. 2017, *ApJ*, 846, 98
- Karamanavis, V., Fuhrmann, L., Krichbaum, T. P., et al. 2016, *A&A*, 586, A60
- Kim, J. Y., Krichbaum, T. P., Lu, R. S., et al. 2018, *A&A*, 616, A188
- Kim, J. Y., Krichbaum, T. P., Marscher, A. P., et al. 2019, *A&A*, 622, A196
- Komissarov, S. S. 1990, *Sov. Astron. Lett.*, 16, 284
- Komissarov, S. S., Barkov, M. V., Vlahakis, N., & Königl, A. 2007, *MNRAS*, 380, 51
- Komissarov, S. S., Vlahakis, N., Königl, A., & Barkov, M. V. 2009, *MNRAS*, 394, 1182
- Krichbaum, T. P., Witzel, A., Graham, D. A., et al. 1992, *A&A*, 260, 33
- Landau, R., Jones, T. W., Epstein, E. E., et al. 1983, *ApJ*, 268, 68
- Linhoff, L., Sandrock, A., Kadler, M., Elsässer, D., & Rhode, W. 2021, *MNRAS*, 500, 4671
- Lister, M. L., Cohen, M. H., Homan, D. C., et al. 2009a, *AJ*, 138, 1874
- Lister, M. L., Aller, H. D., Aller, M. F., et al. 2009b, *AJ*, 137, 3718
- Lyubarsky, Y. 2009, *ApJ*, 698, 1570
- Martí-Vidal, I., Krichbaum, T. P., Marscher, A., et al. 2012, *A&A*, 542, A107
- McKinney, W. 2010, in *Proceedings of the 9th Python in Science Conference*, eds. S. van der Walt, & J. Millman, 56
- Mertens, F., & Lobanov, A. 2015, *A&A*, 574, A67
- Mizuno, Y. 2022, *Universe*, 8, 85
- Nagai, H., Suzuki, K., Asada, K., et al. 2010, *PASJ*, 62, L11
- Nagai, H., Orienti, M., Kino, M., et al. 2012, *MNRAS*, 423, L122
- Nagai, H., Haga, T., Giovannini, G., et al. 2014, *ApJ*, 785, 53
- Nagai, H., Chida, H., Kino, M., et al. 2016, *Astron. Nachr.*, 337, 69
- Nagai, H., Fujita, Y., Nakamura, M., et al. 2017, *ApJ*, 849, 52
- Oh, J., Hodgson, J. A., Trippie, S., et al. 2022, *MNRAS*, 509, 1024
- O'Sullivan, S. P., & Gabuzda, D. C. 2009, *MNRAS*, 400, 26
- Pandas Development Team. 2020, <https://doi.org/10.5281/zenodo.3509134>
- Paraschos, G. F., Kim, J. Y., Krichbaum, T. P., & Zensus, J. A. 2021, *A&A*, 650, L18
- Pelletier, G., & Roland, J. 1989, *A&A*, 224, 24
- Planck Collaboration XIII. 2016, *A&A*, 594, A13
- Punsly, B. 2021, *ApJ*, 918, 4
- Punsly, B., Nagai, H., Savolainen, T., & Orienti, M. 2021, *ApJ*, 911, 19
- Richards, J. L., Max-Moerbeck, W., Pavlidou, V., et al. 2011, *ApJS*, 194, 29
- Roellig, T. L., Becklin, E. E., Impey, C. D., & Werner, M. W. 1986, *ApJ*, 304, 646
- Romney, J. D., Benson, J. M., Dhawan, V., et al. 1995, *Proc. Nat. Academy Sci.*, 92, 11360
- Rybicki, G. B., & Lightman, A. P. 1979, *Radiative Processes in Astrophysics* (New York: Wiley)
- Savitzky, A., & Golay, M. J. E. 1964, *Anal. Chem.*, 36, 1627
- Savolainen, T., Wiik, K., Valtaoja, E., Jorstad, S. G., & Marscher, A. P. 2002, *A&A*, 394, 851
- Savolainen, T., Giovannini, G., Kovalev, Y. Y., et al. 2021, *A&A*, submitted [arXiv:2111.04481]
- Scharwächter, J., McGregor, P. J., Dopita, M. A., & Beck, T. L. 2013, *MNRAS*, 429, 2315
- Shepherd, M. C., Pearson, T. J., & Taylor, G. B. 1994, in *Bull. Am. Astron. Soc.*, 26, 987
- Silver, C. S., Taylor, G. B., & Vermeulen, R. C. 1998, *ApJ*, 502, 229
- Sol, H., Pelletier, G., & Asseo, E. 1989, *MNRAS*, 237, 411
- Strauss, M. A., Huchra, J. P., Davis, M., et al. 1992, *ApJS*, 83, 29
- Suzuki, K., Nagai, H., Kino, M., et al. 2012, *ApJ*, 746, 140
- Taylor, G. B., & Vermeulen, R. C. 1996, *ApJ*, 457, L69
- Tchekhovskoy, A. 2015, in *The Formation and Disruption of Black Hole Jets*, eds. I. Contopoulos, D. Gabuzda, & N. Kylafis, *Astrophys. Space Sci. Library*, 414, 45
- Tchekhovskoy, A., McKinney, J. C., & Narayan, R. 2008, *MNRAS*, 388, 551
- Venturi, T., Readhead, A. C. S., Marr, J. M., & Backer, D. C. 1993, *ApJ*, 411, 552
- Vermeulen, R. C., Readhead, A. C. S., & Backer, D. C. 1994, *ApJ*, 430, L41
- Virtanen, P., Gommers, R., Oliphant, T. E., et al. 2020, *Nat. Methods*, 17, 261
- Wajima, K., Kino, M., & Kawakatu, N. 2020, *ApJ*, 895, 35
- Walker, R. C., Romney, J. D., & Benson, J. M. 1994, *ApJ*, 430, L45
- Walker, R. C., Dhawan, V., Romney, J. D., Kellermann, K. I., & Vermeulen, R. C. 2000, *ApJ*, 530, 233
- Waskom, M. L. 2021, *J. Open Source Softw.*, 6, 3021
- Weaver, Z. R., Jorstad, S. G., Marscher, A. P., et al. 2022, *ApJS*, 260, 12

Appendix A: 43 and 86 GHz contour images

Here, we briefly describe the CC images of 3C 84 at 86 and 43 GHz. They are displayed in Figs. 1 and 2, respectively. Superimposed are circular Gaussian components used to model the flux. The features belonging to close in time epochs exhibit similar structure, which confirms our modelling. The naming convention we used is based on the observing band, plus the timestamp of the ejected feature. For example, the two features in the top left panel of Fig. 1, are labelled W2 and W1, because 86 GHz observations correspond to the W band, and W2 is upstream of W1, and therefore it was ejected first. All described motions concern the alignment centre, which is the north-westernmost feature in the VLBI core.

Appendix B: Individual feature velocity modelling

After having identified the travelling features, we used a linear fit of the following form:

$$d(t) = v_0 t + d_0, \quad (\text{B.1})$$

where $d(t)$ is the distance travelled during t , v_0 is the approximately constant velocity, and d_0 is the initial point of ejection, in order to estimate the velocities. Since the cross-identified features correspond to the same physical feature, we fitted a single

line to both 43 and 86 GHz data points, which is displayed in Fig. 3. The fit parameters are summarised in Table F.6. Here, we implicitly assumed that position deviations due to opacity shifts are negligible. We also fitted lines to the features individually per frequency. The fit was applied to the averaged feature positions, calculated from the circular Gaussian components and the CC clusters. These individual fit parameters are summarised in Tables F.7, and F.8, as well as being displayed in Fig. B.1. We used the inverse of the uncertainties squared as weights. For our conservative uncertainty estimation, we used the approach described by Eqs. (14-5) in Fomalont (1999) for the weights, or 1/5 of the beam size (commonly used as a lower limit estimate for sufficiently high S/N images, as is the case here; see e.g. Hodgson et al. 2018; Oh et al. 2022), depending on which value was greater, for the component distance and component size uncertainties. For the P. A. errors, we used the simple error propagation of the formula $\theta = 2 \cdot \arctan(\text{size}/\text{distance})$. All the aforementioned parameters, for all components, at both 43 and 86 GHz, are shown in Tables F.4 and F.5. With this careful approach, we incorporated systemic uncertainties, while also exceeding stochastic noise uncertainties. All parameters, describing the individual features, are summed up in Tables F.4 and F.5. The velocities together with their uncertainties derived from the fit are listed in Tables F.7 and F.8.

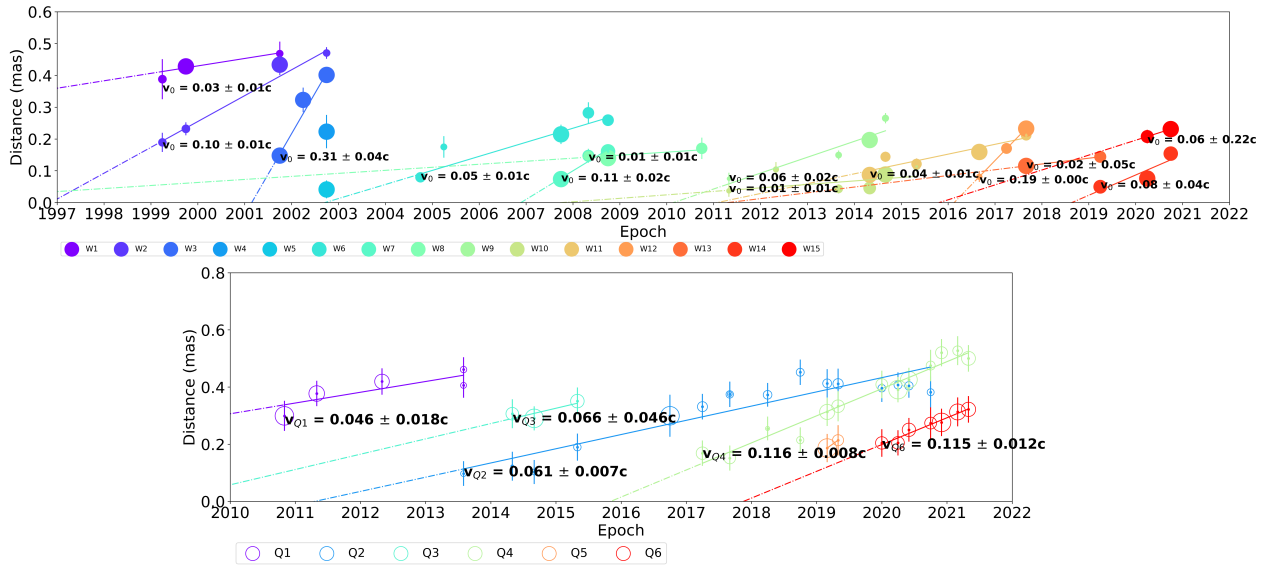


Fig. B.1. Plot of motion of all colour-coded features. *Top:* Motion of the 86 GHz features identified through all available epochs. The velocity fit with the uncertainty is displayed above the first occurrence of each feature. The size of each feature is normalised to the flux of the central feature (C) of that epoch. The velocities are also given in Table F.7. *Bottom:* Same as above, but for the 43 GHz features. The velocities are also given in Table F.8.

Appendix C: Image stacking

Below, we present the image stacking and Gaussian function fitting procedure used to create Figs. 6 and 8, in detail. Since individual VLBI images can be subjective and single epochs can suffer from sidelobes and similar related imaging issues, stacking all available epochs and analysing the time-averaged image provides the highest level of confidence for our results⁶. Before stacking the maps, we convolved each input image with a circular Gaussian beam, the size of which was computed by averaging the major and minor axes of all input images and then calculating the geometrical beam of these averaged major and minor axes. The values of the convolving beam radii are listed in Table F.9. Since all our maps were already aligned at the origin, we need not apply any further shifts prior to averaging the images. The time-averaged maps are shown in the panels of Fig. 6, with details of the contour levels and cut-offs described in the caption. We implemented three different weighting methods to ascertain which features of the images are robust. Specifically, we applied dynamical range and rms weighting of each epoch, as well as equal weighting for all epochs. The displayed images in Fig. 6 were produced with the latter method. We find that the lower frequency flux consistently envelops the higher frequency flux.

For the jet width calculation, we made slices oriented parallel to the abscissa. We chose this approach to focus on the overall bulk jet flow and disregard individual features, which cause the ridge line to deviate locally from the overall north-south flow direction. To counteract the local deviations and better compare the mean jet widths at each frequency, we performed a Savitzky-Golay filtering (Savitzky & Golay 1964) and interpolation of the data. Here, we define the ridge line as the point of maximum intensity at each slice. The minimum distance of the first slice intersection with the ridge line to the core is dictated by the beam size: anything smaller we treat as unresolved.

To extract the jet width, for the core region at 86 GHz ($z_0 < 0.75$ mas) we used a single Gaussian function of the following form:

$$G_{\text{tot}}(x; A, \mu, \sigma) = A \exp\left(\frac{-(x - \mu)^2}{2\sigma^2}\right), \quad (\text{C.1})$$

where $G_{\text{tot}}(x)$ is the Gaussian function at the position x , A is the amplitude, μ is the mean value, and σ is the variance from which the FWHM of the slices transversely drawn to the bulk jet flow are calculated. For the 15 and 43 GHz observations, as well as further downstream for the 86 GHz observations, we used a sum of two Gaussian functions, $G_{\text{tot}} = G_{\text{bright}} + G_{\text{faint}}$, and considered the FWHM of the brighter Gaussian G_{bright} . We calculated the deconvolved FWHM denoted as θ using the following equation:

$$\theta = \sqrt{\text{FWHM}^2 - \text{beam}^2}. \quad (\text{C.2})$$

Figure C.1 displays the 15, 43, and 86 GHz jet profile at representative distances from the VLBI core.

For data weighting, we used the rms from the averaged maps. The uncertainty budget of the fit $\delta\theta$ consists of three parts: (i) the uncertainty of the FWHM (δFWHM) of the slice for which we used the Fomalont (1999) description; (ii) the uncertainty of the fit (δfit); and (iii) an uncertainty introduced by the convolution beam (δbeam) (assumed to be 1/5 of its radius). We added them in quadrature: $\delta\theta = \sqrt{\delta\text{FWHM}^2 + \delta\text{fit}^2 + \delta\text{beam}^2}$.

We characterised the dependence of the jet width as function of core separation using a power law of the following form:

$$w(z_0) = c_1 z_0^\gamma, \quad (\text{C.3})$$

where $w(z_0)$ is the width at distance z_0 from the core, c_1 is a multiplicative constant, and γ is the power-law index describing the jet expansion, with the results showcased in Fig. 8. In Table F.12, we summarise the power-law index for each frequency.

Having obtained the deconvolved bulk jet flow width, we fitted a power law of the following form:

$$w(z_0) = c_1 z_0^\gamma, \quad (\text{C.4})$$

where $w(z_0)$ is the width at distance z_0 from the core, c_1 is a multiplicative constant, and γ is the power-law index describing the widening rate of the jet, with the results given in Fig. 8. The power-law index per frequency is displayed in Table F.12.

⁶ We considered all available epochs up to October 2020 for the 43 GHz observations, to match the time frame imposed by the 86 GHz data availability.

G. F. Paraschos et al.: Jet kinematics in the transversely stratified jet

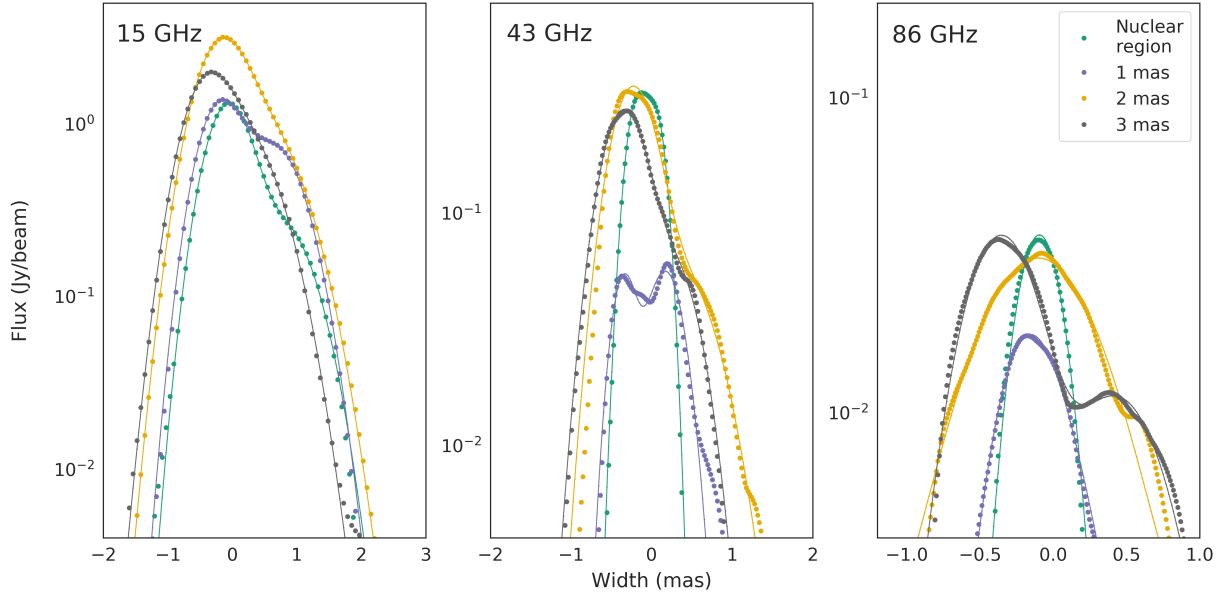


Fig. C.1. Representative transverse jet profiles (dots) and single and double Gaussian function fits (continuous lines) at 15, 43, and 86 GHz. Different colours represent slices in the nuclear region ($z_0 = 0.6$ mas at 15 GHz; $z_0 = 0.4$ mas at 43 and 86 GHz) and at separations of $z_0 = 1$ mas, 2 mas, and 3 mas from the core, with the colour-coding as displayed in the figure legend.

Appendix D: Spectral index uncertainty

Figure D.1 provides the spectral index uncertainty maps of the individual epochs. The uncertainty in each map can be separated into two parts: the uncertainty in the spectral index gradient P. A. and the uncertainty of the absolute values of the spectral index. The latter exists because the 86 GHz VLBI flux measurements are constantly lower than the flux measured with single-dish telescopes, as the small VLBI beam resolves out much of the diffuse flux. Thus, the flux at 86 GHz needs to be scaled up. Finally, there is some uncertainty in the registration of the phase centre of each epoch (i.e. the location of the core feature C). Paraschos et al. (2021) showed that this uncertainty is less than the pixel scale and can therefore be neglected.

We followed the procedure described in the appendix of Kim et al. (2019) to find the scaling factor g and its uncertainty δg per epoch. The spectral index is defined as

$$\alpha = \frac{\log\left(\frac{S_{43}}{gS_{86}}\right)}{\log\left(\frac{\nu_{43}}{\nu_{86}}\right)}, \quad (\text{D.1})$$

where (ν_{43}, S_{43}) and (ν_{86}, S_{86}) are the frequency and flux at 43 and 86 GHz, respectively. We then calculated the spectral index uncertainty through standard error propagation, taking into account the uncertainties from the fluxes (δS_{43} , and δS_{86}) and from the scaling factor (δg). The resulting maps exhibit values between $\alpha^{43-86} \sim 0.1 - 0.7$, except for the May 2014 and September 2014 observations, where the uncertainty rises to $\alpha^{43-86} \sim 1.0 - 1.2$.

For the estimation of the robustness of the P. A. of the spectral index gradient to the change from north-south to northwest-southeast, we shifted the October 2020 map in both x and y axes and studied the directionality of the spectral index gradient. In the currently displayed image, the P. A. of the shift between the 43 and 86 GHz image is P.A. $\approx 68^\circ$. We found that in order to produce a north-south-oriented spectral index, we needed to shift the same two images by P.A. $\approx 21^\circ$, which is a significant offset. We can thus conclude, that the orientation of the spectral index gradient is robust.

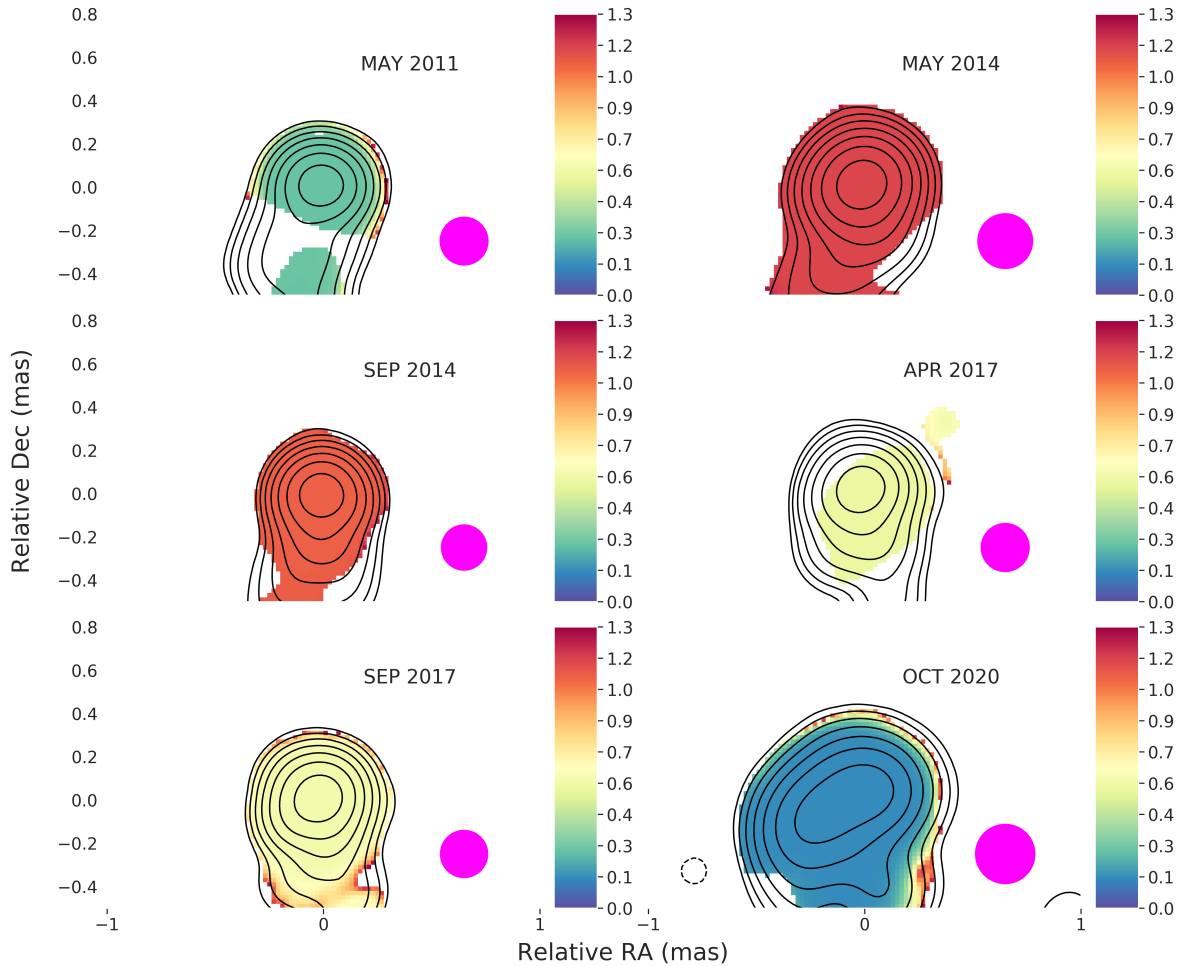


Fig. D.1. Individual spectral index error maps of 3C 84 between 43 and 86 GHz for the same selected epochs as in Fig. 7. The same contour levels and beam sizes were applied. A summary of the image parameters is presented in Table F.10. The procedure to determine the uncertainties is described in Appendix D.

Appendix E: Time binning

Figure F.1 displays two different time binning methods of the epochs presented in Fig. 1. The top four panels show a six-year bin, whereas the bottom two ones show an approximately ten-year bin. In the six-year binned images, we can recognise the swinging of the P. A. of the southern jet. In the first bin, the bulk of the jet flow follow a southwest trajectory. In the second bin, we find a purely southern flow. The third bin is less conclusive, although a tendency towards a southeast trajectory can be recognised, which is then confirmed in the last bin. We can conclude that the period swing is approximately six years, which agrees well with the estimate of five to ten years found by Punsly et al. (2021). On the other hand, in the ten year bin, this behaviour is less pronounced. One conclusion we can draw from the ten-year time bins is that the jet has expanded towards the south, from ~ 1.5 mas to ~ 3.5 mas.

Zooming in on the core region in Fig. F.1, the east-west elongation seems absent in the first time bin and can only be tentatively detected in second time bin. Then, it features more prominently in the third and fourth bins. Moving further south to the 0.5 – 1.5 mas region, the jet seems ridge brightened, before turning limb brightened in the mid 2000s. This is in line with the previous work by other authors at lower frequencies (e.g. Walker et al. 2000; Nagai et al. 2014 at 22 and 43 GHz).

Appendix F: Parameter tables

In this section, we present all the tables mentioned in the main text. Table F.1 displays the 86 GHz epoch, synthesised beam size of the array, pixel scale of the images created, as well as the total intensity maximum in Jy/beam. Accordingly, Table F.2 and Table F.3 refer to the same parameters for the 43 and 15 GHz epochs. Homan et al. (2002) estimated a flux uncertainty of the order of 5% to 10% for individual features in 22 GHz images, and Punsly (2021) estimated 10% for 43 GHz images. Our approach is to be conservative with our error estimation;

therefore, we factor in a 20% uncertainty for all our epochs at each frequency. It should be noted here that the GMVA is known to suffer from large uncertainties in the flux density. A visibility scaling method is introduced by Kim et al. (2019), culminating in an up-scaling factor of the order two. Our analysis is independent of the absolute flux densities, and thus we opted not to apply this correction. The reader should therefore keep in mind that the various GMVA fluxes reported in this study might be underestimated by a factor of ~ 2 .

Tables F.4 and F.5 summarise all the moving features we identified at 86 and 43 GHz, respectively. The first column denotes the individual feature ID. The second column is the observing epoch; column three denotes the flux of the fit feature. The final three columns correspond in sequence to the distance and the P. A. between each feature and the core, and the size of the feature, defined as the width of the feature.

Table F.6 contains a list of the IDs and velocities of the cross-identified features. For these cross-identified features, we estimate the error for the ejection year to be ± 6 months, which is set by the average cadence of available 86 GHz epochs. Tables F.7 and F.8 display the feature IDs and corresponding interpolated velocity at 86 and 43 GHz, respectively. Components ‘W4’, ‘W5’, and ‘W13’ were only identified in one epoch and we therefore could not derive a velocity estimate. For the individual features, we impose a 5σ uncertainty (with $1\sigma = 0.5$ years, from the cross-identified features), and thus conservatively estimate the error for the ejection year to be ± 2.5 years. A description of the fitting method and error estimation is offered in Appendix B.

Table F.9 displays the circular convolving beam used to produce the stacked images of Fig. 6, per frequency. The last two columns correspond to the intensity peak of the stacked image and the rms error. Similarly, Table F.11 displays the parameters associated with Fig. F.1.

Finally, Table F.12 displays the power-law indices per frequency. The fitting procedure and error estimation is explained in Appendix C.

A&A 665, A1 (2022)

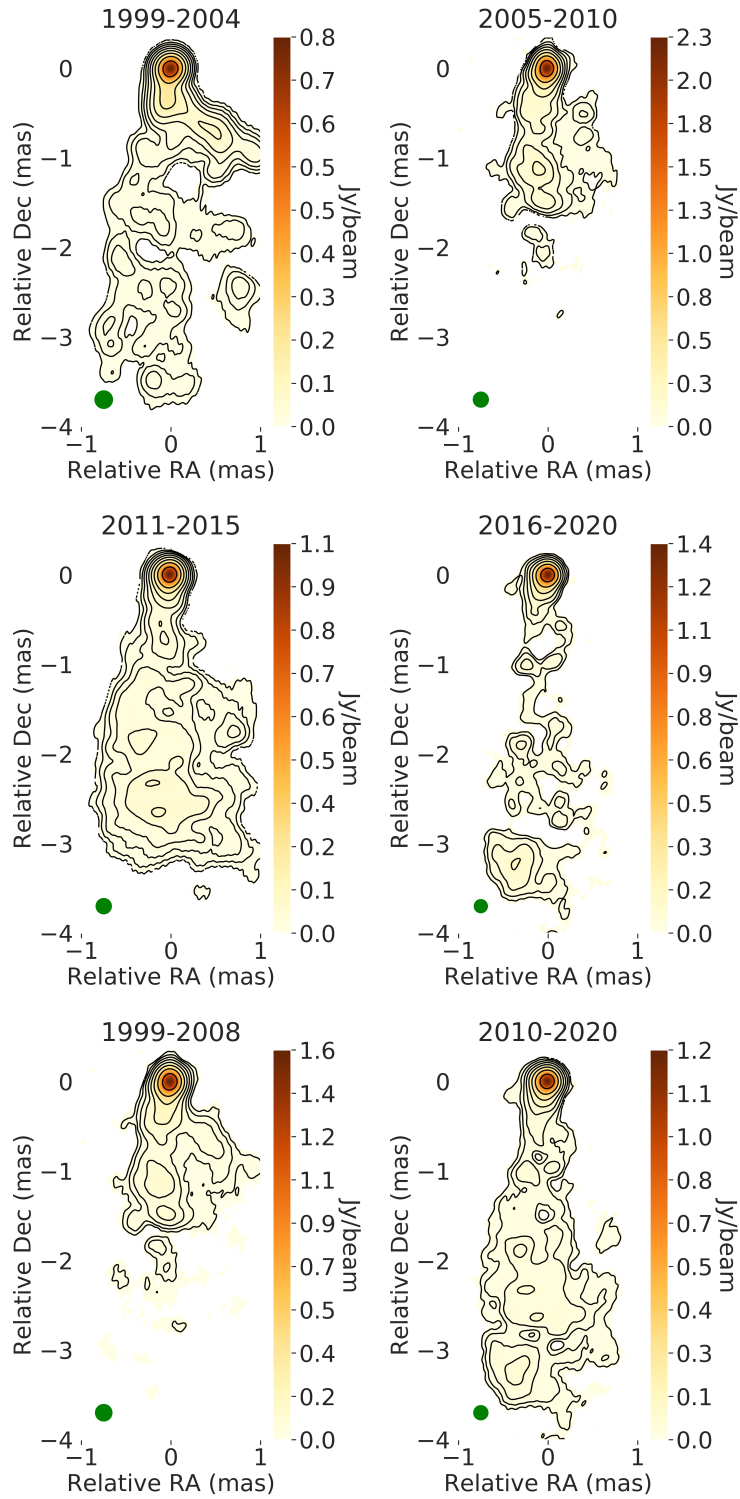


Fig. F.1. Full showcase of stacked images of 3C 84 at 86 GHz, with different time bins. The title of each panel indicates the time bin used. The same procedure was followed to produce the panels, as described in the caption of Fig. 6. All image parameters are summarised in Table F.11

5 PAPER 3: JET KINEMATICS IN THE TRANSVERSELY STRATIFIED JET OF 3C 84: A TWO-DECADE OVERVIEW

G. F. Paraschos et al.: Jet kinematics in the transversely stratified jet

Table F.1. Summary of image parameters at 86 GHz.

Epoch	Beam size (mas)	Beam orientation (deg)	Pixel scale (mas/pixel)	S_{\max} (Jy/beam)	rms_{mean} (mJy/beam)
1999.25	0.16×0.07	-7.29°	0.01	0.69 ± 0.14	0.69
1999.75	0.16×0.06	-12.08°	0.01	0.84 ± 0.17	0.01
2001.75	0.21×0.04	-9.46°	0.01	0.47 ± 0.09	0.75
2002.25	0.31×0.06	-3.74°	0.01	0.48 ± 0.10	0.63
2002.75	0.23×0.04	-20.62°	0.01	0.27 ± 0.05	0.26
2004.75	0.14×0.04	-10.58°	0.01	0.52 ± 0.10	0.87
2005.25	0.11×0.04	-3.11°	0.01	0.42 ± 0.08	0.84
2007.33	0.10×0.04	-3.89°	0.01	1.01 ± 0.20	1.21
2007.75	0.12×0.04	-2.48°	0.01	2.06 ± 0.41	2.85
2008.33	0.12×0.04	-15.53°	0.01	0.78 ± 0.16	1.30
2008.75	0.14×0.05	-25.49°	0.01	4.08 ± 0.82	10.22
2010.75	0.09×0.09	0.00°	0.01	0.52 ± 0.10	0.88
2011.33	0.15×0.06	-16.89°	0.01	0.25 ± 0.05	0.63
2012.33	0.16×0.08	-2.46°	0.01	0.31 ± 0.06	0.52
2013.67	0.12×0.04	-11.03°	0.01	0.30 ± 0.06	0.58
2014.33	0.11×0.04	-11.06°	0.01	1.20 ± 0.24	0.48
2014.67	0.19×0.03	-20.88°	0.01	0.50 ± 0.10	1.45
2015.33	0.14×0.05	-13.81°	0.01	0.65 ± 0.13	0.85
2016.67	0.17×0.04	-21.96°	0.01	0.63 ± 0.13	0.25
2017.25	0.10×0.04	-13.30°	0.01	0.25 ± 0.05	0.16
2017.67	0.11×0.05	-24.02°	0.01	2.87 ± 0.57	9.03
2019.25	0.15×0.04	-29.45°	0.01	0.67 ± 0.13	1.21
2020.25	0.11×0.05	-16.07°	0.01	0.54 ± 0.11	3.16
2020.75	0.15×0.04	-7.89°	0.01	0.35 ± 0.07	0.66

Table F.2. Summary of image parameters at 43 GHz.

Epoch	Beam size (mas)	Beam orientation (deg)	Pixel scale (mas/pixel)	S_{\max} (Jy/beam)	rms_{mean} (mJy/beam)
2010.83	0.45×0.15	-22.70°	0.02	2.20 ± 0.44	0.85
2011.33	0.35×0.14	8.69°	0.02	1.92 ± 0.38	0.32
2012.33	0.36×0.15	16.47°	0.02	2.13 ± 0.43	0.58
2013.58	0.31×0.15	-3.40°	0.02	1.90 ± 0.38	0.19
2014.33	0.40×0.16	16.26°	0.02	3.43 ± 0.69	0.28
2014.67	0.34×0.13	-1.14°	0.02	3.20 ± 0.64	0.20
2015.33	0.29×0.20	-4.05°	0.02	3.93 ± 0.79	0.42
2016.75	0.52×0.26	23.41°	0.02	7.81 ± 1.56	2.22
2017.25	0.33×0.15	1.75°	0.02	3.47 ± 0.69	0.72
2017.67	0.34×0.14	8.37°	0.02	3.34 ± 0.67	0.44
2018.25	0.28×0.15	-6.95°	0.02	2.47 ± 0.49	1.02
2018.75	0.31×0.16	6.05°	0.02	3.53 ± 0.71	1.15
2019.16	0.35×0.18	7.39°	0.02	2.51 ± 0.50	0.90
2019.33	0.41×0.17	-12.05°	0.02	2.40 ± 0.48	0.87
2020.00	0.35×0.17	-2.33°	0.02	1.73 ± 0.35	0.30
2020.25	0.33×0.15	3.25°	0.02	2.24 ± 0.45	0.37
2020.42	0.28×0.16	11.05°	0.02	1.71 ± 0.34	0.58
2020.75	0.44×0.17	4.61°	0.02	1.81 ± 0.36	0.40
2020.92	0.36×0.16	7.71°	0.02	1.89 ± 0.38	0.59
2021.16	0.36×0.18	12.62°	0.02	1.59 ± 0.32	1.45
2021.33	0.29×0.19	-16.99°	0.02	2.08 ± 0.42	1.03

5 PAPER 3: JET KINEMATICS IN THE TRANSVERSELY STRATIFIED JET OF 3C 84: A TWO-DECADE OVERVIEW

A&A 665, A1 (2022)

Table F.3. Summary of image parameters at 15 GHz.

Epoch	Beam size (mas)	Beam orientation (deg)	Pixel scale (mas/pixel)	S_{\max} (Jy/beam)	rms_{mean} (mJy/beam)
2010.58	0.69×0.47	-11.98°	0.03	4.9 ± 0.98	1.64
2011.41	0.66×0.49	-12.79°	0.03	4.7 ± 0.94	1.33
2012.16	0.91×0.56	25.77°	0.03	8.99 ± 1.8	1.34
2013.50	0.72×0.55	-57.56°	0.03	7.39 ± 1.48	0.91
2014.50	0.64×0.38	-7.82°	0.03	6.74 ± 1.35	0.65
2015.41	0.64×0.44	-28.44°	0.03	4.05 ± 0.81	0.96
2016.42	0.64×0.36	-7.52°	0.03	8.19 ± 1.64	0.67
2017.25	0.61×0.38	-11.74°	0.03	5.15 ± 1.03	0.67
2018.50	0.7×0.39	-8.97°	0.03	3.74 ± 0.75	0.97
2019.41	0.86×0.46	-24.84°	0.03	5.22 ± 1.04	0.75
2020.50	0.67×0.37	-4.10°	0.03	3.47 ± 0.69	0.81

Table F.4. Physical parameters of each model feature at 43 GHz.

ID	Epoch	Flux Density (Jy/beam)	Distance (mas)	P. A. (deg)	Size (mas)
Q1	2010.83	2.29 ± 0.46	0.33 ± 0.05	151.28 ± 13.15	0.17 ± 0.03
Q1	2011.33	1.61 ± 0.32	0.37 ± 0.04	161.39 ± 10.89	0.23 ± 0.02
Q1	2012.33	1.42 ± 0.28	0.42 ± 0.05	170.78 ± 12.28	0.35 ± 0.02
Q1	2013.58	0.23 ± 0.17	0.41 ± 0.04	-176.01 ± 7.29	0.13 ± 0.02
Q1	2013.58	0.27 ± 0.21	0.47 ± 0.04	154.38 ± 5.72	0.10 ± 0.02
Q2	2013.58	0.25 ± 0.05	0.10 ± 0.04	107.37 ± 39.05	0.06 ± 0.02
Q2	2014.33	0.06 ± 0.01	0.12 ± 0.05	141.03 ± 37.77	0.08 ± 0.03
Q2	2014.67	0.24 ± 0.05	0.12 ± 0.04	152.29 ± 39.77	0.09 ± 0.02
Q2	2015.33	0.41 ± 0.08	0.19 ± 0.05	154.31 ± 19.64	0.09 ± 0.02
Q2	2016.75	2.55 ± 1.91	0.29 ± 0.16	-172.28 ± 75.31	0.32 ± 0.08
Q2	2017.25	0.74 ± 0.15	0.33 ± 0.04	-165.23 ± 10.39	0.15 ± 0.02
Q2	2017.67	0.41 ± 0.08	0.37 ± 0.04	-166.32 ± 7.82	0.11 ± 0.02
Q2	2017.67	0.17 ± 0.03	0.38 ± 0.04	160.18 ± 9.78	0.20 ± 0.02
Q2	2018.25	0.55 ± 0.11	0.37 ± 0.04	-170.32 ± 10.06	0.23 ± 0.02
Q2	2018.75	0.47 ± 0.09	0.44 ± 0.04	-161.40 ± 7.31	0.17 ± 0.02
Q2	2019.16	0.58 ± 0.12	0.40 ± 0.05	-170.28 ± 10.08	0.20 ± 0.03
Q2	2019.33	0.78 ± 0.16	0.42 ± 0.05	-172.00 ± 11.45	0.26 ± 0.03
Q2	2020.00	0.43 ± 0.09	0.40 ± 0.05	-176.60 ± 9.88	0.20 ± 0.02
Q2	2020.25	0.47 ± 0.09	0.41 ± 0.04	-174.63 ± 6.59	0.07 ± 0.02
Q2	2020.42	0.52 ± 0.10	0.40 ± 0.04	-177.43 ± 6.88	0.12 ± 0.02
Q2	2020.75	0.36 ± 0.07	0.38 ± 0.06	-178.46 ± 11.11	0.17 ± 0.03
Q3	2014.33	0.50 ± 0.10	0.31 ± 0.05	163.50 ± 20.34	0.29 ± 0.03
Q3	2014.67	1.08 ± 0.81	0.29 ± 0.04	177.71 ± 12.79	0.17 ± 0.02
Q3	2015.33	0.57 ± 0.11	0.35 ± 0.05	-162.78 ± 11.54	0.19 ± 0.02
Q4	2017.25	0.68 ± 0.14	0.17 ± 0.04	136.26 ± 20.97	0.08 ± 0.02
Q4	2017.67	0.58 ± 0.12	0.16 ± 0.04	125.81 ± 21.33	0.08 ± 0.02
Q4	2018.25	0.08 ± 0.02	0.25 ± 0.04	125.67 ± 12.58	0.12 ± 0.02
Q4	2018.75	0.23 ± 0.05	0.21 ± 0.04	106.07 ± 23.73	0.18 ± 0.02
Q4	2019.16	0.99 ± 0.20	0.31 ± 0.05	138.69 ± 12.45	0.15 ± 0.03
Q4	2019.33	0.69 ± 0.14	0.34 ± 0.05	140.35 ± 10.65	0.11 ± 0.03
Q4	2020.00	0.60 ± 0.12	0.41 ± 0.05	142.80 ± 7.26	0.09 ± 0.02
Q4	2020.25	1.50 ± 1.12	0.38 ± 0.04	143.21 ± 8.19	0.13 ± 0.02
Q4	2020.42	1.22 ± 0.91	0.43 ± 0.04	145.06 ± 7.42	0.18 ± 0.02
Q4	2020.75	0.35 ± 0.07	0.49 ± 0.06	153.65 ± 7.26	0.13 ± 0.03
Q4	2020.92	0.62 ± 0.12	0.52 ± 0.05	131.26 ± 5.29	0.02 ± 0.02
Q4	2021.16	0.40 ± 0.08	0.55 ± 0.05	129.77 ± 5.68	0.11 ± 0.03
Q4	2021.33	0.83 ± 0.17	0.50 ± 0.05	124.54 ± 5.37	0.03 ± 0.02
Q5	2019.16	1.13 ± 0.85	0.19 ± 0.05	90.36 ± 18.47	0.06 ± 0.03
Q5	2019.33	0.40 ± 0.08	0.21 ± 0.05	98.63 ± 17.98	0.09 ± 0.03
Q6	2020.00	1.70 ± 0.34	0.21 ± 0.05	107.76 ± 19.15	0.11 ± 0.02
Q6	2020.25	1.76 ± 0.35	0.21 ± 0.04	106.71 ± 14.60	0.07 ± 0.02
Q6	2020.42	1.96 ± 0.39	0.25 ± 0.04	111.53 ± 12.84	0.11 ± 0.02

5 PAPER 3: JET KINEMATICS IN THE TRANSVERSELY STRATIFIED JET OF 3C 84: A TWO-DECADE OVERVIEW

G. F. Paraschos et al.: Jet kinematics in the transversely stratified jet

Table F.4. continued.

ID	Epoch	Flux Density (Jy/beam)	Distance (mas)	P. A. (deg)	Size (mas)
Q6	2020.75	1.54 ± 0.31	0.27 ± 0.06	114.92 ± 13.57	0.09 ± 0.03
Q6	2020.92	3.78 ± 0.76	0.28 ± 0.05	112.53 ± 19.62	0.24 ± 0.02
Q6	2021.16	2.80 ± 0.56	0.32 ± 0.05	113.74 ± 16.76	0.24 ± 0.03
Q6	2021.33	2.24 ± 0.45	0.31 ± 0.05	110.00 ± 11.85	0.14 ± 0.02

Table F.5. Physical parameters of each model feature at 86 GHz.

ID	Epoch	Flux Density (Jy/beam)	Distance (mas)	P. A. (deg)	Size (mas)
W1	1999.25	0.11 ± 0.02	0.38 ± 0.19	-163.48 ± 39.86	0.19 ± 0.09
W1	1999.75	0.42 ± 0.08	0.42 ± 0.07	-164.85 ± 10.54	0.07 ± 0.04
W1	2001.75	0.08 ± 0.02	0.47 ± 0.07	-164.83 ± 9.04	0.07 ± 0.04
W2	1999.25	0.12 ± 0.02	0.19 ± 0.12	160.03 ± 55.28	0.12 ± 0.06
W2	1999.75	0.12 ± 0.02	0.23 ± 0.07	171.15 ± 19.63	0.07 ± 0.03
W2	2001.75	0.49 ± 0.10	0.43 ± 0.13	170.32 ± 20.47	0.13 ± 0.07
W2	2002.75	0.09 ± 0.02	0.47 ± 0.04	163.98 ± 4.68	0.04 ± 0.02
W3	2001.75	0.25 ± 0.05	0.15 ± 0.04	176.11 ± 16.78	0.04 ± 0.02
W3	2002.25	0.24 ± 0.05	0.31 ± 0.12	178.72 ± 26.71	0.12 ± 0.06
W3	2002.75	0.25 ± 0.05	0.39 ± 0.06	175.11 ± 9.05	0.06 ± 0.03
W4	2002.75	0.07 ± 0.01	0.22 ± 0.05	164.33 ± 15.35	0.05 ± 0.03
W5	2002.75	0.26 ± 0.05	0.04 ± 0.03	-160.75 ± 62.06	0.03 ± 0.01
W6	2004.75	0.56 ± 0.11	0.07 ± 0.05	116.79 ± 65.90	0.05 ± 0.03
W6	2005.25	0.23 ± 0.05	0.18 ± 0.17	155.33 ± 118.69	0.17 ± 0.09
W6	2007.75	1.46 ± 0.29	0.20 ± 0.15	172.03 ± 77.76	0.15 ± 0.07
W6	2008.33	0.71 ± 0.14	0.28 ± 0.16	158.93 ± 49.09	0.16 ± 0.08
W6	2008.75	0.72 ± 0.14	0.26 ± 0.07	156.89 ± 17.74	0.07 ± 0.04
W7	2007.75	0.70 ± 0.14	0.07 ± 0.02	169.50 ± 17.13	0.02 ± 0.01
W7	2008.33	0.36 ± 0.07	0.16 ± 0.06	144.20 ± 26.67	0.06 ± 0.03
W7	2008.75	0.54 ± 0.11	0.17 ± 0.04	119.22 ± 15.17	0.04 ± 0.02
W8	2008.33	0.37 ± 0.07	0.13 ± 0.04	179.03 ± 20.07	0.04 ± 0.02
W8	2008.75	1.09 ± 0.22	0.14 ± 0.03	154.30 ± 11.76	0.03 ± 0.01
W8	2010.75	0.51 ± 0.10	0.20 ± 0.10	-175.97 ± 39.25	0.10 ± 0.05
W9	2011.33	0.02 ± 0.00	0.08 ± 0.02	157.51 ± 16.56	0.02 ± 0.01
W9	2013.67	0.05 ± 0.01	0.15 ± 0.01	-179.69 ± 6.64	0.05 ± 0.01
W9	2014.33	0.36 ± 0.07	0.20 ± 0.01	168.14 ± 4.26	0.05 ± 0.01
W9	2014.67	0.06 ± 0.01	0.27 ± 0.02	176.51 ± 3.86	0.06 ± 0.01
W10	2011.33	0.10 ± 0.02	0.04 ± 0.02	95.73 ± 71.27	0.05 ± 0.01
W10	2012.33	0.13 ± 0.03	0.10 ± 0.02	95.46 ± 20.38	0.06 ± 0.01
W10	2013.67	0.27 ± 0.05	0.04 ± 0.01	79.48 ± 39.22	0.04 ± 0.01
W10	2014.33	0.61 ± 0.12	0.05 ± 0.01	74.04 ± 23.92	0.02 ± 0.01
W10	2014.67	1.04 ± 0.21	0.09 ± 0.02	87.86 ± 17.78	0.06 ± 0.01
W10	2015.33	0.23 ± 0.05	0.12 ± 0.02	96.81 ± 11.30	0.05 ± 0.01
W11	2014.33	1.15 ± 0.23	0.08 ± 0.01	165.62 ± 15.53	0.06 ± 0.01
W11	2014.67	0.44 ± 0.09	0.15 ± 0.02	141.40 ± 11.26	0.11 ± 0.01
W11	2015.33	0.47 ± 0.09	0.15 ± 0.02	157.32 ± 14.09	0.13 ± 0.01
W11	2016.67	1.21 ± 0.24	0.16 ± 0.02	164.22 ± 11.06	0.14 ± 0.01
W11	2017.67	0.48 ± 0.10	0.21 ± 0.02	175.87 ± 5.37	0.09 ± 0.01
W12	2016.67	0.02 ± 0.00	0.08 ± 0.02	133.28 ± 18.83	0.05 ± 0.01
W12	2017.25	0.07 ± 0.01	0.17 ± 0.01	151.50 ± 5.73	0.07 ± 0.01
W12	2017.67	0.18 ± 0.04	0.23 ± 0.02	142.48 ± 4.36	0.07 ± 0.01
W13	2017.67	1.26 ± 0.25	0.12 ± 0.02	92.64 ± 11.13	0.07 ± 0.01
W13	2019.25	0.66 ± 0.13	0.14 ± 0.02	154.19 ± 8.46	0.07 ± 0.01
W14	2019.25	0.43 ± 0.09	0.05 ± 0.02	30.50 ± 28.16	0.03 ± 0.01
W14	2020.25	0.62 ± 0.12	0.07 ± 0.01	84.37 ± 13.39	0.03 ± 0.01
W14	2020.75	0.48 ± 0.10	0.16 ± 0.01	74.03 ± 7.11	0.07 ± 0.01
W15	2020.25	0.06 ± 0.01	0.21 ± 0.01	170.47 ± 4.12	0.04 ± 0.01
W15	2020.75	0.10 ± 0.02	0.23 ± 0.01	164.54 ± 3.79	0.04 ± 0.01

5 PAPER 3: JET KINEMATICS IN THE TRANSVERSELY STRATIFIED JET OF 3C 84: A TWO-DECADE OVERVIEW

A&A 665, A1 (2022)

Table F.6. Combined feature velocity and ejection date of cross-identified features.

ID	ID ₄₃	ID ₈₆	Ejection date	Velocity (c)
F1	Q1	W6	2001.96 ± 0.5	0.047 ± 0.004
F2	Q2	W9	2003.50 ± 0.5	0.034 ± 0.004
F3	Q3	W8	2011.79 ± 0.5	0.066 ± 0.005
F4	Q4	W12	2015.86 ± 0.5	0.117 ± 0.007
F5	Q6	W15	2017.88 ± 0.5	0.115 ± 0.010

Table F.7. Component velocity and ejection date at 86 GHz.

ID	Ejection date (year)	Velocity (c)
W1	1981.63 ± 2.5	0.029 ± 0.011
W2	1996.86 ± 2.5	0.100 ± 0.008
W3	2001.15 ± 2.5	0.312 ± 0.039
W4	–	–
W5	–	–
W6	2002.72 ± 2.5	0.054 ± 0.008
W7	2006.89 ± 2.5	0.110 ± 0.024
W8	1993.38 ± 2.5	0.012 ± 0.010
W9	2010.15 ± 2.5	0.061 ± 0.020
W10	2007.79 ± 2.5	0.013 ± 0.013
W11	2011.08 ± 2.5	0.038 ± 0.010
W12	2016.13 ± 2.5	0.186 ± 0.002
W13	–	–
W14	2018.64 ± 2.5	0.078 ± 0.042
W15	–	–

Table F.8. Component velocity and ejection date at 43 GHz.

ID	Ejection date (year)	Velocity (c)
Q1	2001.87 ± 2.5	0.05 ± 0.02
Q2	2011.30 ± 2.5	0.06 ± 0.01
Q3	2008.92 ± 2.5	0.07 ± 0.05
Q4	2015.84 ± 2.5	0.12 ± 0.01
Q5	–	–
Q6	2017.88 ± 2.5	0.11 ± 0.01

Table F.9. Summary of image parameters for the stacked images.

Frequency (GHz)	Beam radius (mas)	Pixel scale (mas/pixel)	S _{max} (Jy/beam)	rms (mJy/beam)
15.4	0.56	0.03	3.18 ± 0.64	0.45
43.1	0.24	0.02	3.02 ± 0.60	0.24
86.3	0.08	0.01	0.75 ± 0.15	0.77

5 PAPER 3: JET KINEMATICS IN THE TRANSVERSELY STRATIFIED JET OF 3C 84: A TWO-DECADE OVERVIEW

G. F. Paraschos et al.: Jet kinematics in the transversely stratified jet

Table F.10. Summary of image parameters of the spectral index maps.

Epoch	Beam radius (mas)	Pixel scale (mas/pixel)
Stacked	0.24	0.02
2011.33	0.22	0.02
2014.33	0.25	0.02
2014.67	0.21	0.02
2017.25	0.22	0.02
2017.67	0.22	0.02
2020.75	0.28	0.02

Table F.11. Summary of image parameters of the time binned stacked images.

Time bin (years)	Beam radius (mas)	Pixel scale (mas/pixel)	S_{\max} (Jy/beam)	rms (mJy/beam)
1999-2004	0.20	0.01	0.81 ± 0.16	0.25
2005-2010	0.17	0.01	2.31 ± 0.46	1.82
2011-2015	0.17	0.01	1.06 ± 0.21	0.33
2016-2020	0.15	0.01	1.38 ± 0.28	1.61
1999-2008	0.19	0.01	1.60 ± 0.32	0.92
2010-2020	0.16	0.01	1.23 ± 0.25	0.83

Table F.12. Power-law fit parameters for the stacked images per frequency.

Frequency (GHz)	Power law index
15.4	0.36 ± 0.38
43.1	0.27 ± 0.13
86.3	0.90 ± 0.06

6 Conclusions

The focus of this thesis is to address a number of open questions related to AGN-launched jets. To achieve this scientific goal, one must study the jet launching processes around a SMBH in nearby AGN. Only a handful of extra-galactic sources fulfil the requirements necessary to successfully research jet launching. The main requirements rendering a radio-source suitable for such a study is the mass of the central SMBH, which should be as large as possible (a larger mass corresponds to fewer Schwarzschild radii per pc); the distance to Earth, which should be as small as possible; and the viewing angle, which should also be as slight as possible, to avoid strong Doppler boosting effects.

3C 84 is perfectly suited for such a study, as it fulfils all three major requirements, and as such, was chosen to be the primary target of this thesis. VLBI observations of the source, both at centimetre and millimetre wavelengths, are the primary means of penetrating the otherwise opaque medium around the SMBH and resolving the ultimate vicinity around it. They were thus utilised in the present thesis. Below the main conclusions of the three projects constituting this thesis are presented, aimed at achieving this common goal.

In Sect. 3 we presented our work, which revolved around the nuclear region of 3C 84, by taking advantage of quasi-simultaneous observations of the source (at 15, 43, and 86 GHz), taken in May of 2015 (Kim et al. 2019). Using the technique of two-dimensional cross-correlation, we aligned the images of 3C 84 at these three frequencies, and determined the core shift (i.e. the distance of the jet apex to the 86 GHz VLBI core). Byproducts of this analysis are the spectral index maps between the 15 – 43 and 43 – 86 GHz pairs, as well as the computation of the magnetic field. The 2D cross-correlation analysis yielded a distance of $76 - 90 \mu\text{as}$ ($400 - 1500$ Schwarzschild radii or $0.028 - 0.11$ pc) between the 86 GHz VLBI core and the jet apex. This core shift analysis places the location of the BH further upstream, rendering the previously seen elongated VLBI core structure (Giovannini et al. 2018) less probable to be the actual physical origin of the jet. A location this north would also put a constraint on the apparent jet opening angle, confining it to smaller values ($< 21^\circ$) than the 130° reported in Giovannini et al. (2018). In the new spectral index images, we detected a strong spectral index gradient in the northwest-southeast direction with an inverted spectrum of the millimetre-VLBI core ($\alpha_{43-86} \sim +2$). This indicates the presence of strong synchrotron self-absorption or free-free absorption by some matter in the foreground. For a synchrotron turnover frequency of $\nu_m \leq 86$ GHz, 3C 84 would present itself as a highly suitable target for higher frequency VLBI studies (e.g. with the Event Horizon Telescope;

Event Horizon Telescope Collaboration et al. 2019b). Calculating the magnetic field strength and topology at the jet apex (at a de-projected distance of $400 - 1500 R_s$ or $76 - 90 \mu\text{as}$) is of major importance to make a statement about the potential jet launching scenarios, in addition to comparing 3C 84 to other prominent AGN sources. We find that the magnetic field topology is not purely poloidal; rather a mixed poloidal/toroidal configuration is put forth. This suggests a stratified combination of the BP and BZ models (acting simultaneously). Another possibility is the alteration of the initial magnetic field configuration caused by shocks and instabilities. The actual magnetic field strength was measured in the range $B_0 = 1.80 - 4.0 \text{ G}$ at the jet apex, which is lower than the maximum possible magnetic field strength derived from the total jet power (which is $\lesssim 30 - 60 \text{ G}$). The derived value of the magnetic field strength is on par with the one measured in M 87 and NGC 1052, two comparable nearby AGN, and suggests magnetic jet launching.

We continued our focus of the inner region of 3C 84 in Sect. 4, where we introduced our analysis of six high-resolution (beam $< 50 \mu\text{as}$) GMVA maps of the source over the period between 2008–2015. We detect a persistent transverse nuclear structure. An analysis of the $H\beta$ lines revealed that the C1 complex is unlikely to be the jet base or the accretion disc, which confirms the result by Paraschos et al. (2021) that the BH is probably located upstream of the VLBI core. Utilising both conical and parabolic profile model fitting, we computed with this method that the jet apex is located $\sim 600 - 2400 R_g$ upstream and under the assumption of a BH mass of $3.2 \times 10^8 M_\odot$ (or $\sim 200 - 3000 R_g$ using the same BH mass and viewing angle assumptions as in Paraschos et al. 2021). A foreground absorber influencing these results cannot be ruled out, however. We also report tentative evidence for the correlation between the P. A. and the brightness temperature T_B of the C1a and C1b regions along with a tentative differentiation in the viewing angle between the C1 and C3 regions of 3C 84. This result might suggest that the jet is indeed spatially bent. It might also be indicative of the presence of moving jet components, in addition to being indirect evidence of γ -ray emission occurring within the C1 region.

Section 5 is a culmination of our efforts to understand the inner physical processes taking place in the nucleus of 3C 84. In this work, we analysed and are presenting a comprehensive historical view of 3C 84, based on more than two decades of observations at 86 GHz. We detected numerous components being ejected from the VLBI core, some of which we cross-identified at 43 and 86 GHz. We find that the 86 GHz components move marginally faster (2σ) than the 43 GHz components ($\mu_{\text{avg}}^{W2010} = 0.15 \pm 0.03 \text{ mas/yr}$ or $\beta_{\text{app}}^{W2010} = 0.18 \pm 0.04 c$ versus $\mu_{\text{avg}}^{Q2010} = 0.071 \pm 0.026 \text{ mas/yr}$ or $\beta_{\text{app}}^{Q2010} = 0.087 \pm 0.032 c$). We fit-

ted Gaussian functions to the jet profile, to determine the transverse jet width. Beside the inner core region at 86 GHz, where only one Gaussian function was sufficient, we fitted a sum of two Gaussian functions and considered the FWHM of the brighter of the two as indicative of the jet width. We find that jet width depends on the observing frequency in the ≤ 1.5 pc region, with the jet width increasing with decreasing frequency. This indicates a frequency dependent stratification of the jet. Fitting a power law index to the initial jet expansion region within the core points to a conical jet profile, with the power law indices being: $\gamma_{15} = 0.36 \pm 0.38$, $\gamma_{43} = 0.27 \pm 0.13$, and $\gamma_{86} = 0.90 \pm 0.06$. Finally, the spectral index maps of the individual epochs revealed that the spectral index gradient changes with orientation, indicating that jet features might be ejected into different directions at different times. The spectral index values range from $\alpha \sim 3 - 4$ in the north/northwest to $\alpha \sim -2$ in the south/southeast.

7 Outlook

The work in this thesis presents new findings from ultra-high-resolution VLBI imaging at short, millimetre wavelengths and a multi-frequency view of the nuclear and few-pc region of 3C 84. This was achieved by presenting detailed, high angular resolution observations of 3C 84 at 15, 43, and 86 GHz. However, many questions regarding the true physical nature of the jet base and jet origin of 3C 84 still remain unanswered.

Towards answering them, a series of new, multi-frequency, high-resolution observations of 3C 84 are ongoing. A three epoch monitoring of 3C 84 at 86 GHz with the GMVA, taking advantage of the improved recording capabilities of the involved stations, as well as the recent technological improvements, promises to reveal the inner depths of the core of the source in unprecedented detail. At the moment of the conclusion of this PhD thesis, the analysis of the first epoch is already taking place. Furthermore, 22 and 43 GHz observations, simultaneously observed the Global-EVN array, will provide the opportunity to study this source with polarimetry, in addition to spectrally. Specifically, 22 GHz observations can also serve as a direct comparison to the data from the *RadioAstron* mission, captured at the same frequency. Moreover, the EHT observed 3C 84 in its spring 2022 campaign. At 230 GHz these observations signify the highest resolution of the core of 3C 84 to date and show that imaging studies at these shorter wavelengths are feasible and promising. Besides the direct imaging of the jet origin, a combination of the quasi-simultaneous observations of the source at 86 GHz with the GMVA (just weeks apart), will also yield the highest resolution and highest frequency-pair spectral index maps.

Apart from the already conducted observations, it is vitally important to continue observing 3C 84 and other nearby AGN with next generation instruments. The VLBA-BU-BLAZAR project conducted by the Boston University AGN group and its successor BEAM-ME have been observing 3C 84 in an almost monthly cadence for more than a decade, with the VLBA array, at 43 GHz. Keeping up this observation rhythm is of utmost importance, since 3C 84 exhibits structural variability in time frames as short as few weeks. In the same vein, the in-house recently started M2FINDERS²² program aims to also monitor 3C 84 at 86 GHz. The next generation VLA (ngVLA), which will serve as a successor to the VLBA, will be highly important in this endeavour. It improves the current capabilities of the VLA and ALMA by increasing the sensitivity and spatial resolution by an order of magnitude, at the same wavelengths. Similarly the next generation EHT (ngEHT), will add ten more antennae to the existing EHT array,

²²<https://www.mpifr-bonn.mpg.de/m2finders>

thus improving its sensitivity and spatial resolution, promising even sharper images of 3C 84. Space-VLBI will also play a prominent role in the future observations of radio-galaxies like 3C 84. Even though the *RadioAstron* mission ceased its operation, a successor mission is on its way, named *Millimetron*. It will be placed at the Lagrange point L2 of the solar system in the anti-solar direction and will observe at wavelengths between 0.07 and 10 mm.

In summary, the multi-frequency and high-resolution imaging presented in this work demonstrates the capabilities of millimetre-VLBI, when applied to nearby radio-galaxies. In the near future and with further improved sensitivity, other nearby, but fainter radio-galaxies could be studied as well. Pilot surveys to find suitable candidates are already underway. For a systematic study of jet launching in different types of radio-galaxies (e.g. FRI and FRII) a more flexible scheduling of the EHT – also at other times of the year – would be highly desirable. Overall the future of VLBI observations in general, as well as specifically of 3C 84, looms brightly.

A Appendix

Here all the images of 3C 84, at 15, 43, and 86 GHz are presented, which are listed in Tables F1, F2, and F3, in Sect. 5.

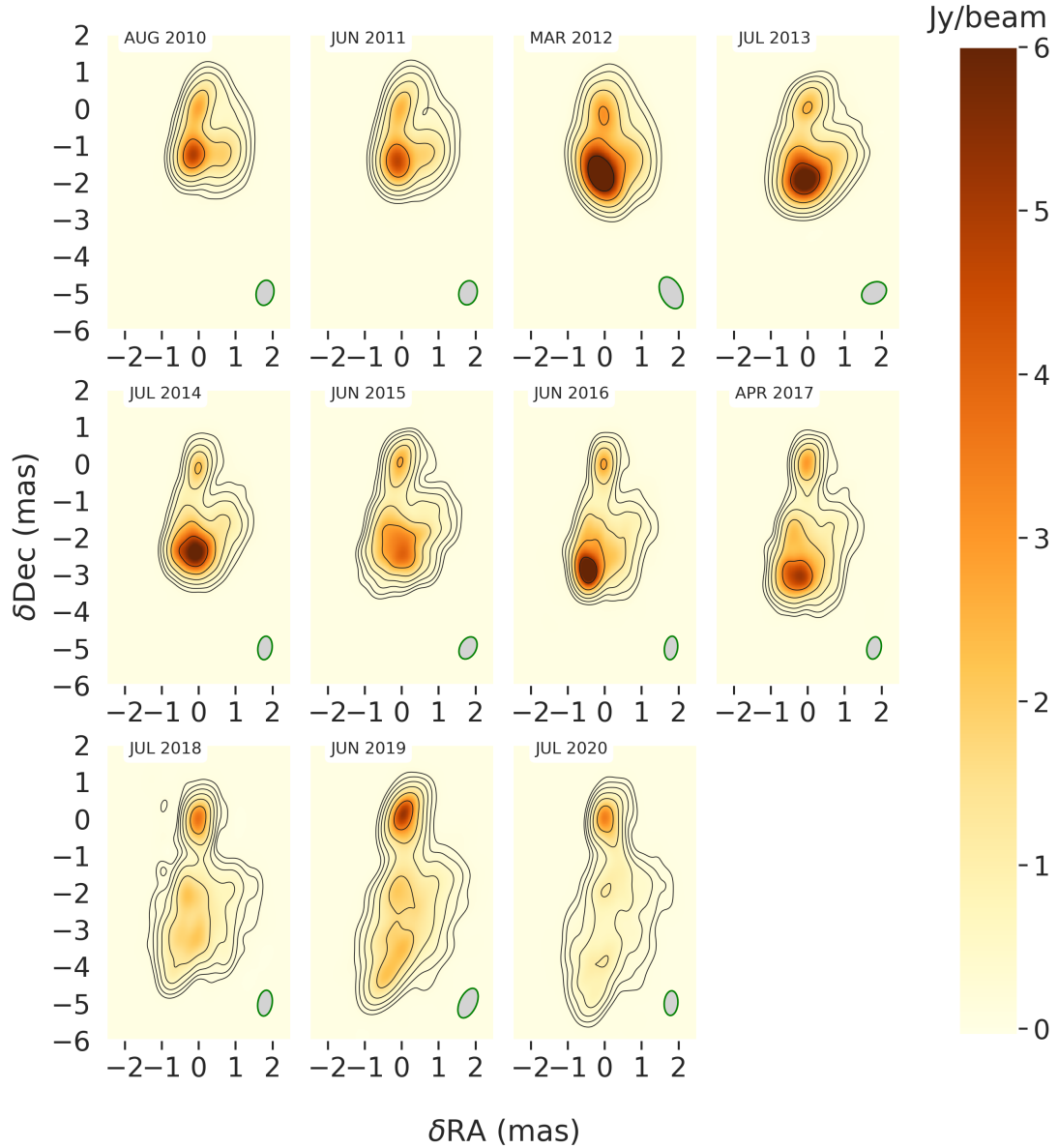


Figure 1.27: Total intensity images of 3C 84 at 15 GHz. The contour levels are 2, 4, 8, 16, 32, and 64% of the intensity maximum of each epoch. The ellipses in the bottom right corner of each plot represents the convolving beam size and are given, together with the maximum flux and rms, in Table F3 of Sect. 5.

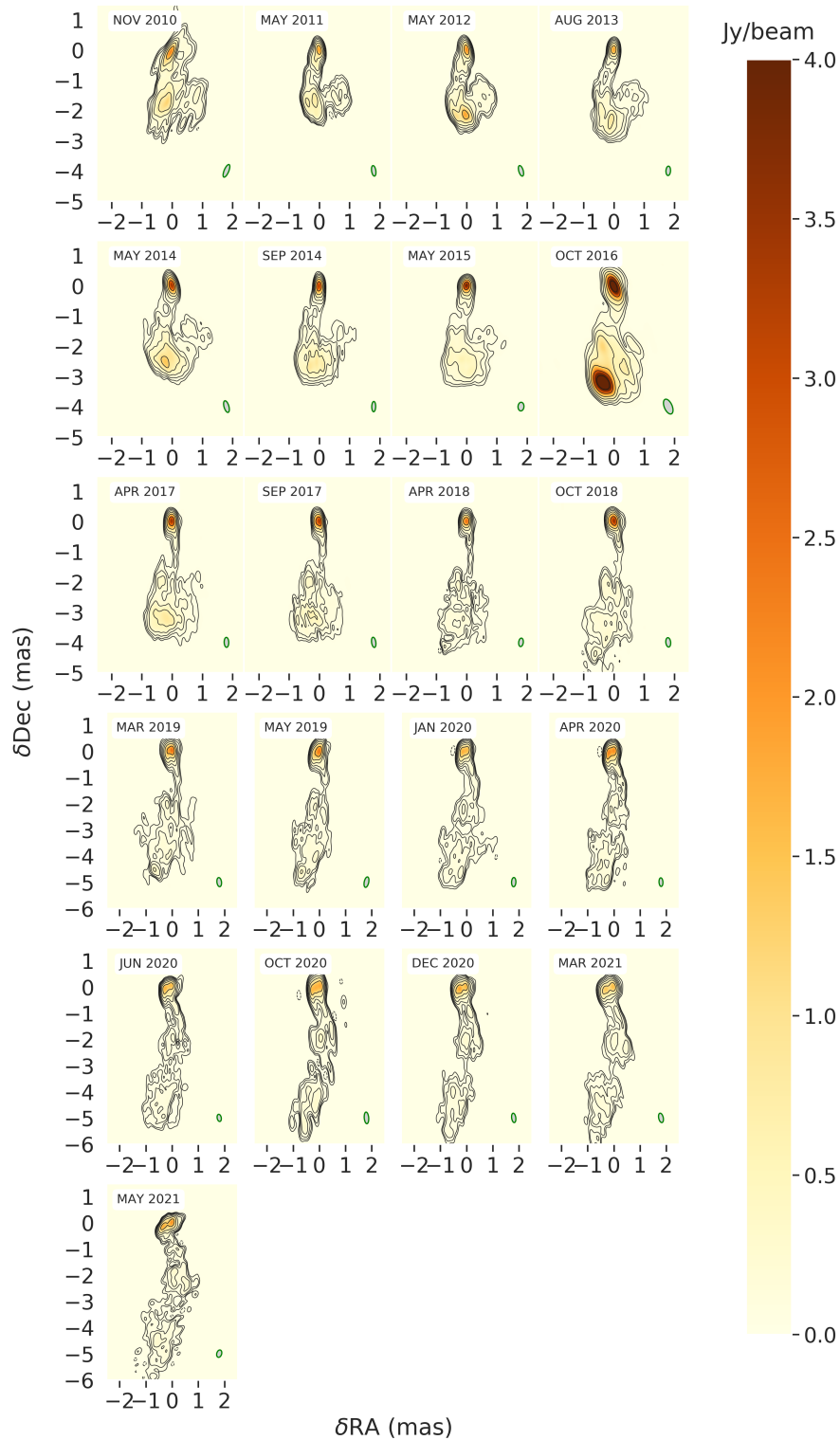


Figure 1.28: Total intensity images of 3C 84 at 43 GHz. The contour levels are the same as in Fig. 2 of Sect. 5. The ellipses in the bottom right corner of each plot represents the convolving beam size and are given, together with the maximum flux and rms, in Table F2 of Sect. 5.

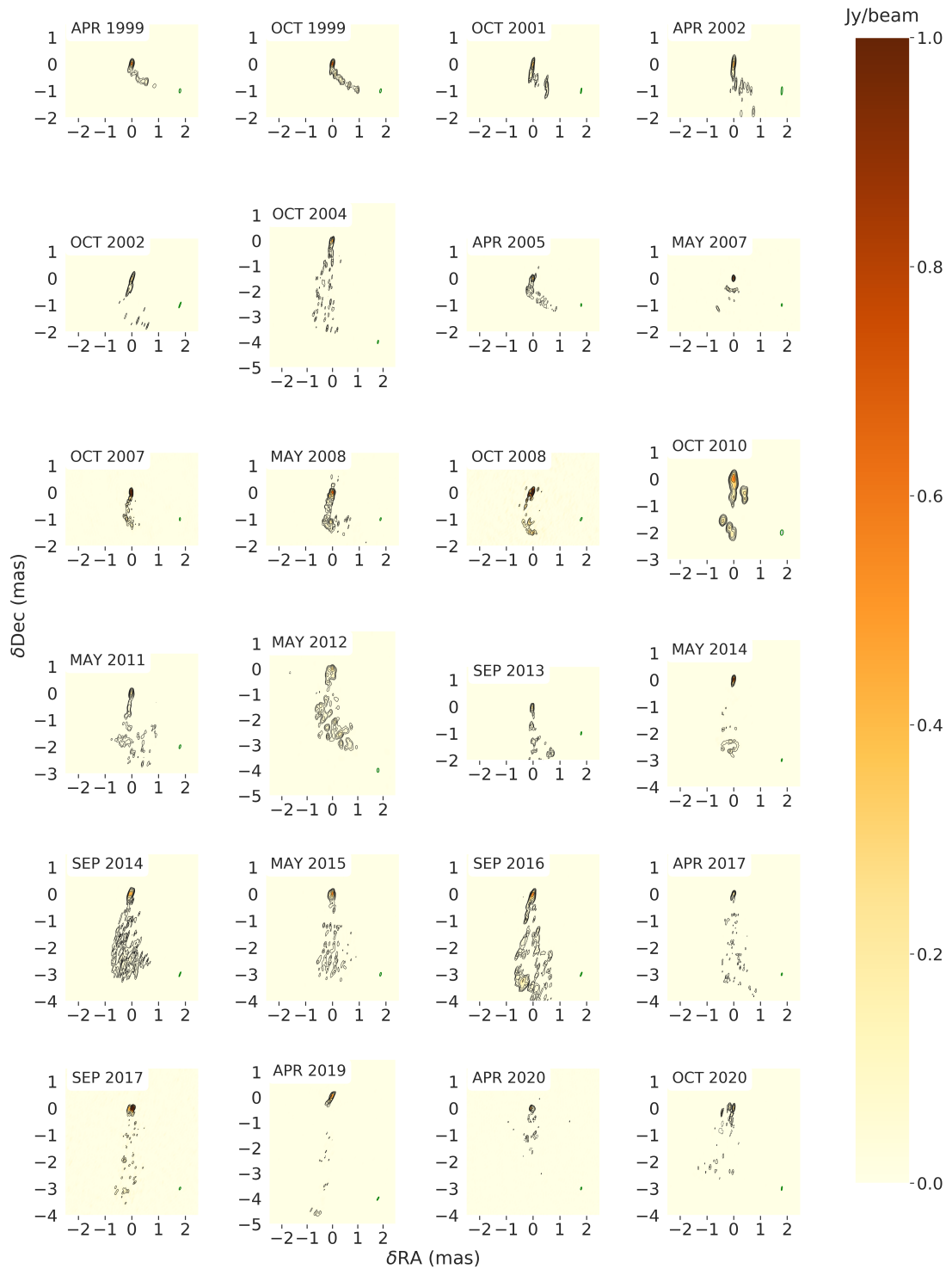


Figure 1.29: Total intensity images of 3C 84 at 86 GHz. The contour levels are the same as in Fig. 1 of Sect. 5. The ellipses in the bottom right corner of each plot represents the convolving beam size and are given, together with the maximum flux and rms, in Table F1 of Sect. 5.

References

- Abdo, A. A., Ackermann, M., Ajello, M., et al. 2009, *ApJ*, 699, 31
- Aleksić, J., Alvarez, E. A., Antonelli, L. A., et al. 2012, *A&A*, 539, L2
- Antonucci, R. 1993, *ARA&A*, 31, 473
- Astropy Collaboration, Price-Whelan, A. M., Sipőcz, B. M., et al. 2018, *AJ*, 156, 123
- Astropy Collaboration, Robitaille, T. P., Tollerud, E. J., et al. 2013, *A&A*, 558, A33
- Baade, W. & Minkowski, R. 1954, *ApJ*, 119, 215
- Baath, L. B., Rogers, A. E. E., Inoue, M., et al. 1992, *A&A*, 257, 31
- Backer, D. C., Wright, M. C. H., Plambeck, R. L., et al. 1987, *ApJ*, 322, 74
- Baldwin, J. E. & Elsmore, B. 1954, *Nature*, 173, 818
- Balick, B. & Brown, R. L. 1974, *ApJ*, 194, 265
- Balick, B. & Sanders, R. H. 1974, *ApJ*, 192, 325
- Bao, G. & Wiita, P. J. 1997, *ApJ*, 485, 136
- Bardeen, J. M. 1973, in *Black Holes (Les Astres Occlus)*, 215–239
- Bardeen, J. M., Press, W. H., & Teukolsky, S. A. 1972, *ApJ*, 178, 347
- Bartel, N., Dhawan, V., Krichbaum, T., Graham, D. A., & Pauliny-Toth, I. I. K. 1988, *Nature*, 334, 131
- Barthel, P. D. 1989, *ApJ*, 336, 606
- Bateman, G. 1978, *MHD instabilities*
- Beasley, A. J., Gordon, D., Peck, A. B., et al. 2002, *ApJS*, 141, 13
- Beckmann, V. & Shrader, C. R. 2012, *Active Galactic Nuclei*
- Blandford, R. D. & Payne, D. G. 1982, *MNRAS*, 199, 883
- Blandford, R. D. & Rees, M. J. 1978, in *BL Lac Objects*, ed. A. M. Wolfe, 328–341

REFERENCES

- Blandford, R. D. & Znajek, R. L. 1977, *MNRAS*, 179, 433
- Blumenthal, G. R. & Gould, R. J. 1970, *Reviews of Modern Physics*, 42, 237
- Boccardi, B., Krichbaum, T. P., Ros, E., & Zensus, J. A. 2017, *A&A Rev.*, 25, 4
- Bondi, H. 1952, *MNRAS*, 112, 195
- Bromley, B. C., Chen, K., & Miller, W. A. 1997, *ApJ*, 475, 57
- Burbidge, E. M. & Burbidge, G. R. 1965, *ApJ*, 142, 1351
- Burbidge, G. R., Burbidge, E. M., & Sandage, A. R. 1963, *Reviews of Modern Physics*, 35, 947
- Compton, A. H. 1923, *Physical Review*, 21, 483
- Condon, J. J. & Ransom, S. M. 2016, *Essential Radio Astronomy*
- Cornwell, T. & Fomalont, E. B. 1999, in *Astronomical Society of the Pacific Conference Series*, Vol. 180, *Synthesis Imaging in Radio Astronomy II*, ed. G. B. Taylor, C. L. Carilli, & R. A. Perley, 187
- Cornwell, T. J. & Evans, K. F. 1985, *A&A*, 143, 77
- Cotton, W. D. 1995, in *Astronomical Society of the Pacific Conference Series*, Vol. 82, *Very Long Baseline Interferometry and the VLBA*, ed. J. A. Zensus, P. J. Diamond, & P. J. Napier, 189
- Cunningham, C. T. & Bardeen, J. M. 1973, *ApJ*, 183, 237
- Davis, S. W. & Tchekhovskoy, A. 2020, *ARA&A*, 58, 407
- Deller, A. T., Brisken, W. F., Phillips, C. J., et al. 2011, *PASP*, 123, 275
- Dhawan, V., Bartel, N., Rogers, A. E. E., et al. 1990, *ApJ*, 360, L43
- Dhawan, V., Kellermann, K. I., & Romney, J. D. 1998, *ApJ*, 498, L111
- Doeleman, S. S., Shen, Z. Q., Rogers, A. E. E., et al. 2001, *AJ*, 121, 2610
- Event Horizon Telescope Collaboration, Akiyama, K., Alberdi, A., et al. 2022a, *ApJ*, 930, L12
- Event Horizon Telescope Collaboration, Akiyama, K., Alberdi, A., et al. 2022b, *ApJ*, 930, L13
- Event Horizon Telescope Collaboration, Akiyama, K., Alberdi, A., et al. 2022c, *ApJ*, 930, L14

REFERENCES

- Event Horizon Telescope Collaboration, Akiyama, K., Alberdi, A., et al. 2022d, *ApJ*, 930, L15
- Event Horizon Telescope Collaboration, Akiyama, K., Alberdi, A., et al. 2022e, *ApJ*, 930, L16
- Event Horizon Telescope Collaboration, Akiyama, K., Alberdi, A., et al. 2022f, *ApJ*, 930, L17
- Event Horizon Telescope Collaboration, Akiyama, K., Alberdi, A., et al. 2019a, *ApJ*, 875, L1
- Event Horizon Telescope Collaboration, Akiyama, K., Alberdi, A., et al. 2019b, *ApJ*, 875, L2
- Event Horizon Telescope Collaboration, Akiyama, K., Alberdi, A., et al. 2019c, *ApJ*, 875, L3
- Event Horizon Telescope Collaboration, Akiyama, K., Alberdi, A., et al. 2019d, *ApJ*, 875, L4
- Event Horizon Telescope Collaboration, Akiyama, K., Alberdi, A., et al. 2019e, *ApJ*, 875, L5
- Event Horizon Telescope Collaboration, Akiyama, K., Alberdi, A., et al. 2019f, *ApJ*, 875, L6
- Event Horizon Telescope Collaboration, Akiyama, K., Algaba, J. C., et al. 2021, *ApJ*, 910, L12
- Ewen, H. I. & Purcell, E. M. 1951, *Nature*, 168, 356
- Fabian, A. C., Sanders, J. S., Allen, S. W., et al. 2011, *MNRAS*, 418, 2154
- Falcke, H., Melia, F., & Agol, E. 2000, *ApJ*, 528, L13
- Fanaroff, B. L. & Riley, J. M. 1974, *MNRAS*, 167, 31P
- Fanton, C., Calvani, M., de Felice, F., & Cadez, A. 1997, *PASJ*, 49, 159
- Fath, E. A. 1909, *Lick Observatory Bulletin*, 149, 71
- Ferrari, A., Trussoni, E., & Zaninetti, L. 1978, *A&A*, 64, 43
- Frey, S. & Mosoni, L. 2009, *New A Rev.*, 53, 307
- Fujita, Y. & Nagai, H. 2017, *MNRAS*, 465, L94

REFERENCES

- Fukue, J. & Yokoyama, T. 1988, PASJ, 40, 15
- Giacconi, R. 1974, in Gravitational Radiation and Gravitational Collapse, ed. C. Dewitt-Morette, Vol. 64, 147
- Giacconi, R., Murray, S., Gursky, H., et al. 1974, ApJS, 27, 37
- Giovannini, G., Savolainen, T., Orienti, M., et al. 2018, Nature Astronomy, 2, 472
- Greisen, E. W. 1990, in Acquisition, Processing and Archiving of Astronomical Images, 125–142
- Gull, S. F. & Daniell, G. J. 1978, Nature, 272, 686
- Harris, C. R., Millman, K. J., van der Walt, S. J., et al. 2020, Nature, 585, 357
- Haschick, A. D., Crane, P. C., & van der Hulst, J. M. 1982, ApJ, 262, 81
- Hewish, A., Bell, S. J., Pilkington, J. D. H., Scott, P. F., & Collins, R. A. 1968, Nature, 217, 709
- Hewitt, A. & Burbidge, G. 1993, ApJS, 87, 451
- Hey, J. S. 1946, Nature, 157, 47
- Hodgson, J. A., Rani, B., Oh, J., et al. 2021, ApJ, 914, 43
- Högbom, J. A. 1974, A&AS, 15, 417
- Homan, D. C. & Wardle, J. F. C. 2004, ApJ, 602, L13
- Hu, E. M., Cowie, L. L., Kaaret, P., et al. 1983, ApJ, 275, L27
- Hubble, E. & Humason, M. L. 1931, ApJ, 74, 43
- Humason, M. L. 1932, PASP, 44, 267
- Hunter, J. D. 2007, Computing in Science & Engineering, 9, 90
- Jansky, K. G. 1933a, Popular Astronomy, 41, 548
- Jansky, K. G. 1933b, Nature, 132, 66
- Jaynes, E. T. 1957, Physical Review, 106, 620
- Jorstad, S. G., Marscher, A. P., Morozova, D. A., et al. 2017, ApJ, 846, 98
- Karamanavis, V. V. 2015, PhD thesis, Max-Planck-Institut für Radioastronomie
- Kellermann, K. I. & Moran, J. M. 2001, ARA&A, 39, 457

REFERENCES

- Kellermann, K. I. & Pauliny-Toth, I. I. K. 1969, *ApJ*, 155, L71
- Kellermann, K. I., Sramek, R., Schmidt, M., Shaffer, D. B., & Green, R. 1989, *AJ*, 98, 1195
- Kellermann, K. I., Sramek, R. A., Schmidt, M., Green, R. F., & Shaffer, D. B. 1994, *AJ*, 108, 1163
- Kerr, R. P. 1963, *Phys. Rev. Lett.*, 11, 237
- Kettenis, M., van Langevelde, H. J., Reynolds, C., & Cotton, B. 2006, in *Astronomical Society of the Pacific Conference Series*, Vol. 351, *Astronomical Data Analysis Software and Systems XV*, ed. C. Gabriel, C. Arviset, D. Ponz, & S. Enrique, 497
- Kim, J.-Y., Krichbaum, T. P., Broderick, A. E., et al. 2020, *A&A*, 640, A69
- Kim, J. Y., Krichbaum, T. P., Marscher, A. P., et al. 2019, *A&A*, 622, A196
- Krichbaum, T. P., Witzel, A., Graham, D. A., et al. 1992, *A&A*, 260, 33
- Kristian, J. 1973, *ApJ*, 179, L61
- Linhoff, L., Sandrock, A., Kadler, M., Elsässer, D., & Rhode, W. 2021, *MNRAS*, 500, 4671
- Lister, M. L., Aller, H. D., Aller, M. F., et al. 2009, *AJ*, 137, 3718
- Liu, B. F. 2013, in *Feeding Compact Objects: Accretion on All Scales*, ed. C. M. Zhang, T. Belloni, M. Méndez, & S. N. Zhang, Vol. 290, 62–65
- Lobanov, A. 2015, *A&A*, 574, A84
- Longair, M. S. 2011, *High Energy Astrophysics*
- Luminet, J. P. 1979, *A&A*, 75, 228
- Luminet, J.-P. 2019, *arXiv e-prints*, arXiv:1902.11196
- Lynden-Bell, D. 1969, *Nature*, 223, 690
- Lynden-Bell, D. & Rees, M. J. 1971, *MNRAS*, 152, 461
- Lynds, R. 1970, *ApJ*, 159, L151
- MAGIC Collaboration, Ansoldi, S., Antonelli, L. A., et al. 2018, *A&A*, 617, A91
- Marr, J. M., Backer, D. C., Wright, M. C. H., Readhead, A. C. S., & Moore, R. 1989, *ApJ*, 337, 671

REFERENCES

- Martí-Vidal, I., Krichbaum, T. P., Marscher, A., et al. 2012, *A&A*, 542, A107
- Mastichiadis, A. & Vlahakis, N. 2015, *Αστροφυσική υψηλών ενεργειών*
- Mertens, F. & Lobanov, A. 2015, *A&A*, 574, A67
- Misner, C. W., Thorne, K. S., & Wheeler, J. A. 1973, *Gravitation*
- Mizuno, Y., Hardee, P., & Nishikawa, K.-I. 2007, *ApJ*, 662, 835
- Mizuno, Y., Hardee, P. E., & Nishikawa, K.-I. 2011, *ApJ*, 734, 19
- Moran, J. M. 1998, in *Astronomical Society of the Pacific Conference Series, Vol. 144, IAU Colloq. 164: Radio Emission from Galactic and Extragalactic Compact Sources*, ed. J. A. Zensus, G. B. Taylor, & J. M. Wrobel, 1
- Nagai, H., Chida, H., Kino, M., et al. 2016, *Astronomische Nachrichten*, 337, 69
- Nagai, H., Fujita, Y., Nakamura, M., et al. 2017, *ApJ*, 849, 52
- Nagai, H., Haga, T., Giovannini, G., et al. 2014, *ApJ*, 785, 53
- Nagai, H., Orienti, M., Kino, M., et al. 2012, *MNRAS*, 423, L122
- Nagai, H., Suzuki, K., Asada, K., et al. 2010, *PASJ*, 62, L11
- Novikov, I. D. & Thorne, K. S. 1973, in *Black Holes (Les Astres Occlus)*, 343–450
- Oh, J., Hodgson, J. A., Trippe, S., et al. 2022, *MNRAS*, 509, 1024
- Orr, M. J. L. & Browne, I. W. A. 1982, *MNRAS*, 200, 1067
- Padovani, P. 1999, in *Vulcano Workshop 1998: Frontier Objects in Astrophysics and Particle Physics*, ed. F. Giovannelli & G. Mannocchi, Vol. 65, 159
- Page, D. N. & Thorne, K. S. 1974, *ApJ*, 191, 499
- pandas development team, T. 2020, *pandas-dev/pandas: Pandas*
- Paraschos, G., Kim, J. Y., Krichbaum, T., et al. 2022a, in *European VLBI Network Mini-Symposium and Users' Meeting 2021*, 43
- Paraschos, G. F., Kim, J. Y., Krichbaum, T. P., & Zensus, J. A. 2021, *A&A*, 650, L18
- Paraschos, G. F., Krichbaum, T. P., Kim, J. Y., et al. 2022b, *arXiv e-prints*, arXiv:2205.10281
- Park, J. & Trippe, S. 2017, *ApJ*, 834, 157

REFERENCES

- Penrose, R. 1969, *Nuovo Cimento Rivista Serie*, 1, 252
- Penrose, R. & Floyd, R. M. 1971, *Nature Physical Science*, 229, 177
- Penston, M. V., Penston, M. J., Selmes, R. A., Becklin, E. E., & Neugebauer, G. 1974, *MNRAS*, 169, 357
- Penzias, A. A. & Wilson, R. W. 1965, *ApJ*, 142, 419
- Planck Collaboration, Ade, P. A. R., Aghanim, N., et al. 2016, *A&A*, 594, A13
- Punsly, B., Nagai, H., Savolainen, T., & Orienti, M. 2021, *ApJ*, 911, 19
- Reber, G. 1944, *ApJ*, 100, 279
- Richards, J. L., Max-Moerbeck, W., Pavlidou, V., et al. 2011, *ApJS*, 194, 29
- Romero, G. & Gutiérrez, E. 2020, *Universe*, 6, 99
- Rowan, D. J. & Stephenson, G. 1977, *Journal of Physics A Mathematical General*, 10, 15
- Rubin, V. C., Ford, W. K., J., Peterson, C. J., & Oort, J. H. 1977, *ApJ*, 211, 693
- Rybicki, G. B. & Lightman, A. P. 1979, *Radiative processes in astrophysics*
- Ryle, M., Smith, F. G., & Elsmore, B. 1950, *MNRAS*, 110, 508
- Salpeter, E. E. 1964, *ApJ*, 140, 796
- Savolainen, T., Giovannini, G., Kovalev, Y. Y., et al. 2021, *arXiv e-prints*, arXiv:2111.04481
- Scharwächter, J., McGregor, P. J., Dopita, M. A., & Beck, T. L. 2013, *MNRAS*, 429, 2315
- Scheuer, P. A. G. & Readhead, A. C. S. 1979, *Nature*, 277, 182
- Seyfert, C. K. 1943, *ApJ*, 97, 28
- Shakura, N. I. & Sunyaev, R. A. 1973, *A&A*, 500, 33
- Shepherd, M. C., Pearson, T. J., & Taylor, G. B. 1994, in *Bulletin of the American Astronomical Society*, Vol. 26, 987–989
- Stoche, J. T., Morris, S. L., Weymann, R. J., & Foltz, C. B. 1992, *ApJ*, 396, 487
- Strauss, M. A., Huchra, J. P., Davis, M., et al. 1992, *ApJS*, 83, 29

REFERENCES

- Suzuki, K., Nagai, H., Kino, M., et al. 2012, *ApJ*, 746, 140
- Taylor, G. B., Gugliucci, N. E., Fabian, A. C., et al. 2006, *MNRAS*, 368, 1500
- Tchekhovskoy, A. 2015, in *Astrophysics and Space Science Library*, Vol. 414, *The Formation and Disruption of Black Hole Jets*, ed. I. Contopoulos, D. Gabuzda, & N. Kylafis, 45
- Tchekhovskoy, A. & Bromberg, O. 2016, *MNRAS*, 461, L46
- Thompson, A. R., Moran, J. M., & Swenson, George W., J. 2017, *Interferometry and Synthesis in Radio Astronomy*, 3rd Edition
- Trippe, S., Bremer, M., Krichbaum, T. P., et al. 2012, *MNRAS*, 425, 1192
- Türler, M., Courvoisier, T. J. L., & Paltani, S. 1999, *A&A*, 349, 45
- Turnshek, D. A. 1984, *ApJ*, 280, 51
- Unwin, S. C., Mutel, R. L., Phillips, R. B., & Linfield, R. P. 1982, *ApJ*, 256, 83
- Urry, C. M. & Padovani, P. 1995, *PASP*, 107, 803
- van Cittert, P. H. 1934, *Physica*, 1, 201
- Venturi, T., Readhead, A. C. S., Marr, J. M., & Backer, D. C. 1993, *ApJ*, 411, 552
- Vermeulen, R. C., Readhead, A. C. S., & Backer, D. C. 1994, *ApJ*, 430, L41
- Viergutz, S. U. 1993, *A&A*, 272, 355
- Virtanen, P., Gommers, R., Oliphant, T. E., et al. 2020, *Nature Methods*, 17, 261
- Wajima, K., Kino, M., & Kawakatu, N. 2020, *ApJ*, 895, 35
- Walker, R. C., Dhawan, V., Romney, J. D., Kellermann, K. I., & Vermeulen, R. C. 2000, *ApJ*, 530, 233
- Walker, R. C., Romney, J. D., & Benson, J. M. 1994, *ApJ*, 430, L45
- Waskom, M. L. 2021, *Journal of Open Source Software*, 6, 3021
- Weaver, H., Williams, D. R. W., Dieter, N. H., & Lum, W. T. 1965, *Nature*, 208, 29
- Weedman, D. W. 1973, *ApJ*, 183, 29
- Wernecke, S. J. & D'Addario, L. R. 1977, *IEEE Transactions on Communications*, 26, 351

REFERENCES

- Wes McKinney. 2010, in Proceedings of the 9th Python in Science Conference, ed. Stéfan van der Walt & Jarrod Millman, 56 – 61
- Wilkinson, P. N. 1989, in NATO Advanced Study Institute (ASI) Series C, Vol. 283, Techniques and Applications of Very Long Baseline Interferometry, ed. M. Felli & R. E. Spencer, 69–93
- Wilson, T. L., Rohlfs, K., & Hüttemeister, S. 2013, Tools of Radio Astronomy
- Wolf, M. 1906, *Astronomische Nachrichten*, 170, 211
- Wright, M. C. H., Backer, D. C., Carlstrom, J. E., et al. 1988, *ApJ*, 329, L61
- Zernike, F. 1938, *Physica*, 5, 785

Astronomy and Astrophysics

Editor in Chief: T. Forveille

T. Forveille

Astronomy & Astrophysics
Observatoire de Paris
61, avenue de l'Observatoire
75014 Paris, France

Tel.: 33 0(1) 43 29 05 41
Fax: 33 0(1) 43 29 05 57
e-mail: aanda.paris@obspm.fr
Web: <http://www.aanda.org>

merging
Annales d'Astrophysique
Arkiv for Astronomi
Bulletin of the Astronomical Institutes
of the Netherlands
Bulletin Astronomique
Journal des Observateurs
Zeitschrift fur Astrophysik
Bulletin of the Astronomical Institutes
of Czechoslovakia

Paris, 17 January 2022

Reprint Permission

Material:

Article by Paraschos et al. 2021, A&A, 650, L18

To be used in:

PhD dissertation, at the University of Cologne

Permission granted to:

Georgios Filippou Paraschos
gfparaschos@mpifr-bonn.mpg.de

I hold copyright on the material referred to above, and hereby grant permission for its use as requested herewith.

The article should be reproduced as a whole in a coherent fashion fully consistent with the version published in A&A.

Credit should be given as follows:

Credit: Author, A&A, vol, page, year, reproduced with permission © ESO.



Thierry Forveille
A&A Editor-in-Chief

Sponsored by Argentina, Armenia, Austria, Belgium, Bulgaria, Chile, Croatia, Czech Republic, Denmark, Estonia, Finland, France, Germany, Greece, Hungary, Italy, Lithuania, Netherlands, Norway, Poland, Portugal, Slovak Republic, Spain, Sweden, and Switzerland.

Produced and distributed by EDP Sciences for ESO.

Astronomy and Astrophysics

Editor in Chief: T. Forveille

T. Forveille

Astronomy & Astrophysics
Observatoire de Paris
61, avenue de l'Observatoire
75014 Paris, France

Tel.: 33 0(1) 43 29 05 41
Fax: 33 0(1) 43 29 05 57
e-mail: aanda.paris@obspm.fr
Web: <http://www.aanda.org>

merging
Annales d'Astrophysique
Arkiv for Astronomi
Bulletin of the Astronomical Institutes
of the Netherlands
Bulletin Astronomique
Journal des Observateurs
Zeitschrift fur Astrophysik
Bulletin of the Astronomical Institutes
of Czechoslovakia

Paris, 8 September 2022

Reprint Permission

Material:

Article by Paraschos et al. 2022, A&A, 665, A1

To be used in:

PhD dissertation, at the University of Cologne

Permission granted to:

Georgios Filippou Paraschos
gffparaschos@mpifr-bonn.mpg.de

I hold copyright on the material referred to above, and hereby grant permission for its use as requested herewith.

The article should be reproduced as a whole in a coherent fashion fully consistent with the version published in A&A.

Credit should be given as follows:

Credit: Author, A&A, vol, page, year, reproduced with permission © ESO.



Thierry Forveille
A&A Editor-in-Chief

Sponsored by Argentina, Armenia, Austria, Belgium, Bulgaria, Chile, Croatia, Czech Republic, Denmark, Estonia, Finland, France, Germany, Greece, Hungary, Italy, Lithuania, Netherlands, Norway, Poland, Portugal, Slovak Republic, Spain, Sweden, and Switzerland.

Produced and distributed by EDP Sciences for ESO.

Acknowledgements

G. F. Paraschos is supported for this research by the International Max-Planck Research School (IMPRS) for Astronomy and Astrophysics at the University of Bonn and Cologne. This research has made use of data obtained with the Global Millimeter VLBI Array (GMVA), which consists of telescopes operated by the MPIfR, IRAM, Onsala, Metsähovi, Yebes, the Korean VLBI Network, the Green Bank Observatory and the Long Baseline Observatory (LBO). The VLBA is an instrument of the LBO, which is a facility of the National Science Foundation operated by Associated Universities, Inc. The data were correlated at the correlator of the MPIfR in Bonn, Germany. This work makes use of the Swinburne University of Technology software correlator, developed as part of the Australian Major National Research Facilities Programme and operated under licence.

This work makes use of 43 GHz VLBA data from the VLBA-BU Blazar Monitoring Program (VLBA-BU-BLAZAR; <http://www.bu.edu/blazars/VLBAproject.html>), funded by NASA through the Fermi Guest Investigator Program.

This work makes use of data from the MOJAVE database that is maintained by the MOJAVE team (Lister et al. 2009).

This work makes use of ALMA data. ALMA is a partnership of ESO (representing its member states), NSF (USA) and NINS (Japan), together with NRC (Canada), MOST and ASIAA (Taiwan), and KASI (Republic of Korea), in cooperation with the Republic of Chile. The Joint ALMA Observatory is operated by ESO, AUI/NRAO and NAOJ.

This work makes use of 37 GHz, and 230 and 345 GHz light curves kindly provided by the Metsähovi Radio Observatory and the Submillimeter Array (SMA), respectively. The SMA is a joint project between the Smithsonian Astrophysical Observatory and the Academia Sinica Institute of Astronomy and Astrophysics and is funded by the Smithsonian Institution and the Academia Sinica. This work makes use of data from the University of Michigan Radio Astronomy Observatory which has been supported by the University of Michigan and by a series of grants from the National Science Foundation, most recently AST-0607523. This research has also made use of data from the OVRO 40-m monitoring program (Richards et al. 2011), supported by private funding from the California Institute of Technology and the Max Planck Institute for Radio Astronomy, and by NASA grants NNX08AW31G, NNX11A043G, and NNX14AQ89G and NSF grants AST-0808050 and AST-1109911.

This work makes use of the NASA/IPAC Extragalactic Database (NED), which is operated by the Jet Propulsion Laboratory, California Institute of Technology, under contract with the National Aeronautics and Space Administration. This work has also makes use of NASA's Astrophysics Data System Bibliographic

Acknowledgements

Services.

Finally, this work made use of the following python packages: numpy (Harris et al. 2020), scipy (Virtanen et al. 2020), matplotlib (Hunter 2007), astropy (Astropy Collaboration et al. 2018, 2013), pandas (pandas development team 2020; Wes McKinney 2010), seaborn (Waskom 2021), and Uncertainties: a Python package for calculations with uncertainties.

Personal acknowledgement

At this point I would like to take the opportunity to thank everyone who contributed to the realisation and completion of this thesis. First and foremost I would like to thank my supervisor Dr. Thomas Krichbaum, whose scientific guidance over the past three years ensured the success of this thesis. His door being always open and his willingness to share his depth of knowledge made our day-to-day interaction a pleasure, and I look forward to further collaboration.

Of course, my deep gratitude goes to Prof. Dr. Anton Zensus, who welcomed me to his group and provided me with the opportunity to conduct this thesis, with the support of the International Max Planck Research School. My gratitude also goes to Prof. Dr. Jae-Young Kim, with whom I enjoyed an excellent collaboration. I would furthermore like to thank the other members of my Thesis Advisory Committee, Prof. Dr. Andreas Eckart, Prof. Dr. Eduardo Ros, and Dr. Gunther Witzel, whose advice and counsel throughout this journey were pivotal. My gratitude also goes to Dr. Nicholas MacDonald for reviewing and improving the included manuscripts and Dr. Uwe Bach and Dr. Alex Kraus for the technical assistance they provided during observations. I am also thankful to all the other members of the VLBI group, who were always there and willing to share their knowledge and experiences.

I would also like to thank my office mates Hui-Hsuan, Pedro, Dongjin, Aleksei, Felix, and Thalia for the pleasant interactions and fond memories.

Maintaining a work-life balance was another important aspect to completing this work. In this regard, I would like to thank my friends for keeping me company both in person and over the internet. A special thanks goes out to Andreas, Thodoris, and Vasilis, with whom I started this journey into physics together some years ago. I also sincerely thank my basketball teammates from the Blazing Suns, for allowing me to pursue my hobby and all the fun we have had.

In closing, I would like to extend my deepest gratitude to my supportive family, specifically my parents Dimosthenis and Cosima, as well as my girlfriend Van, who have been standing by me unconditionally.



Georgios Filippas Paraschos

Personal data

Place, D.o.B. Athens, Greece, 04 September 1995.

Work address **Auf dem Hügel**, 53121, Bonn, Germany.

Contact **+49 1627003436**, **+30 697 8379711**, gparaschos@mpifr.de, gepara@phys.uoa.gr.

ORCID [0000-0001-6757-3098](https://orcid.org/0000-0001-6757-3098).

Academic track

- 2019–2022 **PhD Diploma**, *Max Planck Institute for Radio Astronomy*, Bonn,
Title: *A comprehensive analysis of the nucleus of the radio source 3C 84 with VLBI* | Scientific supervisor: Dr. T. P. Krichbaum.
- 2018–2019 Master thesis in the research group of Prof. K. Dasyra at the National Observatory of Athens.
- 2017–2019 **Master Diploma**, *National and Kapodistrian University*, Athens, Grade: *Highest ranking grade*.
Thesis: [Spatially resolved excitation study of CO molecules in active galactic nuclei](#)
- 2014–2017 **Ptychion**, *National and Kapodistrian University*, Athens, Grade: *First class honours*.
Thesis: [Study of the excitation of the molecular gas in typical conditions of the interstellar space](#)

Full list of publications

- 2022 **Paraschos** et al. 2022, submitted: A multiband study and exploration of the radio wave – γ -ray connection in 3C 84
- 2022 **Paraschos** et al. 2022: [Jet kinematics in the transversely stratified jet of 3C 84: A two-decade overview](#)
- 2022 **Paraschos** et al. 2022: [Pinpointing the jet apex in 3C 84](#)
- 2022 Dasyra, **Paraschos** et al. 2022: [Linking pressure gradients with the stability of molecular clouds in galactic outflows](#)
- 2022 Event Horizon Telescope Collaboration et al. (incl. **Paraschos**) 2022: [First Sagittarius A* Event Horizon Telescope Results. I. The Shadow of the Supermassive Black Hole in the Center of the Milky Way](#)
- 2022 Event Horizon Telescope Collaboration et al. (incl. **Paraschos**) 2022: [First Sagittarius A* Event Horizon Telescope Results. II. EHT and Multiwavelength Observations, Data Processing, and Calibration](#)
- 2022 Event Horizon Telescope Collaboration et al. (incl. **Paraschos**) 2022: [First Sagittarius A* Event Horizon Telescope Results. III. Imaging of the Galactic Center Supermassive Black Hole](#)
- 2022 Event Horizon Telescope Collaboration et al. (incl. **Paraschos**) 2022: [First Sagittarius A* Event Horizon Telescope Results. IV. Variability, Morphology, and Black Hole Mass](#)
- 2022 Event Horizon Telescope Collaboration et al. (incl. **Paraschos**) 2022: [First Sagittarius A* Event Horizon Telescope Results. V. Testing Astrophysical Models of the Galactic Center Black Hole](#)
- 2022 Event Horizon Telescope Collaboration et al. (incl. **Paraschos**) 2022: [First Sagittarius A* Event Horizon Telescope Results. VI. Testing the Black Hole Metric](#)
- 2022 Broderick et al. (incl. **Paraschos**) 2022: [Characterizing and Mitigating Intraday Variability: Reconstructing Source Structure in Accreting Black Holes with mm-VLBI](#)
- 2022 Issaoun et al. (incl. **Paraschos**) 2022: [Resolving the Inner Parsec of the Blazar J1924-2914 with the Event Horizon Telescope](#)
- 2022 Georgiev et al. (incl. **Paraschos**) 2022: [A Universal Power-law Prescription for Variability from Synthetic Images of Black Hole Accretion Flows](#)
- 2022 Wielgus et al. (incl. **Paraschos**) 2022: [Millimeter Light Curves of Sagittarius A* Observed during the 2017 Event Horizon Telescope Campaign](#)

Curriculum Vitae

- 2022 Plavin et al. (incl. **Paraschos**) 2022: [The radio blazar TXS 1749-101 coincident with two high-energy neutrinos: IceCube alerts 181023A and the recent 220425A](#)
- 2022 Kadler et al. (incl. **Paraschos**) 2022: [TELAMON: Monitoring of AGN with the Effelsberg 100-m Telescope in the Context of Astroparticle Physics](#)
- 2022 deMenezes et al. (incl. **Paraschos**) 2022: [Multi-Messenger observations of the Fermi-LAT blazar 4FGL J0658.6+0636 consistent with an IceCube high-energy neutrino](#)
- 2022 The MAGIC Collaboration et al. (incl. **Paraschos**) 2022: [Multi-epoch monitoring of TXS 0506+056 with MAGIC and MWL partners](#)
- 2022 Oh et al. (incl. **Paraschos**) 2022: [A persistent double nuclear structure in 3C 84](#)
- 2021 Kadler et al. (incl. **Paraschos**) 2021: [TELAMON: Effelsberg Monitoring of AGN Jets with Very-High-Energy Astroparticle Emissions](#)
- 2021 **Paraschos** et al. 2021: [Pinpointing the jet apex of 3C 84](#)